Universität Hamburg
DER FORSCHUNG | DER LEHRE | DER BILDUNG

Simulations of Dark Matter with Frequent and Rare Self-Interactions

Dissertation

zur Erlangung des Doktorgrades
an der Fakultät für Mathematik,
Informatik und Naturwissenschaften

Fachbereich Physik
der Universität Hamburg

vorgelegt von
Moritz Serenus Fischer

Hamburg
2022

Gutachter der Dissertation:	Prof. Dr. Marcus Brüggen Dr. Kai Schmidt-Hoberg
Zusammensetzung der Prüfungskommission:	Prof. Dr. Marcus Brüggen Dr. Kai Schmidt-Hoberg Prof. Dr. Jochen Liske Prof. Dr. Peter H. Hauschildt Prof. Dr. Stephan Rosswog
Vorsitzender der Prüfungskommission:	Prof. Dr. Jochen Liske
Datum der Disputation:	22.08.2022
Vorsitzender Fach-Promotionsausschusses PHYSIK:	Prof. Dr. Wolfgang J. Parak
Leiter des Fachbereichs PHYSIK:	Prof. Dr. Günter H. W. Sigl
Dekan der Fakultät MIN:	Prof. Dr. Heinrich Graener

Zusammenfassung

Die Natur der Dunklen Materie (DM) ist eine der großen unbeantworteten Fragen der heutigen Physik. Eine Vielzahl an Modellen wurde vorgeschlagen, um die Beobachtungen, die auf DM hinweisen zu erklären. Die Phänomenologie dieser Modelle zu verstehen und Grenzen für selbige abzuleiten oder sie ganz auszuschließen, ist ein ständig voranschreitendes Unterfangen der aktuellen Forschung. In dieser Arbeit konzentrieren wir uns auf eine bestimmte Klasse von Modellen, die selbstwechselwirkende dunkle Materie (SIDM). Diese Klasse ist vielversprechend, um Diskrepanzen zwischen Beobachtungen und Vorhersagen auf der Größenskala von Galaxien erklären zu können oder zumindest abzuschwächen. Insbesondere untersuchen wir Teilchenmodelle, die kleine Streuwinkel bevorzugen (häufige Selbstwechselwirkungen).

In der Vergangenheit hat sich gezeigt, dass es schwierig ist, solche sehr anisotropen differentiellen Wirkungsquerschnitte in N-Körpersimulationen zu modellieren. Bisher gab es hierfür kein Verfahren, auch wenn Simulationen von Modellen mit einem typischerweise großen Streuwinkel (seltene Selbstwechselwirkungen) seit mehr als zwei Jahrzehnten durchgeführt werden. Wir haben dieses Problem gelöst und das erste numerische Schema eingeführt, das es erlaubt, häufige Streuung für Probleme wie die Verschmelzungen von Galaxienhaufen oder auch kosmische Strukturbildung zu simulieren.

Anhand einer Reihe von Problemen untersuchen wir die Unterschiede zwischen selten selbstwechselwirkender dunkler Materie (rSIDM) und häufig selbstwechselwirkender dunkler Materie (fSIDM). Bei der Verschmelzung von Galaxien und Galaxienhaufen stellen wir fest, dass fSIDM in der Lage ist, einen größeren Versatz zwischen der DM und einer kollisionsfreien Komponente (Sterne, Galaxien) zu erklären. Bei Verschmelzungen mit ungleichem Massenverhältnis wird die Winkelabhängigkeit der Streuung für die resultierende Materieverteilung noch wichtiger als bei Verschmelzungen mit gleichem Massenverhältnis.

Außerdem untersuchen wir die Phänomenologie der Selbstwechselwirkungen im kosmologischen Kontext. Hierbei stellt sich heraus, dass sich rSIDM und fSIDM in vielen Aspekten ähnlich verhalten, zum Beispiel bei den Dichte- und Formprofilen der DM-Halos. Die Häufigkeit der Satellitenhalos zeigt jedoch, dass häufige Selbstwechselwirkung die Satelliten stärker unterdrückt als seltene Selbstwechselwirkungen. In Kombination mit anderen Größen wie der Ausdehnung des DM-Kerns oder der Form der Materieverteilung könnte es schließlich möglich sein, zwischen einem isotropen und einem sehr anisotropen Wechselwirkungsquerschnitt zu unterscheiden.

Abstract

The nature of dark matter (DM) is one of the big unanswered questions of physics today. A plethora of models has been proposed to explain DM. Understanding their phenomenology and putting constraints on them is an ongoing task. In this thesis, we focus on one particular class of models, self-interacting dark matter (SIDM). This class is promising to solve or at least mitigate the small-scale crisis of the cosmological standard model. We pay particular attention to models favouring small scattering angles (frequent self-interactions).

In the past, it turned out to be difficult, to model very anisotropic differential cross-sections having high scattering rates within N-body simulations, although simulations of large-angle scattering (rare self-interactions) are common. We have solved this problem and introduced the first numerical scheme that allows simulating frequent scattering for problems such as mergers or cosmic structure formation.

Through several problems, we study differences between rarely self-interacting dark matter (rSIDM) and frequently self-interacting dark matter (fSIDM). For mergers of galaxies and galaxy clusters, we find fSIDM to be capable of explaining larger offsets between DM and a collisionless component (stars, galaxies). For unequal-mass mergers, the angular dependence of the scattering is even more relevant for the resulting matter distribution than in equal-mass mergers.

Furthermore, we study the phenomenology of self-interactions in the cosmological context. We find that rSIDM and fSIDM behave similar in many aspects, for example, the density and shape profiles of DM haloes. In contrast, the abundance of satellites reveals that frequent scattering suppresses satellites more efficiently than rare self-interactions do. In combination with constraints from other measures such as the DM core size or the shape, it could eventually be possible to distinguish between an isotropic and a very anisotropic cross-section.

Acknowledgements

The emergence of this thesis has different roots and may seem rather coincidental with me as a doctoral candidate, but it was a number of people who made it possible this way and have thus enabled a small scientific step forward, at least I hope so. I am grateful to all those who have contributed to my path, even if without the least intention to do so.

I would especially like to thank my supervisor Marcus Brüggen, on whom I could always rely and who supported me as much as possible. My thanks go to my co-supervisor Kai Schmidt-Hoberg for our discussions and his contributions. Unfortunately, our offline meetings stopped with the onset of the COVID-19 pandemic. Moreover, I want to thank all my further collaborators for their contributions to our publications. They are Felix Kahlhöfer, Antonio Raganin, Andrew Robertson and Klaus Dolag, who allows me to continue my scientific career beyond the PhD. My thanks also go to Janis Kummer for helpful comments and discussions. He did his PhD on SIDM in Hamburg and studied fSIDM too (Kummer, 2019) and I sort of continued his work with this thesis. Moreover, I would like to thank all the people at the Hamburg Observatory who have turned this beautiful place into a wonderful research environment and made my time there very enjoyable. I am also grateful to have had the opportunity to supervise two talented students, Lenard Kasselmann and Nils Durke, who also worked on simulations of SIDM.

But it took a lot more than this to get me here. All the support I received before and during my physics studies can hardly be mentioned here. My thanks also go to the people who were involved in the Heidelberg Life-Science Lab and accompanied me on my way at that stage. For the time in Heidelberg and the path towards my doctoral studies, I would like to explicitly thank Hubert Klahr, Ahmad A. Hujeirat and especially Eva K. Grebel. Even if I can not prove it, there is one book whose importance can hardly be underestimated, if I learned to think for myself it was through the Critique of Pure Reason (Kant, 1787).

My special thanks go to my family and, in particular, my mother. They have always supported me and without them I would certainly not be where I am today. Finally, my thanks go to Alaa and her support as well as those I may have missed mentioning explicitly but made me have a great time during my PhD.

This thesis was funded by the Deutsche Forschungsgemeinschaft (DFG, German Research Foundation) under Germany's Excellence Strategy – EXC 2121 "Quantum Universe" – 390833306.

This thesis is based on the following publications:

- M. S. Fischer, M. Brüggen, K. Schmidt-Hoberg, K. Dolag, F. Kahlhoefer, A. Ragagnin, and A. Robertson, N-body simulations of dark matter with frequent self-interactions, 2021a, MNRAS, 505, 851
- M. S. Fischer, M. Brüggen, K. Schmidt-Hoberg, K. Dolag, A. Ragagnin, and A. Robertson, Unequal-mass mergers of dark matter haloes with rare and frequent self-interactions, 2021b, MNRAS, 510, 4080
- M. S. Fischer, M. Brüggen, K. Schmidt-Hoberg, K. Dolag, F. Kahlhoefer, A. Ragagnin, and A. Robertson, Cosmological simulations with rare and frequent dark matter self-interactions, 2022, arXiv: 2205.02243

Contents

List of Abbreviations

AGN	**A**ctive **G**alatic **N**uclei
BCG	**B**rightest **C**luster **G**alaxy
BH	**B**lack **H**ole
CDM	**C**old **D**ark **M**atter
CMB	**C**osmological **M**icrowave **B**ackground
DM	**D**ark **M**atter
FDM	**F**uzzy **D**ark **M**atter
fSIDM	**f**requently **S**elf-**I**nteracting **D**ark **M**atter
GR	**G**eneral **R**elativity
ICM	**I**ntra **C**luster **M**edium
ΛCDM	**L**ambda **C**old **D**ark **M**atter
JWST	**J**ames **W**ebb **S**pace **T**elescope
MW	**M**ilky **W**ay
MMR	**M**erger **M**ass **R**atio
NFW	**N**avarro–**F**renk–**W**hite
PBH	**P**rimordial **B**lack **H**ole
PDF	**P**robability **D**ensity **F**unction
rSIDM	**r**arely **S**elf-**I**nteracting **D**ark **M**atter
SIDM	**S**elf-**I**nteracting **D**ark **M**atter
SKA	**S**quare **K**ilometer **A**rray
SM	**S**tandard **M**odel
UDG	**U**ltra-**D**iffuse **G**alaxy
WDM	**W**arm **D**ark **M**atter
WIMP	**W**eakly **I**nteracting **M**assive **P**article

1 Motivation

Astronomy has a history that dates long back to the early civilisations of mankind. Its subject has always been intertwined with big questions and answers that shaped the human view of the world. Many things that appear self-evident to us today required great effort. What is the nature of the shining dots in the night sky? Are they of the same kind as the sun? And how distant are they? Today we know this and many other things about our Universe. But new questions have always arisen as we gained further insights. Thanks to Galileo Galilei and the invention of the telescope, we know that the diffusely glowing band in the night sky consists of numerous stars, our galactic home, the Milky Way (MW) (Galilei, 1610). The modern view dates back to Thomas Wright, who thought of the MW as a system of rotating stars bound by gravity (Wright, 1750). Furthermore, he speculated that there might be many systems like our Galaxy. His ideas became popular with Immanuel Kant's progression and refinement of them (Kant, 1755). From that time, it took more than a century until it became clear that objects such as the Andromeda nebula are separate galaxies on their own. There had been quite a controversy about this issue leading to a debate between Harlow Shapley and Heber Curtis in 1920. Today it is known to astronomers as the Great Debate. A few years later, Edwin Hubble resolved that pressing question. In the 1920s, he was able to demonstrate with observations of Cepheid variable stars that Andromeda is far outside the MW (Hubble, 1929). It is the case that when we take a closer look at things, new questions emerge. Vera Rubin and Kent Ford studied the rotation velocity of stars in spiral galaxies, starting with Andromeda. They found a miss-match between observed rotation curves and the one predicted based on the distribution of luminous matter. With this, they provided a key piece of evidence for the existence of DM, which can explain the observed rotation curves (Rubin & Ford, 1970). The potential existence of a matter component, which we do not see, had been pointed out earlier by other astrophysicists. Among the first ones was Fritz Zwicky with his studies of the Coma Cluster (Zwicky, 1933, 1937). Numerous observations of the large-scale structure, galaxy cluster masses, gravitational lensing studies and more followed, pointing towards DM too (e.g. Arbey & Mahmoudi, 2021). It became clear that DM makes up the largest fraction of the matter in the universe, estimated to be about 84% (Planck Collaboration et al., 2020). But until today, the nature of DM remains largely unknown. A vast number of models exist that eventually could explain DM. Many studies are carried out to shrink the possible parameter space for DM candidates. With this, we are at the very issue of this thesis.

Here, we study the phenomenology of a class of particle physics models that do not only

interact via gravity but also involve new physics allowing the DM particles to scatter about each other, known as self-interacting dark matter (SIDM). These models are of particular interest to resolve discrepancies between simulations of the cosmological standard model, ΛCDM, and observations on small, i.e. galactic scales. There exist several problems, and many of them are closely connected, forming together the small-scale crisis of ΛCDM. Specifically, we are interested in understanding the phenomenology of models that typically scatter about a tiny angle. Compared to models having a larger typical scattering angle or even an isotropic cross-section, which we also call rarely self-interacting dark matter (rSIDM), they would interact frequently (fSIDM). Such a cross-section is well motivated from the particle physics side by light mediator models (e.g. Buckley & Fox, 2010; Loeb & Weiner, 2011; Bringmann et al., 2017). But fSIDM has only been studied poorly, as it has not been possible to faithfully model problems such as mergers of galaxies or galaxy clusters, although there has been a lot of interest. We aim to overcome this unsatisfactory situation by developing a novel scheme that allows general modelling of fSIDM and by undertaking corresponding studies. With this, we gain new insights into the phenomenology of DM models and thus hopefully get a little closer to a comprehension of the nature of DM.

The only way DM physics is accessible to us today is through astronomical surveys. Hence it is crucial to derive predictions from DM models for observations. The formation of cosmic structures behaves non-linearly, and many physical processes play a role. Consequently, the problem becomes complicated and usually requires running computationally expensive simulations. We undertake our studies employing N-body simulations to investigate various DM models. As we are interested in fSIDM, we introduce a numerical scheme that allows – for the first time – to model frequent self-interactions from first principles. We use this scheme to study mergers of galaxies and galaxy clusters as well as cosmic structure formation. From our simulations, we gain new insights into the role of the angular dependence of the differential cross-section for the phenomenology of DM models. We describe qualitative differences between rSIDM and fSIDM as well as give the first constraints on the fSIDM cross-section.

Outline

This thesis is structured as follows. In Chapter 2, we explain the theoretical background for our work. In particular, we describe the cosmological standard model ΛCDM, its small-scale crisis and elaborate on SIDM. In the following, we introduce in Chapter 3 the first numerical scheme that allows for N-body simulations of frequent DM scattering without making simplifying assumptions about the problem at hand, such as assuming quasi-equilibrium. Besides, we introduce a number of test problems for this new scheme and perform simulations of equal mass mergers. The concern of Chapter 4 are unequal mass mergers. Here, we study the morphology of the mergers, their DM–galaxy offsets as well as their shape and additional properties. In Chapter 5 we focus on cosmological simulations and study the qualitative differences between rare and frequent self-interactions

by measuring various properties such as the power spectrum, the halo mass function, density and shape profile. These chapters correspond each to a separate publication, i.e. Chapter 3 to Fischer et al. (2021a), Chapter 4 to Fischer et al. (2021b) and Chapter 5 to Fischer et al. (2022). Finally, we conclude in Chapter 6 and give an outlook on the research perspective for SIDM.

2 Introduction

We begin this chapter by briefly reviewing the cosmological standard model and describing the current state of DM research. It follows a more detailed description of SIDM, including a discussion about particle physics models, methods to model their phenomenology and observational constraints.

2.1 The cosmological standard model and its small-scale crisis

Edwin Hubble did not only discover that Andromeda is a separate galaxy on its own. But he also found that most galaxies are receding, which makes their spectrum appear shifted towards lower frequencies, i.e. they are redshifted. This has been a key observation for the construction of the cosmological standard model, ΛCDM. This observation is explained by the expansion of space which is mathematically described by the Friedmann-Lemaître equation derived from general relativity (GR). It connects the energy and matter content of the Universe to its expansion rate and is based on two fundamental assumptions. First, the Universe is assumed to be isotropic, which means that there is no preferred direction. Secondly, the Copernican principle, which states our place (and any other place) in the Universe is not special. From these assumptions, also known as the cosmological principle, it follows that the universe is homogeneous. The Friedmann-Lemaître equation describes the evolution of the Hubble parameter, $H \coloneqq \dot{a}/a$, as a function of time.

$$H^2(t) = H_0^2 \left[\Omega_{\mathrm{r},0}\, a^{-4} + \Omega_{\mathrm{m},0}\, a^{-3} + \Omega_\Lambda + \Omega_{\mathrm{K},0} a^{-2} \right] . \tag{2.1}$$

The scale factor a describes how large a length has been compared to its toady's value and the Hubble constant H_0 gives the current expansion rate. From GR follows that the structure of the space-time depends on the energy and mass content of the Universe. There are three corresponding parameters describing the radiation, $\Omega_{\mathrm{r},0}$, and matter, $\Omega_{\mathrm{m},0}$, content of today's Universe as well as the current values of the cosmological constant or vacuum density, Ω_Λ. The parameters are given by the corresponding density divided by the critical density, which specifies the density required for a flat space-time according to GR. Note, that the matter density is the sum of the baryonic and DM components. The cosmological constant, Λ, does not evolve with time and makes up $\sim 69\%$ of the energy content of the Universe (Planck Collaboration et al., 2020). The last parameter, $\Omega_{\mathrm{K},0}$, specifies the "curvature density" and satisfies the relation $\Omega_\mathrm{K} = 1 - \Omega_\mathrm{r} - \Omega_\mathrm{m} - \Omega_\Lambda$.

Furthermore, ΛCDM has proven to explain the observed large-scale structure remarkably

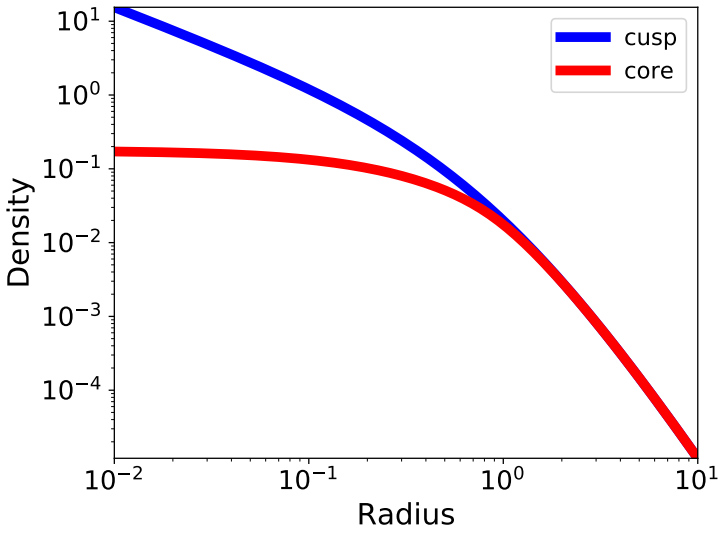

Figure 2.1: The density as a function of radius is shown for an NFW profile (blue) and a cored profile (red).

well.[1] Here, DM is assumed to be cold and collisionless. Early predictions for the large-scale structure have been obtained from N-body simulations modelling only DM. In particular, the Millennium Run (Springel et al., 2005) and the Bolshoi Simulation (Klypin et al., 2011) played an important role. Despite the success on large scales, it turned out that these simulations disagree with observations on small scales, i.e. the scales of galaxies and below. There are discrepancies in a number of aspects, such as the density profile of DM haloes, the variation of rotation curves between objects or the abundance of satellites. These issues are closely related and together they form the small-scale crisis of ΛCDM, which is by now known for more than two decades.

One of those problems is the core-cusp problem. Haloes that form in a DM-only simulation are well described by the Navarro–Frenk–White (NFW) profile. However, in general, this is not true for observed haloes. Often they appear to have a constant density in the central region. In contrast, an NFW profile has a higher central density with a steep density gradient. We illustrate the different density profiles in Fig. 2.1. Further small-scale problems are the diversity problem, concerning the huge variation of rotation curves between objects. Or the too-big-to-fail problem, describing discrepancies between the most massive satellites of observed systems and ΛCDM predictions. For a review of those and further small-scale issues, we refer to Bullock & Boylan-Kolchin (2017).

Over the last two decades, several approaches that may solve the small-scale crisis have been pursued. A clear solution has not been found yet, it seems more plausible that a combination of multiple attempts to solve small-scale issues will resolve them. In the following, we discuss briefly several efforts that are undertaken.

First, one avenue to find a potential solution is to investigate alternative theories of

[1] Nevertheless, ΛCDM is facing challenges on large and small scales, for a review see Perivolaropoulos & Skara (2021).

gravity. They were first studied as an alternative to DM but would ideally also solve problems of collisionless cold dark matter (CDM). A variety of theories that could replace GR have been investigated. The best known is probably modified Newtonian dynamics (Milgrom, 1983) but there exist many more. However, these models face problems in explaining some astronomical observations. Precisely, merging galaxy clusters, where the gravitational lensing signal has been found to not coincide with the location of the gas, pose a challenge (e.g. Clowe et al., 2006). Moreover, the first detection of gravitational waves (Abbott et al., 2017) ruled out several alternatives to GR. For more details see the review by Baker et al. (2021).

Secondly, we want to mention alternative DM models. As the predictions derived from CDM do not accurately describe observed small-scale structures, alternative DM models have been investigated. Of particular interest are warm dark matter (WDM), fuzzy dark matter (FDM) and SIDM as they are capable of suppressing substructure. In the next section, we will discuss the DM research and these models in larger detail.

Third, there is another important aspect to consider, the impact of baryons. The first cosmological simulations that revealed differences between ΛCDM and observations did only model DM without including the effect of baryons. Though baryons can impact the matter distribution on small scales, for example, the feedback from supernovae can create density cores (e.g. Read & Gilmore, 2005). But it is difficult to quantify their impact, because modelling feedback mechanisms in cosmological simulations, is subject to sizeable uncertainties. Further insights into the physics of these feedback mechanisms which take place below the resolution length of the simulation may help to improve the modelling.

Lastly, we want to mention that it is crucial how accurate observations and ΛCDM predictions are compared. This is, in particular, relevant to the core-cusp problem. It has turned out that the analysis of observed galaxies tends to be biassed towards a cored halo. Inaccuracies in the characterisation make the central density appear lower. Actually, the halo might be cuspy, but due to the analysis, it appears to be cored. This affects many dwarf galaxies where the density profile is inferred from rotation curves (e.g. Pineda et al., 2016; Read et al., 2016; Genina et al., 2018; Oman et al., 2019; Roper et al., 2022). Consequently, it is important to carefully model the internal dynamics of galaxies to reduce the bias towards a cored halo.

2.2 Dark matter research

Gaining insights into the nature of DM is one of the great challenges of physics today. Numerous approaches are being pursued, theorists have developed a variety of models, many experiments are underway, and astrophysicists have come up with various observational strategies and are conducting large surveys. The following section is a brief discussion of efforts to search for DM, as well as potential DM candidates. For more details, see one of the numerous reviews that exist on DM (e.g. Arun et al., 2017; Buckley & Peter, 2018;

Salucci, 2019; Arbey & Mahmoudi, 2021; Boddy et al., 2022).

2.2.1 Search for dark matter

DM research started with astronomical observations that pointed towards a missing force that could be explained by additional matter. This matter, called dark matter, has not been observed directly. Hence it does not or only very weakly interact electromagnetically. However, the influence of DM via gravity is observable. For instance, gravitational lensing studies allow inferring the distribution of DM in the Universe. Besides, a variety of experiments are carried out to detect potential interactions between DM and standard model (SM) particles. We focus first on astronomical studies and then discuss particle physics experiments.

Astronomical evidence for dark matter

All evidence for DM comes from astronomy, implying that it is the only way that gives us direct access to DM physics today. Moreover, it could be that SM and DM sectors are decoupled and DM physics is only accessible through observations. The properties of DM models and potential new DM physics leave their imprint on the distribution of matter in the Universe and can be probed through astronomical surveys. In turn, there is a chance that we can learn about the microscopical properties of DM through observations. A variety of probes to study DM physics exists in astronomy, for a review on galactic scales see Salucci (2019).

We have already mentioned the rotation curves of spiral galaxies (Rubin & Ford, 1970), but there exists more evidence for DM. In elliptical galaxies, the mass can be inferred in a similar way to the rotation curves of spiral galaxies. The velocity dispersion of their stars depends on the depth of the gravitational potential and thus allows for measuring the mass (e.g. Cappellari et al., 2006; Churazov et al., 2010). Such studies indicate that DM would make up a major fraction of the mass of these objects. There are several other dynamical measurements of the mass distribution that provide evidence for DM. Such measures are not only applied to galaxies but also to galaxy clusters. For the latter, for instance, the observed X-ray emission of the intracluster medium (ICM) allows for mass estimates (e.g. Amodeo, S. et al., 2016).

A powerful tool to probe the distribution of DM is gravitational lensing. Light rays are bent under the influence of mass, which allows inferring information about the distribution of matter from images of lensed objects, such as galaxies. The images of the lensed objects are distorted by the mass of the lens and may appear as multiple arcs depending on the exact configuration of the lens and the lensed objects. The distortion of the lensed images allows inferences to be drawn about the mass distribution of the lens. For a review on gravitational lensing see Bartelmann (2010). In the case of galaxies and galaxy clusters, gravitational lensing observations yield that most of the mass is not directly visible and therefore counted as DM (Massey et al., 2010).

Photons that have been emitted in the early Universe at the time of recombination, corresponding to a redshift of about $z \sim 1100$, are today observed as the cosmological microwave background (CMB). These photons allow us to draw numerous conclusions about the Universe and make the CMB a tremendous powerful probe for cosmology. Several satellites and ground-based experiments have been used or are used to measure the CMB. These include the COBE satellite (Smoot et al., 1992; Bennett et al., 1996) and the later satellite missions with superior instruments, WMAP (Wilkinson Microwave Anisotropy Probe, Bennett et al., 2003, 2013) and Planck (Planck Collaboration et al., 2014, 2016). CMB measurements and the inferred power spectrum allow to constrain DM models (e.g. Sarkar et al., 2017; Huo et al., 2018).

Observations of the large-scale structure, i.e. the distribution of galaxies in the Universe, enable us to draw conclusions about DM. The distance between galaxies and how they clump together depends crucially on DM. Predictions from ΛCDM simulations (e.g. Springel et al., 2006) match the observations remarkably well (e.g. Rodríguez-Torres et al., 2016). This is seen as another piece of evidence for DM and detailed measures of the galaxy distribution such as the two-point correlation function (see Section 5.3.4) are used to constrain DM models.

A lot of attention has been paid to galactic scales as the ΛCDM predictions seem to deviate from the observations at these scales. There is the hope that small-scale issues could allow to rule out ΛCDM. However, it remains open whether this will happen or not. Recent reviews of DM in the context of small-scale problems have been written by de Martino et al. (2020) and Fairbairn (2022). Our Galaxy, the MW, is here of particular interest. Thanks to high precision astrometry with Gaia, stellar positions and velocities are measured with unprecedented accuracy (Gaia Collaboration et al., 2016). Especially, stellar stream, the MW satellites and field stars allow deriving new constraints on DM models (e.g. Gardner et al., 2021). Besides, dwarf galaxies are of particular interest for DM studies as the baryonic component is less dominant than in more massive objects. Hence, dwarfs provide a good testbed for DM physics (e.g. Lelli, 2022). Future surveys will allow us to study these objects and others in larger detail. In Section 6.2, we briefly review the role of upcoming observatories and future surveys for DM, specifically SIDM.

Experimental search

The astronomical evidence for DM matter has fostered experimental search programs in the particle physics community to find particles beyond the SM. Such searches aim to find DM particles, which would require interactions between the dark sector and SM particles. Unfortunately, there has yet not been any evidence for this, rather all evidence for DM comes from astronomy. Moreover, experimental evidence for particles beyond the SM does not necessarily imply that it is connected to the astrophysical probes of DM but would require additional evidence. There are three different types of experiments that are conducted to find DM. We illustrate these different approaches in Fig. 2.2 and discuss them

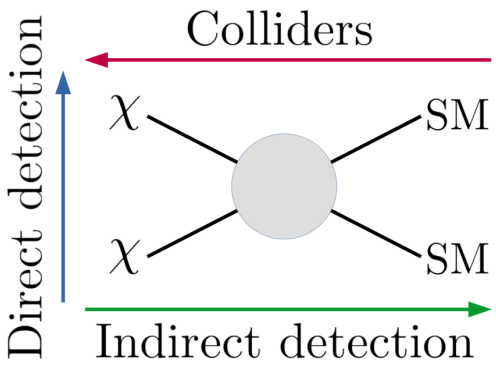

Figure 2.2: Schematic representation of DM particle search types. This figure is reproduced from fig. 9 of Arbey & Mahmoudi (2021).

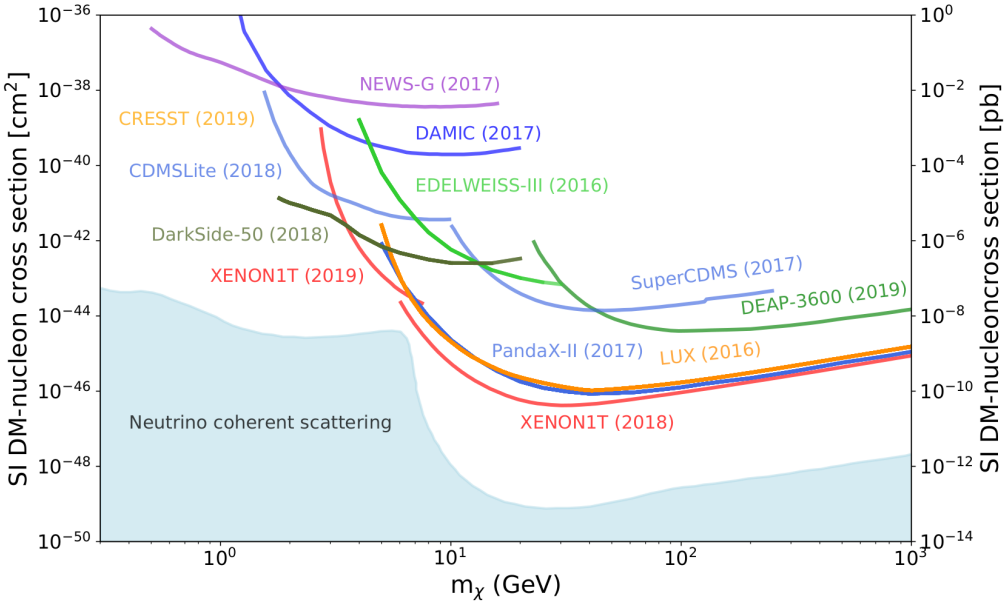

Figure 2.3: Upper limits on the spin-independent DM-nucleon cross-section are shown as a function of DM mass. This figure is reproduced from fig. 27.1 of Particle Data Group et al. (2020).

briefly. For more details, we refer to a review of DM research from the particle physics perspective (chap. 27, Particle Data Group et al., 2020).

First, there are direct detection experiments. Here, DM would interact with SM particles such as the nucleons or electrons of an atom. Experimentalists try to measure the recoil energy of nuclei to detect potential DM–SM interactions. There exist a number of experiments to constrain the DM particle mass and the scattering cross-section (e.g. Cui et al., 2017; Agnese et al., 2018; Arnaud et al., 2018; Agnese et al., 2019; Aprile et al., 2019a,b). In Fig. 2.3 we show recent constraints on DM properties from direct detection experiments.

Secondly, there are indirect detection experiments that aim to detect either the annihilation or decay products of DM particles. DM annihilation usually produces γ-rays, which in

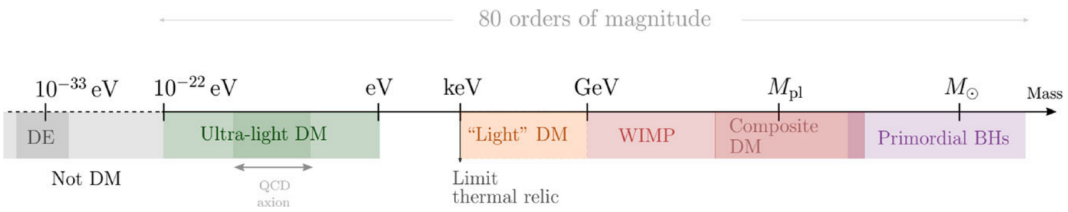

Figure 2.4: Illustration of the mass range of DM models that have been studied. This figure is reproduced from fig. 1 of Ferreira (2021).

principle could be detected. Observatories such as the Fermi Large Area Telescope (Atwood et al., 2009) and ground-based facilities provide γ-ray surveys that allow searching for DM signals. One of the most stringent constraints on DM pair-annihilation comes from dwarf spheroidal galaxies (Ackermann et al., 2015). Other typical end states of DM annihilation or decay are cosmic rays and neutrinos. Facilities such as IceCube or ANTARES look for DM signals in neutrino fluxes but yield null results (Aartsen et al., 2016; Adrián-Martínez et al., 2016).

Thirdly, collider experiments, i.e. the production of DM in accelerators, could provide evidence. The DM particles would be invisible to the detectors and thus carry energy and momentum away. This lack of energy and momentum would point towards new physics beyond the SM. A number of searches have been carried out by the CMS and ATLAS collaborations at the LHC (e.g. Kahlhoefer, 2017; Trevisani, 2018; Vannerom, 2019). However, so far there has not been any positive detection and only upper limits on the interaction between SM and DM particles have been placed.

2.2.2 Dark matter models

Here we review the various classes of DM models. We start with cold and collisionless DM and discuss more complex DM candidates. They are spanning a large mass range of about 80 orders of magnitude (see Fig. 2.4) and hence require different approaches to be constrained. Here we will not be able to mention all models, but at least some of them. It should be mentioned that DM could consist of multiple components, i.e. DM comprises various candidates, each making up a fraction of the mass budget. How rich the physics of the dark sector are, is yet to be discovered. In the following, we will go through a variety of DM model classes and some of their candidates.

Cold dark matter

Cold dark matter, usually thought to be collisionless, is a crucial part of the cosmological standard model and can explain the observed large-scale structure quite well. From the particle physics side, there has been a lot of research on weakly interacting massive particles (WIMPs), which are good candidates for CDM (Steigman & Turner, 1985; Griest, 1988). Often DM candidates arise naturally by solving issues in particle physics. In this sense, WIMPs are connected with electroweak-scale new physics that address the hierarchy

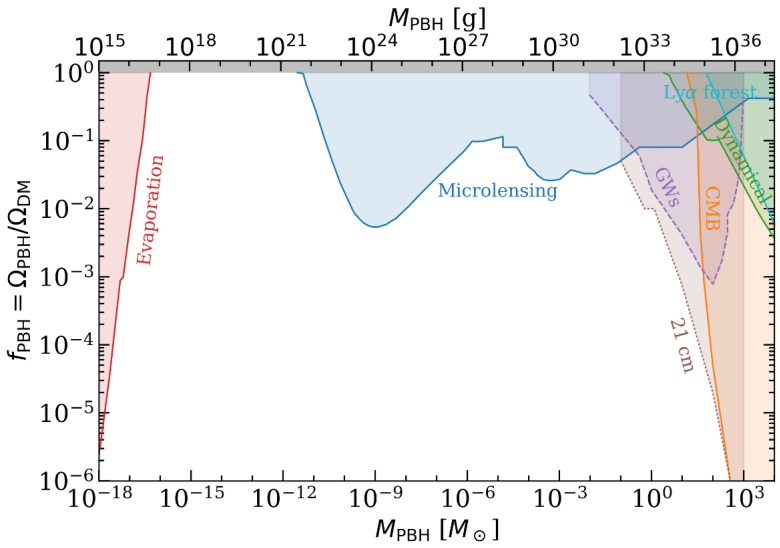

Figure 2.5: The proportion of PBHs to the total DM mass is shown as a function of the PBH mass. The shaded regions indicate the excluded parameter space by various probes. This figure is reproduced from fig. 2 of Villanueva-Domingo et al. (2021).

problem. Particles that behave as CDM could interact with the SM sector and may be visible in direct or indirect detection experiments (see Section 2.2.2). However, potential interactions between SM and DM particles may not only be probed by particle physics experiments. Astrophysical observations can allow to constrain such interactions too (e.g. Buen-Abad et al., 2022).

Interesting particle candidates in this context are axions, which have a putative coupling to photons (e.g. chap. 91, Particle Data Group et al., 2020). Given a sufficient particle mass, they can be considered as CDM. The QCD axion was introduced as a solution to the strong CP problem and provides a viable DM candidate (Peccei & Quinn, 1977; Weinberg, 1978; Wilczek, 1978). Several astronomical studies try to indirectly detect axions using radio (e.g. Bai & Hamada, 2018; Battye et al., 2020; Wang et al., 2021), X-ray (e.g. Day & Krippendorf, 2018; Buschmann et al., 2021) or γ-ray (e.g. Hooper & Serpico, 2007) observations. For further experimental detection strategies see Semertzidis & Youn (2022).

Another group of models that falls into the class of CDM are primordial black holes (PBH), which form soon after the Big Bang. The key parameter is their mass and various surveys have been used to constrain PBHs. For instance, these are microlensing studies such as OGLE (Udalski et al., 1992). A major part of the mass range has been excluded such that PBHs are unlikely to explain the entire DM but eventually make up a minor fraction. This can be seen from Fig. 2.5 and more details can be found in the review of Villanueva-Domingo et al. (2021) or Carr & Kühnel (2022).

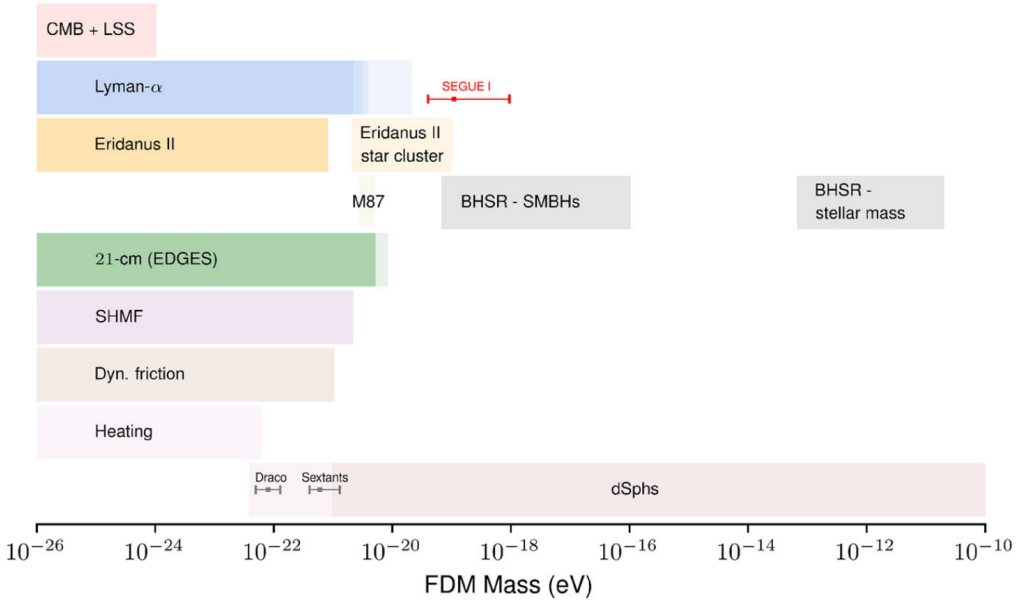

Figure 2.6: Constraints on the FDM particle mass from various studies are shown (for details see Ferreira, 2021). Under the assumption that FDM makes up most of the DM in the Universe, the shaded regions are excluded. This figure is reproduced from fig. 18 of Ferreira (2021).

Warm dark matter

In Dodelson & Widrow (1994), WDM is introduced by considering sterile neutrinos as DM candidates. The small mass of the particles leads to a significant thermal velocity dispersion. The success of CDM is kept on large scales, but WDM predicts a different DM distribution on small scales with suppressed substructure below its free-streaming length (Colin et al., 2000). Observations of the Lyman-α forest appear to be compatible with CDM and thus imply a very strong bound on how warm DM could be (e.g. Efstathiou et al., 2000; Viel et al., 2013; Palanque-Delabrouille et al., 2020; Garzilli et al., 2021).

Fuzzy dark matter

The idea that DM could consist of particles as light such as their de Broglie wavelength is larger than the interparticle distance has been explored as a solution to the small-scale problems (Hu et al., 2000). In this context axions and axion-like particles are studied, but generally, ultra-light bosonic DM candidates would imply the imprint of quantum effects on astrophysical scales. These models keep the success of CDM on large scales but form soliton-like cores in DM haloes that can be described as a Bose-Einstein condensate. Several studies using various probes for FDM, for example, the Lyman-α forest (Rogers & Peiris, 2021), have been conducted. In consequence, a lot of the parameter space for FDM candidates has been excluded as shown in Fig. 2.6. For a recent review on FDM see Ferreira (2021).

Self-interacting dark matter

In addition to the models already discussed, there has been quite some effort in studying DM candidates, which do not only interact via gravity but have additional self-interactions. This class of models is known as self-interacting dark matter. If the DM particle self-scattering is strong enough it can alter the matter distribution on small scales and in the limit of a vanishing self-interaction cross-section, it behaves as CDM. It is worth mentioning that one does not explicitly assume interactions between DM and SM particles to be present. Consequently, SIDM research focuses on physics which is, as a matter of principle, inaccessible for experimental searches but requires astronomical studies. Nevertheless, SIDM candidates could also couple to the SM sector and for example be detected in collider searches. In the next section, we discuss SIDM in larger detail.

2.3 Self-interacting dark matter

SIDM has gained a lot of interest in recent years as it is a promising avenue to address small-scale problems. There has been substantial research from both sides, the astrophysical and particle physics community. Their efforts have been reviewed in Tulin & Yu (2018).

However, the idea that DM could have self-interactions dates back several years. It was first expressed by Carlson et al. (1992), though in a different context. Spergel & Steinhardt (2000) proposed SIDM for the first time as a solution to the small-scale crisis. In consequence, researchers tried to model the scattering of DM particles in their simulations. Burkert (2000) did the first N-body simulation modelling the self-interactions based on a Monte Carlo scheme. Quite a number of studies followed in that early SIDM research phase. At that time Miralda-Escude (2002) and Meneghetti et al. (2001) obtained quite stringent limits on the self-interaction cross-section. Therefore, SIDM did not seem to be a likely solution to the small-scale issues as this would have required a substantially larger cross-section. In addition, a study of the Bullet cluster favoured collisionless DM (Randall et al., 2008). As a consequence, the interest in SIDM faded away.

However, in recent years there have been a lot of studies on SIDM. Earlier constraints turned out to be much too stringent in the light of studies with higher resolution and better halo statistics (Vogelsberger et al., 2012; Rocha et al., 2013; Peter et al., 2013; Zavala et al., 2013; Vogelsberger et al., 2014; Elbert et al., 2015; Fry et al., 2015; Dooley et al., 2016). There are many recent studies of SIDM that model self-interactions within the cosmological context including various processes related to baryonic physics (e.g. Robertson et al., 2019, 2020; Bondarenko et al., 2021; Harvey et al., 2021; Sameie et al., 2021; Shen et al., 2022; Sirks et al., 2022; Despali et al., 2022). Moreover, studies consider various SIDM models beyond elastic scattering with a velocity-independent and isotropic cross-section (e.g. Robertson et al., 2017b; Vogelsberger et al., 2019; Huo et al., 2020; Nadler et al., 2020; Bondarenko et al., 2021; Shen et al., 2021). Nowadays, SIDM is a vivid research field and seems promising to solve or, at least, mitigate problems on small scales.

In the following, we describe various particle physics models and discuss the properties of SIDM candidates. In addition, we explain how to model the phenomenology of SIDM on astrophysical scales and review constraints from observations.

2.3.1 Particle physics models

A large variety of particle physics models for SIDM exists and can differ substantially in their phenomenology. They typically involve new forces from the dark sector as the cross-section for interactions with SM particles has experimentally been constrained to be tiny. Exploring their impact on the DM distribution in the Universe and shrinking the available parameter space for those models is an ongoing and challenging task. In the following, we briefly review some of these particle models.

A simple SIDM model would be a self-coupled scalar (Bento et al., 2000; Burgess et al., 2001). In principle, a real scalar field can provide a suitable DM candidate, but the major disadvantage is that the cross-section is velocity-independent (see also Sec. 2.3.2).

Frequent self-interactions, the focus of this thesis, are strongly motivated by light mediator models (Feng et al., 2009; Buckley & Fox, 2010; Loeb & Weiner, 2011; Tulin et al., 2013a,b; Agrawal et al., 2017). The interaction between the DM particles is mediated by a light boson and thus falls into the regime of long-range interactions[2]. The scattering is usually described by a Yukawa potential implying for light mediators a velocity-dependent cross-section. In the perturbative limit ($\alpha\, m_\chi / m_\Phi \ll 1$) the differential cross-section is

$$\frac{\mathrm{d}\sigma}{\mathrm{d}\Omega} = \frac{\alpha^2 m_\chi^2}{\left(m_\chi^2 v^2 (1-\cos\theta)/2 + m_\phi^2\right)^2} \,. \tag{2.2}$$

The dark fine structure constant is given by α. m_χ denotes the particle mass and m_ϕ the mediator mass. The scattering velocity is v and the scattering angle is given by θ. At low velocities, the cross-section is almost independent of velocity but above a given velocity scale, set by the mediator mass, the cross-section is decreasing with velocity. This is even the case for a massless mediator (Ackerman et al., 2009; Feng et al., 2009; Agrawal et al., 2017).

DM could be similar to the SM, including the existence of dark atoms. In the simplest form, there would be a hydrogen-like atom, formed from dark electrons and dark protons. These dark atoms can be subject to self-interactions (Cline et al., 2014; Boddy et al., 2016) and are thus of interest in the context of SIDM. The dark sector could be even richer, for example like a mirror copy of the SM sector (Mohapatra et al., 2002; Mohapatra & Teplitz, 2000; Foot & Vagnozzi, 2015) or dark atoms make up only a small fraction of the DM as in the double disk DM model (Fan et al., 2013).

[2]This does not mean that the interaction scale is inevitably long in respect to galactic scales, but compared to the de Broglie wavelength of the DM particles. Furthermore, numerical schemes to model SIDM within N-body simulations typically assume the interaction scale of DM particles to be below the resolution limit.

DM interactions are not necessarily elastic, they also could be inelastic with an excited state. Such models have been motivated by experimental search programs. But could also be relevant for the astrophysical studies of SIDM. Inelastic scattering could occur in models of atomic DM (Cline et al., 2014; Boddy et al., 2016) or strongly interacting composite DM (Boddy et al., 2014).

An approach to generalise over multiple DM models is the effective range framework (Chu et al., 2020). It aims to be a model-independent approach to approximate the self-interaction cross-section using only two parameters. The effective-range-framework can be interpreted in terms of various scenarios, including self-interactions induced by Yukawa forces, Breit–Wigner resonances and bound states. However, we have to note that this is not applicable to the type of models falling into the regime of fSIDM. For them, S-wave scattering is not sufficient, but higher partial waves have to be taken into account.

Besides SIDM, there exist many more particle candidates, and their prospects might be affected by research on SIDM. In case there is evidence for significant DM self-interactions, this would rule out or at least lead to rigorous constraints on some popular DM candidates, such as supersymmetric neutralinos or axions.

It has been recently pointed out by Loeb (2022) that if DM particle masses are large enough the gravitational interaction could explain DM self-interactions. However, this is hardly a new insight as the gravothermal fluid formalism (Lynden-Bell & Eggleton, 1980) used to model SIDM is based on the assumption that a gravitational bound system can behave similarly to SIDM haloes (see also Section 2.3.3). For the long-mean-free-path regime, the formalism relies on an empirical formula which well-describes the gravothermal collapse of globular clusters. Furthermore, the DM particles would need to be extended objects. Otherwise, the relevant mass range of 10^3–$10^4\,\mathrm{M}_\odot$ would already be excluded by PBH studies (see Fig. 2.5).

2.3.2 Properties of SIDM models

Particle models for SIDM can have various properties, for many astrophysical studies elastic velocity-independent isotropic scattering has been assumed. Several recent studies considered more complicated models resulting in a different phenomenology. In the following, we want to discuss the angular and velocity dependence of the differential cross-section but also consider the effect that DM models can have on the matter power spectrum in the linear regime.

Rare and Frequent self-interactions

The angular dependence of particle candidates for SIDM differs between the models. For instance, particles can be subject to hard-sphere scattering with an isotropic cross-section or could have an anisotropic cross-section as in light mediator models with long-range interactions. Models that typically scatter about a large angle, transfer on average a lot of momentum and energy per scattering event. In contrast, momentum and energy transfer

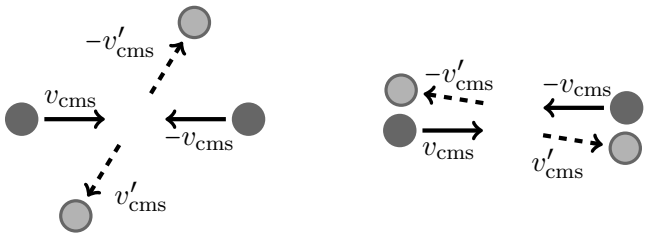

Figure 2.7: Illustration of scattering events in the centre of mass frame. Left side: large-angle scattering, which is rare. Right side: small-angle scattering, which is frequent.

are fairly low for models that prefer small scattering angels. In consequence, DM with a strongly anisotropic cross-section would need many more scattering events to have a comparable impact on the DM distribution. Therefore we also refer to such scattering as frequent in contrast to rare scattering of cross-sections that are closer to an isotropic cross-section (also illustrated in Fig. 2.7).

There exist a variety of particle models that may scatter frequently via long-range interactions. Those are models of mirror DM (Blinnikov & Khlopov, 1983; Kolb et al., 1985; Berezhiani et al., 1996; Foot, 2004) or atomic DM (Kaplan et al., 2010; Cline et al., 2012; Cyr-Racine & Sigurdson, 2013) as well as all light mediator models (Feng et al., 2009; Buckley & Fox, 2010; Loeb & Weiner, 2011; Tulin et al., 2013a; Bringmann et al., 2017).

Frequent DM scattering has received some attention in the context of galaxy cluster mergers. In the literature, these systems have been studied to investigate a potential offset between the DM component and galaxy distribution (e.g. Randall et al., 2008; Robertson et al., 2017a; Kim et al., 2017). Besides, also the offset on an individual galaxy falling into a cluster has been investigated (Kahlhoefer et al., 2015). In this context, fSIDM models which typically scatter about small angles are of particular interest as they behave qualitatively different compared to rSIDM. For models with long-range interactions, a drag force can occur and decelerate the DM component which leads to an offset (Kahlhoefer et al., 2014). In Fig. 2.8 we illustrate this for an individual particle travelling through a constant density.

In Chapter 3, we use the drag force to derive a numerical scheme that allows us to model fSIDM within N-body simulations and we study the DM–galaxy offset in mergers of galaxy clusters.

Velocity dependence

There exist motivation from astrophysics and particle physics for velocity-dependent self-interactions. Various studies have used the core sizes of DM haloes to constrain the strength of the DM self-interaction using velocity-independent scattering. For galaxy

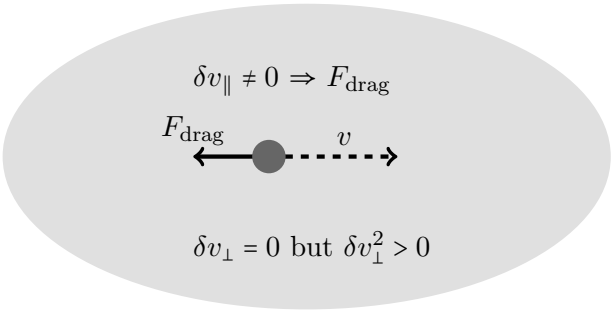

Figure 2.8: Illustration of the drag force acting on a DM particle or a phase-space patch of DM particles as it moves through a background density. The velocity changes of many small-angle scattering events average out for the perpendicular component but sum up for the parallel component and thus lead to a deceleration.

clusters relatively strict limits on σ/m_χ of the order of $\sim 0.1\,\mathrm{cm^2\,g^{-1}}$ have been obtained (Kaplinghat et al., 2016; Elbert et al., 2018; Sagunski et al., 2021; Eckert et al., 2022). In contrast, for galaxies the limits are lower, $\sim 1.0\,\mathrm{cm^2\,g^{-1}}$ (Davé et al., 2001; Kaplinghat et al., 2016; Shi et al., 2021; Ray et al., 2022). This could be explained by a velocity-dependent cross-section. If σ/m_χ decreases with velocity, it affects high mass objects less because they have a higher velocity dispersion. In Fig. 2.9 we show a plot of Kaplinghat et al. (2016) to illustrate this with constraints from various systems.

There exists a variety of particle models with velocity-dependent scattering. Naturally, this arises in models with Yukawa or Rutherford-like long-range interactions with a light mediator (e.g. Feng et al., 2009; Loeb & Weiner, 2011; Tulin et al., 2013b). The differential cross-section for these models is anisotropic. But also resonant scattering could explain a velocity-dependence (Chu et al., 2019, 2020; Tsai et al., 2022). In these models, no light mediator is needed and the differential cross-section would be isotropic.

Impact on the matter power spectrum

Most SIDM studies assume that the matter power spectrum in the linear regime remains unchanged compared to CDM. This is relevant for the initial conditions of N-body simulations. Such studies, using the same initial conditions as for CDM, find the matter power spectrum at late, non-linear, stages to be suppressed at small scales due to the self-interactions (e.g. Rocha et al., 2013; Stafford et al., 2021). However, there have been a few studies that investigated models with a modified initial matter power spectrum (e.g. Huo et al., 2018). In particular, the ETHOS collaboration studied SIDM with damping due to dark radiation (Cyr-Racine et al., 2016; Vogelsberger et al., 2016). The considered power spectrum in the linear regime is already suppressed at small scales, implying a suppression of substructure at later stages too. Whether the matter power spectrum in the linear regime differs from CDM depends on the particle physics model. Multiple processes could lead to a damping on small scales, such as coupling between DM and a dark radiation component (Boddy et al., 2016; Feng et al., 2009; van den Aarssen et al., 2012; Buckley

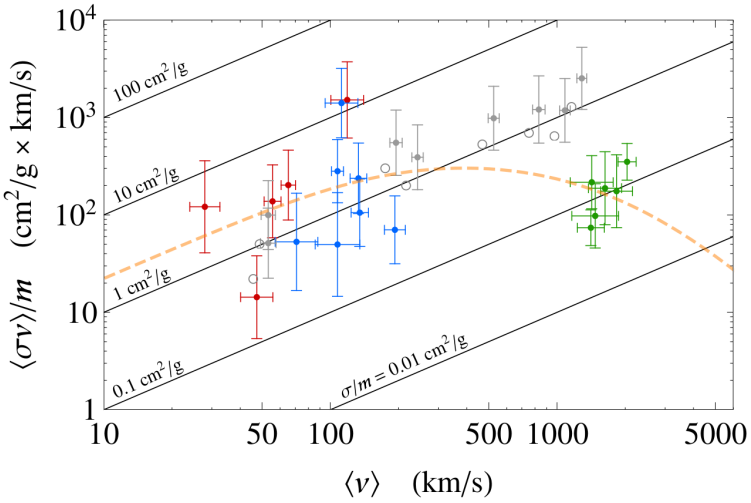

Figure 2.9: The velocity weighted self-scattering cross-section is plotted as a function of the average velocity for various systems. Observational limits for dwarf galaxies (red), low surface brightness galaxies (blue) and clusters (green) are shown. A velocity-dependent model is fitted to the data (yellow). Besides bounds derived from simulated systems with $\sigma/m_\chi = 1\,\mathrm{cm}^2\,\mathrm{g}^{-1}$ are displayed (grey). Contours of constant σ/m_χ are given by the diagonal lines. This figure is a reprint of fig. 1 of Kaplinghat et al. (2016).

et al., 2014; Cyr-Racine & Sigurdson, 2013; Cyr-Racine et al., 2014) or slow cooling during freeze-out in cannibalisation models (Carlson et al., 1992; de Laix et al., 1995).

In this thesis, we focus only on the late time effects of SIDM assuming a CDM initial power spectrum.

2.3.3 Modelling SIDM

Several methods have been used in the literature to study SIDM. Some of them make simplifying assumptions, limiting the range of problems that can be studied. But therefore they are computationally cheaper. In the following, we discuss the three most common methods for SIDM.

Gravothermal fluid formalism

The gravothermal fluid formalism for SIDM is used to model individual haloes. It was first introduced by Lynden-Bell & Eggleton (1980) to describe the evolution of globular clusters and has been transferred to SIDM haloes. Here, the influence of self-interactions is effectively described as heat conduction. Early studies of SIDM (Gnedin & Ostriker, 2001; Balberg & Shapiro, 2002; Balberg et al., 2002) used that formalism to study the evolution of DM haloes. It should be mentioned that it is not derived from first principles but needs to be calibrated against simulations. A detailed comparison of the fluid model with N-body simulations was done by Koda & Shapiro (2011). An advantage of the gravothermal fluid formalism is not only being computationally cheap but also that it is able to model the

core-collapse phase of DM halos (e.g. Pollack et al., 2015; Essig et al., 2019), which is impossible or at least difficult for other methods. There have been attempts to include further physical processes into the formalism, for instance, cosmic infall (Ahn & Shapiro, 2005) or tidal stripping (Nishikawa et al., 2020) or a GR formulation to include BHs (Shapiro, 2018). The fluid model was mainly used for elastic isotropic velocity-independent scattering. However, (Essig et al., 2019) used it to investigate dissipative self-interactions and recent work extended it to velocity-dependent cross-sections (Outmezguine et al., 2022; Yang et al., 2022).

Isothermal Jeans approach

The isothermal Jeans approach for SIDM was introduced by Kaplinghat et al. (2016) and allows to describe cored density profiles of SIDM haloes and estimate the corresponding self-interaction cross-section. Although it is subject to a few internal inconsistencies (Sokolenko et al., 2018), Robertson et al. (2020) found the isothermal Jeans model to provide a surprisingly accurate description of SIDM haloes. However, Jeans modelling can only be used to describe the core formation phase but not the core-collapse phase. It has been applied to low mass DM haloes (Gilman et al., 2021) as well as to high mass DM haloes (Sagunski et al., 2021).

Simulations from first principles

Numerical schemes for SIDM derived from first principles tend to be computationally expensive. Though, they are the only way to accurately model systems far from equilibrium, such as merging DM haloes or the formation of the large-scale structure. So far, all these approaches are based on the framework of N-body simulations. Here, the mass distribution is discretised by N resolution elements each representing a mass element. In astrophysical simulations, these resolution elements typically follow the influence of gravity and eventually other forces that act on them. Generally speaking, the Vlasov-Poisson[3] equation is solved. In case of SIDM we have an additional collision term $\mathscr{C}$ that describes the self-interactions.

$$\frac{\partial f}{\partial t} + \mathbf{v} \cdot \nabla_x f - \nabla_x \Phi \cdot \nabla_v f = \mathscr{C}[f]\,. \tag{2.3}$$

Here, f denotes the phase-space density, $\mathbf{x}$ the spatial position and $\mathbf{v}$ the velocity. The gravitational potential Φ follows from the Poisson equation,

$$\Delta\Phi = 4\pi\,\mathrm{G} \int f(\vec{x}, \vec{v}, t)\, d\vec{v}\,. \tag{2.4}$$

There have been early attempts to simulate SIDM based on a gas dynamical approach (Moore et al., 2000; Yoshida et al., 2000a), thus not directly derived from first principles. It was Burkert (2000) who did the first simulation that was based on a Monte Carlo scheme.

[3]For a review of numerical and analytical method to solve the Vlasov-Poisson equation and its connections to plasma physics see Rampf (2021).

The numerical resolution elements are treated analogously to physical DM particles. Several early studies adopted that approach or used a similar one to study the evolution of SIDM haloes (Yoshida et al., 2000b; Kochanek & White, 2000; Craig & Davis, 2001; Davé et al., 2001; Colin et al., 2002). Later on, this scheme has been significantly improved by Rocha et al. (2013). Almost all schemes used today are similar but differ in the way the interaction probability of the numerical resolution elements is computed. Unfortunately, the prescriptions of those schemes usually lack a derivation of this probability. In this context, we want to highlight the derivation we provide in Sec. 3.B.

The first simulation with a velocity-dependent cross-section may have been performed by Colin et al. (2002). Also further properties of SIDM models have been simulated, such as anisotropic scattering (e.g. Robertson et al., 2017b), inelastic scattering (e.g. Huo et al., 2020) or multistate scattering (e.g. Vogelsberger et al., 2019). Simulating extreme anisotropic cross-sections has turned out to be challenging as the required time step in rSIDM schemes would become prohibitively small. Consequently, the numerical schemes mentioned above were exclusively used to simulate rSIDM. There have been a few attempts to simulate fSIDM (Kahlhoefer et al., 2014; Kummer et al., 2019), but these schemes were not derived from first principles and thus made simplifying assumptions. We have finally resolved this issue by introducing a novel scheme that allows us to simulate fSIDM without simplifications (see Chapter 3.2). In contrast to rSIDM schemes, we do not treat the resolution elements analogously to physical DM particles.

Overall, N-body simulations are an important tool for SIDM studies. They are capable of incorporating further physical processes, in particular, those related to baryons, which is crucial for a comparison of simulation results to observational data (e.g. Vogelsberger et al., 2020).

Although modelling SIDM from first principles has so far solely relied on N-body simulations it could be possible to discretise the relevant equations differently. The Vlasov-Poisson equation is not only relevant in astrophysics, but in plasma physics too (for a review see Palmroth et al., 2018). In both fields there are studies that resolve the phase-space in terms of a 6-dimensional phase-space grid (e.g. Yoshikawa et al., 2012; Tanaka et al., 2017; Deriaz & Peirani, 2018; Kormann et al., 2019). However, the interest in this type of simulation code might be larger in the plasma physics community. For SIDM, these codes may provide an alternative possibility to formulate the effect of self-interactions. But until now, the use of such a framework has not been explored. The computational costs might be much larger than in N-body simulations and thus be prohibitive.

In addition, various techniques for simulations of DM, including SIDM, are reviewed in Angulo & Hahn (2022).

2.3.4 Observational constraints

There exist a variety of constraints on SIDM models derived from various observations. Usually, bounds on the cross-section are given, but other properties such as the angular

dependence are not constrained. However, studies at various mass scales have obtained quite different limits on the cross-section, making it plausible that the strength of self-interactions is decreasing with velocity. In the following, we discuss some studies and their SIDM constraints.

Rotation curves and core sizes

SIDM can explain observations of cored DM haloes. This is probably the most studied phenomenological feature of SIDM. It has been investigated at very different mass scales, from MW satellites and dwarf galaxies to galaxy clusters (e.g Zavala et al., 2013; Kaplinghat et al., 2016; Elbert et al., 2015; Elbert et al., 2018). Depending on the system, different methods such as rotation curves or gravitational lensing are used to probe the matter distribution. Recently, constraints for MW satellites have been obtained by Correa (2021) and Sagunski et al. (2021) studied groups and galaxy clusters. But there are more studies that derived bounds on the cross-section (e.g. Eckert et al., 2022; Ray et al., 2022) or claim that observed cores of ultra-diffuse galaxies (UDG) are inconsistent with state-of-the-art ΛCDM simulations (Kong et al., 2022). In particular, Andrade et al. (2021) studied the density profiles of galaxy clusters and derived an upper limit of $\sigma/m_\chi = 0.13\,\mathrm{cm^2 g^{-1}}$ at an confidence level of 95%.

Besides, less massive system have been studied and their density profile has often been inferred from rotation curves. But there exist also other arguments for density cores, for example the orbits of globular clusters in the dwarf galaxy Fornax (e.g. Oh et al., 2000; Angus & Diaferio, 2009; Boldrini et al., 2020; Bar et al., 2021; Genina et al., 2021). In ΛCDM, one would expect their orbital decay times to be shorter than their age. In contrast to observations, one would expect them to have formed a nuclear star cluster. This problem is also known as the Fornax timing problem. It could potentially be solved by a density core reducing the dynamical friction. But we have to note, that such timing arguments can not conclusively rule out a cuspy density profile (Cole et al., 2012; Meadows et al., 2019; Shao et al., 2021).

Many other dwarfs have been studied and used to constrain DM physics. Shi et al. (2021) studied an UDG and claim that it has a cuspy density profile excluding cross-section of $\sigma/m_\chi \geq 1.63\,\mathrm{cm^2 g^{-1}}$. In this line is also the work of Roper et al. (2022). They and other authors (Pineda et al., 2016; Read et al., 2016; Genina et al., 2018; Oman et al., 2019) have pointed out that rotation curve measurements may make galaxies appear cored although they have a cuspy density profile. This can be caused by not taking non-circular gas motions properly into account when measuring the rotation curves of dwarf galaxies. Hence it is important to analyse observational data more carefully than this has often been done in the past. Recently, the core-cusp problem of dwarf spheroidal galaxies has been reviewed by Boldrini (2022).

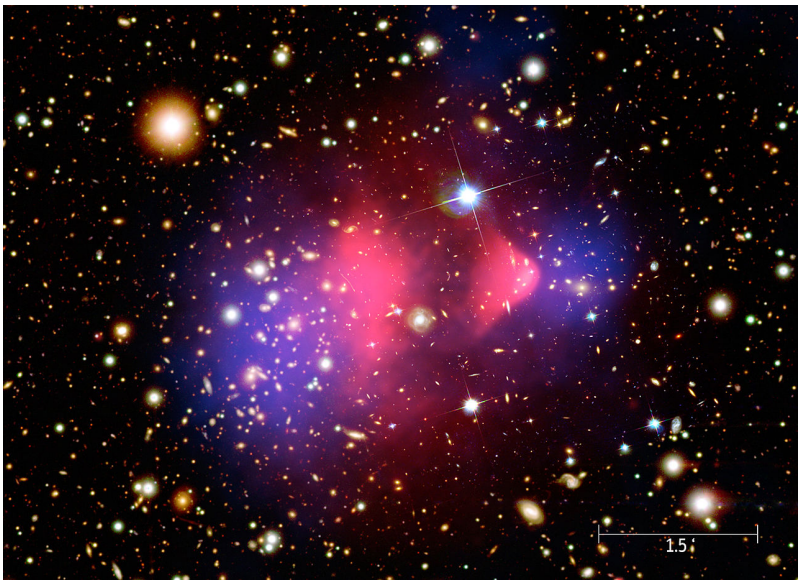

Figure 2.10: An image of the galaxy cluster 1E 0657-56, better known as Bullet Cluster, is shown. It is composed of multiple observations with different telescopes. The data in the visible spectrum stems from Magellan and Hubble Space Telescope (Clowe et al., 2006). In pink, the x-ray emission as detected by the Chandra Telescope, is visualised (Markevitch, 2005). From gravitational lensing, the mass distribution has been calculated and is shown in blue (Clowe et al., 2006). Author: NASA/CXC/M. Weiss, Source: Chandra X-Ray Observatory: 1E 0657-56

DM–galaxy offsets

Numerous publications on SIDM discussed the offsets in mergers of galaxy clusters. From the theoretical side, exist several studies concerning the emergence of offsets between the DM component and the galaxies (e.g. Kahlhoefer et al., 2014; Kim et al., 2017; Robertson et al., 2017b). For fSIDM, an effective drag force (see Fig. 2.8) would decelerate the DM component but leave the galaxies unaffected, thereby creating an offset. And from the observational side, the reliability of measured offsets has been discussed (e.g. Bradač et al., 2008; Dawson et al., 2012; Dawson, 2013; Jee et al., 2015; Harvey et al., 2017; Peel et al., 2017; Taylor et al., 2017; Wittman et al., 2018). Especially the galaxy cluster 1E 0657-56, also known as the Bullet Cluster, gained a lot of attention. Fig. 2.10 clearly shows that the mass distribution derived from the gravitational lensing effect (blue) is offset from the ICM (pink). However, an offset between the DM and galactic component being in tension with ΛCDM has not been found (e.g. Randall et al., 2008; Robertson et al., 2017a,b). To date, there is no conclusive observation of an offset between the DM and galactic component in any galaxy clusters that would favour substantial self-interactions. Furthermore, it should be noted that even in ΛCDM, the DM component could appear to be offset from the galaxies (Ng et al., 2017). For individual systems, uncertainties about the exact merger configuration worsen the situation. Consequently, it is difficult to derive reliable constraints on the self-interaction cross-section from DM-galaxy offsets.

DM halo shapes

DM haloes are typically not spherically symmetric but are better described by a triaxial ellipsoid. On average, self-interactions make DM halos rounder compared to their CDM counterparts. Due to the scattering, the velocity distribution becomes more isotropic and thus the shape of the DM halo changes. This has been used to constrain the strength of self-interactions. For velocity-independent elastic scattering Miralda-Escude (2002) found a total cross-sections with $\sigma/m_\chi > 0.02\,\mathrm{cm}^2\mathrm{g}^{-1}$ to be excluded. Later Peter et al. (2013) studied the ellipticity of haloes and found these bounds to be far too tight. Instead, only a cross-section of $\sigma/m_\chi \geq 1.0$ is unlikely larger for galaxy clusters. However, recent halo ellipticity measurements are in good agreement with ΛCDM (Schrabback, Tim et al., 2021). Moreover, Despali et al. (2022) studied early-type galaxies and found CDM as well as SIDM to be capable of explaining observations when accounting for the effect of baryons.

DM substructure and gravitational lensing

The abundance of substructure is a promising probe to study DM microphysics. The self-interactions lead to DM cores making satellites more prone to tidal disruption. As a result, one would typically expect that SIDM haloes have fewer satellites. However, given that the self-interactions are strong enough, satellites can enter the core-collapse phase and have central densities much larger than in CDM. Meneghetti et al. (2020) reported an excess of small-scale lenses in galaxy clusters compared to CDM predictions, which could be explained by collapsing SIDM satellites (Yang & Yu, 2021). However, there has been a discussion on how reliable these results are. Bahé (2021) and Robertson (2021) disagree with Meneghetti et al. (2020) and do not find a tension with ΛCDM predictions.

Not only the substructure in galaxy clusters is of interest but also less massive systems. Studies of the substructure in the MW with weak gravitational lensing (e.g. Mondino et al., 2020) could also help to constrain SIDM. In this context, density cores would help to solve the too-big-to-fail problem (e.g. Kaplinghat et al., 2016).

3 N-body simulations of dark matter with frequent self-interactions

This chapter presents work as published in Fischer et al. (2021a).

Abstract Self-interacting dark matter (SIDM) models have the potential to solve the small-scale problems that arise in the cold dark matter paradigm. Simulations are a powerful tool for studying SIDM in the context of astrophysics, but it is numerically challenging to study differential cross-sections that favour small-angle scattering, as in light-mediator models. Here, we present a novel approach to model frequent scattering based on an effective drag force, which we have implemented into the N-body code GADGET-3. In a range of test problems, we demonstrate that our implementation accurately models frequent scattering. Our implementation can be used to study differences between SIDM models that predict rare and frequent scattering. We simulate core formation in isolated dark matter haloes, as well as major mergers of galaxy clusters and find that SIDM models with rare and frequent interactions make different predictions. In particular, frequent interactions are able to produce larger offsets between the distribution of galaxies and dark matter in equal-mass mergers.

3.1 Introduction

Dark matter (DM) is an essential component of the standard cosmological model (Lambda cold dark matter, ΛCDM), which was introduced to explain a variety of observations, such as the formation of large-scale structure and the cosmic microwave background. These observations can be explained remarkably well under the assumption that DM is cold and collisionless (e.g. Planck Collaboration et al., 2020). Nevertheless, on small scales, i.e. galactic scales, the predictions of ΛCDM are in tension with observations. The different aspects in which the predictions deviate from observations on small spatial scales could present a challenge to our ΛCDM model. Usually, up to five small-scale problems are considered. These are the missing satellites problem, the too-big-to-fail problem, the diversity problem, the core-cusp problem, and the plane-of-satellites problem (for a review see Bullock & Boylan-Kolchin, 2017). Not all of them describe actual problems of ΛCDM and at least the missing satellites can be explained within the cosmological standard model (e.g. Kim et al., 2018).

In order to resolve the small-scale problems, a number of potential solutions have been

proposed. Some of them attempt to mitigate the tensions by more accurate subgrid models of the baryonic physics in cosmological simulations. It has been shown by numerous studies that DM cores can be created by feedback processes such as outflows from supernovae (Read & Gilmore, 2005; Governato et al., 2012; Pontzen & Governato, 2012; Di Cintio et al., 2013; Brooks & Zolotov, 2014; Cintio et al., 2014; Pontzen & Governato, 2014; Oñorbe et al., 2015; Tollet et al., 2016; Benítez-Llambay et al., 2019) as well as due to black holes (e.g. Martizzi et al., 2013; Peirani et al., 2017; Silk, 2017). Other work shows that tensions can be reduced by improving the modelling of the internal dynamics of observed galaxies (Oman et al., 2019).

An alternative to these small-scale problems pointing towards some deficiency in the modelling of baryons is that they are telling us something fundamental about the nature of DM. DM that is 'warm' (Dodelson & Widrow, 1994) or 'fuzzy' (Hu et al., 2000) would change the abundance and internal structure of DM haloes. Along this line, a promising alternative DM model is self-interacting dark matter (SIDM) (for a review see Tulin & Yu, 2018), which was proposed by Spergel & Steinhardt (2000) as a solution to some of the small-scale problems.[1]

More precisely, SIDM is a class of many physics models that all have in common that DM consists of particles and these particles interact with each other so strongly that the interaction can alter the distribution of DM on astrophysical scales significantly, e.g. create density cores in haloes of DM. From observations, the interesting range of cross-sections divided by DM mass is of the order of 1 $\mathrm{cm}^2\ \mathrm{g}^{-1}$. In the limit of a negligible cross-section, SIDM behaves the same way as CDM.

A range of methods have been proposed to study the effects of SIDM on cosmic structures. The isothermal Jeans approach (Kaplinghat et al., 2014; Kaplinghat et al., 2016) and the gravothermal fluid model (Gnedin & Ostriker, 2001; Balberg & Shapiro, 2002; Balberg et al., 2002; Koda & Shapiro, 2011; Pollack et al., 2015) are based on assuming that self-interactions maintain an equilibrium state, in which the full phase-space information is not required. However, in many situations DM is neither collisionless nor fully collisional, which means that the simplifying assumption of local equilibrium cannot be made. The most general – but also computationally most expensive – method to study SIDM is to run N-body simulations. Here, the Vlasov–Poisson equation with a collision term for DM self-interactions is solved in six-dimensional phase-space. The scattering of the numerical particles is treated analogously to physical particles. The first such simulation using a Monte Carlo scheme for the scattering angle was performed by Burkert (2000). Modern schemes used for SIDM only differ from this approach in the way in which scattering probabilities are computed.

The common approach of explicitly simulating individual scattering events leads to complications when the differential cross-section favours scattering by small angles. In this case it becomes necessary to simulate large numbers of scattering events that individually

[1] Cold dark matter with self-interactions was first proposed by Carlson et al. (1992), but this was in a different context.

have negligible impact on the phase-space distribution. For very frequent scattering events, this becomes prohibitively expensive (Robertson et al., 2017b) because the required time-steps become too small.

Previous attempts to address this problem have relied on a number of simplifying assumptions. Kahlhoefer et al. (2014) performed simplistic N-body simulations of mergers by using an external gravitational potential for each halo and sampling the DM and galaxies with test particles. In this set-up, the effects of frequent self-interactions were modelled with an effective drag force. Kummer et al. (2019) combined the heat conduction approach from fluid models with N-body simulations, which assumes that the system is in local equilibrium such that a well-defined temperature exists. Consequently, this approach is limited in its versatility, and, for instance, cannot be applied to merging systems.

In this paper, we present a novel method designed for the frequent scattering regime, which enables general astrophysical simulations of frequent self-interacting dark matter (fSIDM). Our method employs a fundamentally different formulation of the collision term compared to the state-of-the-art schemes for rare self-interacting dark matter (rSIDM) and makes use of the fact that the effect of frequent scattering events in fSIDM can be described by an effective drag force (Kahlhoefer et al., 2014).

In fSIDM, a DM particle travelling through a space filled with other DM particles would undergo many small-angle scattering events. Each scattering event leads to a small change of the velocity, but the cumulative velocity change perpendicular to the initial direction of motion will tend to average out, with an expectation value: $\langle \delta v_\perp \rangle = 0$. The expected parallel component of the velocity change is non-zero ($\langle \delta v_\parallel \rangle \neq 0$), which can be interpreted as a drag force. At the same time one finds $\langle \delta v_\perp^2 \rangle > 0$, which can be regarded as kinetic heating.

Rare self-interactions have a much larger velocity change per scattering event and thus cannot, in general, be described by a drag force. Only when the density is very high, an effective drag can occur (Kim et al., 2017). As we will explore in this paper, the different effective descriptions of fSIDM and rSIDM lead to significant differences in the predicted DM distributions in astrophysical systems. In particular systems far away from equilibrium, such as ongoing major mergers of galaxy clusters respond in different ways to frequent and rare self-interactions. Indeed, we find that the effects for fSIDM can be substantially larger than those previously found for rSIDM.

This paper has several aims: First, we present a new numerical scheme to simulate frequent self-interactions of DM, which is described in Section 3.2. Secondly, in Section 3.3 we validate our scheme and its implementation in the N-body code GADGET-3 using a number of test problems. We then study core formation in an isolated Hernquist halo (see Section 3.4) and compare the effects of fSIDM and rSIDM. Finally, we explore differences between fSIDM and rSIDM in equal-mass mergers. In Section 3.5, we simulate a merger of DM haloes with parameters typical of galaxy clusters. In Section 3.6, we elaborate on various technical aspects of our code and discuss the physical implications of our results.

Finally, we summarize and conclude in Section 3.7. Additional details are provided in the appendices.

3.2 Numerical Method

In this section, we first describe the key aspects of our method to simulate frequent scatterings. We then explain its implementation in the N-body code GADGET-3, which contains a description of the parallelization. Finally, we point out differences between state-of-the-art schemes for rSIDM and our formulation of fSIDM.

In N-body codes, the phase-space distribution of DM is represented by numerical particles. These particles each represent phase-space patches consisting of many physical particles. They are assigned a velocity and to smooth the represented matter distribution in configuration space a kernel is employed. Such a Lagrangian description has some advantages over an Eulerian approach, such as Galilean invariance. But there are also disadvantages, for instance when it comes to the parallelization (see below).

Let us first look at the interaction of two phase-space patches, i.e. two numerical particles, which we assume to have equal mass. If the scattering is elastic, we can derive the post-scattering velocities of the particles from energy and momentum conservation: $E_i' + E_j' = E_i + E_j$ and $\boldsymbol{p}_i' + \boldsymbol{p}_j' = \boldsymbol{p}_i + \boldsymbol{p}_j$.

We divide the scattering process into two steps: The first one applies a drag force and the second one re-adds the energy lost in the first step. The latter is done in a random direction but perpendicular to the direction of motion to model kinetic heating. We indicate the intermediate state between the two steps by the superscript *. The velocity of the two numerical particles can be expressed as follows:

$$\boldsymbol{v}_i^* = \boldsymbol{v}_i - \Delta\boldsymbol{v}_{\mathrm{drag}}\,, \qquad \boldsymbol{v}_j^* = \boldsymbol{v}_j + \Delta\boldsymbol{v}_{\mathrm{drag}}\,, \tag{3.1}$$

$$\boldsymbol{v}_i{}' = \boldsymbol{v}_i^* + \Delta\boldsymbol{v}_{\mathrm{rand}}\,, \qquad \boldsymbol{v}_j{}' = \boldsymbol{v}_j^* - \Delta\boldsymbol{v}_{\mathrm{rand}}\,. \tag{3.2}$$

Here, $\Delta\boldsymbol{v}_{\mathrm{drag}}$ denotes the velocity change due to the effective drag force. $\Delta\boldsymbol{v}_{\mathrm{rand}}$ denotes the velocity which is added to ensure energy conservation, while momentum conservation is guaranteed as velocity changes are symmetric for the two particles.

3.2.1 First step: apply drag force

We introduce the relative velocity $\Delta\boldsymbol{v}_{ij} = \boldsymbol{v}_i - \boldsymbol{v}_j$ and use it to express the velocity change $\Delta\boldsymbol{v}_{\mathrm{drag}}$ due to the drag force,

$$\Delta\boldsymbol{v}_{\mathrm{drag}} = |\Delta\boldsymbol{v}_{\mathrm{drag}}| \cdot \frac{\Delta\boldsymbol{v}_{ij}}{|\Delta\boldsymbol{v}_{ij}|}\,. \tag{3.3}$$

Next, $|\Delta \boldsymbol{v}_{\rm drag}|$ can be written as:

$$|\Delta \boldsymbol{v}_{\rm drag}| = \frac{F_{\rm drag}}{m} \cdot \Delta t \,. \tag{3.4}$$

The drag force is given by $F_{\rm drag}$ and Δt denotes the time-step.

To derive the drag force, we start from the same assumptions as made by Kahlhoefer et al. (2014). They derived the deceleration rate ($R_{\rm dec} \equiv v_0^{-1}\, {\rm d}v_\parallel/{\rm d}t$) of an individual physical DM particle travelling with velocity v_0 through a background density ρ_j and found

$$R_{\rm dec} = \frac{\rho_j\, v_0\, \sigma_{\tilde{\rm T}}}{2\, m_\chi} \,. \tag{3.5}$$

Here, m_χ denotes the mass of a DM particle and

$$\sigma_{\tilde{\rm T}} = 4\pi \int_0^1 \frac{{\rm d}\sigma}{{\rm d}\Omega_{\rm cms}} (1 - \cos\theta_{\rm cms}) {\rm d}\cos\theta_{\rm cms} \tag{3.6}$$

denotes the momentum transfer cross-section.[2] In the regime of isotropic scattering, this definition is a factor of 2 smaller than the one commonly used in studies of rSIDM.

To apply this calculation to our simulations we interpret the background density ρ_j as the density of a single phase-space patch represented by a numerical particle. Moreover, we need to consider the scattering of many particles and their total momentum change, which can be written as

$${\rm d}p_\parallel = \int n_i\, m_\chi\, {\rm d}v_\parallel {\rm d}V = \int \rho_i\, {\rm d}v_\parallel {\rm d}V \,. \tag{3.7}$$

Here, the number density of physical DM particles belonging to phase-space patch i is given by $n_i = \rho_i/m_\chi$, where ρ_i denotes the mass of the numerical particle multiplied by the kernel: $\rho_i(\boldsymbol{x}) = m_i \cdot W(|\boldsymbol{x} - \boldsymbol{x}_i|, h_i)$ with h_i being the kernel size (see below). The physical density can then be obtained by summing over all numerical particles at a given position.

Using the deceleration rate from equation (3.5) we can therefore express the resulting drag force acting on a phase-space patch as

$$F_{\rm drag} = \frac{1}{2} |\Delta \boldsymbol{v}_{ij}|^2 \frac{\sigma_{\tilde{\rm T}}}{m_\chi} \int \rho_i\, \rho_j\, {\rm d}V \,. \tag{3.8}$$

Using the kernel $W(|\boldsymbol{x} - \boldsymbol{x}_i|, h_i)$, we can express the drag force as

$$\begin{aligned} F_{\rm drag} = &\frac{1}{2} |\Delta \boldsymbol{v}_{ij}|^2 \frac{\sigma_{\tilde{\rm T}}}{m_\chi}\, m_i\, m_j \\ &\cdot \int W(|\boldsymbol{x} - \boldsymbol{x}_i|, h_i) \cdot W(|\boldsymbol{x} - \boldsymbol{x}_j|, h_j)\, {\rm d}\boldsymbol{x} \,. \end{aligned} \tag{3.9}$$

Note that we do not consider interactions between particles belonging to the same phase-

[2] Note that if the differential cross section is invariant under the exchange $\theta \to \pi - \theta$ (as in the case of the scattering of identical particles), this definition is equivalent to the one advocated by Robertson et al. (2017b); Kahlhoefer et al. (2017): $\sigma_{\tilde{\rm T}} = 2\pi \int_{-1}^1 \frac{{\rm d}\sigma}{{\rm d}\Omega_{\rm cms}} (1 - |\cos\theta_{\rm cms}|) {\rm d}\cos\theta_{\rm cms}$.

space patch, as they have parallel trajectories. Furthermore, we assume $\sigma_{\tilde{\mathrm{T}}}$ to be velocity independent in this work.

3.2.2 Second step: re-add energy

In the second step, we re-add the energy ΔE that is lost due to the drag force. It can be written as

$$\frac{2\,\Delta E}{m} = |\Delta \boldsymbol{v}_{\mathrm{drag}}| \left(|\Delta \boldsymbol{v}_{ij}| - |\Delta \boldsymbol{v}_{\mathrm{drag}}| \right) . \tag{3.10}$$

To ensure that the local velocity distribution evolves towards thermal equilibrium, the added velocity $\Delta \boldsymbol{v}_{\mathrm{rand}}$ needs to be perpendicular to the relative velocity $\Delta \boldsymbol{v}^*$. We then find that

$$|\Delta \boldsymbol{v}_{\mathrm{rand}}| = \sqrt{\frac{2\Delta E}{m}} . \tag{3.11}$$

The direction of $\Delta \boldsymbol{v}_{\mathrm{rand}}$ is chosen randomly in the plane orthogonal to $\Delta \boldsymbol{v}_{ij}$. Once the velocity change due to the random component has been computed, we can update the velocity according to equation (3.2) and continue with the next particle pair.

Note, that the post-scattered velocities $\boldsymbol{v}'$ are treated as pre-scattered velocities $\boldsymbol{v}$ for any subsequent pair computations in the same time-step. This implies that the result depends on the exact order in which the particle pairs are considered. However, this is an effect which is only relevant at the level of individual particle trajectories. It has no meaning for the statistical properties of the DM distribution. Treating particle pairs in a different order would lead to a different N-body representation of the same distribution, as would different random directions for the re-added energy.

3.2.3 Kernel

The drag force computation is based on a kernel function representing the DM density distribution of a numerical particle in configuration space. Here, we will discuss the use of kernel functions, describe how we compute the overlap and explain how we choose the kernel size.

The application of kernel functions in this work is quite different from the one in smoothed particle hydrodynamics (SPH), where they are used to compute derivatives and therefore need to be differentiable. For the scheme presented here, we only need to integrate the kernel functions as described in Section 3.2.1. We have tried a number of different kernel functions and found that they all perform similarly well in the context of the first test problem presented in sec. 3.3.1. In the end, we choose the spline kernel introduced by Monaghan & Lattanzio (1985), which is very popular in SPH. For our studies, we use a scaled version such that it becomes zero for $r \geq h$, where h denotes the kernel size:

$$W(r,h) = \begin{cases} \frac{8}{\pi h^3} \left[1 - 6\,(r/h)^2\,(1 - r/h) \right] & \text{if} \quad 0 \leq r/h < 0.5, \\ \frac{16}{\pi h^3} \left[1 - (r/h) \right]^3 & \text{if} \quad 0.5 \leq r/h < 1, \\ 0 & \text{if} \quad 1 \leq r/h. \end{cases} \tag{3.12}$$

Using this kernel, we can calculate the overlap Λ_{ij} of the particles i and j, which corresponds to the integral of equation (3.9):

$$\Lambda_{ij} = \int W(|\boldsymbol{x} - \boldsymbol{x}_i|, h_i) \cdot W(|\boldsymbol{x} - \boldsymbol{x}_j|, h_j)\, \mathrm{d}\boldsymbol{x}\,. \tag{3.13}$$

Details on how this integral is calculated in practice, are given in Appendix 3.A.

The kernel size should be chosen adaptively to reach a high resolution in regions with a large particle number density. Simultaneously, the kernel size needs to be large in low-density regions to ensure that each particle has a sufficient number of neighbours to interact with. We use the common method to set the kernel size to a length such that the kernel includes a given number of neighbouring particles N_{ngb}.

3.2.4 Time-step

Our implementation of frequent scattering does not introduce an additional time-step constraint. This is because for our simulations the gravitational time-step is smaller than what is required for the frequent self-interactions. However, for different applications it is conceivable that the gravitational time-step becomes larger than what is needed for the scattering, for example in the phase of gravothermal collapse of a DM halo. Let us therefore briefly outline how the time-step requirements depend on the relevant quantities.

For the derivation of a time-step criterion one can start from the drag force:

$$F_{\mathrm{drag}} = \frac{1}{2}\,|\Delta v|^2\,\frac{\sigma_{\tilde{\mathrm{T}}}}{m_\chi}\,m^2\,\Lambda\,, \tag{3.14}$$

where m denotes the simulation particle mass and we have dropped the subscripts i, j. This equation implies a velocity change of

$$\Delta v_{\mathrm{drag}} = \frac{F_{\mathrm{drag}}}{m}\Delta t = \frac{1}{2}\,|\Delta v|^2\,\frac{\sigma_{\tilde{\mathrm{T}}}}{m_\chi}\,m\,\Lambda\,\Delta t\,. \tag{3.15}$$

Here, Δt denotes the time-step. For a conservative estimate we replace $m\,\Lambda$ with $\tilde{\rho}$, which is inversely proportional to N_{ngb}:

$$\tilde{\rho} = \frac{3\,m}{4\pi\,h^3} \sim \frac{\rho}{N_{\mathrm{ngb}}}\,. \tag{3.16}$$

From equations (3.15) and (3.16), we derive the time-step assuming the numerical error is kept constant ($\Delta v_{\mathrm{drag}}/|\Delta v| = \mathrm{const}$):

$$\frac{1}{\Delta t} \sim |\Delta v|\,\frac{\sigma_{\tilde{\mathrm{T}}}}{m_\chi}\,\frac{\rho}{N_{\mathrm{ngb}}}\,. \tag{3.17}$$

One finds that a smaller time-step is required when using a larger SIDM cross-section or when the relative velocities, i.e. the velocity dispersion, increases. Moreover, a smaller time-step is reasonable in dense regions. From equation (3.17), we also obtain a dependence

on the number of neighbours, choosing a larger value can relax the time-step constraint.

3.2.5 Implementation in gadget-3

We implement the DM self-interactions in GADGET-3, which is an updated version of the N-body code GADGET-2 (Springel, 2005).[3] Here, we will describe our implementation in the simulation code. We begin by describing how to find pairs of particles that should interact. Then, we comment on adaptive time-stepping. Lastly, we explain how we deal with the largest challenge posed by the parallelization.

How to find interacting particles?

In GADGET-3 a tree structure is used in the gravity calculation, and we use this same tree to find neighbouring particles that will scatter with one another. Defining the distance between particles i and j as d_{ij}, we use the tree to find all particle pairs for which $d_{ij} < h_i + h_j$. For all pairs of particles that fulfil this relation, we compute the effect of the frequent self-interactions and apply the velocity changes. Note, that for particles separated by more than the sum of their kernel sizes the overlap expressed by equation 3.13 vanishes.

Adaptive time-stepping

GADGET-3 uses an adaptive time-stepping scheme, where individual time-steps are assigned to each particles, with a power-of-two hierarchy of time-step lengths. Our scheme for frequent self-interactions is not based on individual particles, but on pairs of particles. Consequently, we need to compute a time-step for a pair.

The adaptive time-stepping scheme assigns particles to time-step bins, which leads to active and passive particles. The details can be found in the GADGET-2 paper (Springel, 2005). In consequence, a pair consists of one active particle and one which is active or passive. For an active–active pair, the time-step of the pair is given by

$$\Delta t = \frac{\min(\Delta t_i, \Delta t_j)}{2}\,, \tag{3.18}$$

where we divide by two because active–active pairs are considered twice per time-step (i.e. particle i finds particle j as a neighbour and vice versa). In the active–passive case, the pair is considered only once per time-step. Assuming that the active particle has the index i, the time-step can be written as

$$\Delta t = \Delta t_i\,. \tag{3.19}$$

We wish to point out that the time-step of the active particle is always shorter than that of the passive one. The time-step Δt computed as described above is used to compute the change in velocity due to the drag force using equation (3.4).

[3] Recently, the latest version GADGET-4 has been published (Springel et al., 2021).

Parallelization

The parallelization of our scheme for frequent self-interactions is more complicated than for classical gravity or hydrodynamic schemes. The difficulties arise from the fact that one cannot treat the velocity change due to the particle–particle self-interactions cumulatively. Rather the computation of a scattering event requires the information from previous scatterings. Consequently, we cannot send one particle to multiple processes (execution instances of a computer program) simultaneously to make sure that each particle is only used by one process at a time. In addition, when sending particles to other processes it needs to be ensured that they are not needed locally (by the sending process) to scatter with particles received from other processes. This is ensured by allowing only half of the processes to send particles at a time, while the other half only receives particles. Consequently, only the processes that receive particles compute the scattering, while the other half of the processes wait.

The communication between the processes is done in multiple sub-steps. We allow every process to communicate with all the other processes, but only one per sub-step. Given N processes we have $B = N - 1$ sub-steps. In each of these sub-steps, we create pairs of processes and the two processes of a pair communicate with each other, i.e. exchange particle data. The pairs of a sub-step do not have common members, i.e. they are disjoint sets. In practice, we have $2B$ sub-steps, i.e. every pair is considered twice. The first B sub-steps are used for sending particles to the process of a pair that has the larger ID (a unique number for identification) and in the second B sub-steps data is sent to the process with the smaller ID. Theoretically, sending particles to only one process of a pair could be enough, i.e. having B sub-steps. But in practice, it is more complicated than the exchange in both directions due to the use of adaptive time-stepping. The local process p given a sub-step b communicates with $c = p \oplus b$. Here, $b \in [1, B]$ and $\oplus$ denotes the XOR operator. This scheme has the advantage that it can be easily implemented. However, it does not give the best performance theoretically possible because half of the processes are waiting while the non-local scattering is computed and also because symmetries are not exploited, i.e. each process pair is considered twice per time-step. Nevertheless, the parallelization leads to a large speed-up of the computations and thus allows us to run reasonably large simulations.

This parallelization scheme can also be used for infrequent large-angle scattering. It allows overcoming the problem of 'bad scatterings' observed by Robertson et al. (2017a), although it is more computationally expensive because each process can only communicate with one other process at a time, requiring more communication cycles per simulation time-step. Our implementation of rare scattering is described in Appendix 3.B.

3.2.6 Differences to numerical modelling of infrequent scattering

To conclude the presentation of our numerical method let us discuss the differences to the common Monte-Carlo scheme for large-angle scattering. The modelling of such infrequent

scattering events with the N-body method has similarities to our approach described above in the sense that both methods are based on the same numerical representation, but they are not identical. In the following, we point out differences referring to the scheme used by Rocha et al. (2013).

First of all, the scheme for infrequent scattering computes a probability that two particles with a separation smaller than the kernel size scatter. This is in contrast to the presented scheme for frequent interactions, where a drag force acts on all particle pairs with a sufficiently small separation, i.e. overlapping kernel functions.

Furthermore, the two schemes differ in the magnitude and the direction of the velocity change. For the infrequent scattering the post-scattering velocity of particle 1 interacting with particle 2 can be expressed as

$$\boldsymbol{v}_1{}' = \boldsymbol{v}_1 - \Delta\boldsymbol{v} + |\Delta\boldsymbol{v}| \cdot \boldsymbol{e}_r \qquad \text{with} \qquad \Delta\boldsymbol{v} = \frac{\boldsymbol{v}_1 - \boldsymbol{v}_2}{2}\,, \tag{3.20}$$

where $\boldsymbol{e}_r$ is a random direction. The corresponding equation for the frequent scattering scheme is given by

$$\boldsymbol{v}_1{}' = \boldsymbol{v}_1 - \Delta\boldsymbol{v}_{\mathrm{drag}} + |\Delta\boldsymbol{v}_{\mathrm{rand}}| \cdot \boldsymbol{e}_f\,, \tag{3.21}$$

where $\boldsymbol{e}_f$ denotes a random direction perpendicular to $\Delta\boldsymbol{v}_{\mathrm{drag}}$. Crucially, $|\Delta\boldsymbol{v}_{\mathrm{drag}}|, |\Delta\boldsymbol{v}_{\mathrm{rand}}| \ll |\Delta\boldsymbol{v}|$, i.e. the velocity of the scattering particles change only slightly in fSIDM, while the differences can be of order unity in rSIDM.

Besides, the rSIDM scheme provides a more general description of self-interactions and is also capable of describing highly anisotropic cross-sections, when $\boldsymbol{e}_r$ is chosen according to the differential cross-section. But for those cross-sections favouring small-angle scattering, it would require a very large number of individual scattering events, which would cause a problem in terms of run time.

3.3 Verification tests

To test that our numerical scheme works properly and that the implementation accurately models frequent self-interactions, we use several test-problems, which we present in this section. The first problems study purely self-interactions. In contrast, the last problem, where we simulate an isolated DM halo, is motivated by astrophysics and includes gravity.

3.3.1 Deceleration problems

In our first test problem, we study a particle travelling through a background density, which is sampled by particles at rest. Here, we only consider the drag force and neglect the random component. Due to the drag force the test particle, which has a non-zero initial velocity, is decelerated by the background particles. We compare the trajectory of the test

particle to the exact solution, obtained from

$$\ddot{x} = -\frac{1}{2}\,\dot{x}^2\,\rho\,\frac{\sigma_{\tilde{\mathrm{T}}}}{m_\chi}\,. \tag{3.22}$$

We make use of two different initial conditions. First, we consider a constant density and secondly, we introduce a density gradient. For both we use 10^4 particles. They have a total mass of $10^{10}\,\mathrm{M}_\odot$. A self-interaction cross-section of $\sigma_{\tilde{\mathrm{T}}}/m = 200\,\mathrm{cm}^2\,\mathrm{g}^{-1}$ is used for the test simulations and the time-step is set to $\Delta t = 0.02\,\mathrm{Gyr}$. Besides, $N_{\mathrm{ngb}} = 64$ is used to determine the size of the spline kernel, which is used to compute the drag force.

Without density gradient

First, we choose a constant background density with an average density of 4.46×10^7 $\mathrm{M}_\odot\,\mathrm{kpc}^{-3}$. In Fig. 3.1 (upper panel), we show the velocity (blue) and position (black) of the test particle. For the velocity we find only minor deviations which should be negligible. For the particle position, the deviation is the integral of the minor deviations in the velocity. Here, we find a larger deviation at the end of the simulations. However, we do not expect this numerical error to be of a problematic size. Later we comment on the accuracy and argue that we expect a higher accuracy for typical astrophysical simulations.

With density gradient

Secondly, we choose a linear background density. The density is zero at the initial location of the test particle and increases linearly along its path. The simulation results are shown in Fig. 3.1 (lower panel). The exact solution is computed numerically using a Runge–Kutta fourth-order method. Compared to the problem without density gradient (Fig. 3.1, upper panel) we find even smaller deviations from the exact solution.

It is worth mentioning that in a typical astrophysical simulation of fSIDM the relevant self-interaction cross-sections are smaller than the one simulated here by at least one order of magnitude, while the typical DM densities are comparable. Moreover, in astrophysical simulations the time-steps will usually be much smaller because of the gravity constraints. Both will increase the accuracy of the modelling of frequent interactions.

3.3.2 Thermalization problem

In this test problem, we study a periodic box that contains randomly distributed particles. Initially, all particles have the same absolute velocity but with random orientation. The system is not in equilibrium but is expected to evolve towards an equilibrium state. The velocity distribution should become Maxwellian due to the self-interactions.

For the simulation we used 10^4 particles representing a total mass of $10^{10}\,\mathrm{M}_\odot$ within a cubic box of a side length of 10 kpc, the corresponding density is $10^7\,\mathrm{M}_\odot\,\mathrm{kpc}^{-3}$. Initially, the absolute velocity of all particles is set to $2\,\mathrm{kpc\,Gyr}^{-1}$. We use a self-interaction cross-section of $\sigma_{\tilde{\mathrm{T}}}/m = 10\,\mathrm{cm}^2\,\mathrm{g}^{-1}$, a time-step of $\Delta t = 0.012\,\mathrm{Gyr}$ and $N_{\mathrm{ngb}} = 64$.

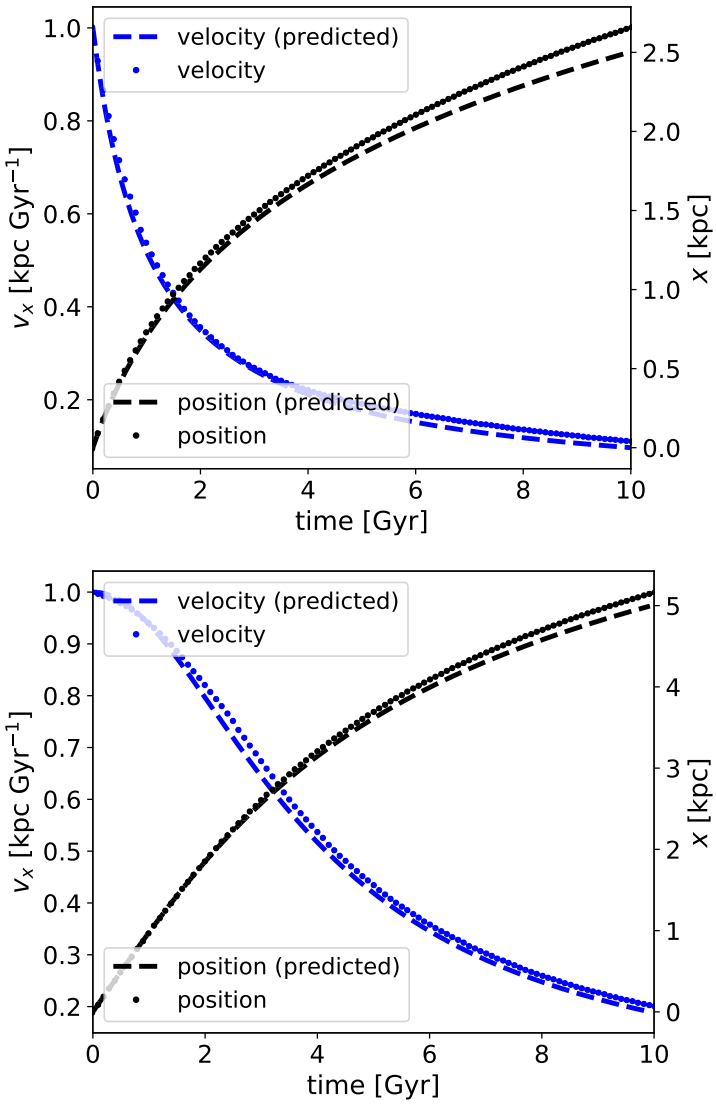

Figure 3.1: A particle is travelling through a constant background density (upper panel) or a linear background density with positive gradient (lower panel) and is decelerated through DM self-interactions. A velocity-independent cross-section of $\sigma_{\tilde{\mathrm{T}}}/m = 200\,\mathrm{cm}^2\,\mathrm{g}^{-1}$ is applied. The desired number of neighbours is set to 64.

In Fig. 3.2, we show our results for this test problem. We simulated the test problem with rare and frequent self-interactions. Our implementation of rare scattering is described in Appendix 3.B. Indeed, for both fSIDM and rSIDM we ultimately obtain a Maxwellian velocity distribution which is stable over time (lower panel). However, the shapes of the intermediate velocity distributions (upper and middle panels) are quite different for the two cases. The velocity distribution peak of rare self-interactions at $2\,\mathrm{kpc\,Gyr^{-1}}$ is mainly due to unscattered particles. The sharp cut at large velocities after 1 Gyr (upper panel) can be explained by the maximum velocity that a particle can gain due to a single scattering event, $v_{\mathrm{max}} = \sqrt{2}\,v_{\mathrm{ini}}$. The distribution function can become non-zero beyond that limit only if particles scatter multiple times. The middle panel reveals that rare self-interactions lead to more particles in the low-velocity regime, whereas frequent interactions produce more high-velocity particles.

3.3.3 Angular deflection problem

Our last test problem that purely studies the frequent self-interactions deals with a particle travelling through a constant background density. Along its path, the particle undergoes many small-angle scattering events and gets deflected. We measure the total deflection angle of many particles and compare them to the probability density function of Molière's theory (Moliere, 1948)[4].

We are simulating 8000 test particles with an additional 92 000 particles to model the density background. In total, the simulation contains a mass of $10^{10}\,\mathrm{M_\odot}$, which resides in a cube with a side length of 14 kpc. This implies a background density of $\rho = 3.353 \times 10^6\,\mathrm{M_\odot\,kpc^{-3}}$. The initial velocity of the test particles is $v_{\mathrm{init}} = 2.0\,\mathrm{kpc\,Gyr^{-1}}$, while the background particles are at rest. For the simulation we use a cross-section of $\sigma_{\tilde{\mathrm{T}}} = 10\,\mathrm{cm^2\,g^{-1}}$, a time-step of $\Delta t = 0.001\,\mathrm{Gyr}$ and $N_{\mathrm{ngb}} = 64$. The deflection angle θ of the test particles is defined as the angle between the initial and the current velocity vectors in the centre-of-mass system of the scattering physical particles, i.e. where they have the initial velocity of $v_{\mathrm{init}}/2$. The details about the derivation of the prediction from Molière's theory can be found in Appendix 3.C.

In Fig. 3.3, we show our results for the distribution of the deflection angles. The left-hand panel shows the distribution after the particles have travelled 0.01 Gyr within the target and the right one is for $t = 0.1\,\mathrm{Gyr}$. The plots demonstrate that our simulation agrees well with Molière's theory. From the test problems studied so far, we can conclude that we are able to model frequent self-interactions accurately.

3.3.4 NFW halo

To test our scheme for frequent self-interactions in an astrophysical context including gravity we simulate an isolated DM halo. As initial condition we choose a halo with a Navarro–Frenk–White (NFW) profile (Navarro et al., 1996) with $M_{\mathrm{vir}} = 10^{15}\,\mathrm{M_\odot}$, $r_{\mathrm{s}} = 300\,\mathrm{kpc}$,

[4]For a paper written in English on Molière's theory, we refer to Voskresenskaya & Tarasov (2012).

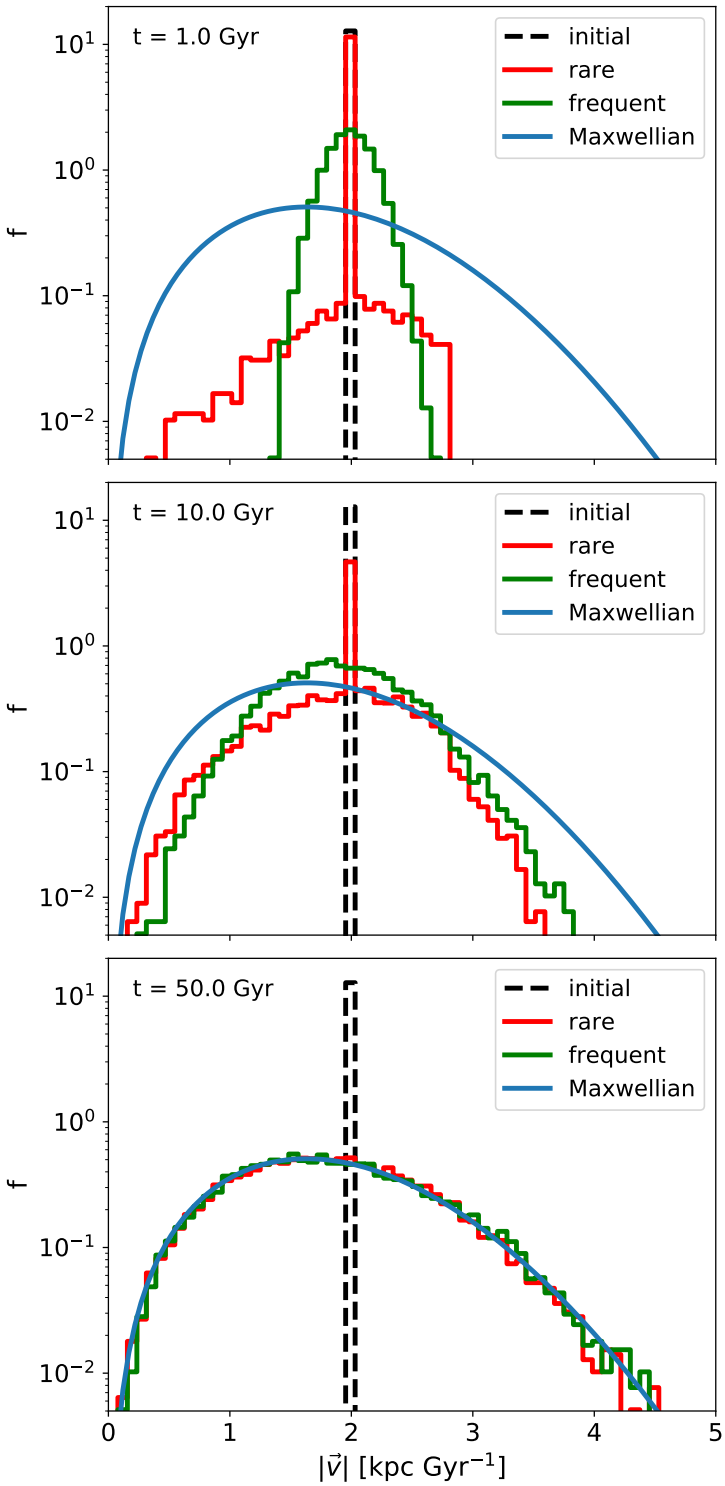

Figure 3.2: The velocity distributions for the thermalization problem are shown. The initial distribution is given in black. The evolution for rare (red) and frequent (green) self-interactions is shown for $t = 1$ Gyr (upper panel), 10 Gyr (middle panel) and 50 Gyr (lower panel). The plots demonstrate that the system evolves towards a Maxwell–Boltzmann distribution. The expected Maxwellian is plotted as well. In total 10000 particles were simulated with a cross-section of $\sigma_{\tilde{\mathrm{T}}}/m = 10\,\mathrm{cm}^2\,\mathrm{g}^{-1}$.

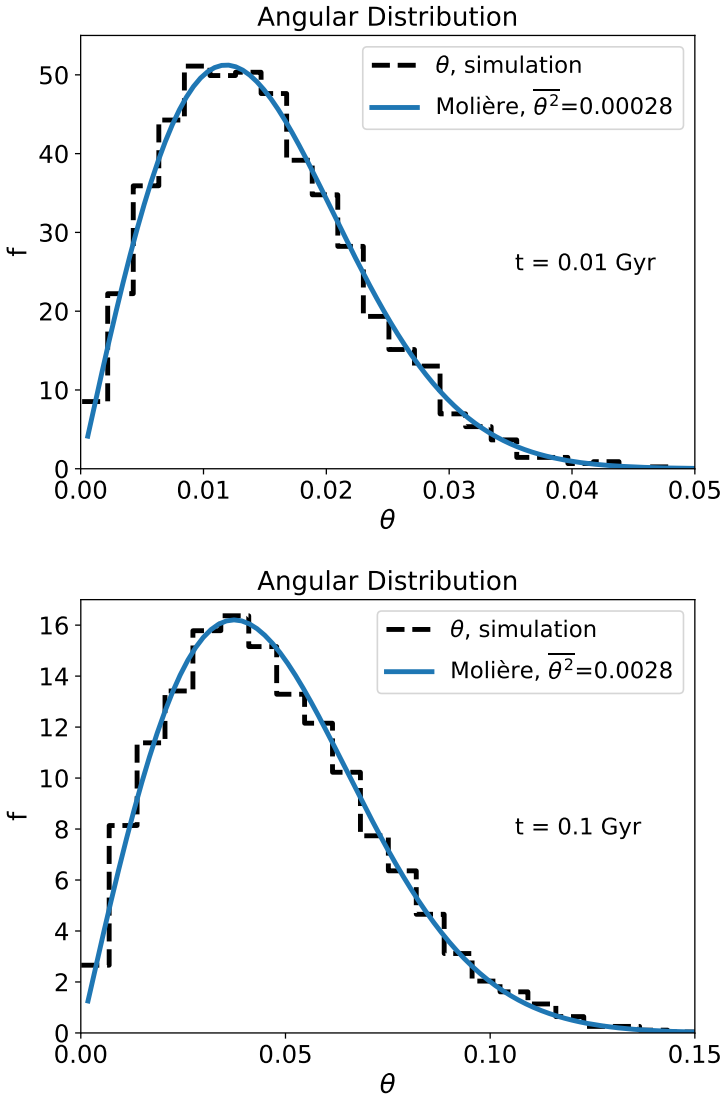

Figure 3.3: The distribution of the total deflection angle after 0.01 Gyr (upper panel) and 0.1 Gyr (lower panel). The self-interaction cross-section was chosen as $\sigma_{\tilde{\mathrm{T}}}/m = 10\,\mathrm{cm}^2\,\mathrm{g}^{-1}$. A number of 8000 test particles were used and in total 100 000 particles were simulated.

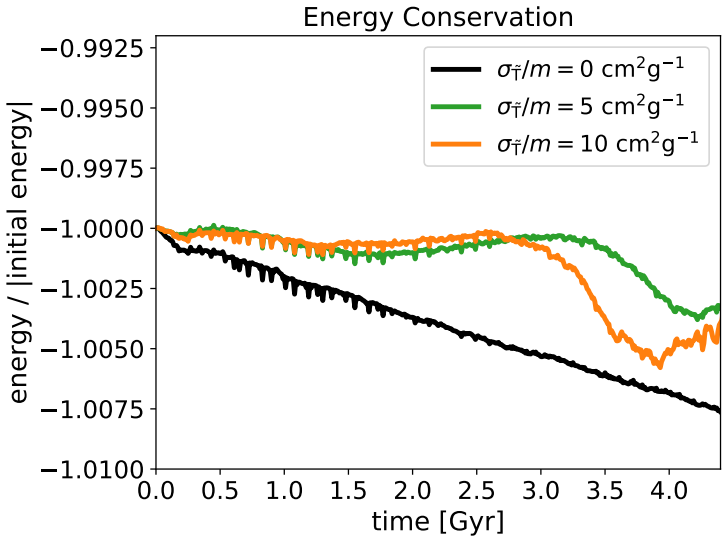

Figure 3.4: We show the evolution of the total energy for simulations of an initial NFW halo evolved with three different cross-sections. The black curve corresponds to $\sigma_{\tilde{T}}/m = 0\,\mathrm{cm^2\,g^{-1}}$, which is identical to the collisionless CDM.

and $\rho_s \equiv \rho(r_s) = 7.25 \times 10^5\,\mathrm{M_\odot\,kpc^{-3}}$. The NFW halo is sampled up to the virial radius ($r_{\mathrm{vir}} = 1626\,\mathrm{kpc}$). We integrate the Jeans equation to obtain the velocity dispersion. To sample the initial velocities, we locally approximate the velocity distribution by a Maxwell–Boltzmann distribution, i.e. we draw the velocity components randomly from a Gaussian. The gravitational softening length is set to $\epsilon = 0.56\,\mathrm{kpc}$ and $N_{\mathrm{ngb}} = 64$ is used. In Appendix 3.D, we demonstrate the stability of our initial conditions for a resolution of $N = 10^5$ particles when evolved without self-interactions.

First, we study the energy conservation for three different cross-sections using a resolution of $N = 10^5$ particles. For this purpose we compute the total energy of the entire halo and divide it by the absolute value of the initial total energy. Our results are shown in Fig. 3.4. The total energy is not perfectly conserved as the formulation of the Poisson solver does not explicitly conserve energy. This is in contrast to the formulation of frequent self-interactions, which does conserve energy explicitly. Nevertheless, the deviation from the initial energy is small enough that we can consider it as conserved for our purpose of astrophysical simulations.

Finally, we investigate the convergence of our numerical scheme. We simulate the DM halo choosing different resolutions and a self-interaction cross-section of $\sigma_{\tilde{T}}/m = 10\,\mathrm{cm^2\,g^{-1}}$. In Fig. 3.5, we show our results, i.e. density profiles at several times for different resolutions. The upper panel represents the initial conditions, the middle and lower panel are for $t = 1\,\mathrm{Gyr}$ and $t = 4\,\mathrm{Gyr}$. We can see that the density profile converges for increasing resolution, which confirms that our scheme is suitable for the application to astrophysical problems.

Fig. 3.5 shows that initially a constant-density core forms, whereas at later times the central density increases. This is because the self-interactions lead to a transport of energy

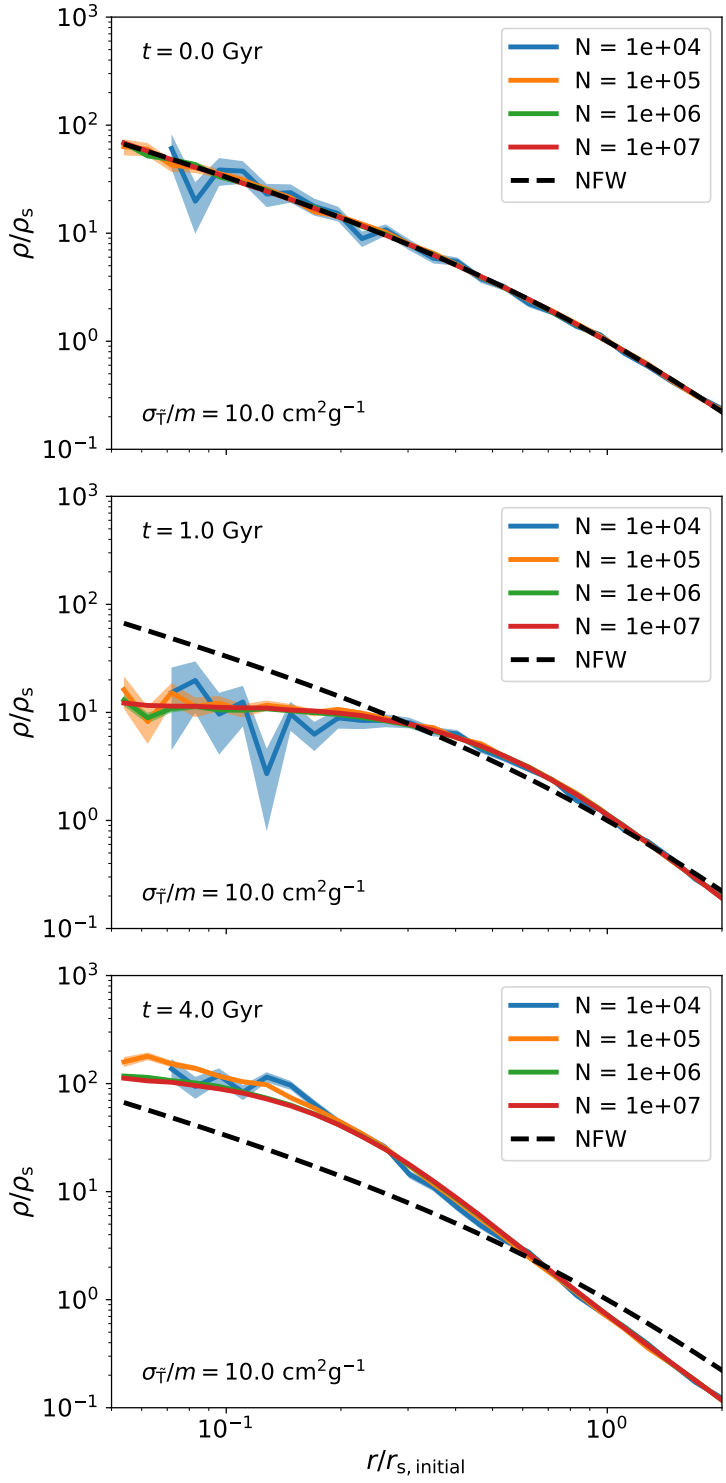

Figure 3.5: Density profiles for an initial NFW halo simulated with a cross-section of $\sigma_{\tilde{\mathrm{T}}}/m = 10\,\mathrm{cm}^2\,\mathrm{g}^{-1}$ are shown. Different resolutions were chosen to demonstrate convergence. The upper panel gives the initial conditions, the middle panel gives the DM halo after 1.0 Gyr and the lower panel for 4.0 Gyr. For comparison, we show the analytical NFW profile in black.

in the outward direction. This energy loss causes the core to shrink which, eventually, leads to a gravothermal core-collapse like in rSIDM (e.g. Burkert, 2000; Kochanek & White, 2000; Koda & Shapiro, 2011). This process will be investigated in more detail in the following section.

3.4 Core Size of Dark Matter Haloes

In this section, we study the formation and evolution of a DM core in an isolated halo and compare frequent and rare self-interactions. We first describe the simulation set-up, then explain how we measure the core size and finally present our results.

As initial conditions, we take similar ones to Robertson et al. (2017b). The initial density follows a Hernquist profile (Hernquist, 1990) with a mass of $M = 2.46 \times 10^{14}\,\mathrm{M}_\odot$ and a scale radius of $r_s = 279\,\mathrm{kpc}$. We sample the halo up to $r = 400 r_s$ using $N = 10^7$ DM particles.

We explore the same cross-sections as in fig. 1 in Robertson et al. (2017b), chosen as $\hat{\sigma} \in \{0, 1, 3, 10\}$ with $\hat{\sigma} = (2\sigma_{\tilde{\mathrm{T}}}/m)(M/r_s^2)$, which implies $\sigma_{\tilde{\mathrm{T}}}/m \in \{0, 0.227, 0.757, 2.272, 7.574\}$ $(\mathrm{cm}^2\,\mathrm{g}^{-1})$.[5] We simulate these cross-sections both as frequent and rare scattering using our respective implementation in GADGET-3, assuming the rare scattering to be isotropic. This approach allows us to study differences between fSIDM and rSIDM in the context of core formation. We conduct our simulations with a gravitational softening length of $\epsilon = 0.56\,\mathrm{kpc}$ and use $N_{\mathrm{ngb}} = 64$ for the scattering.

In order to measure core sizes, we follow Robertson et al. (2017b), i.e. we fit a cored Hernquist profile to the radial density distribution,

$$\rho(r) = \frac{M}{2\pi} \frac{r_s}{(r^\beta + r_{\mathrm{core}}^\beta)^{1/\beta}} \frac{1}{(r + r_s)^3}. \tag{3.23}$$

As free parameters we take the core radius r_{core}, the scale radius r_s and the mass M, while β is kept fixed to $\beta = 4$. We then determine the number of particles N_i in several radial bins with boundaries r_i and r_{i+1} and compare this number to the expected value λ_i according to the cored density profile:

$$\lambda_i = \frac{4\pi}{m} \int_{r_i}^{r_{i+1}} r^2 \rho(r)\,\mathrm{d}r\,, \tag{3.24}$$

where m denotes the mass of a simulation particle. To fit the density profile we maximize a likelihood based on Poisson statistics,

$$\mathcal{L} = \prod_i \frac{\lambda_i^{N_i}\, e^{-\lambda_i}}{N_i!}\,. \tag{3.25}$$

In Fig. 3.6, we show the evolution of the core size over a time of 7.2 Gyr. Within the studied range of $\hat{\sigma}$, we find the time it takes for the core to grow and collapse to decrease

[5] We use $\sigma_{\tilde{\mathrm{T}}}$ as defined in Kahlhoefer et al. (2014), which is a factor of 2 smaller in the regime of isotropic scattering compared to the commonly used values given in terms of σ_{T}.

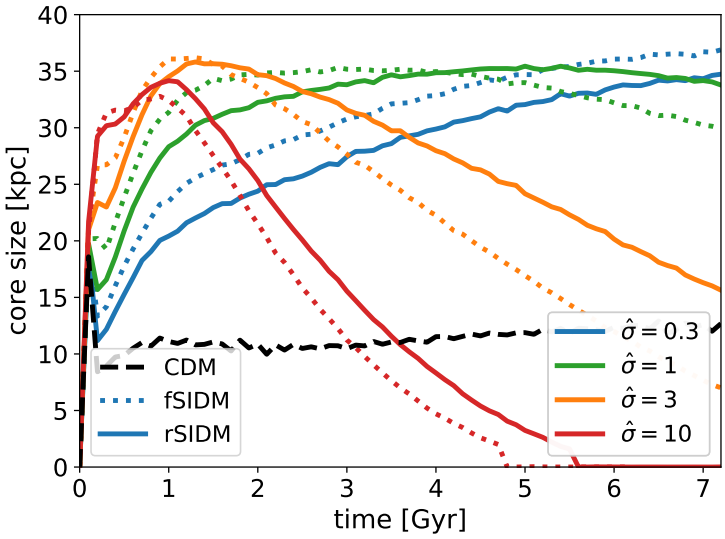

Figure 3.6: The evolution of the core size for an isolated DM halo is shown. The halo has initially the shape of an Hernquist profile. The halo was simulated using several cross-sections for frequent and rare self-interacting DM. The errors correspond to the 16% and 84% levels. They were computed using the Markov chain Monte Carlo sampling implementation of emcee (Foreman-Mackey et al., 2013).

with increasing self-interaction cross-section. Moreover, the core formation happens much faster than the core-collapse. We find that the maximum core size is nearly independent of the self-interaction cross-section for both rSIDM and fSIDM, in agreement with earlier findings for rare self-interactions (e.g. Kochanek & White, 2000).

When comparing frequent and rare self-interactions with the same momentum transfer cross-section, the evolution of fSIDM is a bit faster, i.e. maximum core size is reached earlier. Nevertheless, there is no big difference between frequent and rare scattering. The largest deviation is found at late times for a cross-section of $\hat{\sigma} = 3$. The other free parameters of our fit (e.g. M and r_s) behave very similar for rSIDM and fSIDM. Similar to the difference in core size we observe differences in the central density of the halo.

In comparison to fig. 1 Robertson et al. (2017b), we find a smaller maximum core-size, but overall a similar evolution. The differences may be due to slight differences in the initial conditions. Here, we approximated the local velocity distribution of the halo by a Maxwellian to sample the initial velocities. As one can see in Fig. 3.6, at the very beginning of the simulation a core forms. This is because the initial conditions are not in perfect equilibrium. Even for a CDM run with flawless initial conditions, the core formation cannot be avoided completely as numerical effects lead to a small core.

We also note that core-collapse happens much faster in isolated DM haloes than in cosmological simulations, where the core is heated up through late-time infall.

3.5 Equal-Mass Merger

In this section, we study the evolution of an equal-mass merger using frequent and isotropic rare scattering. We investigate several cross-sections and compare the two types of scattering. This is interesting because merging systems allow to constrain DM self-interactions. The scattering does lead to drag-like behaviour under given circumstances. This decelerates the DM component but does not affect the galaxies[6] and thus leads to an offset between the two. There have been several studies on merging systems with DM self-interactions in the literature (e.g. Randall et al., 2008; Kahlhoefer et al., 2015; Robertson et al., 2017a) as well as discussions on the size of observed offsets (e.g. Bradač et al., 2008; Dawson et al., 2012; Dawson, 2013; Jee et al., 2015; Harvey et al., 2017; Peel et al., 2017; Taylor et al., 2017; Wittman et al., 2018). There is also an extensive literature on how the self-interactions affect the merger evolution and under which conditions the picture of a drag force is appropriate (e.g. Markevitch et al., 2004; Harvey et al., 2014; Kahlhoefer et al., 2014; Kim et al., 2017; Robertson et al., 2017b). As the drag-like behaviour is expected to depend on the shape of the differential cross-section, merging systems potentially allow for constraining not only the strength of the self-interactions but also its angular dependence.

We start with a description of our simulation set-up and then explain how we analyse the simulation. Finally, we present and interpret our findings, in particular how the merger leads to offsets between DM and galaxies. A schematic illustration of the merger is shown in Fig. 3.7. The various details shown in this figure will be discussed in the remainder of this section.

Our initial conditions are chosen similar to the ones of Kim et al. (2017). We set up two NFW haloes, each with a virial mass of $M_{\rm vir} = 10^{15}\,{\rm M}_\odot$. They are separated by 4000 kpc and move initially with a relative velocity of $1000\,{\rm km\,s^{-1}}$ along the merger axis towards each other, such that the impact parameter of the merger is zero. The two DM haloes are described by the same parameters but sampled independently. The concentration parameter is $c = 3.3$ and the scale radius is $r_{\rm s} = 630\,{\rm kpc}$. We sample each halo up to a radius of 2667 kpc using 6×10^6 DM particles for each halo with a particle mass of $m_{\rm DM} = 2 \times 10^8\,{\rm M}_\odot$.

In addition, we include particles representing galaxies in our simulations. Each halo has 3×10^4 of these particles with a mass of $m_{\rm Gal} = 8 \times 10^8\,{\rm M}_\odot$ each. These particles do not represent individual galaxies (they are more abundant than galaxies in clusters) but they can be seen as a "smoothed out" galaxy distribution. As in Kim et al. (2017), we place a particle at the centre of each halo to model the brightest cluster galaxy (BCG). These particles have a mass of $m_{\rm BCG} = 7 \cdot 10^{10}\,{\rm M}_\odot$. This is a very idealized treatment of the BCGs as we neglect their extension. In Appendix 3.D, we demonstrate that the haloes used for the merger simulation are stable when simulated in isolation without self-scattering.

We simulate the same self-interaction cross-sections as in Kim et al. (2017) plus some additional ones, i.e. $\sigma_{\tilde{\rm T}}/m \in \{0.0, 0.5, 1.0, 1.5, 2.0, 2.5, 3.5, 5.0\}({\rm cm^2\,g^{-1}})$. In practice we

[6] Note that we treat galaxies as collisionless test particles in this work as is mostly done in the literature.

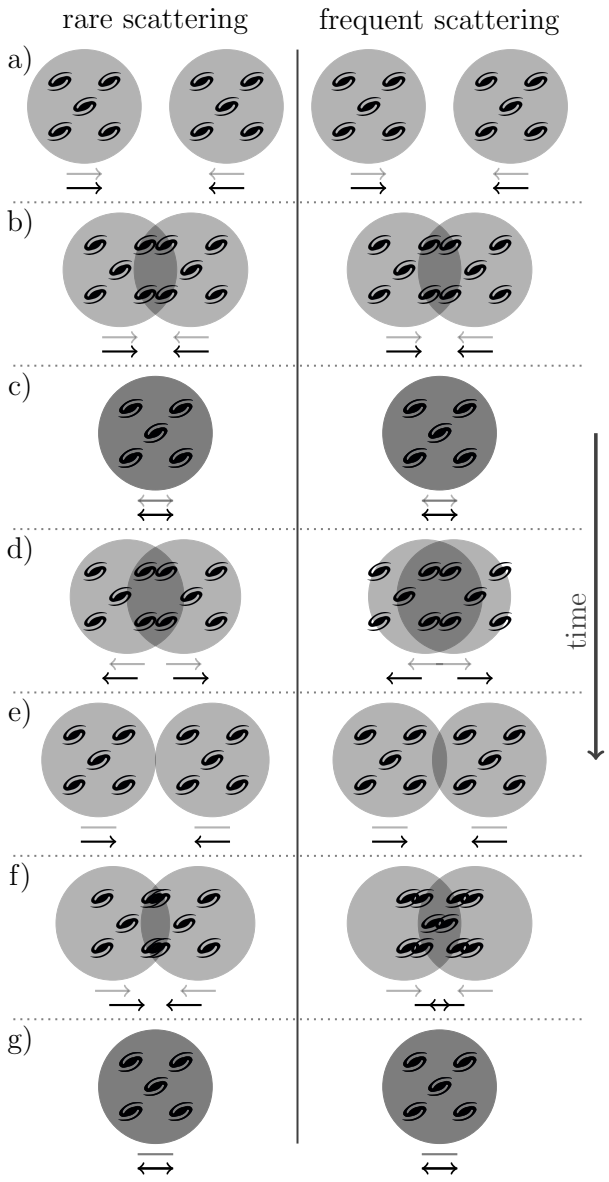

Figure 3.7: The evolution of an equal-mass galaxy cluster merger for frequent and rare DM self-interactions is illustrated. We only illustrate the DM (grey circles) and Galaxy (black spirals) positions as well as their direction of motion indicated by the arrows. The shape of the DM haloes is not taken into account. Rare scattering is shown on the left-hand side and frequent scattering on the right-hand side. The time propagates from the top to the bottom. The evolution we illustrate here is similar to the one we found for a cross-section of $\sigma_{\tilde{\mathrm{T}}}/m = 1.5\,\mathrm{cm}^2\,\mathrm{g}^{-1}$, but exaggerated. In (a) we show the initial state and in (b) we illustrate the infall-phase. The first pericentre passage is displayed in (c) and (d) gives a time a little bit later. This is the first time where we find a significant difference between rSIDM and fSIDM. For the frequent interactions, the DM is closer to barycentre, but the galaxies behave similarly implying larger offsets for fSIDM. About the first apocentre passage both components reach a larger distance from barycentre if the self-interactions are rare. This is illustrated in (e). In (f), at a later time we find larger offsets for fSIDM, although the DM component is closer to barycentre than in rSIDM. Finally, we illustrate the second pericentre in (g).

match rare and frequent cross-section using $\sigma_{\tilde{\mathrm{T}}} = \sigma/2$ as appropriate for isotropic scattering (see Appendix 3.B).[7] For the gravitational softening length we use a value of $\epsilon = 0.56\,\mathrm{kpc}$ and employ $N_{\mathrm{ngb}} = 64$ for the scattering.

3.5.1 Method of analysis

Before discussing our results in detail, let us first give an overview of the various figures that we have produced and the methods used to obtain them. To analyse the simulations we find the peaks of the DM and galactic component (see Fig. 3.8). Several methods for peak finding can be found in the literature. In this work, we follow the algorithm described in Kim et al. (2017), i.e. we use a kernel density estimate (KDE) with a 2D Gaussian smoothing kernel with a width of 100 kpc, while we project along one axis perpendicular to the merger axis. As we only study simulations with an impact parameter equal to zero, we perform the peak search only along the merger axis, i.e. we take the positions with maximum density according to the KDE. In order to obtain uncertainties on the peak position, we bootstrap the galaxy distribution 1000 times and the much better sampled DM component 10 times.

We then compute offsets between the components as the distance between their density peaks. Therefore we define the "half"-separation between two peaks of the same species, i.e. the two DM peaks, the two galaxy peaks or the two BCGs.

$$d := \frac{|x_1 - x_0|}{2}\,, \tag{3.26}$$

where x is the x coordinate with respect to barycentre. The offsets shown in Fig. 3.9 are the mean offset of the two haloes, with positive values implying that the galaxies are closer to the barycentre than the DM and negative values corresponding to the opposite case. In Fig. 3.10, we show the maximum positive offset as function of the self-interaction cross-section. Furthermore, we compute how much the peaks for fSIDM and rSIDM deviate from each other (Fig. 3.11). For this purpose, we define a quantity δ that is based on the mean of the two haloes,

$$\delta := \frac{|x_{\mathrm{r},0} - x_{\mathrm{r},1}| - |x_{\mathrm{f},0} - x_{\mathrm{f},1}|}{2}\,. \tag{3.27}$$

Here, x denotes the peak position of the DM haloes (0 and 1) for rare (r) and frequent (f) self-interactions. A positive value of δ implies that the fSIDM peaks are closer to barycentre than the rSIDM peaks and vice versa.

When the peak separation is small the peak identification becomes inaccurate and biased towards the barycentre (as can be seen in Fig. 3.8). This is why we do not show offsets and peak deviation for separations less than the scale radius ($r_s = 630\,\mathrm{kpc}$). We also do not consider these values for the subsequent analysis.

[7] This definition differs from the one in Kim et al. (2017), where $\sigma_{\mathrm{T}} = \sigma$ is used.

3.5.2 Results

The upper panel of Fig. 3.8 shows how the density peaks of all components evolve with time for frequent scatterings with a cross-section $\sigma_{\tilde{\mathrm{T}}}/m = 1.5\,\mathrm{cm}^2\,\mathrm{g}^{-1}$. The DM component coalesces earlier than the galactic component due to the self-interactions. Similar to Kim et al. (2017), we find long-lasting oscillations of the BCG particles. The same plot for several other runs can be found in Appendix 3.E. From these plots, we can see that the galaxies and BCGs behave differently, depending on the type of DM self-interaction. An exaggerated illustration of the merger evolution for rSIDM and fSIDM inspired by simulations with a cross-section of $\sigma_{\tilde{\mathrm{T}}}/m = 1.5\,\mathrm{cm}^2\,\mathrm{g}^{-1}$ is shown in Fig. 3.7.

In general, we find that larger cross-sections lead to shorter merger times for both rSIDM and fSIDM. This is shown in the lower panel of Fig. 3.8, where we show the evolution of the DM peak position for selected merger simulations. Furthermore, the distance of the DM peaks at first apocentre passage shrinks with increasing cross-section. The evolution of the DM peaks for rSIDM and fSIDM is similar but not identical. For the shown simulations the largest difference occurs in our run with a self-interaction cross-section of $\sigma_{\tilde{\mathrm{T}}}/m = 1.5\,\mathrm{cm}^2\,\mathrm{g}^{-1}$. For large cross-sections the differences vanish since the two haloes coalesce on contact.

Next, we study galaxy–DM and BCG–DM offsets for fSIDM and rSIDM, which are shown in Fig. 3.9. In general, we find the offsets to be larger for fSIDM when comparing to the same rSIDM momentum transfer cross-section. Also, the offsets of the BCG particles are larger than the offsets of the galactic component. This is probably a consequence of modelling them as point-like instead of treating them as extended objects. For $\sigma_{\tilde{\mathrm{T}}}/m = 1.5\,\mathrm{cm}^2\,\mathrm{g}^{-1}$, the offsets are zero when the galaxies are roughly at apocentre, but before and afterwards they are non-zero with different signs. Compared to the first apocentre passage the point in time when the sign of the offsets changes becomes earlier with decreasing cross-section. For the early offsets, the DM component is closer to barycentre (i.e. the offset is negative), but for the late offsets, the DM is more distant from the barycentre than the galaxies (i.e. the offset becomes positive). It is worth mentioning that the difference between fSIDM and rSIDM in the offsets shortly after the first pericentre passage are mainly due to different peak positions of the DM as we explain below. But for the later offsets it is the other way around because then the offsets are caused by differences in the galaxy peak positions. Note, here we only considered offsets before the second pericentre passage. For even later offsets, the sign potentially changes again, but typically the offsets are smaller.

In the literature, the early offsets, e.g. for the Bullet Cluster, have been studied, which arise directly after the first pericentre passage. In contrast, we will mainly focus on a later stage of the merger evolution. In Fig. 3.10, we compare the maximum size of the offsets in the stage where the galaxies are closer to barycentre. We find the largest offset for fSIDM in the simulation with $\sigma_{\tilde{\mathrm{T}}}/m = 1.0\,\mathrm{cm}^2\,\mathrm{g}^{-1}$ and for rSIDM in the simulation with $\sigma_{\tilde{\mathrm{T}}}/m = 1.5\,\mathrm{cm}^2\,\mathrm{g}^{-1}$. The largest fSIDM offset is more than a factor of 2 larger than the largest rSIDM offset. In other words, frequent self-interactions can cause much larger

offsets (when the galaxies are closer to barycentre) than rare self-interactions. For smaller cross-sections ($\sigma_{\tilde{\mathrm{T}}}/m \lesssim 1.0\,\mathrm{cm}^2\,\mathrm{g}^{-1}$), the maximum offset decreases, but there are still difference of more than a factor of 2 between fSIDM and rSIDM. The larger offsets of fSIDM at small cross-sections ($\sigma_{\tilde{\mathrm{T}}}/m \sim 0.5\,\mathrm{cm}^2\,\mathrm{g}^{-1}$) are particularly interesting as they could potentially be observable.

For large cross-sections ($\sigma_{\tilde{\mathrm{T}}}/m \gtrsim 1.5\,\mathrm{cm}^2\,\mathrm{g}^{-1}$), the maximum offsets decrease with increasing cross-section and so does the difference between simulations of rare and frequent scattering. For $\sigma_{\tilde{\mathrm{T}}}/m \gtrsim 5.0\,\mathrm{cm}^2\,\mathrm{g}^{-1}$ the DM haloes coalescence on contact and the type of offsets we discuss here no longer occurs. We note that measuring offsets with our peak finding method could be inaccurate for some cross-sections, i.e. for $\sigma_{\tilde{\mathrm{T}}}/m \in \{2.0, 2.5, 3.5\}(\mathrm{cm}^2\,\mathrm{g}^{-1})$, since we neglect the offsets for small halo separations as the peaks are biased towards barycentre.

Finally, we compare the peak positions in rSIDM and fSIDM. In Fig. 3.11 we show the quantity δ defined in equation 3.27 and find that δ increases with $\sigma_{\tilde{\mathrm{T}}}/m$ in the regime of small cross-sections. Of particular interest is the evolution between the first pericentre passage and the second one, which occurs $\sim 1.9\,\mathrm{Gyr}$ after the first one for $\sigma_{\tilde{\mathrm{T}}}/m = 0.5\,\mathrm{cm}^2\,\mathrm{g}^{-1}$ and for larger cross-sections earlier. The DM peaks of the fSIDM run are found to be closer to the barycentre than for the corresponding rSIDM run, corresponding to $\delta > 0$ (solid lines). The same is true for the galaxies (dashed lines) and the BCGs (dotted lines). Shortly after the pericentre passage, δ is smaller for the galaxies than for the DM component because only the DM and not the galaxies are affected by the self-interactions. However, the deviation of the galaxy peaks grows subsequently and becomes larger than the one for DM well before the first apocentre ($\sigma_{\tilde{\mathrm{T}}}/m = 0.5\,\mathrm{cm}^2\,\mathrm{g}^{-1}$) or at a somewhat later time around the first apocentre ($\sigma_{\tilde{\mathrm{T}}}/m = 1.5\,\mathrm{cm}^2\,\mathrm{g}^{-1}$). This is a consequence of how the galaxies respond to differences in the DM distribution via gravitational interaction. This response leads to a greater difference in the galaxy distribution and creates the larger offsets for frequent scattering compared to rare scattering shown in Fig. 3.10. In Appendix 3.F, we provide further details on this amplification mechanism.

Overall, we found that the phenomenology of fSIDM differs significantly from the one of rSIDM. In particular, frequent self-interactions can lead to much larger offsets than rare scattering. Consequently, it should be possible at least in principle to distinguish between the two types of DM self-interactions using detailed observations of merging galaxy clusters.

3.6 Discussion

In this section, we first discuss technical issues concerning the numerical scheme, its implementation and the analysis of our simulation. Then we elaborate on the physical implications of our results.

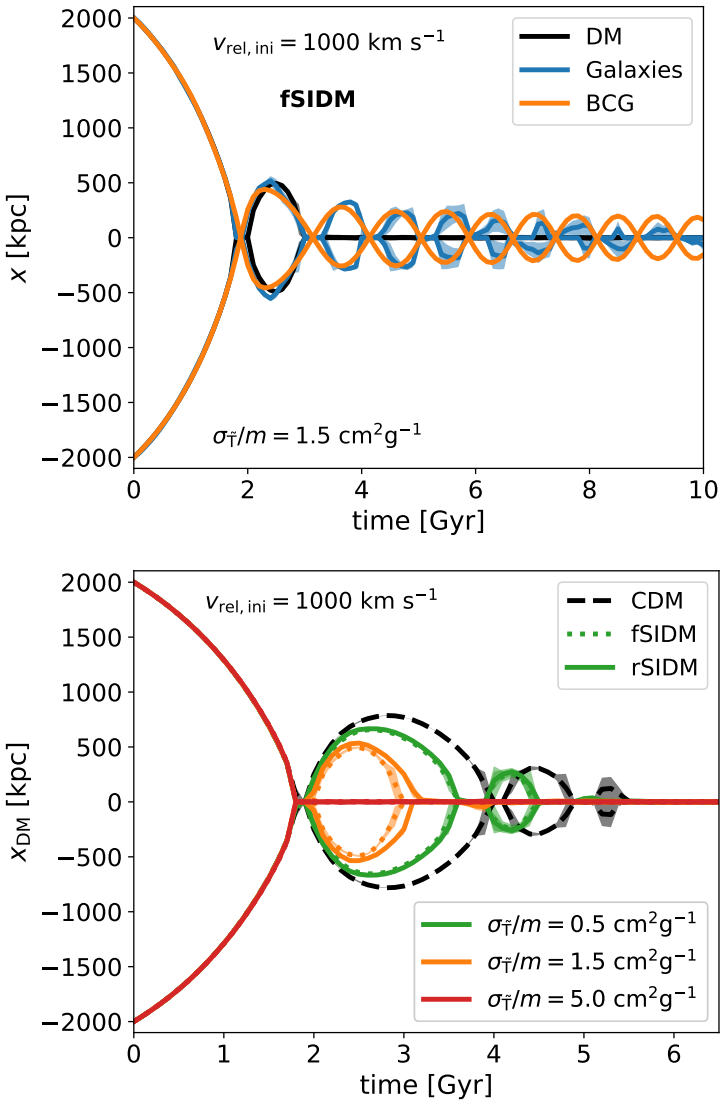

Figure 3.8: Upper panel: The density peak distance to barycentre for various components of a merger is shown as a function of time. Two NFW haloes were merged using frequent self-interacting DM with a cross-section of $\sigma_{\tilde{\Gamma}}/m = 1.5\,\mathrm{cm}^2\,\mathrm{g}^{-1}$. We measure the density peak for each of the two haloes. We do this separately for the DM and galaxies. Each halo contains one particle to model the BCGs. For the plot we simply use the position of that particle. The plot shows the distance to the barycentre along the merger axis. Lower panel: The plot is similar to the upper one. Here, we show the DM component only, but for several merger simulations with different self-interaction cross-sections.

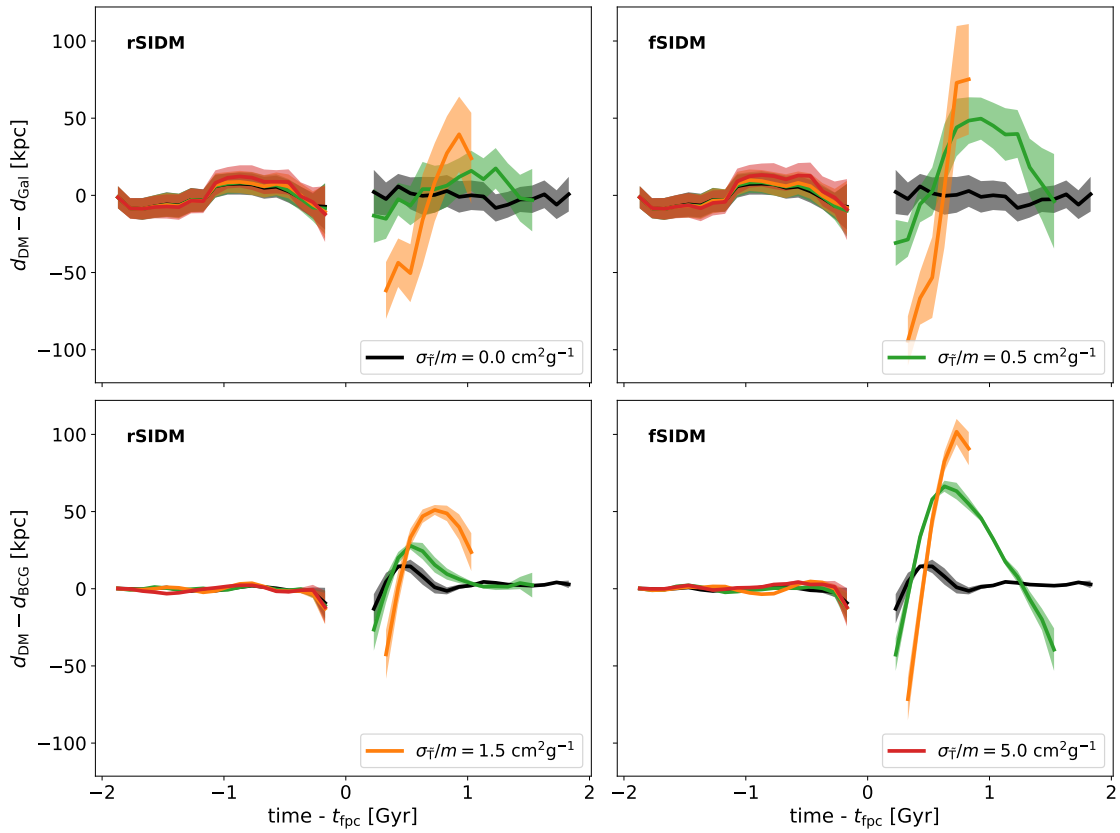

Figure 3.9: Offsets between DM and galaxies (upper panels) or BCGs (lower panels) are shown as function of time. Here we measure the time with respect to the first pericentre passage (t_{fpc} = 1.87 Gyr). We display results for several self-interaction cross-sections. The left-hand panels give the offsets for rare self-interactions and the right-hand panels for frequent scattering. The galaxy offsets before the first pericentre passage are mainly due to the uncertainty in the galaxy peaks (compare upper and lower panels).

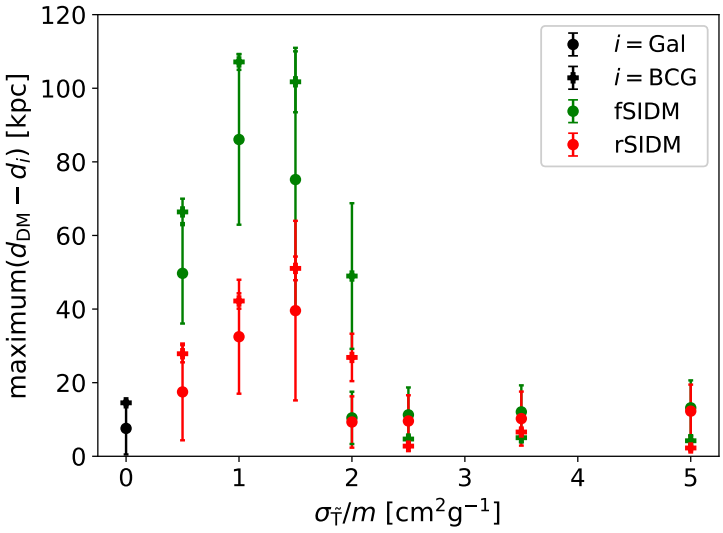

Figure 3.10: We show the maximum offset as function of self-interaction cross-section. We consider the distance between DM peaks and the peak of the galactic component or the BCG as shown in Fig. 3.9. The offsets are shown for both, frequent and rare self-interactions. It should be mentioned that we only consider offsets where the DM component is more distant to the centre of mass than the galaxies. The shown results for $\sigma_{\tilde{T}}/m \in \{2.0, 2.5, 3.5\}(\mathrm{cm}^2\,\mathrm{g}^{-1})$ are likely inaccurate due to the peak finding method.

3.6.1 Technical aspects

From a technical perspective, there are several interesting directions for future extensions and improvements. An obvious next step would be to include an angular dependence in the rSIDM scheme (Robertson et al., 2017b). It should then be possible to simulate arbitrary differential cross-sections, including those that have significant scattering probabilities in both the rare and the frequent scattering regime. For this purpose one could for example introduce a cut-off angle that distinguishes between the two cases, such that small-angle scattering is treated in the frequent regime while large-angle scattering is simulated explicitly in the scheme for rare scattering. To validate this approach one needs to confirm that results do not depend on the precise value of the cut-off angle.

Another important extension will be to model velocity-dependent differential cross-sections, which appear to be preferred by observational data (e.g. Correa, 2021; Sagunski et al., 2021) and have been investigated in several N-body studies (e.g. Colin et al., 2002; Vogelsberger et al., 2012; Banerjee et al., 2020). In fact such a velocity dependence is very natural from the particle physics perspective, in particular for frequent DM scatterings induced by light-mediator exchange, see e.g. Buckley & Fox (2010); Loeb & Weiner (2011); Bringmann et al. (2017). Such a velocity dependence can be easily implemented in our code, for both rSIDM as well as fSIDM. Furthermore, one could abandon the assumption that scattering is elastic and also model dissipative scattering processes within the N-body method (Huo et al., 2020).

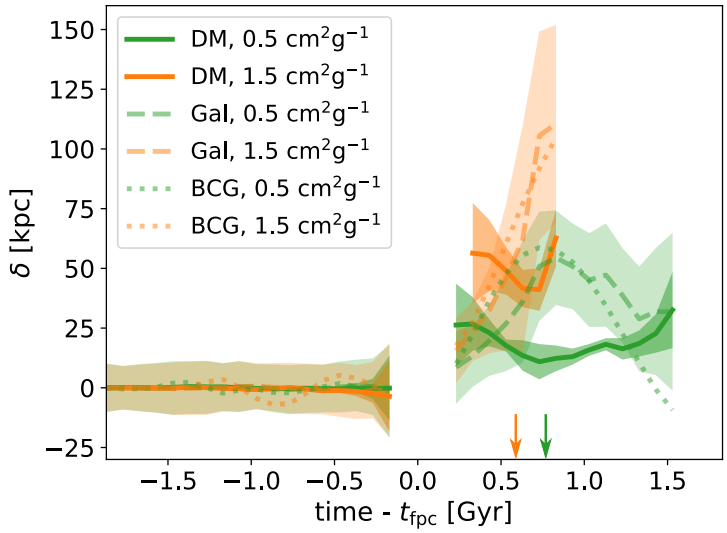

Figure 3.11: The deviation (δ, see equation 3.27) of peaks between the fSIDM and rSIDM runs is shown as function of time. We measure the time with respect to the first pericentre passage ($t_{\mathrm{fpc}} = 1.87\,\mathrm{Gyr}$). A positive value of δ implies that the peak of the fSIDM simulation is closer to barycentre than the rSIDM one. We compare DM and galaxy peaks as well as the positions of the BCGs. Results are plotted for $\sigma_{\tilde{\mathrm{T}}}/m = 0.5\,\mathrm{cm}^2\,\mathrm{g}^{-1}$ (green) and $\sigma_{\tilde{\mathrm{T}}}/m = 1.5\,\mathrm{cm}^2\,\mathrm{g}^{-1}$ (orange). Note, the peak deviation is only shown when the distance of the peaks is larger than the scale radius (630 kpc). We also apply this to the BCGs. The first apocentre passage (which is very similar for rSIDM and fSIDM) is indicated by an arrow for each cross-section.

In addition to the scattering process, one could improve the treatment of the galactic component in our simulations. In this study we have treated galaxies as collisionless particles, which may be inaccurate to some extent (Kummer et al., 2018). Moreover, galaxies are extended objects and their size may be too large to be approximated by point masses. Especially the trajectory of BCGs could be affected in relevant ways.

As mentioned in the description of the implementation, the parallelization of the frequent scattering is presently not optimal. One can envision a better scheme that exploits symmetries and does not cause large latency times, even though such a scheme could not make use of the infrastructure (e.g. tree algorithm, domain decomposition) that GADGET-3 provides. However, for our purpose the current parallelization is sufficient to complete our simulations in reasonable times. For example, consider the simulations presented in sec. 3.5, which were executed using MPI parallelization only on 64 logical cores. The computation of the frequent scattering took $\sim 80\%$ of the computing time, out of which a quarter was spent on the scattering itself. The rest of the time was used for other parts of the calculation, such as the neighbour search and the parallelization overhead. In comparison the scheme for rare self-interactions is less complicated and needs less computation time.

The robustness of our implementation could be increased by using an additional time-step constraint for the self-interactions. This would make the simulation code more capable of handling situations like gravothermal core-collapse of DM haloes. For the simulations we presented here, we only relied on the gravitational time-step, which is small enough for the situations we considered.

Finally, for our merger simulations, we used an algorithm to find peaks of the DM and the galactic component based on KDEs. Unfortunately, the results are biased towards the barycentre for small peak separations, which limits the conclusion that can be drawn. Other methods may perform better, for example finding the most tightly bound particle.

3.6.2 Physical considerations

In our various simulations, we found that fSIDM and rSIDM lead to different effects even when using the same momentum transfer cross-section. One may wonder whether this is simply the result of an incorrect matching, i.e. whether for each fSIDM cross-section one can find an rSIDM cross-section that produces the same behaviour. Indeed, Fig. 3.6 suggests that core formation simply proceeds a bit faster in fSIDM than in rSIDM and it should be possible to improve the matching by using slightly larger cross-sections for rare scattering. However, given the physical difference between rare and frequent scattering it is also conceivable that the two cases cannot be matched to one another in a simple way. Rare self-interactions affect only a few particles per time, whereas frequent self-interactions affect all particles, which could contribute to a faster core-collapse for fSIDM. One consequence of this is that systems with frequent or rare scatterings follow different paths to equilibrium, i.e. the velocity distributions are different. This can be seen from the idealized case studied in Fig. 3.2.

Nevertheless, when we go beyond relaxed systems we find that the two types of self-interactions lead to qualitatively different effects. This can be seen most clearly in Fig. 3.10, where the largest offsets found in fSIDM cannot be reproduced for any cross section in rSIDM. In other words, frequent and rare self-interactions cannot be matched by a simple rescaling of the cross-section. It is worth mentioning that the cross-section needed to create the largest possible offset for a given system depends on the central density of the system. Thus, not all systems would allow rare and frequent scatterings to be distinguished observationally, and in the case of very small cross-sections all systems would be consistent with either rare or frequent scatterings. However, in the past, there have been claims of observations of large offsets (Harvey et al., 2015, though see Wittman et al. (2018)). Observed offsets are typically smaller ($\lesssim 60\,\mathrm{kpc}$) than the one that can only be explained with frequent self-interactions in our simulations. Nevertheless, the observed offset of the Musket Ball Cluster ($\sim 80\,\mathrm{kpc}$) is larger (Dawson, 2013).

Furthermore, we have found that the difference between frequent and rare self-interactions results in an amplified difference in the galactic component, i.e. the maximum δ is larger in the galaxy distribution than for DM. Large offsets are easier to detect and their existence or non-existence has the potential to distinguish between frequent and rare scattering. Hence, the amplification process for fSIDM provides an important handle for determining the nature of DM.

Finally, we emphasize that we have adopted a simplified and idealized set-up in our simulations. For instance, we do not include baryons which could affect our results (Zhang et al., 2016). For a detailed comparison with observations, more realistic simulations will be required. As mentioned above, such future simulations should also investigate in more detail the case of non-isotropic and velocity-dependent self-interactions, which has been found to have a significant impact on the offsets in merging galaxy clusters (Robertson et al., 2017b) for rSIDM.

3.7 Summary and Conclusions

In this paper, we have presented a novel method for modelling frequent self-interactions of DM within the framework of the N-body method. Our numerical scheme conserves energy and momentum explicitly. Moreover, it does not rely on equilibrium or quasi-equilibrium states but is capable of treating typical astrophysical initial conditions. We introduced several test problems to demonstrate the accuracy of our numerical scheme. Furthermore, we performed several simulations of isolated haloes and mergers using frequent and rare self-interactions. Our main results from these simulations are as follows:

- fSIDM can be modelled accurately within N-body simulations.
- Rare and frequent interactions lead to similar core formation in DM haloes. When considering the same momentum transfer cross-section, the evolution is slightly faster for fSIDM than for rSIDM.

- We found that fSIDM produces larger DM–galaxy offsets than rSIDM in equal-mass mergers.
- This effect can be traced back to an amplification in the displacement of the galactic component for the case of fSIDM.
- In conclusion, the phenomenology of rSIDM and fSIDM is different in the sense that for a given strength of frequent self-interactions one cannot in general find a rare self-interaction cross-section that gives the same effects.

This paper only constitutes the first steps towards exploring the astrophysical phenomenology of frequently self-interacting DM, in the sense that it provides the numerical methods for further investigations. Future simulations of various astrophysical set-ups may provide deeper insights into the phenomenology of fSIDM and allow for a detailed comparison with observations.

Acknowledgements

This work is funded by the Deutsche Forschungsgemeinschaft (DFG, German Research Foundation) under Germany's Excellence Strategy – EXC 2121 "Quantum Universe" – 390833306, Germany's Excellence Strategy – EXC-2094 "Origins" – 390783311 and the Emmy Noether Grant No. KA 4662/1-1. AR is supported by the European Research Council's Horizon2020 project 'EWC' (award AMD-776247- 6). Preprint number: DESY 20-227, TTK-20-49.
Software: EMCEE (Foreman-Mackey et al., 2013), NUMPY (Harris et al., 2020), MATPLOTLIB (Hunter, 2007), SCIKIT-LEARN (Pedregosa et al., 2011), SCIPY (Virtanen et al., 2020)

Appendices

3.A Kernel overlap

In this appendix we discuss the computation of the kernel overlap Λ_{ij}, which arises from the integral of equation (3.9). To exploit symmetries, we express the integral in cylindrical coordinates,

$$\Lambda_{ij} = 2\pi \int_{-\infty}^{\infty} \int_{0}^{\infty} W\left(\sqrt{z^2+r^2}, h_i\right) \times W\left(\sqrt{(z-d)^2+r^2}, h_j\right) r \,\mathrm{d}r \,\mathrm{d}z \,. \quad (3.28)$$

In order to simplify the notation we have introduced the distance $d = |\Delta \boldsymbol{x}|$ between the two particles. We have also integrated directly over the angle of the cylindrical coordinates, remaining only with two integrals over r and z. Using the assumption that the kernel

function becomes zero beyond h, we can place tighter integration limits. For this purpose, we introduce $\gamma_i = \sqrt{h_i^2 - z^2}$ and $\gamma_j = \sqrt{h_j^2 - (z-d)^2}$, such that

$$\Lambda_{ij} = 2\pi \int_{\max(-h_j, -h_j+d)}^{\min(h_i, h_j+d)} \int_0^{\min(\gamma_i, \gamma_j)} W\left(\sqrt{z^2+r^2}, h_i\right) \times W\left(\sqrt{(z-d)^2+r^2}, h_j\right) r \, \mathrm{d}r \, \mathrm{d}z \,. \quad (3.29)$$

For a given kernel function, $W(r,h)$ values for Λ are tabulated in advance and then interpolated to obtain Λ for given h_i, h_j and d. Although Λ depends on three variables, we need only a two-dimensional table for this purpose, as one variable can be interpreted as a scaling factor. To make this explicit, we introduce $h_{\min} = \min(h_i, h_j)$ and $h_{\max} = \max(h_i, h_j)$ and scale all variables with $h_{\min}$, i.e. we introduce $d' = d/h_{\min}$ and $h' = h_{\max}/h_{\min}$. The scaled version of Λ can then be written as

$$\Lambda'_{ij}(d', h') = 2\pi \int_{z'_{\min}}^{z'_{\max}} \int_{r'_{\min}}^{r'_{\max}} W\left(\sqrt{z'^2 + r'^2}, 1\right) \times W\left(\sqrt{(z'-d')^2 + r'^2}, h'\right) r' \, \mathrm{d}r' \, \mathrm{d}z' \quad (3.30)$$

with $r' = r/h_{\min}$ and $z' = z/h_{\min}$. The unscaled version of Λ is then obtained from

$$\Lambda_{ij} = \frac{\Lambda'_{ij}}{h_{\min}^3} \,. \quad (3.31)$$

3.B Implementation of rare self-interactions

N-body simulations of DM with rare self-interactions employing an isotropic cross-section are well established. There exists a variety of schemes, which differ in the way scatter probabilities are computed (e.g. Burkert, 2000; Vogelsberger et al., 2012; Rocha et al., 2013). Rocha et al. (2013) introduced a scheme where the scattering probability arises from the kernel overlap. We follow this approach because we already compute overlaps for our fSIDM scheme. By using the total cross-section σ and the physical particle mass m_χ we can derive the scattering probability of a numerical particle pair. Similar to the drag force we start from a microparticle travelling through a constant density ρ. The particle has the velocity v and travels for the time t. The probability that it scatters with another particle is given by

$$P_{\text{scatter}} = \frac{\sigma}{m_\chi} \rho \, v \, t \,. \quad (3.32)$$

Note, this is valid only for $P_{\text{scatter}} \ll 1$. Now we consider two overlapping phase-space patches as represented by our numerical particles with densities ρ_i and ρ_j. The expected number of scattering events is given as

$$\langle N \rangle = \int \frac{\rho_i}{m_\chi} P_{\text{scatter}} \, \mathrm{d}V \,. \quad (3.33)$$

Here, $P_{\rm scatter}$ denotes the probability that a microparticle of i scatters with one of j. We multiply by the microparticle mass and obtain the expected value for the mass per phase-space patch that scatters:

$$\langle M \rangle = \frac{\sigma}{m_\chi} |\Delta \mathbf{v}_{ij}| \, \Delta t \int \rho_i \rho_j \mathrm{d}V \,, \tag{3.34}$$

where $\Delta \boldsymbol{v}_{ij} = \boldsymbol{v}_i - \boldsymbol{v}_j$ is the relative velocity and Δt is the simulation time-step. The kernel overlap Λ_{ij} is computed as described in Appendix 3.A. We can then express the scattering probability of i representing a mass of m_i as

$$P_i = \frac{\langle M \rangle}{m_i} = \frac{\sigma}{m_\chi} m_j \, |\Delta \boldsymbol{v}_{ij}| \, \Delta t \, \Lambda_{ij} \,. \tag{3.35}$$

For our implementation we use numerical particles that have the same mass m, such that $P_{ij} = P_i = P_j$. The time-step Δt is kept small enough such that the scattering probability is well below unity. To determine whether two particles scatter during a given time-step we take a random number x from the interval $[0, 1]$ and let the particles scatter if $x \leq P_{ij}$. The scattering process can be described as follows:

$$\boldsymbol{v}_i' = \boldsymbol{v}_{\rm cms} + \frac{|\Delta \boldsymbol{v}_{ij}|}{2} \boldsymbol{e} \tag{3.36}$$

and

$$\boldsymbol{v}_j' = \boldsymbol{v}_{\rm cms} - \frac{|\Delta \boldsymbol{v}_{ij}|}{2} \boldsymbol{e} \,. \tag{3.37}$$

Here, $\boldsymbol{v}_{\rm cms} = (\boldsymbol{v}_i + \boldsymbol{v}_j)/2$, i.e. the centre-of-mass velocity. The vector $\boldsymbol{e}$ is a normalized vector that points into a random direction. Here, we assume the cross-section to be isotropic, but anisotropic cross-sections can also be implemented (Robertson et al., 2017b). Our rSIDM implementation uses the same time-steps as for fSIDM (see Section 3.2.5) and the same parallelization (see Section 3.2.5).

3.C Molière's theory

In Section 3.3.3, we use Molière's theory to predict the result of the angular deflection test problem. Here, we give further details on how to derive the prediction. The probability density distribution of the deflection angle, assuming scattering about small angles, was derived by Moliere (1948) and can be written as [8]

$$f(\theta) = \frac{2\theta}{\overline{\theta^2}} \exp\left(-\frac{\theta^2}{\overline{\theta^2}}\right) . \tag{3.38}$$

[8] Here, we only give the zeroth-order term, because the assumption of our method is that the underlying differential cross-section is extremely forward peaked, such that a given momentum transfer cross-section is achieved in the limit of an infinitely large cross-section for infinitesimally small-angled scattering events. In such a case, the so-called screening angle in Moliere theory is zero, which in turn implies that B (see Moliere, 1948) is infinitely large, which means that the zeroth-order term is the only term that contributes to the distribution of scattering angles.

To compute the distribution of the scattering angle θ one needs $\overline{\theta^2}$, which is given as

$$\overline{\theta^2} = 2\pi\, n_0\, l \int \frac{\mathrm{d}\sigma}{\mathrm{d}\Omega}\, \theta^3\, \mathrm{d}\theta\,. \tag{3.39}$$

Here, n_0 denotes the particle number density. It can be expressed as $n_0 = \rho/m_\chi$, where ρ is the matter density and m_χ the physical particle mass. The distance travelled by a particle through the target is given by l. Equation (3.39) is not directly applicable for us as we only know the momentum transfer cross-section $\sigma_{\tilde{\mathrm{T}}}/m_\chi$. But we can rewrite equation (3.39) using the definition of the momentum transfer cross-section as given in Kahlhoefer et al. (2014).

$$\begin{aligned}\sigma_{\tilde{\mathrm{T}}} &= 4\pi \int_0^1 \frac{\mathrm{d}\sigma}{\mathrm{d}\Omega}\,(1-\cos\theta)\,\mathrm{d}\cos\theta &(3.40)\\ &= -4\pi \int_{\pi/2}^0 \frac{\mathrm{d}\sigma}{\mathrm{d}\Omega}\,\sin\theta\,(1-\cos\theta)\,\mathrm{d}\theta \\ &\approx 2\pi \int_0^{\pi/2} \frac{\mathrm{d}\sigma}{\mathrm{d}\Omega}\,\theta^3\,\mathrm{d}\theta. &(3.41)\end{aligned}$$

In the final step we have assumed that $\mathrm{d}\sigma/\mathrm{d}\Omega$ is strongly peaked at small angles, such that we can approximate $\sin\theta\,(1-\cos\theta) \approx \theta^3/2$. We therefore find

$$\overline{\theta^2} \approx 2\, n_0\, l\, \sigma_{\tilde{\mathrm{T}}} = 2\,\rho\, l\, \frac{\sigma_{\tilde{\mathrm{T}}}}{m_\chi}. \tag{3.42}$$

3.D Stability of initial conditions

Here, we show that the NFW haloes used for our simulations in Sections 3.3.4 and 3.5 are stable when evolved without DM self-interactions.

For the simulations presented in Section 3.3.4, we used an initial NFW halo. The halo has a virial mass of $M_{\mathrm{vir}} = 10^{15}\,\mathrm{M}_\odot$ and is resolved by $N = 10^5$ particles. In the upper panel of Fig. 3.D.1, we demonstrate the stability of these initial conditions.

In the lower panel of Fig. 3.D.1, we demonstrate that the haloes we use for our merger simulations (section 3.5) are stable when simulated without self-interactions. One can only see minor changes of the density profile. The largest difference occurs in the centre of the halo.

3.E Additional Merger Plots

Here, we show additional plots of our merger simulations, which are presented in section 3.5. In particular, we show for peaks of all components the distance to barycentre as a function of time for cross-sections of $\sigma_{\tilde{\mathrm{T}}}/m = 0\,\mathrm{cm}^2\,\mathrm{g}^{-1}$ (Fig. 3.E.1), $\sigma_{\tilde{\mathrm{T}}}/m = 1.5\,\mathrm{cm}^2\,\mathrm{g}^{-1}$ (Fig. 3.E.2), and $\sigma_{\tilde{\mathrm{T}}}/m = 5\,\mathrm{cm}^2\,\mathrm{g}^{-1}$ (Fig. 3.E.3).

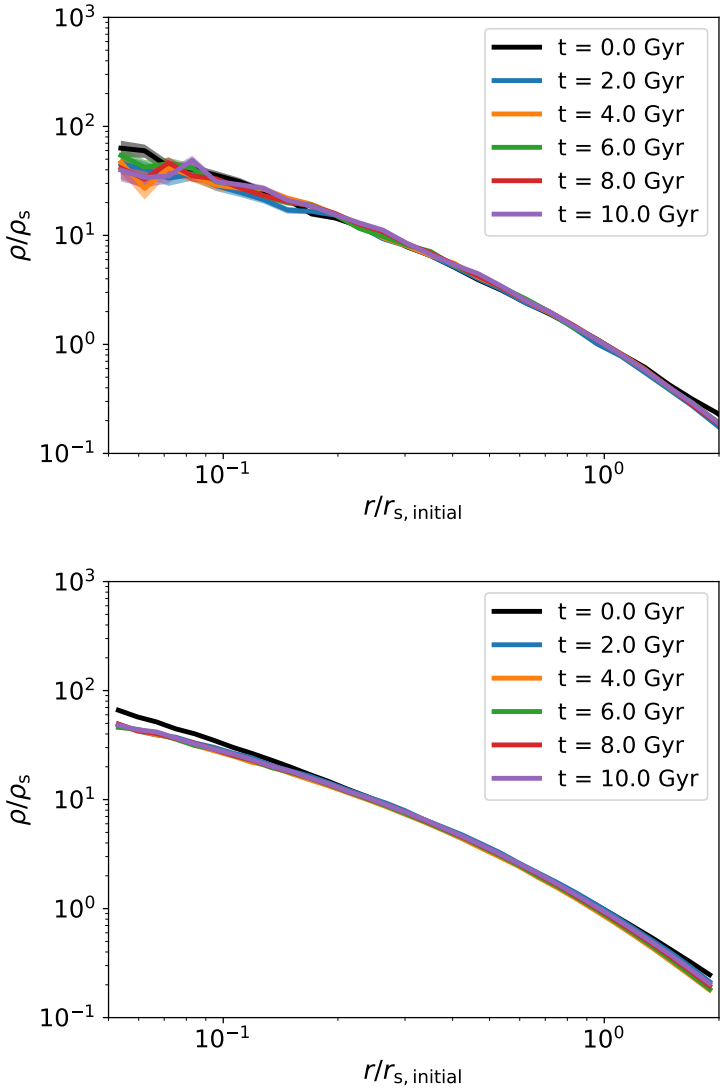

Figure 3.D.1: We show the evolution of an initial NFW halo as used for our test simulations in section 3.3.4 (upper panel) and our merger simulations in section 3.5 (lower panel). The haloes were simulated without DM self-interactions, i.e. consistent with CDM. Here, we display the density profile at several times.

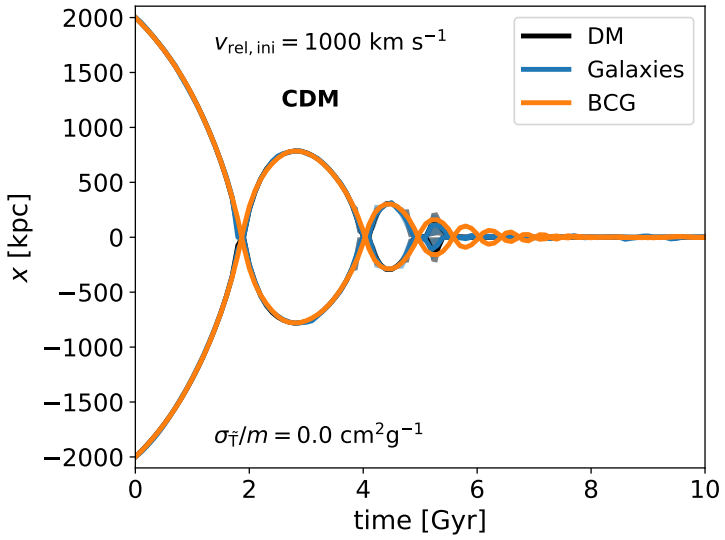

Figure 3.E.1: The same as in Fig. 3.8 but for collisionless DM.

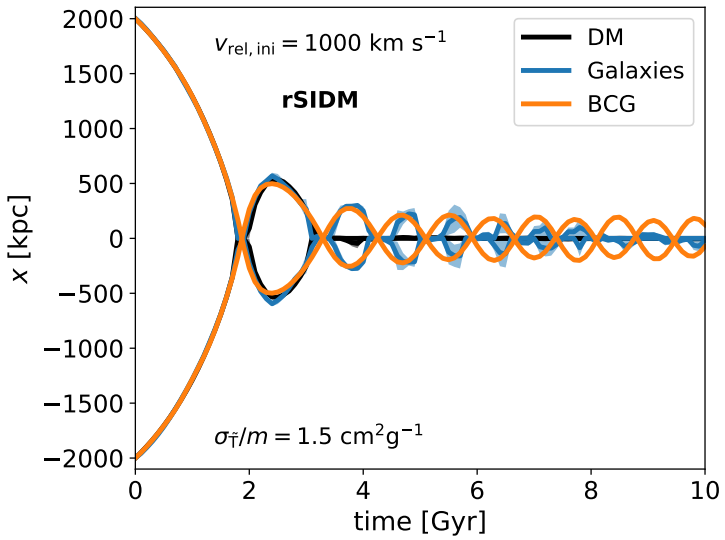

Figure 3.E.2: The same as in Fig. 3.8 but for rare self-interactions. A self-interaction cross-section of $\sigma_{\tilde{\mathrm{T}}}/m = 1.5\,\mathrm{cm}^2\,\mathrm{g}^{-1}$ was employed.

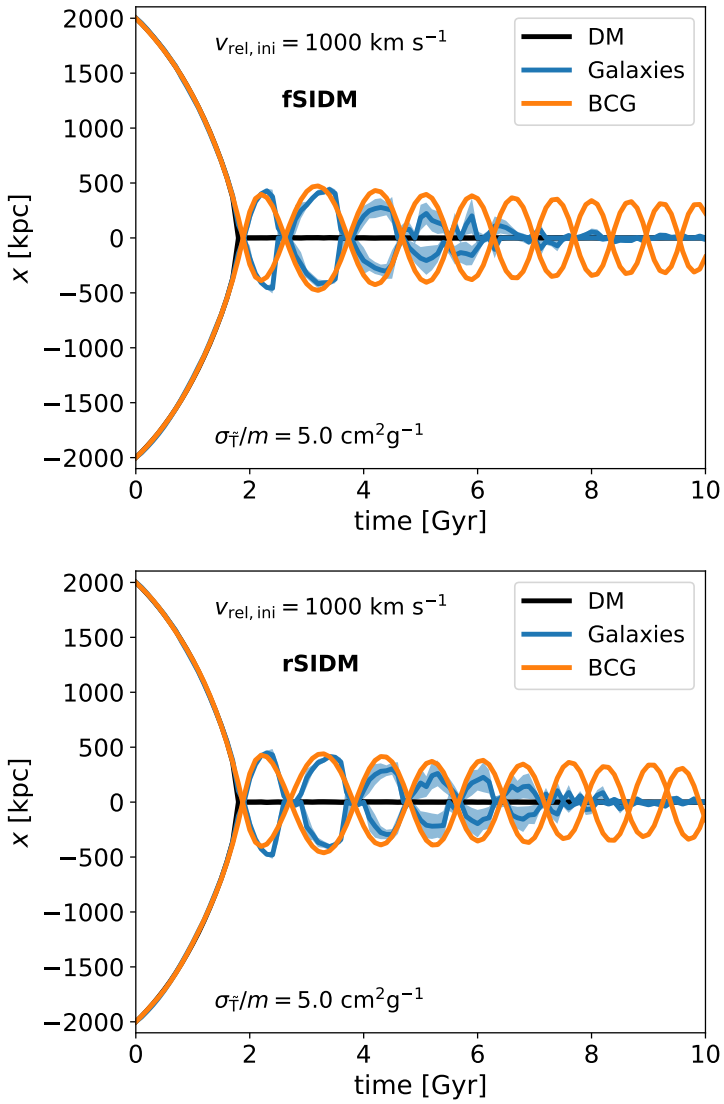

Figure 3.E.3: The same as in Fig. 3.8. The upper panel shows the evolution with frequent self-interactions and the lower panel displays the simulation with rare self-interactions. But for a cross-section of $\sigma_{\tilde{\mathrm{T}}}/m = 5\,\mathrm{cm}^2\,\mathrm{g}^{-1}$. Interestingly, the BCG peak distance at second apocentre is larger than at the first one. This is a consequence of the DM relaxation time. A flatter gravitational potential allows the BCG's to reach a larger distance at the second apocentre.

3.F Amplification Process

As we mentioned in section 3.5.2 the positions of BCGs and galaxy density peaks do not reflect the differences between rSIDM and fSIDM dark matter peaks one-to-one. The deviation in BCGs and galaxies is larger than for the DM distribution when considering the maximum value of δ as shown in Fig. 3.11. In the following, we investigate this observation in more detail.

For this purpose, we compute the projected 1D density along the merger axis using a KDE with a 1D Gaussian smoothing kernel with a width of 50 kpc. From this, we obtain the normalized density as shown in Fig. 3.F.1. We also compute the difference between fSIDM and rSIDM, which is shown in Fig. 3.F.2.

The key observation is that the central region close to the barycentre has a higher projected density for fSIDM than for rSIDM. Although this could be a projection effect and does not necessarily imply that the actual density at the interaction point is larger for fSIDM, it clearly demonstrates that the distribution of DM, and hence the gravitational potential, differs for the two cases shortly after the collision. This observation is readily understood in terms of the underlying differences between the two self-interaction schemes. In fSIDM all DM particles are decelerated and deflected, i.e. some energy from the forward motion is redirected into the perpendicular direction. In rSIDM, on the other hand, most DM particles are unaffected by self-interactions, while some particles scatter and experience a strong deflection.

In rSIDM, the DM halo therefore travels further after pericentre passage than in fSIDM. The deceleration of the DM component in fSIDM leads to a larger galaxy–DM offset. The galaxies hence experience a stronger gravitational pull in fSIDM, which amplifies the differences in the galactic component between rSIDM and fSIDM.

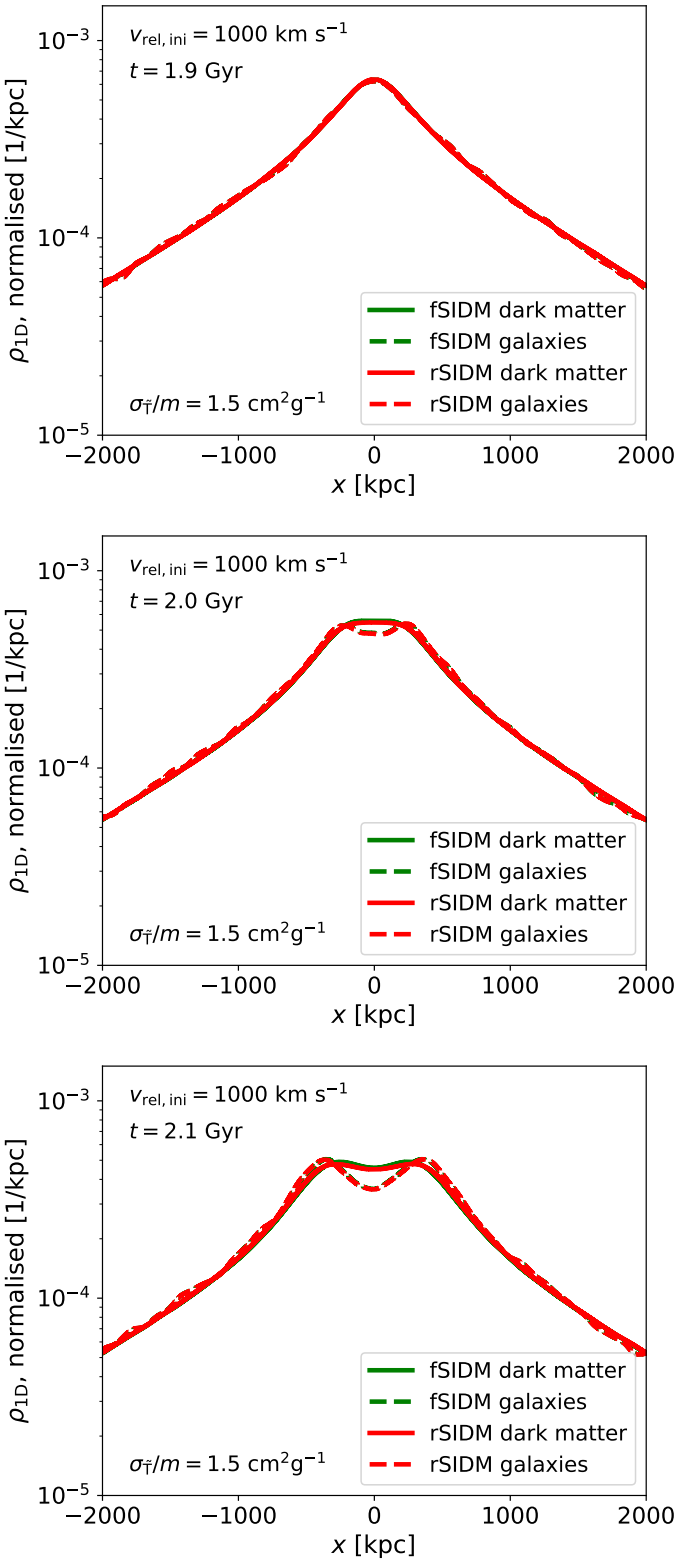

Figure 3.F.1: The normalized projected density along the merger axis is shown. We compare the density of the galactic and DM component for frequent and rare self-interactions. All three panels belong to the same cross-section ($\sigma_{\tilde{\Gamma}}/m = 1.5\,\mathrm{cm}^2\,\mathrm{g}^{-1}$) and give the density for several times at pericentre passage and shortly afterwards.

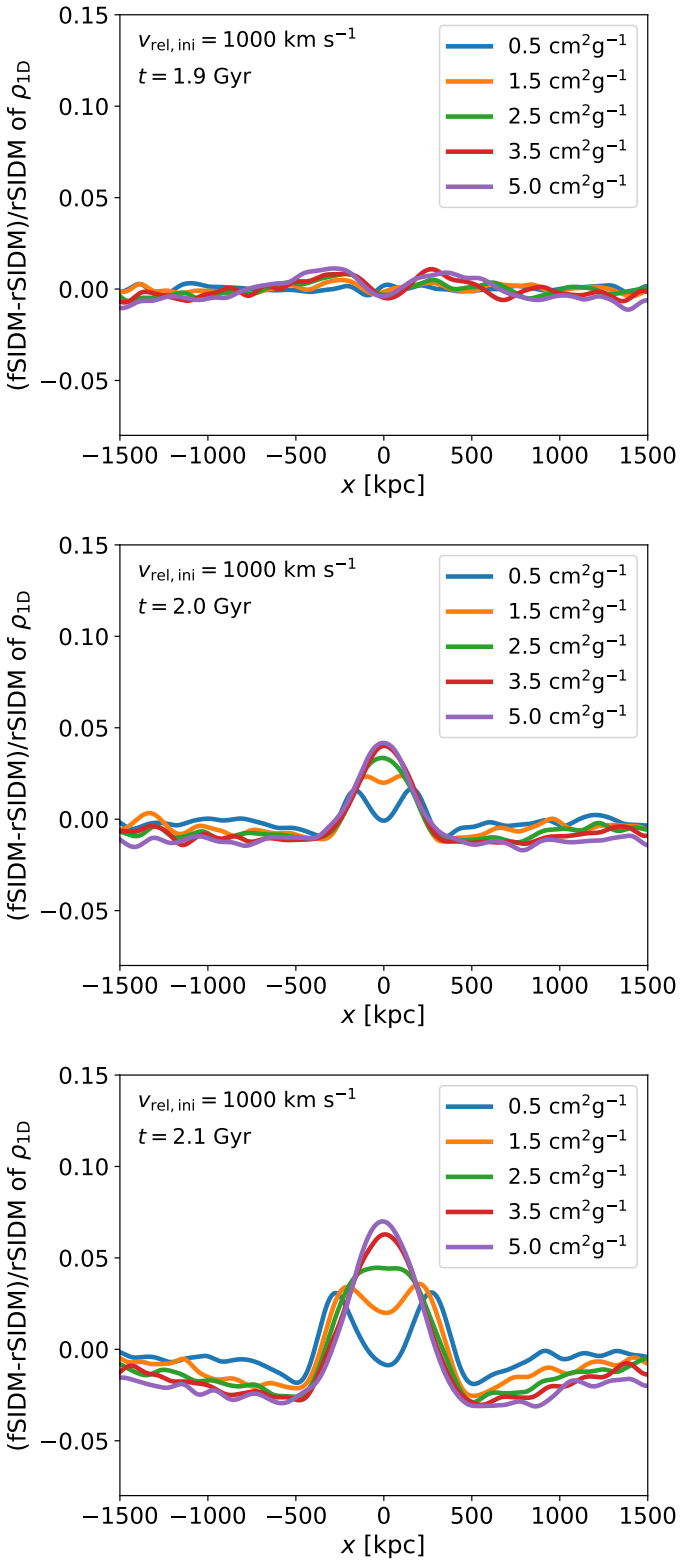

Figure 3.F.2: The relative projected density difference between fSIDM and rSIDM from Fig. 3.F.1, but for several cross-sections. A positive value implies that fSDIM is denser than rSIDM.

4 Unequal-mass mergers of dark matter haloes with rare and frequent self-interactions

This chapter presents work as published in Fischer et al. (2021b).

Abstract Dark matter (DM) self-interactions have been proposed to solve problems on small length scales within the standard cold DM cosmology. Here, we investigate the effects of DM self-interactions in merging systems of galaxies and galaxy clusters with equal and unequal mass ratios. We perform N-body DM-only simulations of idealized setups to study the effects of DM self-interactions that are elastic and velocity-independent. We go beyond the commonly adopted assumption of large-angle (rare) DM scatterings, paying attention to the impact of small-angle (frequent) scatterings on astrophysical observables and related quantities. Specifically, we focus on DM-galaxy offsets, galaxy–galaxy distances, halo shapes, morphology, and the phase–space distribution. Moreover, we compare two methods to identify peaks: one based on the gravitational potential and one based on isodensity contours. We find that the results are sensitive to the peak finding method, which poses a challenge for the analysis of merging systems in simulations and observations, especially for minor mergers. Large DM-galaxy offsets can occur in minor mergers, especially with frequent self-interactions. The subhalo tends to dissolve quickly for these cases. While clusters in late merger phases lead to potentially large differences between rare and frequent scatterings, we believe that these differences are non-trivial to extract from observations. We therefore study the galaxy/star populations which remain distinct even after the DM haloes have coalesced. We find that these collisionless tracers behave differently for rare and frequent scatterings, potentially giving a handle to learn about the micro-physics of DM.

4.1 Introduction

In the standard cosmological model, structures in the Universe such as galaxies and galaxy clusters are thought to form hierarchically, meaning that small objects merge to form larger ones (e.g. Lacey & Cole, 1993). In particular, cosmological N-body simulations have been used to investigate structure formation within the standard ΛCDM model (e.g. Springel et al., 2005; Boylan-Kolchin et al., 2009; Klypin et al., 2011; Pillepich et al., 2017; Hopkins et al., 2018). These simulations agree remarkably well with observations of the large-scale structure (e.g. Springel et al., 2006) and allow us to explain the formation of a wide range

of cosmic objects. In the cosmological standard model, today's Universe mainly consists of dark energy and dark matter (DM), which is thought to be collisionless and cold (cold dark matter – CDM). The underlying nature of those two components is largely unknown.

Although the large-scale structure of our Universe is reproduced well by N-body simulations assuming only CDM, there seem to be discrepancies between predictions and observations on scales of galaxies. This is often referred to as the small-scale crisis of ΛCDM, which manifests itself in the core-cusp problem, the diversity problem, the too-big-to-fail-problem and the plane of satellites problem (for a review see Bullock & Boylan-Kolchin, 2017).

Many solutions have been proposed to solve these problems, including alternative models for DM (e.g. Dodelson & Widrow, 1994; Hu et al., 2000). One class of these models assumes that DM is not fully collisionless but that DM particles scatter off each other with a non-zero cross-section (Spergel & Steinhardt, 2000). Such models with self-interacting dark matter (SIDM) provide a promising solution to the small-scale crisis (for a review see Tulin & Yu, 2018). The dark sector might be strongly coupled to itself, while interactions with standard model particles are weak enough to fulfil current constraints from laboratory experiments. In several particle physics models, this would be natural, (e.g. Carlson et al., 1992; Kusenko & Steinhardt, 2001; Mohapatra et al., 2002; Frandsen et al., 2011).

A variety of SIDM models exist for which the self-interactions can be velocity-independent or velocity-dependent (e.g. Ackerman et al., 2009; Buckley & Fox, 2010; Loeb & Weiner, 2011; van den Aarssen et al., 2012; Tulin et al., 2013a) as several studies have assumed (e.g. Colin et al., 2002; Vogelsberger et al., 2012; Vogelsberger & Zavala, 2013; Vogelsberger et al., 2014; Robertson et al., 2017b; Banerjee et al., 2020; Nadler et al., 2020; Turner et al., 2021). The self-interactions could be elastic or inelastic (e.g. Essig et al., 2019; Huo et al., 2020) and the differential cross-section may have different shapes. The latter implies that the typical scattering angles can be of different sizes. In the regime of rare self-interacting dark matter (rSIDM), the typical scattering angle is large, the scattering can be isotropic as most studies assumed, but there have also been a few studies with anisotropic scattering (e.g. Robertson et al., 2017b; Banerjee et al., 2020; Nadler et al., 2020). In contrast, the regime of frequent self-interacting dark matter (fSIDM) has typical scattering angles that are tiny and thus transfer less momentum per scattering event compared to rSIDM (Kahlhoefer et al., 2014). There exists a variety of particle physics models with long-range interactions arising from a mass-less mediator. These models have a strongly anisotropic cross-section, which typically is velocity-dependent. This is the case for mirror DM (Blinnikov & Khlopov, 1983; Kolb et al., 1985; Berezhiani et al., 1996; Foot, 2004), atomic DM (Kaplan et al., 2010; Cline et al., 2012; Cyr-Racine & Sigurdson, 2013) and some other hidden sector DM models (Feng et al., 2009; Foot & Vagnozzi, 2015; Boddy et al., 2016).

In addition to cosmological simulations, a number of studies have focused on individual mergers to constrain the nature of DM. Several studies simulate galaxy clusters in a ΛCDM

cosmology including the intracluster medium (ICM; Poole et al., 2006; ZuHone, 2011; Machado & Lima Neto, 2015; Zhang et al., 2016; Doubrawa et al., 2020; Moura et al., 2020). Mergers between galaxy clusters provide important test cases for theories of DM. Dissociative mergers, where the intracluster gas becomes separated from the DM haloes, are especially interesting, with known examples including the Bullet Cluster (e.g. Springel & Farrar, 2007; Mastropietro & Burkert, 2008; Lage & Farrar, 2014), the 'El Gordo' cluster (Donnert, 2014; Molnar & Broadhurst, 2015; Zhang et al., 2015, e.g.), the 'Sausage' cluster (Donnert et al., 2017; Molnar & Broadhurst, 2017, e.g.), A1758N (Machado et al., 2015; Monteiro-Oliveira et al., 2016), and ZwCl008.8+52 (Molnar & Broadhurst, 2018).

In the context of SIDM, merging galaxy clusters have attracted attention since offsets between the DM component and the galaxies may provide evidence for DM self-interactions. There have been several observational studies on galaxy cluster offsets that sparked a debate on the reliability of the largest offsets measured (e.g. Bradač et al., 2008; Dawson et al., 2012; Dawson, 2013; Jee et al., 2014, 2015; Harvey et al., 2017; Peel et al., 2017; Taylor et al., 2017; Wittman et al., 2018). Here, we focus on offsets that could discriminate between rSIDM and fSIDM.

From the theoretical side, several numerical studies of galaxy cluster mergers with SIDM have been carried out. Although SIDM encompasses a wide range of models, most studies assumed elastic velocity-independent isotropic scattering (Randall et al., 2008; Kim et al., 2017; Robertson et al., 2017a). Robertson et al. (2017b) performed the first study of anisotropic scattering. Nevertheless, these studies have been limited to large-angle scattering. Meanwhile, frequent self-interactions have only very recently been implemented in N-body simulations based on an effective drag force (Fischer et al., 2021a), which is more generally applicable than the description in terms of a heat conduction approach (Kummer et al., 2019).

Kim et al. (2017) have performed a parameter study of equal-mass mergers that demonstrated that offsets between DM and galaxies can arise from rare self-interactions. Building on this, Fischer et al. (2021a) showed that even larger offsets arise when fSIDM is considered, as expected by Kahlhoefer et al. (2014). Unequal-mass mergers are interesting since they occur much more frequently than equal-mass mergers. In rSIDM, they have been studied in simulations which reproduce the Bullet Cluster (1E 0657–56) (Randall et al., 2008; Robertson et al., 2017a,b). In addition, there are many studies on structure formation in rSIDM using cosmological simulations (e.g. Vogelsberger et al., 2012; Vogelsberger et al., 2014; Vogelsberger & Zavala, 2013; Peter et al., 2013; Rocha et al., 2013; Despali et al., 2019; Banerjee et al., 2020; Nadler et al., 2020; Robertson et al., 2020; Vega-Ferrero et al., 2020; Sameie et al., 2021; Shen et al., 2021).

In this paper, we focus on idealized equal and unequal-mass mergers of galaxies and galaxy clusters using N-body simulations. Although the ICM contributes significantly to the total mass of galaxy clusters, we neglect the contribution from gas and consider idealized systems that only consist of DM and galaxies. Likewise, for the galaxy simulations,

we also consider only DM and stars. In our model, the DM is subject to self-interactions that are elastic and velocity-independent, and we investigate, both, rare and frequent self-interactions.

In Section 4.2, we briefly describe the simulation code with its implementation for DM self-interactions and explain our initial conditions. In Section 4.3, we present the methods of our analysis, especially for the peak finding. Subsequently, we present the results of our simulations in Section 4.4. In particular, we measure offsets and shapes of the merging systems, investigate the morphology and phase–space distribution of the mergers and compare peak finding methods. In Section 4.5, we discuss our results and their physical implications in the light of the assumptions we have made. Finally, we summarize and conclude in Section 4.6. Additional details and plots are provided in the appendices.

4.2 Numerical setup

In this section, we describe our numerical setup including the simulation code and the description of the initial conditions.

4.2.1 Simulation code and implementation of self-interactions

For our simulations, we use the cosmological N-body code GADGET-3, which is a successor of GADGET-2 (Springel, 2005). For rare and frequent self-interactions, we are using the implementation described in Fischer et al. (2021a). This means that for the rare self-interactions, a similar scheme to the one introduced by Rocha et al. (2013) is used and the scheme for frequent self-interactions is based on an effective description employing a drag force (Kahlhoefer et al., 2014) and was introduced in Fischer et al. (2021a). In addition to the existing implementation, we added a time-step criterion and slightly modified the implementation of rSIDM as described below.

Time-step criterion for self-interactions

For both rare and frequent self-interactions, we implemented a time-step criterion that limits the maximum allowed time-step for each particle. In this context, our explanation about the time-step scaling for fSIDM in section 2.4 Fischer et al. (2021a) might be of interest.

In GADGET-3, particles are assigned an individual time-step and our new criterion does not allow it to be larger than Δt_{si}, which is defined as

$$\Delta t_{\mathrm{si}} = \tau \frac{h^3}{\omega_{\max} m} \,. \tag{4.1}$$

Here, h denotes the kernel size (which is used in the implementation of the self-interactions)

and m denotes the numerical particle mass. $\omega_{\max}$ is computed as follows

$$\omega_{\max} = \max(\omega) \qquad \text{with} \quad \omega = \frac{\sigma_{\tilde{T}}}{m_\chi} \Delta v \,, \tag{4.2}$$

where Δv denotes the relative velocity of two particles. We compute ω for each particle interaction, and then determine $\omega_{\max}$ for a given particle as the maximum value of ω over all interactions involving that particle. The size of the time-step can be adjusted by the numerical factor τ. For frequent self-interactions, this enables the control of the relative velocity change per particle interaction. The simulations in this paper were conducted with a value of $\tau = 0.1$.

rSIDM – relabelling of particles

In this paper, we study mergers where we know which halo each particle initially belongs to. This information is used in the peak finding as described in Section 4.3.1. However, when considering rSIDM, the question of which DM halo a particle belongs to is not as clear as it might seem. Consider two indistinguishable particles that belong to different haloes. If they scatter by an angle $\theta < \pi/2$, this cannot be distinguished from an event with a scattering angle $\pi - \theta > \pi/2$ where the two particles are exchanged. Hence, we modify our rSIDM implementation such that particles are not allowed to scatter by angles larger than 90°, but use the smaller angle instead. This has the same effect as relabelling (exchange of host halo labels) the particles for scattering angles larger than 90°. In appendix 4.A, we study the effects of this modification.

4.2.2 Initial conditions and simulation parameters

In this paper, we perform a parameter study of head-on collisions of DM haloes. Initially, the individual haloes are assumed to follow a Navarro–Frenk–White (NFW) profile (Navarro et al., 1996). As the total mass of an NFW halo is infinite, it needs to be truncated at some radius, which we set as 20 times the scale radius, r_s. We ran simulations for galaxy and cluster-scale mergers, i.e. the main haloes have virial masses of $M_{\text{vir,main}} = 10^{12}$ or $10^{15}\,\mathrm{M}_\odot$, respectively. For all haloes, the concentration parameter in the NFW profile, c, was chosen according to Dutton & Macciò (2014). In Tab. 4.2.1, we give the corresponding scale radius and scale density for our haloes. All haloes have an equal number of DM and collisionless galaxy/star particles. Each of these components follow an NFW profile with the same value for r_s. The cluster-scale simulations have a mass resolution of $m_{\text{DM}} = 2 \cdot 10^8\,\mathrm{M}_\odot$ for the DM particles and $m_{\text{Gal}} = 4 \cdot 10^6\,\mathrm{M}_\odot$ for the galaxy particles. For the galaxy-scale simulations, the mass resolution is: $m_{\text{DM}} = 2 \cdot 10^5\,\mathrm{M}_\odot$ and $m_{\text{Star}} = 4 \cdot 10^3\,\mathrm{M}_\odot$. In addition, the haloes contain one more massive collisionless particle at their centre. For the cluster-scale simulations, it may be interpreted as the brightest cluster galaxy (BCG) although it has only a mass of $m_{\text{BCG}} = 7 \cdot 10^{10}\,\mathrm{M}_\odot$.

All our mergers are head-on mergers, i.e. their impact parameters, b, equal zero. Initially,

$M_{\rm vir}$ ($M_\odot$)	r_s (kpc)	ρ_0 ($M_\odot$ kpc^{-3})
10^{15}	389.31	$1.33 \cdot 10^6$
2×10^{14}	194.76	$1.91 \cdot 10^6$
10^{14}	144.53	$2.24 \cdot 10^6$
10^{12}	19.92	$6.56 \cdot 10^6$
2×10^{11}	9.97	$9.64 \cdot 10^6$
10^{11}	7.40	$1.14 \cdot 10^7$

Table 4.2.1: The scale radius r_s and the density $\rho_0 \equiv 4\,\rho(r_s)$ are given for our initial NFW haloes, which have the virial mass $M_{\rm vir}$.

$M_{\rm vir,main}$ ($M_\odot$)	MMR	$d_{\rm ini}$ (kpc)	$\Delta v_{\rm ini}$ (km s^{-1})	$\sigma_{\tilde{\rm T}}/m$ (cm^2 g^{-1})
10^{15}	1:1	4000	1000	0.0, 0.1, 0.3, 0.5
10^{15}	1:5	4000	1000	0.0, 0.1, 0.3, 0.5
10^{15}	1:10	4000	1000	0.0, 0.1, 0.3, 0.5
10^{12}	1:1	500	140	0.0, 1.0, 2.0
10^{12}	1:5	500	140	0.0, 1.0, 2.0
10^{12}	1:10	500	140	0.0, 1.0, 2.0

Table 4.2.2: Initial condition and simulation parameters for the runs presented in this paper. $M_{\rm vir,main}$ denotes the virial mass of the main halo, MMR gives the merger mass ratio in terms of the virial mass. The initial separation of the two haloes centres is given by $d_{\rm ini}$, their initial relative velocity is $\Delta v_{\rm ini}$ and they are all head-on collisions. The self-interaction cross-section is $\sigma_{\tilde{\rm T}}$ (see equation 4.3) and the given values have been simulated with rare and frequent self-interactions, except of $\sigma_{\tilde{\rm T}} = 0.0$ which corresponds to CDM.

they are separated by a distance $d_{\rm ini}$ and they have a relative velocity of $v_{\rm ini}$. We simulate collisionless DM as well as rare and frequent interacting DM with several cross-sections. The initial velocity is chosen such that the sub halo is still gravitationally bound to the main halo. An overview of all runs is given in Tab. 4.2.2. In addition, we simulated the cluster-scale setup of the 1:10 merger employing a cross-section of $\sigma_{\tilde{\rm T}}/m = 0.5{\rm cm}^2\,{\rm g}^{-1}$ with half the resolution to check that our results are converged.

For the self-interactions, we use the momentum transfer cross-section defined as[1]

$$\sigma_{\tilde{\rm T}} = 4\pi \int_0^1 \frac{{\rm d}\sigma}{{\rm d}\Omega_{\rm cms}} (1 - \cos\theta_{\rm cms}) {\rm d}\cos\theta_{\rm cms}\,. \tag{4.3}$$

In addition, we employ a fixed gravitational softening length of $\epsilon = 1.2\,{\rm kpc}$ for the cluster-scale simulations and $\epsilon = 0.06\,{\rm kpc}$ for the galaxy-scale simulations. We use an adaptive kernel size for the DM self-interactions, which varies to keep the number of neighbours within each particles' kernel, $N_{\rm ngb}$, equal to 64. For fSIDM, a larger number would lead to more interactions, enabling the use of a larger time-step and reducing numerical noise, but

[1]Note that for the case of identical particles, as implicitly assumed here, this definition is equivalent to the one advocated by Robertson et al. (2017b) and Kahlhoefer et al. (2017).

at the same time it would reduce spatial resolution and would require the computation of more particle interactions. As a compromise, we choose to use the same value as in Fischer et al. (2021a).

4.3 Methods

In this section, we describe how we determine the peaks of our particle distributions and then how we define offsets. As we will describe below, the peak finding is a complex issue and crucial for the study of self-interactions in halo mergers. Finally, we will explain how we measure halo shapes and compare time-scales across simulations.

4.3.1 Peak finding

In the literature, one can find various methods to find peaks of particle distributions. For instance, the shrinking spheres/circles method (Power et al., 2003) or parametric fits (Robertson et al., 2017a) or the search for density maxima based on kernel density estimates (Kim et al., 2017). Finding peaks for an unequal-mass merger is more difficult than for an equal-mass merger as the peak for the less massive halo vanishes faster and is harder to detect. In this paper, we use two methods to find peaks, as we explain in the following subsections.

Gravitational potential based peaks

We employed a peak search strategy that is based on the gravitational potential energy of the particles. We use the information of which halo a particle initially belongs to, and perform the search for the most gravitationally bound particles of each halo and each particle type separately. For instance, the DM potential based peak of the main halo is the location of the DM particle that experience the lowest potential originally from the main halo, where the potential at each particle is calculated with respect to only the other DM particles that were originally part of the main halo. While this approach does not directly map to observationally available information, it does give an insight into the underlying merger dynamics.

In order to speed up the peak search, we employ an octree-like structure to cluster the particles, where every node is required to contain no more particles than a given maximum. In the first step, we compute the potential using the nodes of the tree and search for local minima. Thus, we estimate the potential at the centre of mass of each node and compare it to the neighbouring nodes.

In a second step, we investigate particles close to the minima, i.e. particles that belong to the corresponding node and its neighbours. For the computation of the binding energy of individual particles, we also use the tree nodes, such that distant particles are not evaluated individually, but are clustered in nodes. For the main halo, we search only for the global

minimum, which is usually the only minimum, although there can be more. The main peak is then given by the coordinates of the particle where the potential is minimal.

For the subhalo we investigate the deepest minimum, but also the second deepest local minimum provided it exists. Typically, a second potential minimum forms at the centre of the main halo and after a while it becomes the dominant peak as the subhalo merges with the main one. It is worth mentioning that the formation of the second peak is strongly affected by the relabelling procedure for rSIDM, which is implemented via a limited scattering angle as described in Section 4.2.1. In Appendix 4.A, we demonstrate the effects from this procedure.

If the subhalo contains a second peak, we check whether the first one coincides with the peak of the main halo. If this is the case, we take the second one as the peak of the subhalo. From some point in time on, this second peak is no longer present as a minimum in the potential and, consequently, we are no longer able to determine the peak position of the dissolving subhalo.

For our computation of the gravitational potential, we also employ a gravitational softening length to avoid artefacts from very close particles. In contrast to the actual simulations and for the sake of simplicity, we use Plummer softening (e.g. Dyer & Ip, 1993). A large softening length would impact the peak positions. Consequently, we choose a value that is small enough to obtain reliable peaks but large enough to avoid misdetections due to close particles. For the analysis of the cluster-scale simulations, we use $\epsilon = 1.2\,\mathrm{kpc}$ and for the galaxy-scale simulations, we employ $\epsilon = 0.06\,\mathrm{kpc}$.

Finally, we estimate the error for the peaks by bootstrapping the particle distribution 24 times and determine the peaks again. We obtain the error on the peak position by simply using the standard deviation of the peaks obtained from the bootstrapped haloes. Finally, we set the error to a value that has at least the value of the softening length.

The peak finding algorithm is illustrated in Fig. 4.3.1 and can be broken down into five steps as follows:

1. Generation of the mesh.
2. Estimation of the potential at the positions of the cells.
3. Search for local minima by comparison with neighbour cells.
4. Determination of the particle with the lowest potential.
5. Bootstrap distribution to obtain errors on peaks, redo (ii)–(iv).

The peak finding method we are using is not affected by projection effects because we work in all three dimensions. For peaks of collisionless particle components, this typically leads to a peak that coincides with the position of the single tracer particle placed initially at the halo centre. Note that this is in contrast to methods that work in projection as in Kim et al. (2017) or Fischer et al. (2021a). However, the three-dimensional approach may not be ideal when comparing DM-galaxy offsets of simulations to observations, where the

three-dimensional information is not available. Moreover, our approach relies on knowledge to which halo each particle originally belongs, which can only be traced in simulations.

For a comparison with observations, fits of parametric models seem to be more interesting. They are often used to analyse observational data. Among other things, Robertson et al. (2017b) employed this method to determine the positions of different components in simulations of a system that was designed to mimic the Bullet Cluster. For isotropic scattering, their measured offsets arise solely from fitting the wake of scattered particles, whereas unscattered particles behave in the same way as the collisionless galaxy particles. In consequence, measured offsets depend strongly on the chosen method and our potential based approach may lead to smaller offsets than parametric fits. Moreover, spherically symmetric parametric models may not always provide a good description of the DM distribution and an asymmetric model is favourable (Taylor et al., 2017). This problem does not arise in other methods, such as the shrinking spheres method.

But the shrinking spheres or its two-dimensional analogue, the shrinking circles method suffers from more severe problems. It is highly sensitive to the starting position and radius (Robertson et al., 2017a). Moreover, for a multiple peak search, extra guidance would be needed to detect the different peaks which is not necessary in the method based on the gravitational potential that can detect multiple peaks more easily. Finally, the position of the subhalo can be strongly affected by the density gradient of the main halo (Robertson et al., 2017a).

Isodensity contour based peaks

In addition to the peak finder based on the gravitational potential, we use a second method which may be more easily transferable to observations. In this second method, we determine the peaks of the particle distributions based on isodensity contours in projected two-dimensional density maps (similar to Kahlhoefer et al., 2014). To this end, we project the density for each component onto a plane in which the merger axis lies and determine how many regions exceed a given threshold in surface density. Initially, we choose a threshold close to the maximum surface density and lower it until we find two separate regions that exceed the threshold. For each region, we compute the centroid of the particles that belong to this region, which gives us the peak position. We perform this procedure for the DM and galactic component, separately. In contrast to the peak finder described above, this method does not require any information about the origin of the particles. In order to still be able to assign peaks to haloes, we linearly extrapolate the peak position of a halo from the past and compare it to the identified peaks. The one which is closer to the linear prediction is associated with the halo.

If the centres of the haloes are too close, we are no longer able to identify them as separate peaks as we find only one region exceeding the density threshold. In this case, we use the only peak found for the two haloes. As a result, we are not able to give accurate peak positions for very small separations and do not show quantities derived from the

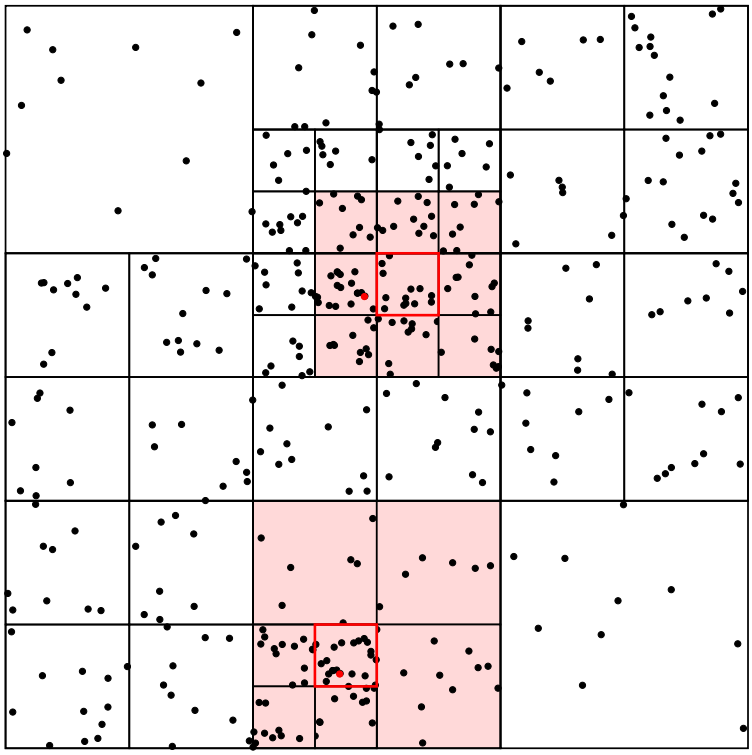

Figure 4.3.1: Illustration of the peak finding method. Particles (black dots) are clustered in cells (squares) of different sizes adapted to the particle number density. On the basis of the cells, a search for local potential minima (squares with red lines) is performed. The particles which have locally the lowest potential (red dots) are searched for in a neighbouring area around the minima (red shaded regions).

peaks if they are close.

Errors on the peak positions are computed via bootstrapping the particle distribution 24 times. In general, the obtained errors are tiny and thus usually not visible in our plots.

4.3.2 Offsets

Here, we describe how we measure offsets between DM and galaxies, i.e. the distance between their respective peaks. There are multiple ways that they could be defined, i.e. how their sign is chosen, but here we define the offsets between DM and the component i by

$$\text{offset} \equiv x_{\text{DM}} - x_i \,, \tag{4.4}$$

where the coordinate along the merger axis is given by x. Note that this definition is different from the one we used previously in Fischer et al. (2021a).

4.3.3 Halo shapes

In order to compute halo shapes we use the inertia tensor $\mathbf{I}$, with its moments of inertia, i.e. its eigenvalues I_1, I_2, and I_3. For N point masses m_n at position $\mathbf{r}_n$, the inertia tensor is

$$\mathbf{I} \equiv \sum_n^N m_n \left[(\boldsymbol{r}_n \cdot \boldsymbol{r}_n)\, \mathbf{1} - \boldsymbol{r}_n \otimes \boldsymbol{r}_n \right]. \tag{4.5}$$

Here, I_1 corresponds to the principal axis (or eigenvector) which is most closely aligned to the merger axis. The ratio of the moments of inertia gives us a shape variable

$$s \equiv \frac{2\, I_1}{I_2 + I_3} \,. \tag{4.6}$$

For our head-on mergers, we expect $I_2 = I_3$ due to the symmetry of the system and initially our haloes are spherical, which implies $s = 1$. Values larger than one correspond to oblate haloes and values smaller than one to prolate haloes. In Section 4.4, we compute the halo shape separately for the components of the haloes and with respect to the peaks determined according to the method based on the gravitational potential described in Section 4.3.1. We consider only particles that are closer than twice the scale radius of the initial NFW profiles.

In contrast to our shape definition often a reduced inertia tensor is used (e.g. Allgood et al., 2006; Bett, 2012; Peter et al., 2013; Vargya et al., 2021). This is in the context of measuring the shape as a function of distance. According to Zemp et al. (2011), the $1/r^2$ weighting of the reduced inertia tensor does not improve the shape measurement and they recommend using elliptical shells. However, for our work, we are only interested in an estimate of the shape that allows us to understand qualitative differences between DM models as a function of time. That is why we pursue a simplified approach.

4.3.4 Merger times

Self-interactions can change the merger time of a system, which can be problematic for a comparison between simulations using different cross-sections. A system evolved with SIDM may have reached the second pericentre but when simulated with CDM after the same time, it could be in a phase before the second pericentre. To allow comparison between the same stages in the evolution of a merger, we define an internal time τ of the system

$$\tau \equiv \frac{t - t_{\text{first pericentre}}}{t_m}, \tag{4.7}$$

where $t_m = t_{\text{second pericentre}} - t_{\text{first pericentre}}$ gives us the merger time. By definition, $\tau = 0$ corresponds to the first pericentre passage and $\tau = 1$ to the second pericentre passage. For the analysis of the simulation, we use the BCGs/BHs to compute the time τ. This has the advantage that the time is independent of the peak finding algorithm and thus always known.

4.4 Results

In this section, we present our results on equal and unequal-mass head-on mergers, both, for frequent and rare self-interactions. In particular, we focus on the morphology (Section 4.4.1), DM-galaxy offsets (Section 4.4.2), shapes of the haloes (Section 4.4.3), compare fSIDM and rSIDM (Section 4.4.4) as well as the peak finding methods (Section 4.4.5) and examine the phase–space distribution (Section 4.4.6). The numerical setup used to produce the results is described in Section 4.2 and the methods employed to analyse the data are explained in Section 4.3.

In the following, we call the more massive halo the 'main halo' and the less massive one the 'subhalo'. We will use this terminology even in the case of an equal-mass merger in which case the assignment of the 'main halo' and 'subhalo' is arbitrary.

In Fig. 4.4.1, we illustrate the evolution of an unequal-mass merger and indicate the different evolution stages of the system. During the infall phase, the self-interactions do not affect the merger, apart from core formation in the two haloes. At the first pericentre passage, self-interactions can be strong and decelerate the DM component. This can lead to a smaller separation of the haloes at the first apocentre passage and a shorter merger time-scale as well as other phenomena such as offsets between the DM and galactic/stellar components. Depending on the DM physics, the haloes coalesce at different rates, such that there can be further apocentre passages or not. In the most extreme case, self-interactions are so strong that the haloes coalesce on contact. Since stars or galaxies are not subject to self-interactions, they behave differently from SIDM but are affected by the overall gravitational potential. This can lead to differences in the distribution of stars and galaxies between different DM models. These differences tend to grow with time as we will see in

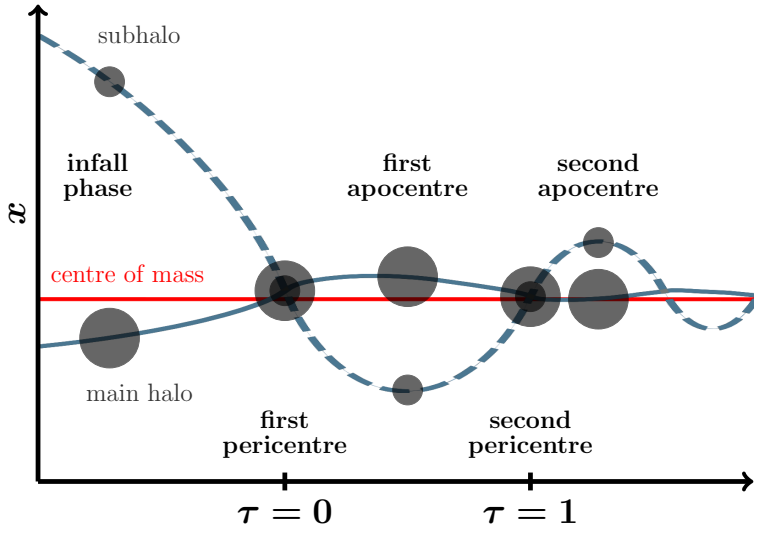

Figure 4.4.1: Illustration of the evolution of an unequal-mass merger without self-interactions. The halo position along the merger axis is shown as a function of the internal merger time τ (see Eq. 4.7).

the following analysis of our merger simulations.

To simplify the discussion, we will largely concentrate on a 1:10 cluster-scale merger for CDM, rSIDM, and fSIDM in the following. We will fix the cross-section to $\sigma_{\tilde{\mathrm{T}}}/m = 0.5\,\mathrm{cm}^2\,\mathrm{g}^{-1}$ for the self-interacting cases, before we come to a comparison of the different mass ratios and cross-sections. Further details on additional runs with other parameters can be found in the Appendices.

4.4.1 Morphology

Let us start with examining the physical DM and galactic densities in the plane of the merger, where we consider particles within a slice of 100 kpc height. An illustration of the time evolution of the merger is provided as supplementary material. For convenience we show both, the density of the two haloes combined as well as only the density of particles which originally belonged to the subhalo to facilitate the physical intuition of the merger process. We also present DM and galactic components separately for clarity. At the first pericentre passage, differences between the different DM models are still very small but they grow over time and become significant at later merger stages, so we will mainly concentrate on these in the following. In Fig. 4.4.2, we show the subhalo density at $\tau = 1.16$, i.e. some time after the second pericentre passage. At these later stages in the evolution we do observe some differences between frequent and rare scatterings.

For example, the DM densities of the left-hand column show that matter is most concentrated for CDM, less for rSIDM, and least for fSIDM. The fSIDM subhalo dissolves faster than its rSIDM counterpart thus distinct DM peaks are only detectable for a shorter period of time. This is related to differences in the gravitational potential, which affect the galaxy particles and creates distributions that differ significantly from each other (see

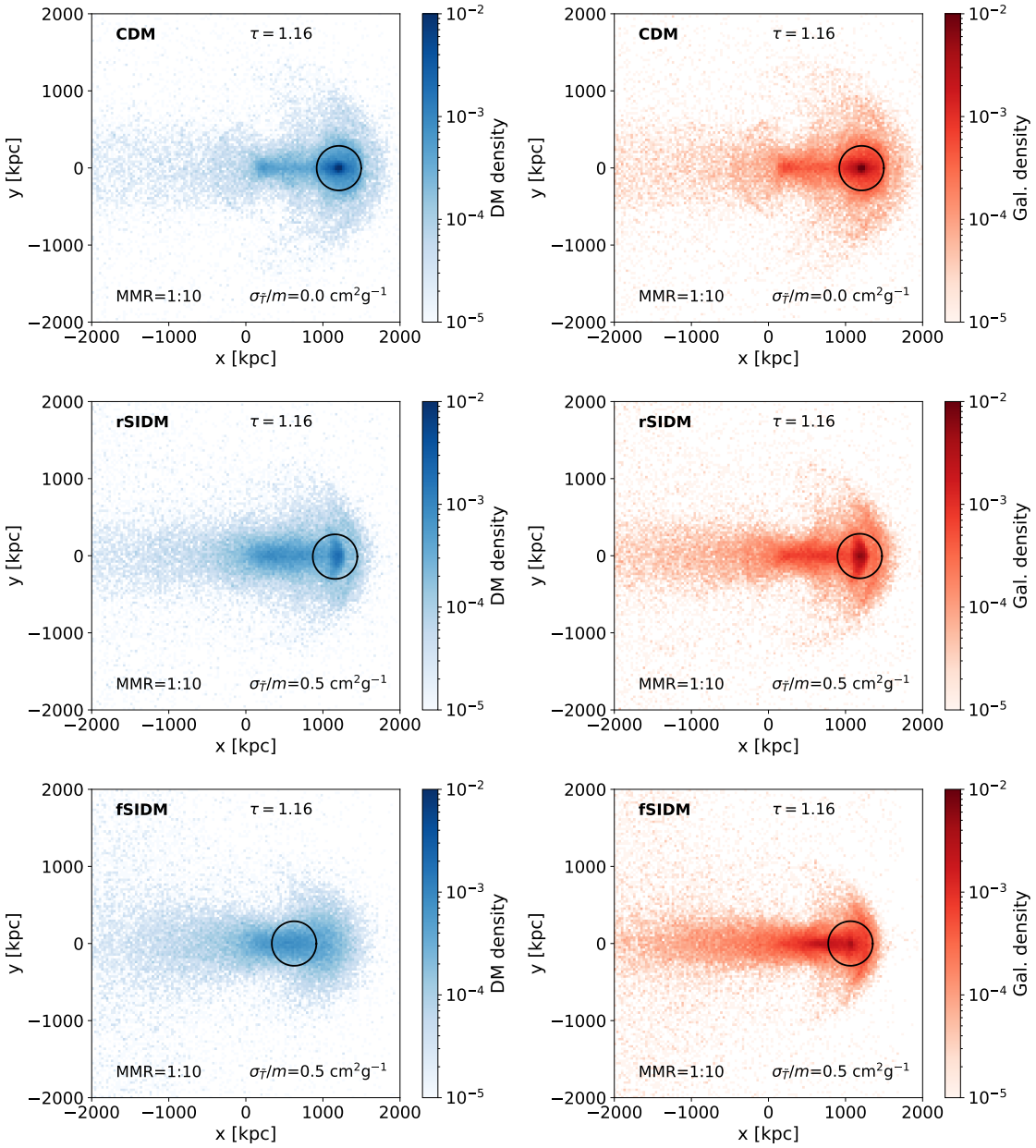

Figure 4.4.2: The subhalo's physical density of the DM (left-hand side) and the galactic component (right-hand side) in the merger plane is shown for cluster-scale mergers with an MMR of 1:10. The upper panel gives the density for the CDM run, the middle panel for rSIDM, and the bottom panel for fSIDM. All panels display the density for τ = 1.16, i.e. sometime after the second pericentre passage. At this stage, the subhalo is moving in the positive x-direction. The self-interaction cross-section is $\sigma_{\tilde{\mathrm{T}}}/m = 0.5\,\mathrm{cm}^2\,\mathrm{g}^{-1}$. The black circles are drawn around the potential based peak position of the subhalo and have a radius of twice the initial scale radius. Hence, they indicate the area from which the particles for the shape computation are selected. However, they are shown even in the case where we considered the peaks as too uncertain for the following analysis (this concerns rSIDM and fSIDM). In the supplementary material, we provide the time evolution as a video.

right-hand column of Fig. 4.4.2).

The density at the peak position as a function of time is shown in Fig. 4.4.3. Here, one can see the quantitative differences between the DM models. The central density of the subhalo is more affected than the main halo and galaxies are less affected than the DM. Usually, the density stays constant or is decreasing, except for short periods of density increase that occur subsequent to pericentre passages. Note that we measured the mean density within a sphere that has a radius of 40 kpc. As the density gradient in the vicinity of the peak position is non-zero, the measured density depends on the chosen radius. However, the results do not qualitatively depend on the selection criterion.

In Fig. 4.4.2, the shapes of the densest regions for rSIDM and fSIDM look rather different. The matter distribution for rSIDM appears to be very oblate in the vicinity of the peak for both DM and galaxies. In contrast, for fSIDM the distribution looks more prolate. In section 4.4.3 and 4.4.4, we study the evolution of the halo shape. However, for the fSIDM and rSIDM, runs we do not consider the potential based peaks to be accurate enough to compute the shape at the merger stage we discuss here.

With time, the subhalo particles get caught by the main halo. For fSIDM, a fraction of stripped particles appear as a dense tail in between the halo peaks (at the left side of the black circle, lower right-hand panel of Fig.4.4.2). This is less the case for rSIDM.

Besides, there are shell-like features in the galactic distribution. For rSIDM, there seem to be two shells, the peak belongs to one of them and another one is in front of it. The fSIDM morphology looks different, there appears to be only one shell which is located in front of the peak.

Based on the morphology, minor mergers seem to be well suited to distinguish rare and frequent self-interactions. However, in practice, observational limitations could alter the picture. It remains to be seen whether this persists in the presence of baryonic matter and this will be the subject of forthcoming work. Moreover, we should note that we have only looked at a slice in the merger plane and not a projected two-dimensional density map, which is more relevant from an observational point of view and may look somewhat different due to projection effects. For clarity, we only considered the particles of the subhalo and ignored the main halo which is the dominant component. But even if the main halo is taken into account, one can recognize differences between DM models as we demonstrate in Appendix 4.B.

4.4.2 Centre of mass distance and offsets

Let us now come to a discussion of the peak positions of the different sub-components as well as the inferred offsets for our merger simulations. In Fig. 4.4.4, we show the positions of the peaks of the various components (DM, galaxies, BCGs) along the merger axis for runs of the 1:10 cluster-scale merger. For the same simulations, we display the offset in Fig. 4.4.5.

The peaks were determined by using the potential-based peak finder described in

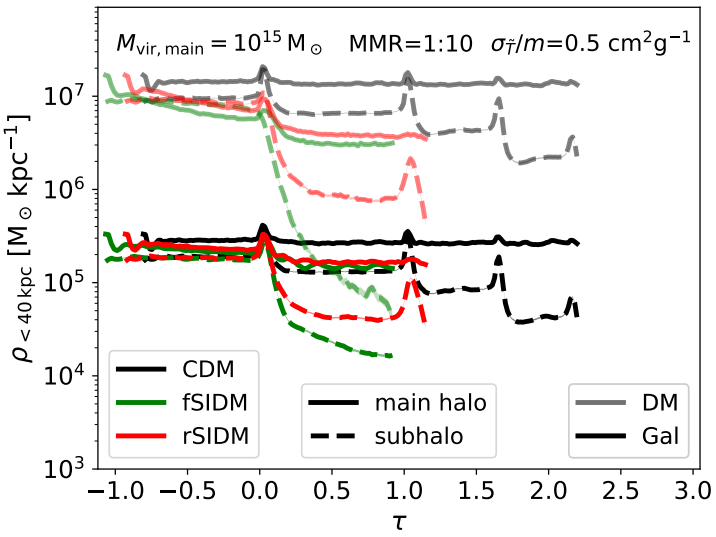

Figure 4.4.3: The density at the location of the halo peak is shown as a function of time. The density is computed from the particles within a sphere of 40 kpc around the peak. Only the particles which initially belonged to the halo in question were considered for the density computation. The shaded regions display the error. Here, we show the central densities for the same simulations as studied in Fig. 4.4.2.

Section 4.3.1. This peak finder has the effect that the peaks of a collisionless component behave very similarly to the BCG positions. This can be seen when comparing the galaxy peaks with the BCG positions. For the CDM run, the DM is collisionless and thus all peaks coincide; the vanishing offsets shown in the upper panel of Fig. 4.4.5 demonstrate this. Furthermore, the vanishing DM–galaxy offset demonstrates how small the peak finding error is. Besides, it seems that the haloes are a little offset from the centre of mass, e.g. the pericentre passage does not coincide with the centre of mass. This is only the case for the unequal-mass mergers and might be caused by the asymmetry of the system. During the infall phase, the haloes are deformed due to tidal forces, which may lead to a shift between the centre of mass and the weighted centre of the two peaks.

For the CDM and fSIDM run, the first pericentre passage occurs after roughly 2.1 Gyr. Self-interactions have the effect of reducing the merger time for the fSIDM run. Also, the second pericentre passage occurs earlier than for CDM. Another difference between SIDM and CDM shows up in the oscillation of the BCGs in the DM potential. For CDM, the amplitude decays much faster than for SIDM where the orbital decay is minimal. This effect exists in unequal-mass mergers as well as in equal-mass mergers as demonstrated in Kim et al. (2017). At a basic level, this reduction in dynamical friction with SIDM results from the lowered DM densities in the merger remnant compared with in the CDM case (e.g. see Fig. 4.4.3), and the fact that the dynamical friction force is proportional to the background density (Chandrasekhar, 1943). We note however (as also discussed in Kim et al., 2017) that dynamical friction acting on bodies orbiting in a cored DM distribution

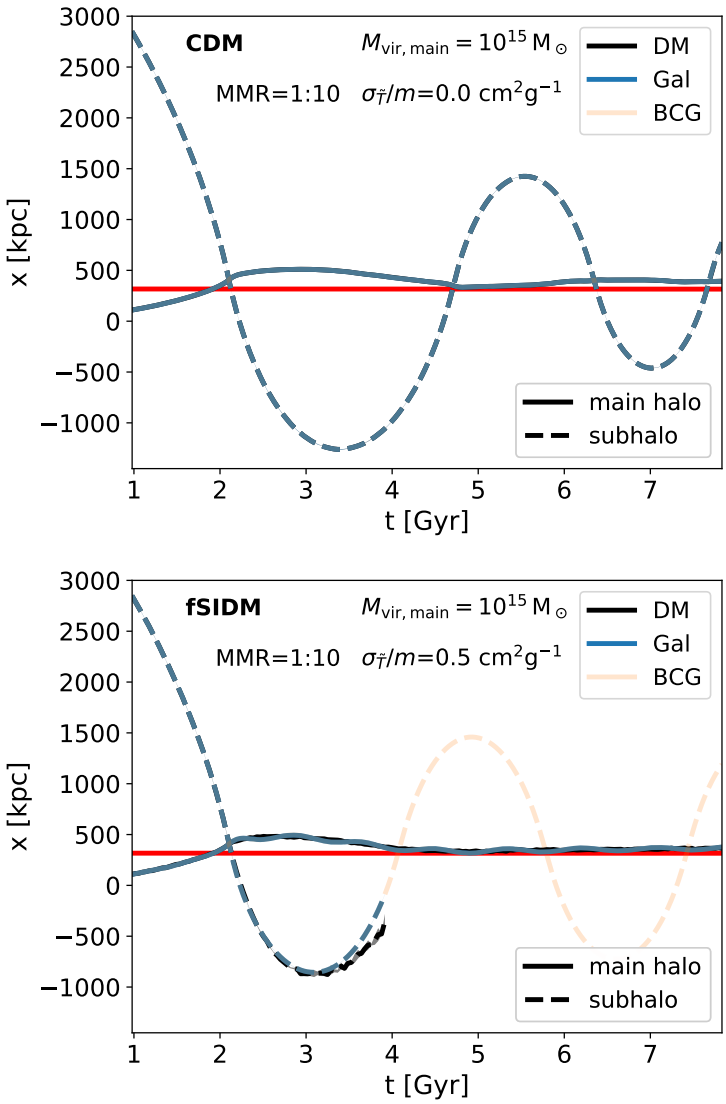

Figure 4.4.4: For a 1:10 merger, the peak positions for various components (DM, galaxies, BCGs) are shown. The red line indicates the centre of mass of the system. The upper panel gives the positions for a simulation with CDM and the lower panel for a simulation with fSIDM and a cross-section of $\sigma_{\tilde{\mathrm{T}}}/m = 0.5\,\mathrm{cm}^2\,\mathrm{g}^{-1}$. Peak positions are shown as long as the peak finder provides reasonable results.

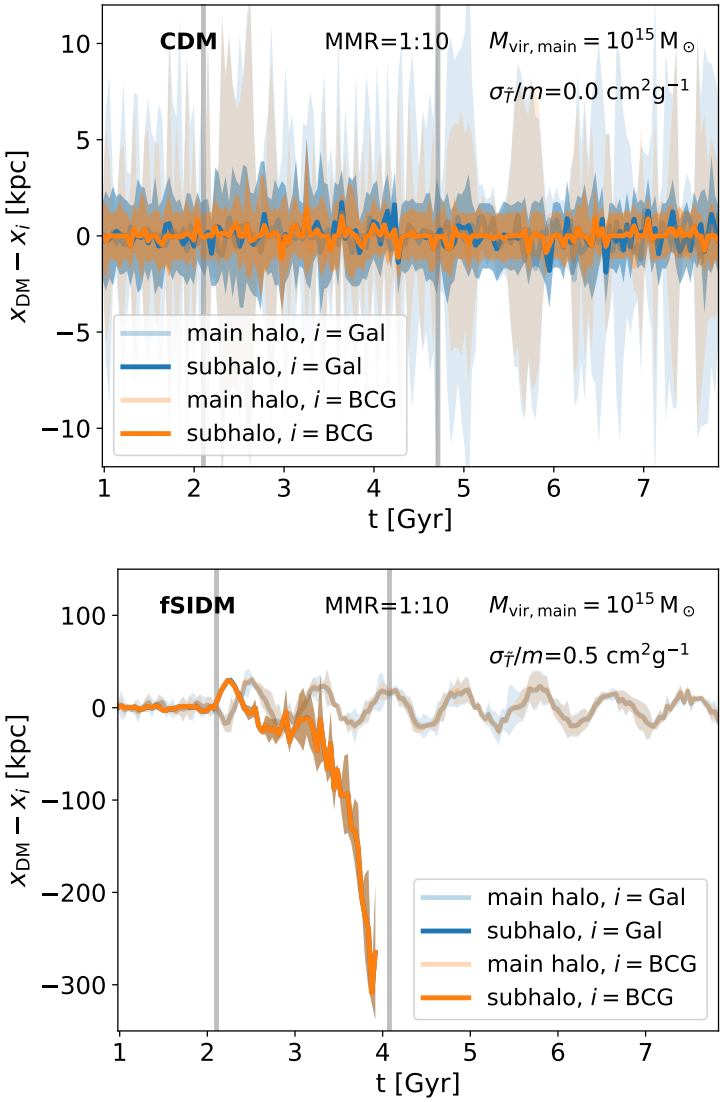

Figure 4.4.5: Offsets for the runs shown in Fig. 4.4.4. The upper panel displays offsets for the CDM merger and the lower panel for the fSIDM merger. The shaded areas indicate the 1σ error. The first and second pericentre passage are indicated by the vertical grey lines.

is more complicated than the motion through an infinite constant-density background considered by Chandrasekhar (1943), and that dynamical friction can vanish almost entirely in such a case (Read et al., 2006).

Before the merging system reaches equilibrium, the common potential becomes deeper and thus the amplitude of the BCGs oscillation decreases until the DM core of the coalesced halo has formed. However, the orbits of the BCG could change once the effects of the ICM are considered and the BCG is modelled more realistically.

The offsets for the fSIDM run are large enough such that they can already be identified in the lower panel of Fig. 4.4.4. These large offsets do not arise close to the first pericentre passage, but between the first apocentre and the second pericentre. However, we should point out that we have no reliable peak positions for the subhalo at times later than 4 Gyr. While in principle a merging system could have its largest offset after the second pericentre passage, the observational identification of separate DM peaks becomes prohibitively difficult at late merger stages as the subhalo dissolves. In contrast, separate stellar or galactic components could be identified more easily and offsets after coalescence of the DM component associated with core sloshing could provide a signature of SIDM (Kim et al., 2017). In particular, the minimally decaying orbit of the BCGs could be of interest. We provide further results on core sloshing using multiple peak finding methods in Section 4.4.5. We also compare offsets of different runs including various merger mass ratios (MMR) and self-interaction cross-sections in Section 4.4.4.

4.4.3 Shapes

DM self-interactions affect the peak positions of the haloes as well as the higher order moments of the DM distribution. Here, we focus on the shape variable of the haloes as defined by Eq. (4.6). In contrast to other studies, we pursue a simplified approach by considering all particles within twice the scale radius of the initial NFW profile instead of measuring the shape as a function of radial distance as done in other studies (e.g. Zemp et al., 2011; Peter et al., 2013; Chua et al., 2020; Vargya et al., 2021).

In Fig. 4.4.6, we show the shape parameter for a 1:10 merger evolved with CDM and fSIDM, the same simulations as shown in Fig. 4.4.4 and Fig. 4.4.5.

Initially, the haloes are spherically symmetric ($s = 1$) and subsequently evolve to become more elliptical owing to gravitational interactions with the other halo. The shape of the main halo indicated by the solid line is only slightly affected by the merger and becomes a little more elliptical, in particular about the pericentre passages. In contrast, the shape of the subhalo is more strongly affected, for both CDM and fSIDM. For the CDM merger, we are able to track the peaks for much longer times and thus can compute shapes for later times compared to fSIDM. As we can see in the upper panel of Fig. 4.4.6, the evolution of the CDM subhalo can be described as follows: During the infall phase directly before the first pericentre passage, the shape becomes much more prolate due to tidal forces and the size of this distortion depends on the mass ratio. Close to the core passage, gravity

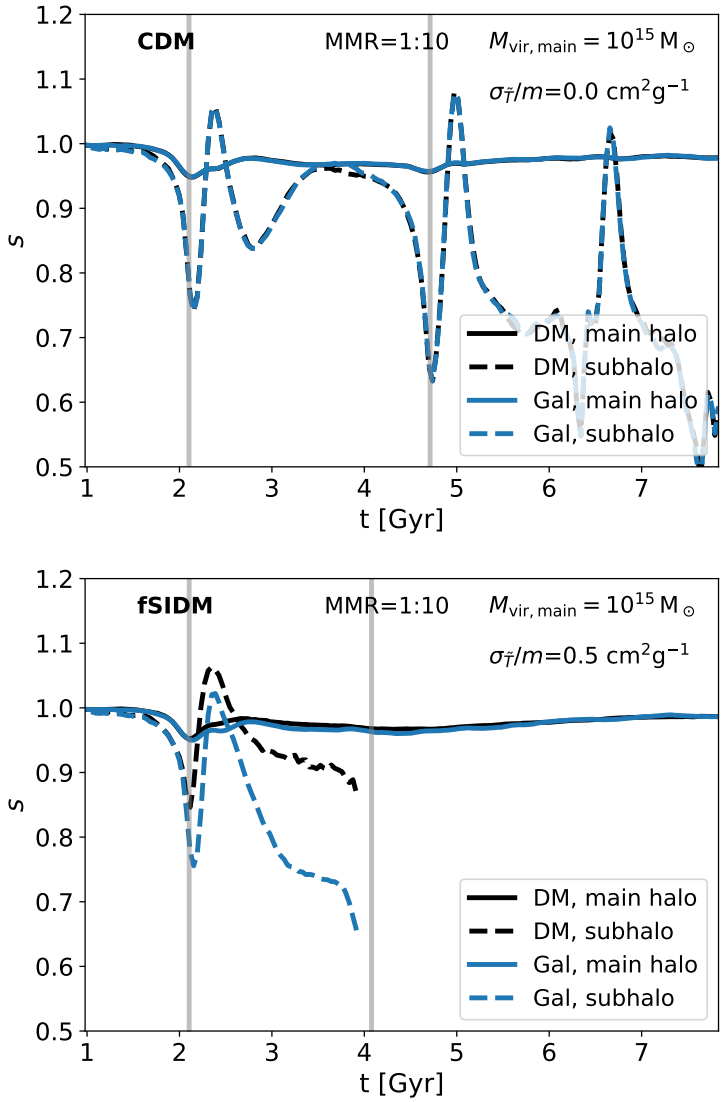

Figure 4.4.6: Shapes for the runs shown in Fig. 4.4.4. The upper panel displays shapes for the CDM merger and the lower panel for the fSIDM merger. The first and second pericentre passage are indicated by the vertical grey lines.

has a different effect, which leads to a more oblate shape. The halo becomes even more oblate than it has been initially. But when it climbs out of the potential of the main halo afterwards, then it becomes more prolate due to tidal forces again. When the separation between the two haloes has grown large enough (about the first apocentre passage, ~ 3.4 Gyr) the tidal force can become small compared to the self-gravity of the subhalo. Hence, the self-gravity makes the subhalo more spherical. A rough estimate of the tidal radius at the first apocentre passage leads to 536 kpc or $3.7\,r_{\rm s}$. Thus, the particles we selected for the shape computation should be within the tidal radius. Later on, when the merger is getting close to the second pericentre passage, tidal forces make the halo more prolate again. The described picture depends strongly on the considered particles. If one would take particles beyond twice the scale radius of the initial NFW profile into account, the evolution of the shape would look very different.

In comparison to CDM, the fSIDM subhalo is less prolate about the first pericentre passage and also the maximum in shape shortly after the core passage is more extreme for fSIDM. Frequent self-interactions transfer energy from the direction of motion to the perpendicular component which contributes to a more oblate halo. Besides, one can observe that a difference between the galaxies and the DM component arises. This is simply due to the collisionless nature of our galaxies that do not undergo frequent self-interactions.

About the first apocentre passage (~ 3.1 Gyr), when the tidal force becomes less important, the self-gravity can lead to a more spherical halo as we found for CDM. But for fSIDM the subhalo's gravitational potential is less deep and the apocentre distance is shorter compared to CDM, resulting in a halo that becomes even more prolate.

Going beyond the parameter values assumed here, we compare shapes of different simulations for a variety of MMRs and cross-sections in Section 4.4.4.

4.4.4 Frequent versus rare interactions

In the following, we compare the effects from rare and frequent self-interactions in mergers for various MMRs. In Fig. 4.4.7, we show DM-galaxy offsets for subhaloes employing several cross-sections and in Fig. 4.4.8, we compare the subhalo shapes of SIDM runs to the CDM shapes. In this section, we concentrate on the cluster-scale simulations. Plots for the galaxy-scale simulations can be found in Appendix 4.C.

Offsets

For the equal-mass mergers, we find that the largest offsets occur at late stages, i.e. after the second apocentre passage (see Fig. 4.4.7) of the mergers as the time difference between the pericentre passages of DM and galaxies becomes larger for late times. This phase shift increases for larger cross-sections, leading to larger offsets. For unequal-mass merger, we find similar results. However, in the latter case, we encounter difficulties in determining the peaks at late times due to the evaporating subhalo.

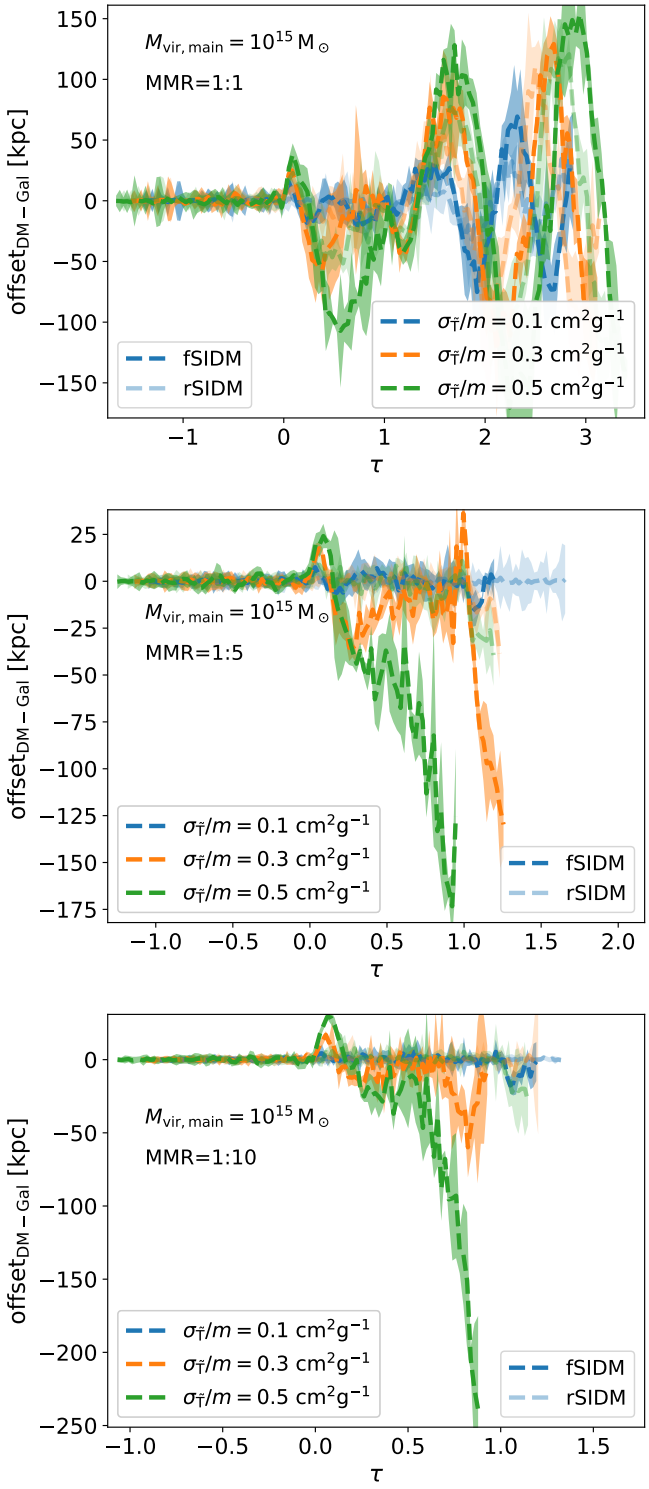

Figure 4.4.7: DM-galaxy offsets from merging system with various MMRs (upper row: 1:1, middle row: 1:5, lower row: 1:10) for the subhaloes. The results were obtained using the potential based peak finder. The offsets are defined according to Eq. (4.4) and shown for frequent (high opacity) and rare (low opacity) self-interactions as well as for several cross-sections: $\sigma_{\tilde{\mathrm{T}}}/m = 0.1\,\mathrm{cm^2\,g^{-1}}$ (blue), $\sigma_{\tilde{\mathrm{T}}}/m = 0.3\,\mathrm{cm^2\,g^{-1}}$ (orange), $\sigma_{\tilde{\mathrm{T}}}/m = 0.5\,\mathrm{cm^2\,g^{-1}}$ (green). The shaded areas indicate the 1σ error.

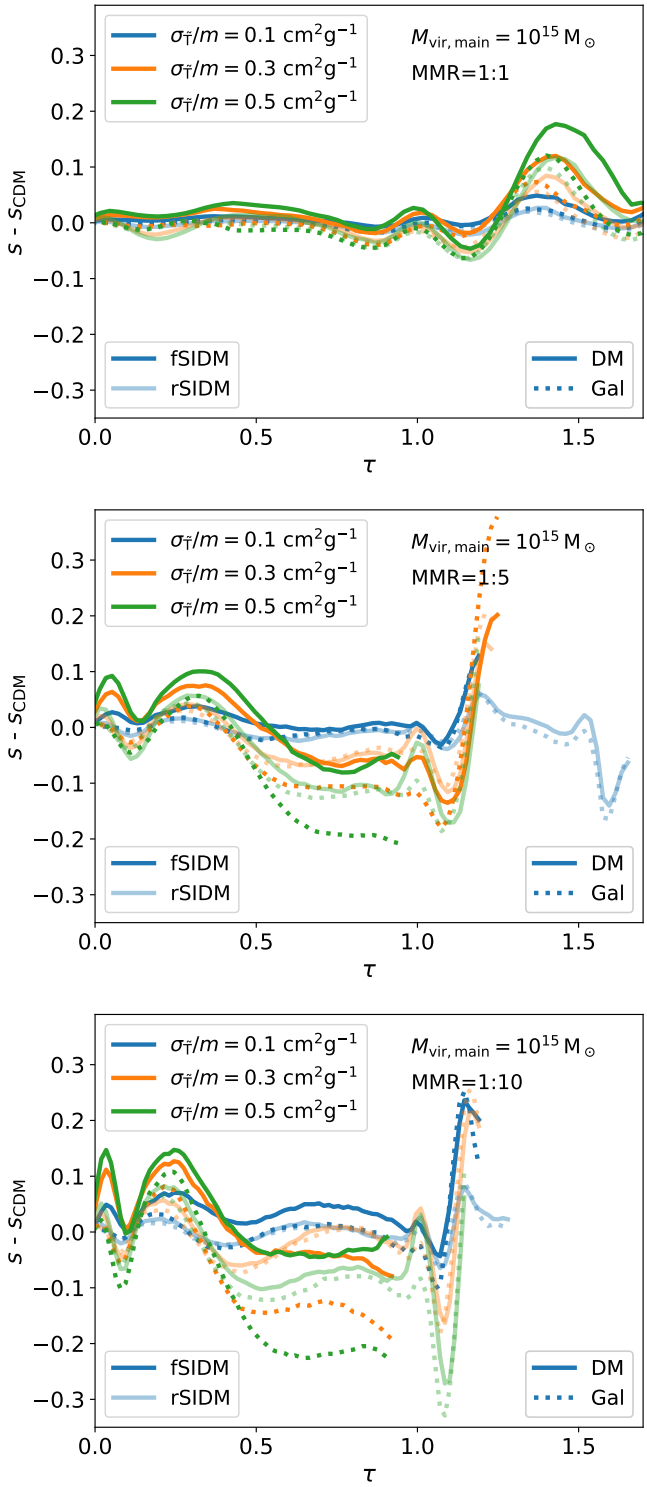

Figure 4.4.8: Differences in the shape between SIDM and CDM subhaloes from merging system with various MMRs (upper panel: 1:1, middle panel: 1:5, lower panel: 1:10). The shapes are defined according to Eq. (4.6) and shown for frequent (high opacity) and rare (low opacity) self-interactions as well as for several cross-sections: $\sigma_{\tilde{\mathrm{T}}}/m = 0.1\,\mathrm{cm}^2\,\mathrm{g}^{-1}$ (blue), $\sigma_{\tilde{\mathrm{T}}}/m = 0.3\,\mathrm{cm}^2\,\mathrm{g}^{-1}$ (orange), $\sigma_{\tilde{\mathrm{T}}}/m = 0.5\,\mathrm{cm}^2\,\mathrm{g}^{-1}$ (green).

For all mergers, we find the general trend that frequent self-interactions produce larger offsets than rare self-interaction when comparing the same momentum transfer cross-section and the size of offsets increases for larger values of $\sigma_{\tilde{\mathrm{T}}}/m$ (see Fig. 4.4.7). In addition, frequent self-interactions usually lead to somewhat shorter merger times than rare self-interactions. We observe that differences between the two cases are maximized for small MMR (i.e. larger difference in mass) and large cross-sections.

Furthermore, we find that runs with smaller MMR show larger offsets. As the subhalo is less massive in this case, its particles are less bound to it. Therefore, DM self-interactions and tidal forces of the main halo can affect it more, resulting in stronger effects of DM scatterings. Moreover, for our unequal mass mergers the merger time is longer, i.e. the time between two pericentre passages, such that the amplification process as observed in Fischer et al. (2021a) has more time to act on the galactic component. By amplification, we denote the process that the small initial offsets created by the self-interactions at the time when the system is close to its first pericentre passage evolve to much larger offsets at a later merger phase. Those offsets are caused by the different shapes of the DM gravitational potential acting on the trajectories of the collisionless galaxies/stars.

The magnitude of the offsets for rare and frequent self-interactions is substantially more different for unequal-mass mergers than for equal-mass mergers when considering the time before the second pericentre passage. In addition, unequal-mass mergers seem to be more sensitive to the cross-section than equal-mass mergers. For instance, consider the 1:5 merger (middle panel of Fig. 4.4.7) and compare the fSIDM offset of the runs with $\sigma_{\tilde{\mathrm{T}}}/m = 0.3\,\mathrm{cm}^2\,\mathrm{g}^{-1}$ (orange) and $\sigma_{\tilde{\mathrm{T}}}/m = 0.5\,\mathrm{cm}^2\,\mathrm{g}^{-1}$ (green). For $\tau \gtrsim 0.4$, the evolution of the offsets is quite different, the smaller cross-section shows decreasing offsets whereas for the larger one the offset continues to grow, implying that the relationship between cross-section and offset size is highly non-linear in general.

To obtain a better understanding of the underlying dynamics, let us now discuss the various effects which enter into the development of the offsets: when the drag force decelerates the DM, an offset between galaxies and DM arises. The gravitational pull of the DM halo acts against the offset. Thus, the smaller the subhalo, the weaker the gravitational attraction and, as a result, larger offsets occur. But it is not as simple as this. The picture is more complicated as the gravitational attraction depends on the gradient of the potential, which is flattened by the self-interactions and on the offset itself. Consequently, the first pericentre passage offsets could also be larger for equal-mass mergers depending on the actual mass profile. The mass profile of galaxy clusters also depends on the ICM, which we did not include in our simulations. However, the description above is only appropriate for the time about the first pericentre passage. At a later time, the DM peak overtakes the galaxies (i.e. becomes more distant to the centre of mass) as the galactic component has experienced a larger deceleration due to the offset, i.e. its corresponding DM halo has led to further deceleration. At the point in time when the DM is overtaking, i.e. the galactic peak is passing the DM peak, the DM gravitational potential is shallower. As a consequence, the

galaxies can escape further and much larger offsets ensue. The size of these offsets depends on how much shallower the gravitational potential becomes compared to the first pericentre passage. Lower mass haloes are less gravitationally bound, they dissolve faster due to self-interactions, and thus their gravitational potential becomes shallower and the offsets larger (and at the same time, harder to observe given the dissolving subhalo). The size of the effective gravitational attraction acting against the offset should depend on the offset and decrease for large enough offsets. Hence, the growth of large offsets can be accelerated further as observed for the unequal-mass mergers evolved with $\sigma_{\tilde{\mathrm{T}}}/m = 0.5\,\mathrm{cm}^2\,\mathrm{g}^{-1}$ (middle and lower panel of the left-hand column of Fig. 4.4.7).

For equal-mass mergers, we find that rSIDM can show large offsets ($\gtrsim 100\,\mathrm{kpc}$) only at late times via an accumulated phase shift. However, due to shallower density gradients at later times peak finding becomes more difficult, directly impacting the observational prospects of finding large offsets. However, also the large offsets of fSIDM will, in general, be difficult to observe as we discuss in Sec. 4.5.1. Nevertheless, the conditions under which an offset of observable size arises are more easily and more often met for fSIDM than for rSIDM.

Shape

In Fig. 4.4.8, we compare the shapes of SIDM subhaloes to the shapes of the corresponding CDM haloes using the time τ as given by Eq. (4.7). The shapes of the individual mergers are displayed in Appendix 4.C. Before the first pericentre passage ($\tau < 0$) differences occur only because of the different merger times as we use τ to match the times of the simulations. If one used the physical time for the infall phase, any significant difference would vanish and we do not display them in Fig. 4.4.8.

At the first pericentre passage ($\tau = 0$), the shapes are almost the same for all cross-sections. However, for the second pericentre passage ($\tau = 1$), this is no longer the case. How much the shapes of SIDM haloes deviate from their CDM counterpart depends strongly on the MMR. For equal-mass mergers, the differences in the shape parameter between CDM and fSIDM are small before the second pericentre passage and become larger for more unequal halo masses. As expected, the difference increases with increasing self-interaction cross-section.

Self-interactions can lead to more oblate as well as more prolate shapes compared to CDM. The difference depends on the merger stage and the self-interaction type. For the phase before the first apocentre passage, frequent self-interactions tend to produce haloes that are always more oblate. In contrast, rare self-interaction show also a phase ($\tau \sim 0.1$–0.2) with a significantly more prolate shape. While both fSIDM and rSIDM lead to a shallower potential, the phase–space distributions are different. Unlike frequent interactions, the isotropic, rare self-interactions do not preferentially transfer the energy from the forward motion to a perpendicular component but can create a tail of back-scattered particles. Hence, the shape of haloes in rSIDM can be more prolate than for fSIDM.

For the unequal-mass mergers, there is a phase at $\tau \sim 0.7$ where the self-interactions – given the cross-section is large enough – lead to more elliptical haloes than CDM. This can be understood in terms of a smaller pericentre distance implying a stronger tidal force and a shallower potential due to the DM scattering as explained in Section 4.4.3. The galactic component can be even more elliptical than the DM as it is not subject to self-interactions. Thus, the naive picture that self-interactions render haloes always more spherical fails in the case of an unequal-mass merger.

In most cases, fSIDM leads to a more oblate DM halo compared to rSIDM assuming that the same momentum transfer cross-sections are compared. In addition to the fact that fSIDM is transferring momentum from the direction of motion to a perpendicular component, there could also be differences between frequent and rare self-interactions regarding the efficiency of making haloes more spherical.

Furthermore, we also observe shape differences between the DM component and the galaxies/stars. The most striking difference can be seen for frequent self-interactions and unequal-mass mergers at around the first apocentre passage. The galactic component is more prolate than the DM and for the 1:10 merger, this phase lasts remarkably long. For rSIDM, there is only a very small difference between galaxies and DM shape. Interestingly, we find that the shape for the galactic component is more prolate for fSIDM than rSIDM. This occurs due to differences in the gravitational potential, for fSIDM, the particles are less strongly bound and thus more prone to tidal disruption.

Finally, we want to emphasize that our results depend on the particles selected for the shape computation. Particles of the inner or outer halo are affected differently during the merger. Hence, any comparison with simulation data or observations needs to be cautious about the scales on which quantities are measured.

4.4.5 Peak finding

In Section 4.3.1, we described two peak finding methods. So far, we have only discussed results relying on the peak finding method based on the gravitational potential. In this section, we will compare these results to the ones we obtain using the method of isodensity contours and discuss the origin of the resulting differences.

In Fig. 4.4.9, we show the peak positions as a function of time for an equal-mass merger evolved with frequent self-interactions and $\sigma_{\tilde{\mathrm{T}}}/m = 0.5\,\mathrm{cm}^2\,\mathrm{g}^{-1}$. The upper panel shows the peak position using the peak finder based on the gravitational potential; and the lower panel displays the positions of the peaks based on isodensity contours. One can recognize two main differences between the peak finding methods: First, in the lower panel, the peak position around the pericentre passages is biased towards the centre of mass as no separate peaks can be identified for small separations and thus the haloes seem to coalesce earlier. Secondly, we observe the offsets to be smaller for the isodensity contour peaks at the first apocentre passage. They are about half the size of the potential-based offsets. This is caused by the projection since self-interactions mainly alter the evolution of the central

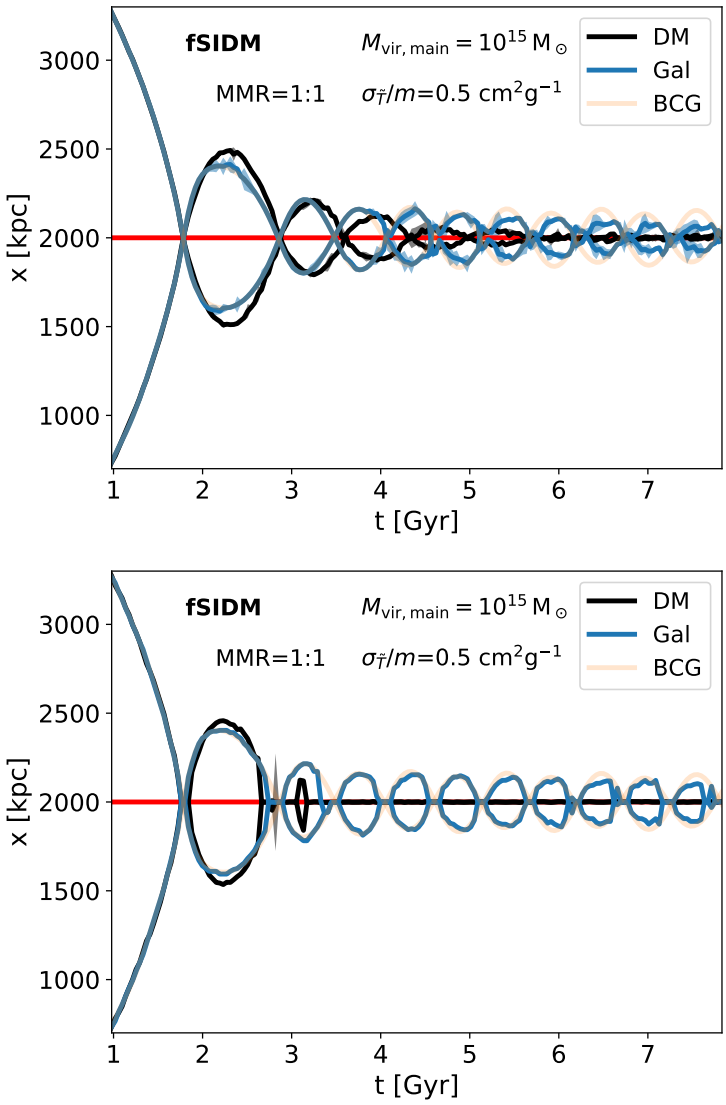

Figure 4.4.9: The peak positions for an equal-mass merger are shown as a function of time. For the upper panel, the gravitational potential-based peak finder was employed and for the lower one, the one based on isodensity contours. DM peaks are indicated in black, galaxy peaks in blue, and the position of BCG particles in orange. The red lines indicate the centre of mass of the system.

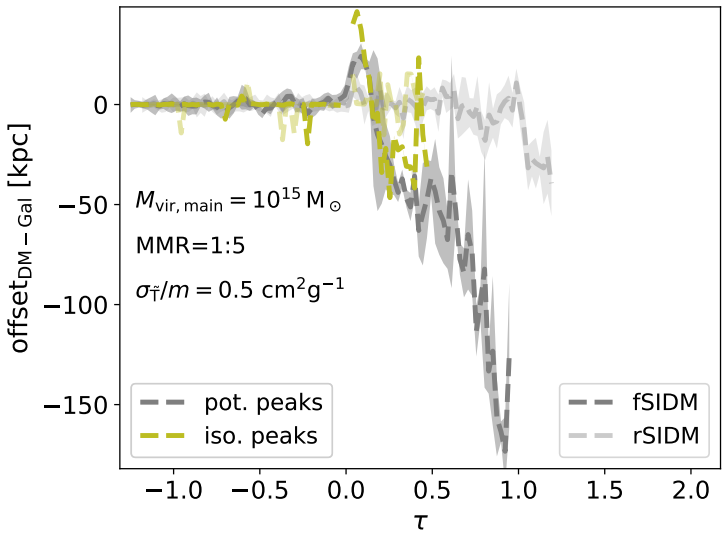

Figure 4.4.10: The DM-galaxy offset is shown as a function of time for an unequal mass merger with an MMR of 1:5 of our cluster-scale mergers. The simulation was evolved with a cross-section of $\sigma_{\tilde{T}}/m = 0.5\,\mathrm{cm}^2\,\mathrm{g}^{-1}$. We display the offset based on the potential-based peak finder as well as the isodensity contour-based peak finder. The shaded areas indicate the error.

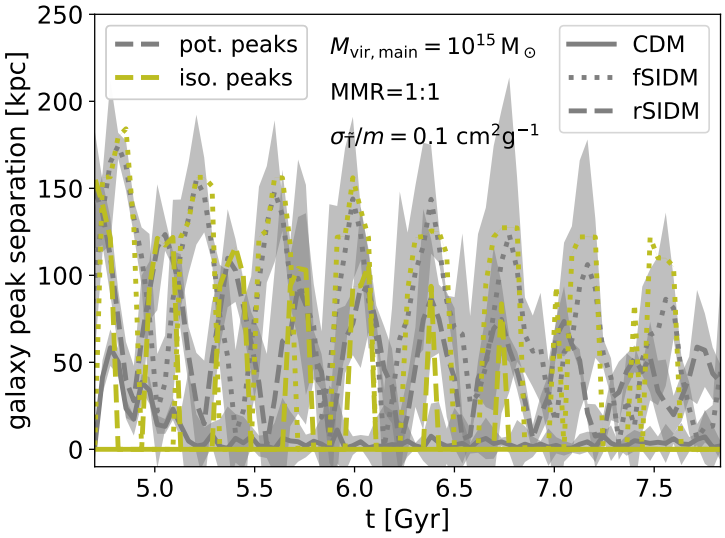

Figure 4.4.11: The separation between the peaks of the galactic component is shown as a function of time for an equal-mass cluster-scale merger at late merger stages. The DM component coalesced, but separate peaks for the galaxies can be identified using the potential-based or isodensity contour-based peak finding. The displayed merger was evolved with the lowest cross-section we present in this paper, $\sigma_{\tilde{T}}/m = 0.1\,\mathrm{cm}^2\,\mathrm{g}^{-1}$. The shaded areas indicate the error.

part of the haloes and the peaks identified in the potential-based method heavily depend on this region, whereas the isodensity contour peaks are due to projection more sensitive to matter in the outer regions of the haloes.

For comparison, the offsets for the two peak finding methods are shown for a 1:5 cluster-scale merger in Fig.4.4.10. The isodensity contour-based offsets are noisier than the potential-based ones, but overall they follow the same trend. Interestingly, also the measured offsets direct after the first pericentre passage appear to be larger in this case. For the isodensity contour peaks, all particles are considered, thus the main halo can influence the position of the subhalo. If the density gradient in the DM component of the subhalo is lower than the one of the galactic component, the DM peak could be more affected by the main halo. Potentially, this could lead to a larger offset measurement. In contrast to the potential-based offset measurements, the isodensity contour-based ones are not much larger about the first apocentre passage (negative sign) compared to the ones subsequent to the first pericentre passage (positive sign), but they last for a longer time and, as such, could be easier to observe. But the isodensity method does not provide reasonable offsets at times as late as for the potential-based peaks. However, for comparison with observations, an observationally motivated peak finding strategy should be employed (Robertson et al., 2017a).

Let us point out that very late merger stages at which the DM haloes already coalesced could nevertheless be of interest from an observational point of view. This is because the presence of self-interactions may lead to distinguishable galactic/stellar components. In Fig. 4.4.11, we show this late stage for an equal-mass merger because for that MMR the peak finding works best. The separation between the galaxy peaks for the cluster-scale merger evolved with $\sigma_{\tilde{\mathrm{T}}}/m = 0.1\,\mathrm{cm}^2\,\mathrm{g}^{-1}$ is shown. For comparison, we also display the separation for the corresponding CDM merger. Here, the separation vanishes quickly. But if self-interactions are present, even if they are rather small, large separations are found with both methods. For fSIDM, the distance between the galaxy peaks tends to be larger than for rSIDM if the same momentum transfer cross-sections are compared. In Section 4.4.2, we mentioned that a lower density due to self-interactions reduces dynamical friction and thus can lead to core sloshing as previously studied by Kim et al. (2017). However, it remains to be seen whether this persists in more realistic simulations including the ICM.

4.4.6 Phase–space

Finally, we study the phase–space distribution of our 1:10 cluster-scale merger using the same simulation as for the morphology. For the phase–space distribution, we do not only consider particles of the subhalo but also from the main halo. In Fig. 4.4.12, we show the distance to the centre of mass as a function of the radial velocity (with respect to the centre of mass) for $\tau = 0.56$. These quantities are all computed in 3 d. We display results for CDM and for rare and frequent self-interactions with a cross-section of $\sigma_{\tilde{\mathrm{T}}}/m = 0.5\,\mathrm{cm}^2\,\mathrm{g}^{-1}$. On the left-hand side, we display the DM and on the right-hand side, the smoothed galactic

component is shown.

A clear difference between the distributions for the DM models is visible, especially when focusing on the clump of particles at $r \sim 1500\,\mathrm{kpc}$. These particles primarily belong to the subhalo and disperse over time depending on the DM physics. If DM self-interactions are present, the gravitational potential is shallower, which also leads to a faster dispersal of the galactic component. As we can see in Fig. 4.4.12, the subhalo clump is strongest for CDM, less strong for rSIDM and the weakest for fSIDM for both DM and galaxies.

4.5 Discussion

In this section, we first discuss aspects relating to the peak finding and the analysis of our simulation. Then, we elaborate on the limitations of our model and the physical implications of our results.

4.5.1 Technical aspects

We compared two peak finding methods, whose results differ significantly. The one based on the gravitational potential is more robust but less useful when it comes to a potential comparison with observational data, whereas the one based on isodensity contours may be more readily applied to observations.

The isodensity contour method suffers from projection effects and difficulties in the peak identification for small peak separations. As a result, we found smaller offsets (about half the size for an equal-mass merger) with the isodensity contour method at the first apocentre passage. However, it is possible that the isodensity contour method provides larger offsets close to the pericentre passages as the measured subhalo peak position is affected by the main halo. Moreover, we failed to identify distinct peaks at an earlier stage of the merging process than with the gravitational potential based method. Furthermore, we only investigated projections of the particle distribution perpendicular to the merger axis, whereas in observations, the line of sight and merger axis need not be perpendicular to one another.

However, in real observations, further difficulties arise. Especially for galaxy clusters, the number of observed galaxies ($\sim$ 100–1000) is much less than the number of particles ($\sim 9 \times 10^5$–10^7) we used for our smoothed galactic cluster component. Nevertheless, this problem could be allayed by using the BCGs to measure offsets.

We find that observations at a later stage of the merger, rather than around the time of the first pericentre passage, might be more interesting because offsets typically become larger with time. However, the largest offsets might be difficult to observe as the subhalo dissolves rather quickly. Nevertheless, a late merger phase when the DM haloes coalesce and form a single DM peak may still provide evidence for DM self-interactions as in general two separate galactic or stellar components will be present. For equal-mass mergers, Kim et al. (2017) found at these later merger stages that BCGs and galaxies oscillated around

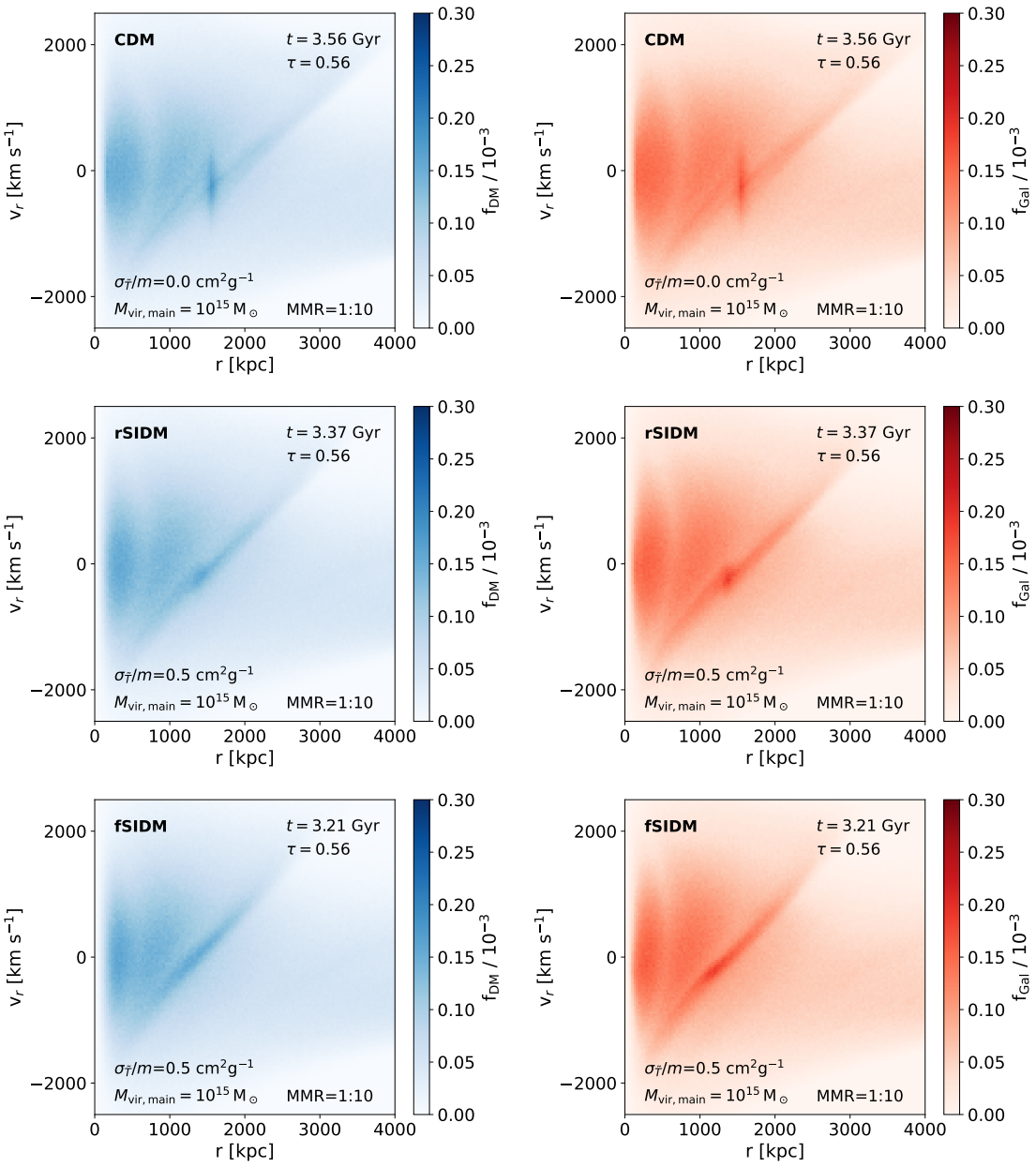

Figure 4.4.12: The phase–space distribution of a 1:10 merger evolved with different DM models is shown at $\tau = 0.56$, i.e. close to the first apocentre passage. The left-hand side column displays the DM distribution and on the right-hand side, the smoothed galactic component is shown. The top row gives the phase–space distribution for CDM and below SIDM is shown with a cross-section of $\sigma_{\tilde{\Gamma}}/m = 0.5\,\mathrm{cm}^2\,\mathrm{g}^{-1}$ for the case of isotropic scattering (middle row) and small-angle scattering (bottom row).

the centre of mass. We make a similar observation in our simulations and find that this also persists for unequal mass mergers. Interestingly, the galactic peak separations are found to be generally large even for rather small cross-sections and can also be seen employing the more observationally motivated peak finding method. Hence, these types of observations could be a promising way to provide evidence for DM self-interactions.

Distinguishing between different DM models through the morphologies of the galaxies within merging galaxy clusters may prove difficult owing to the small number of collisionless tracers (galaxies) on these scales. However, on galaxy scales, stars may provide enough tracers to better estimate the locations and shapes of the collisonless components. In addition, galaxies might also offer a chance to distinguish stellar components according to their origin using stellar population properties such as metallicity. Nevertheless, resolution limits of astronomical observations might pose a challenge for such an approach.

4.5.2 Physical considerations

The focus of this paper lies on understanding the different phenomenologies of rare and frequent self-interactions and not a comparison to observational data. Hence, the dependence of our results on the initial conditions is less of a concern. For example, we find larger offsets than in Fischer et al. (2021a), despite the haloes starting with the same virial masses. This is because they start with higher concentration parameters, which for the present study lead to higher central densities and thus larger offsets. Aside from quantitative differences, some results may change qualitatively as physical processes shaping the evolution of merging systems act on different time-scales. For instance, the merger time-scale differs from the time-scale on which self-interactions isotropize the DM velocity distribution. In particular, this could complicate the evolution of the halo shapes. Consequently, it would be informative to extract merging systems from cosmological simulations to obtain more realistic results that can be directly compared with observations. In addition to the study of individual systems, this would also allow us to estimate how frequently offsets of observable size would occur for various SIDM models. In the literature, observations of fairly large offsets have been claimed but there is also reasonable doubt about them (for references see sec. 4.1). However, in the light of large offsets, fSIDM models are particularly interesting as they can explain larger offsets than rSIDM.

We found minor mergers to be interesting in terms of distinguishing rare and frequent self-interactions. In contrast to equal-mass mergers, they have the advantage of being more abundant in the Universe and thus allow for better statistics than studies based on individual systems. For fSIDM, the subhalo dissolves faster than for rSIDM, but this statement depends on the matching of the cross-section. In terms of $\sigma_{\tilde{\Gamma}}$, the constraints for rare and frequent self-interactions would differ from each other. Together with alternative constraints, there could be a chance to distinguish between rSIDM and fSIDM. However, to derive constraints on the self-interactions with observations would require a stringent observational motivated analysis of the simulations and a more realistic setup as we explain

next. Thus, we do not try to derive any constraints on the differential cross-section.

Here, we studied an idealized setup that neglects various physical aspects. Perhaps, most importantly, we did not include the baryonic matter, i.e. the ICM, which contains a significant fraction ($\sim 10\%$) of the cluster mass. The ICM is likely to change the evolution of a merger as it behaves collisionally (Zhang et al., 2016) and is affected by processes such as star formation and feedback. Moreover, our haloes are totally smooth and do not contain any substructure. The modelling of the BCGs is also very idealized as they are approximated as collisionless point masses with unrealistically low masses. Finally, we treated the galaxies in our cluster simulations as collisionless particles, which neglects the fact that they also have a large DM component (Kummer et al., 2018). More realistic modelling of the BCGs and the ICM could lead to different results, in particular, the pattern of oscillations of the BCGs and the core sloshing of the galaxies could change. It is largely unknown how the evolution of a merger subject to self-interactions would change if one improves on the aspects mentioned above. Hence, we do not want to speculate about this but leave it for future studies.

In the present work, we only modelled a constant cross-section and did not consider SIDM with a velocity-dependent cross-section. A velocity-dependence is natural from a particle physics perspective, especially for light mediator models, which interact frequently (e.g. Buckley & Fox, 2010; Loeb & Weiner, 2011; Bringmann et al., 2017). In future work, it would be interesting to also investigate models with a velocity dependence, particularly as such models appear to be in better agreement with astrophysical observations than constant cross-sections (e.g. Kaplinghat et al., 2016; Correa, 2021; Gilman et al., 2021; Sagunski et al., 2021).

4.6 Summary and Conclusions

In this paper, we have studied idealized equal and unequal-mass mergers undergoing head-on collisions, focusing on the effects arising from DM self-interactions. In particular, we have investigated galaxy cluster and galaxy mergers and compared simulations with collisionless, rare and frequent self-interacting DM. In each simulation, we determined the peaks of the different components (DM, galaxies, and a central massive object) for each of our two merging haloes, and measured the offsets between different components as well as the shapes of the different components. Moreover, we studied the morphology and phase–space distribution of the mergers and compared two peak finding methods. Our main results from this suite of simulations are as follows:

- The morphology of the collisionless particles, i.e. galaxies/stars shows significant differences between rSIDM and fSIDM, especially at a later merger phase and in unequal-mass mergers. It is strongly affected by the faster dissolving fSIDM subhalo.

- Minor mergers with SIDM can produce large offsets between galactic/stellar and DM

peaks. Before the second pericentre passage, we found large offsets only for frequent self-interactions.

- In general, frequent self-interactions tend to produce larger offsets than rare self-interactions if the same momentum transfer cross-sections are compared. This is even more extreme in unequal-mass mergers.

- Separate galactic/stellar components with a coalesced DM component could provide evidence for DM self-interactions. Core sloshing seems to be most interesting in the case of equal-mass mergers, which has been studied by Kim et al. (2017).

- For SIDM, the shapes of DM and the galactic/stellar component can differ significantly from collisionless DM. In unequal-mass mergers, self-interactions can lead to more elliptical distributions between the first apocentre and second pericentre passage.

- We find the merger phase between $\tau \approx 0.25$ (halfway to the first apocentre) and $\tau \approx 1.0$ (second pericentre) to be more interesting in terms of studying effects from self-interactions than the phase near and shortly after the first pericentre passage ($\tau \approx 0.0$). This seems to be true for observations as well, as suggested by our results concerning isodensity peaks. In general, a late phase of a merging system should be more interesting as the non-linear evolution of the system can amplify differences between DM models.

- Peak finding is a major challenge in studying effects of SIDM and distinguishing rare and frequent self-interactions. In observations, it might prohibit detecting the very large offsets at late merger stages. The positions obtained by various methods can differ a lot with respect to one another, which makes it important to analyse observations and simulations in a similar manner.

In this paper, we performed a parameter study on idealized mergers in order to understand the dominant physical effects and to develop an intuition about the best indicators of DM interaction properties. A detailed comparison with observations will require more realistic simulations that include baryonic matter as well as more realistic substructure in the haloes. This is the subject of forthcoming work.

Acknowledgements

We thank Felix Kahlhoefer for useful comments and suggestions. This work is funded by the Deutsche Forschungsgemeinschaft (DFG, German Research Foundation) under Germany's Excellence Strategy – EXC 2121 "Quantum Universe" – 390833306, Germany's Excellence Strategy – EXC-2094 "Origins" – 390783311, and the Emmy Noether Grant No. KA 4662/1-1. AR is supported by the European Research Council's Horizon 2020 project 'EWC' (award AMD-776247- 6). Preprint number: DESY-21-116

Software: numpy (Harris et al., 2020), matplotlib (Hunter, 2007), scipy (Virtanen et al., 2020)

Appendices

4.A Relabelling particles for rSIDM

For rare self-interactions, large scattering angles are common. When two particles (one from each merging halo) scatter, a scattering angle larger than 90° could be interpreted as an exchange of particles. If so, it would make sense to switch the labels of the corresponding particles. We implemented this by limiting the maximum scattering angle to 90°. In Fig. 4.A.1, we show the density of the subhalo of a 1:10 merger for both rSIDM versions at about the first apocentre passage. In the upper panel with and in the lower one without relabelling. One can see that this affects the formation of a second peak at the position of the main halo.

The relabelling procedure suppresses the second peak which in consequence leads to less elliptical haloes. However, how much the shape is affected depends on the particles which are considered in the inertia tensor calculation. If only the matter within twice the scale radius of the initial NFW profile is taken into account, the effects from the relabelling procedure are negligible, but if all particles are considered, it can make a significant difference.

4.B Morphology

In Fig. 4.B.1, we show the same plots as in Fig. 4.4.2 but this time including the main halo. Due to the density contribution of the main halo which has 10 times the mass of the subhalo, it becomes more difficult to identify morphological features. Nevertheless, differences between the DM models are clearly visible.

4.C Peak position, Offset, and Shape

In this appendix, we provide further plots of the merger simulations with the highest cross-section we modelled. In Fig. 4.C.1 - 4.C.6, we show the potential based peak position together with the offset (Eq. (4.4)) and the halo shape (Eq. (4.6)).

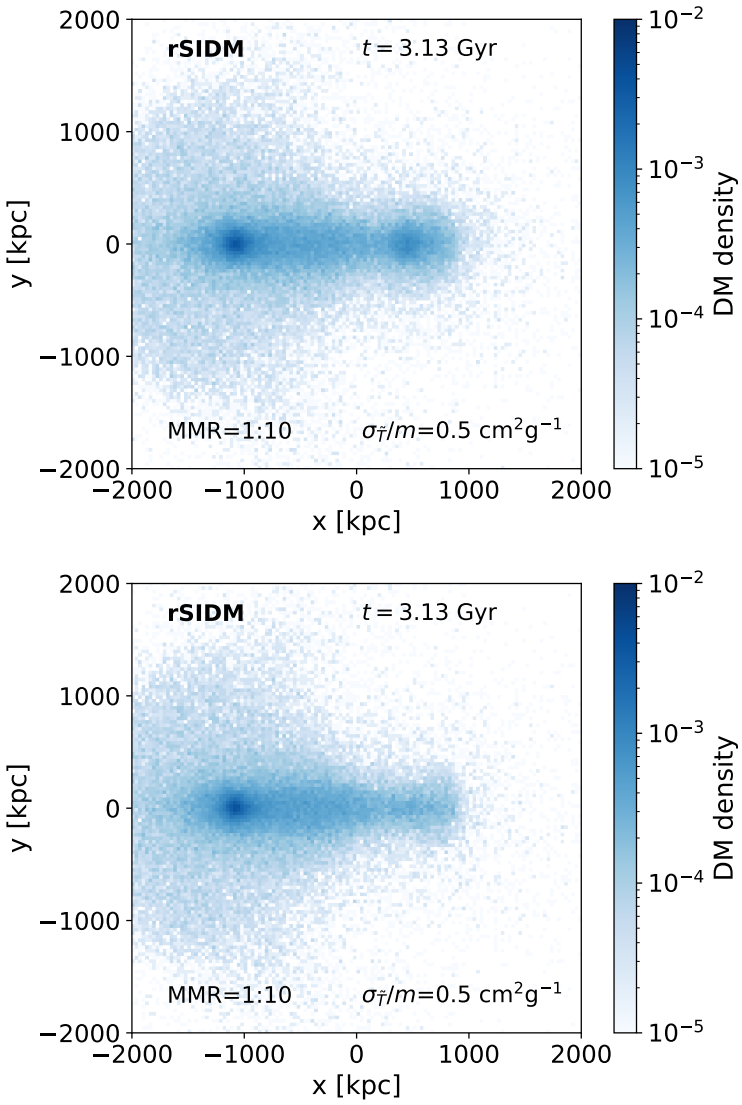

Figure 4.A.1: The physical density of the subhalo of a merging system in the plane of the merger is shown at about the first apocentre passage. The system is a 1:10 merger simulated with rare self-interactions ($\sigma_{\tilde{T}}/m = 0.5\,\mathrm{cm}^2\,\mathrm{g}^{-1}$). The simulation of the upper panel allowed for scattering angles larger than 90°, whereas the lower panel does not.

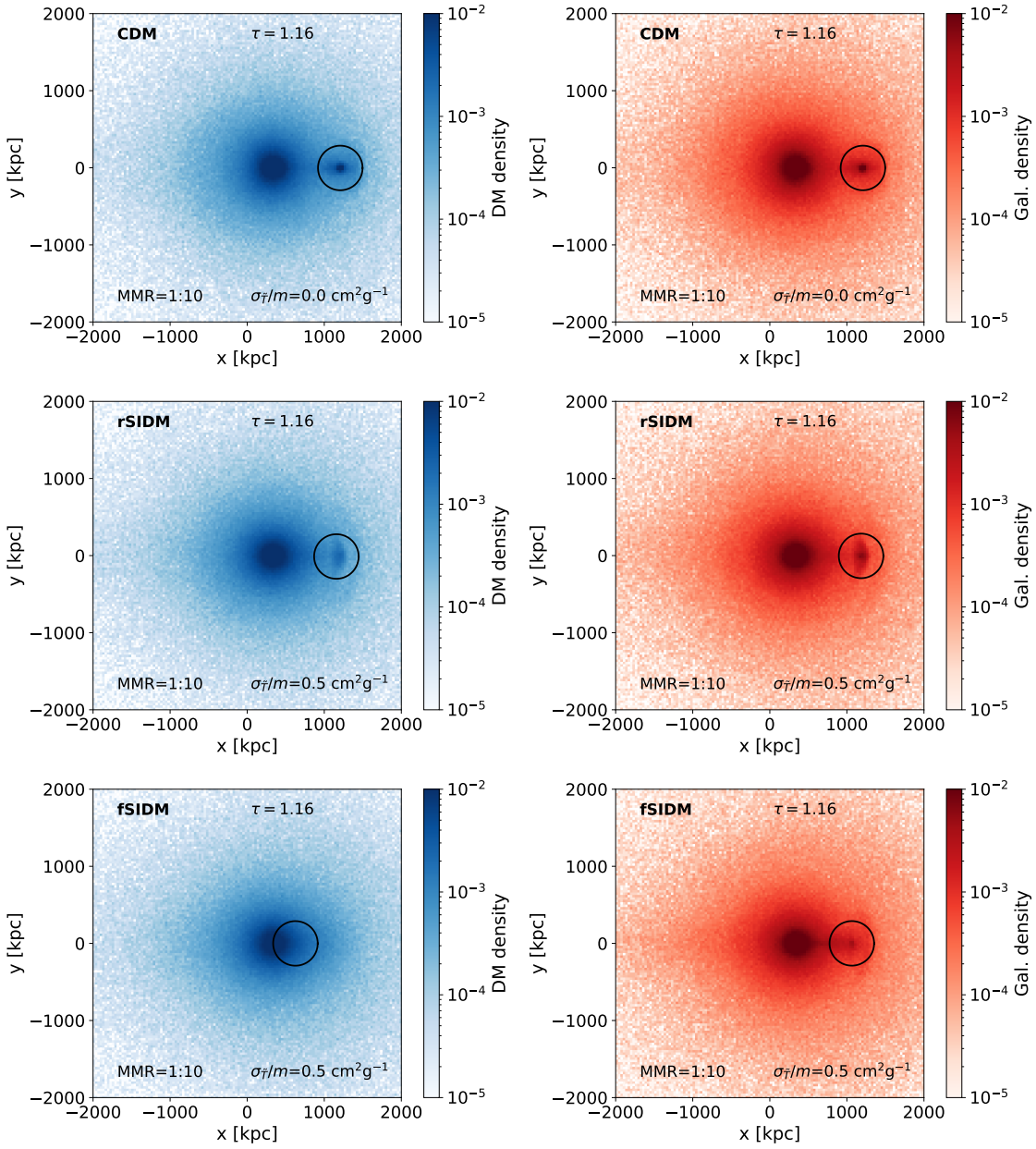

Figure 4.B.1: The same as in Fig. 4.4.2, but considering both haloes. In the supplementary material, we provide the time evolution as a video.

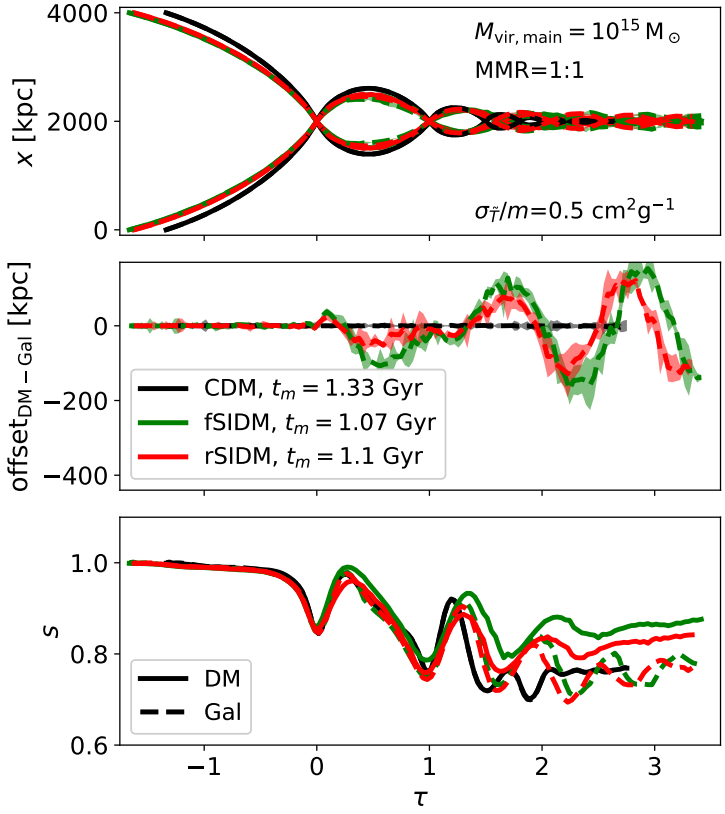

Figure 4.C.1: Peak position along the merger axis (top panel), the DM-galaxy offset (middle panel), and the shape (bottom panel) for an equal mass merger as a function of time. Results for CDM are shown in black, for rSIDM in red, and for fSIDM in green. The SIDM runs were conducted with a cross-section of $\sigma_{\tilde{\mathrm{T}}}/m = 0.5\,\mathrm{cm}^2\,\mathrm{g}^{-1}$. Offsets and shapes are shown only for the subhalo. The DM component is indicated by a solid line and the galaxies by a dashed line.

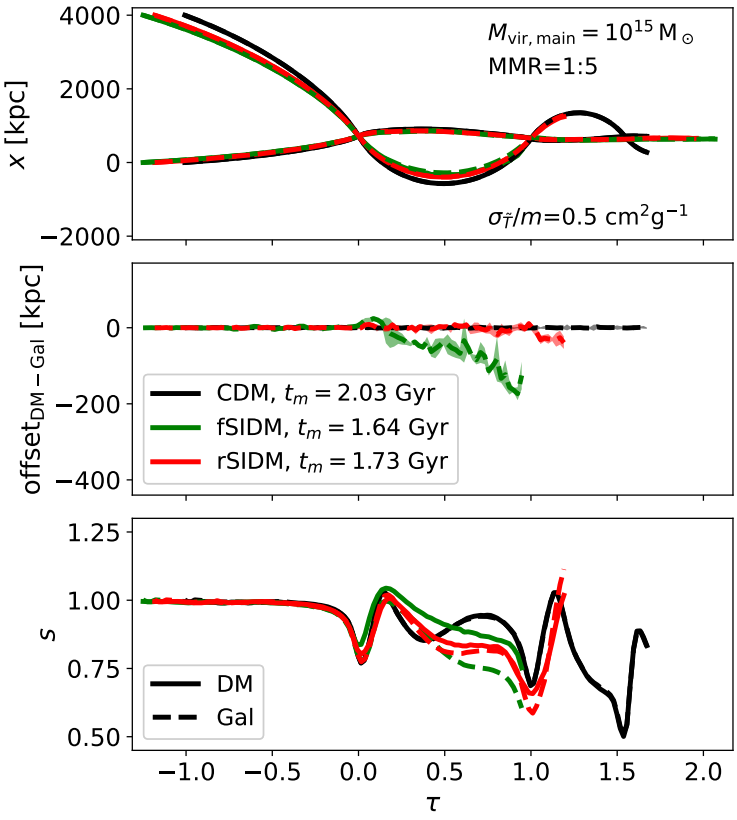

Figure 4.C.2: The same as in Fig. 4.C.1, but for an MMR of 1:5.

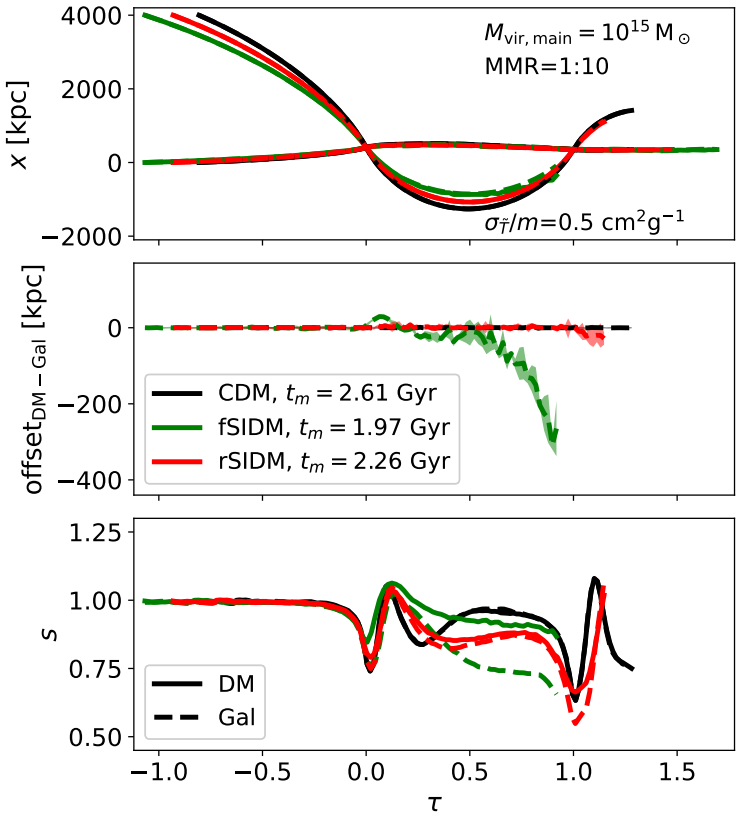

Figure 4.C.3: The same as in Fig. 4.C.1, but for an MMR of 1:10.

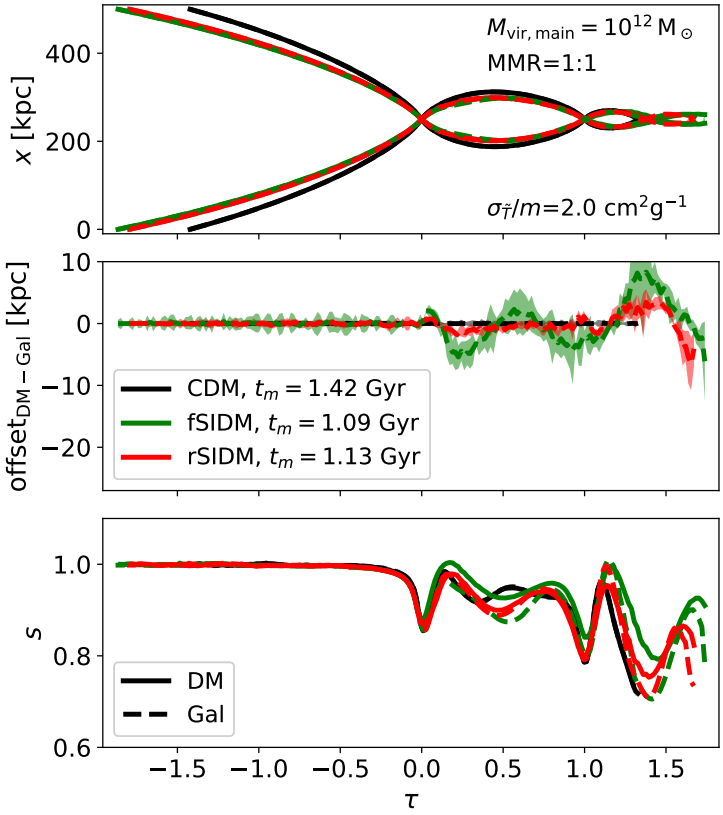

Figure 4.C.4: The same as in Fig. 4.C.1, but for the galaxy-scale runs and with a momentum transfer cross-section of $\sigma_{\tilde{\mathrm{T}}}/m = 2.0\,\mathrm{cm}^2\,\mathrm{g}^{-1}$.

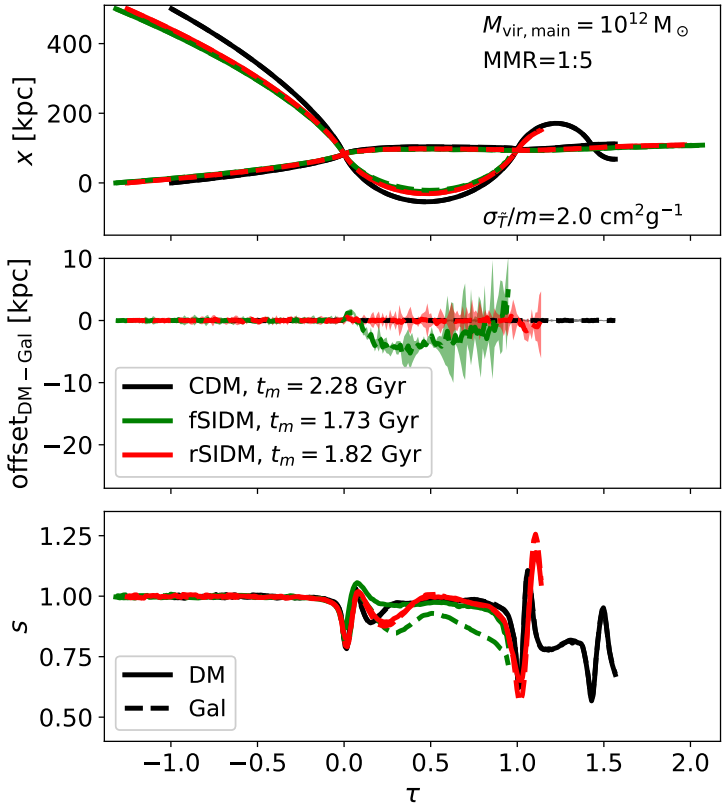

Figure 4.C.5: The same as in Fig. 4.C.4, but for an MMR of 1:5.

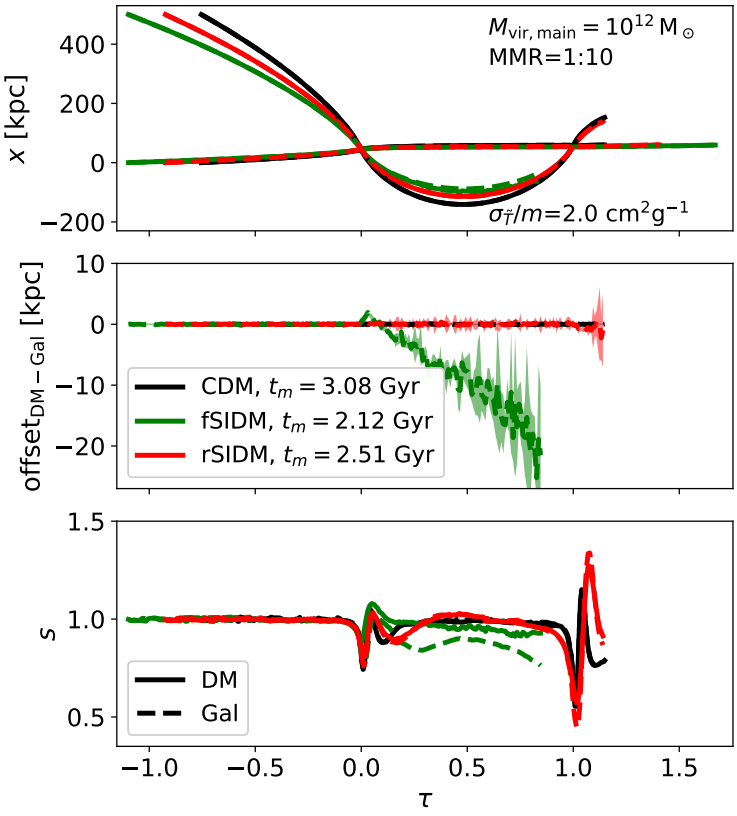

Figure 4.C.6: The same as in Fig. 4.C.4, but for an MMR of 1:10.

5 Cosmological simulations with rare and frequent dark matter self-interactions

This chapter presents work as submitted to Mon. Not. Roy. Astron. Soc. and uploaded to arXiv (Fischer et al., 2022).

Abstract Dark matter (DM) with self-interactions is a promising solution for the small-scale problems of the standard cosmological model. Here we perform the first cosmological simulation of *frequent* DM self-interactions, corresponding to small-angle DM scatterings. The focus of our analysis lies in finding and understanding differences to the traditionally assumed *rare* DM (large-angle) self scatterings. For this purpose, we compute the distribution of DM densities, the matter power spectrum, the two-point correlation function and the halo and subhalo mass functions. Furthermore, we investigate the density profiles of the DM haloes and their shapes. We find that overall large-angle and small-angle scatterings behave fairly similarly with a few exceptions. In particular, the number of satellites is considerably suppressed for frequent compared to rare self-interactions with the same cross-section. Overall we observe that while differences between the two cases may be difficult to establish using a single measure, the degeneracy may be broken through a combination of multiple ones. For instance, the combination of satellite counts with halo density or shape profiles could allow discriminating between rare and frequent self-interactions. As a by-product of our analysis, we provide – for the first time – upper limits on the cross-section for frequent self-interactions.

5.1 Introduction

Although many efforts have been made to uncover the nature of DM, it remains largely unknown even after several decades of research. To narrow down the large number of models that contain potential DM candidates, a huge variety of experiments, based on direct and indirect detection, are being carried out. Moreover, forthcoming astronomical surveys with upcoming telescopes such as Euclid[1] (Euclid Collaboration et al., 2020), Rubin Observatory[2] (Zhan & Tyson, 2018) and Roman[3] (Spergel et al., 2015) promise to tighten constraints on cosmological models and to discriminate between models of DM

[1] Euclid: https://www.euclid-ec.org/
[2] Rubin Observatory: https://www.lsst.org/
[3] Nancy Grace Roman Space Telescope: https://www.jpl.nasa.gov/missions/the-nancy-grace-roman-space-telescope

beyond the cold collisionless DM of the standard ΛCDM model. Among those are warm DM (Dodelson & Widrow, 1994) and fuzzy DM (Hu et al., 2000).

In this paper, we focus on a particular class of DM models called self-interacting DM (SIDM). It was first proposed by Spergel & Steinhardt (2000) in order to resolve tensions between cosmological N-body simulations and observations. These tensions are known as the small-scale crisis of ΛCDM, for a review see Bullock & Boylan-Kolchin (2017). SIDM has been studied in a number of papers and seems to be promising to solve or at least mitigate several small-scale issues. For a review on DM with self-interactions see Tulin & Yu (2018). In the limit of a vanishing cross-section, SIDM becomes identical to the collisionless DM of ΛCDM. But given a large enough cross-section, it alters the DM distribution on small scales and may resolve issues such as the core-cusp problem. Self-interactions can transfer heat into the centres of DM haloes and thus create density cores, in contrast to the cusps of collisionless cold dark matter (CDM). This has been shown, for example, in Davé et al. (2001). Moreover, SIDM can create diverse rotation curves (Creasey et al., 2017; Kamada et al., 2017; Robertson et al., 2018) and may be able to solve the too-big-to-fail problem (Zavala et al., 2013; Elbert et al., 2015; Kaplinghat et al., 2019).

There exist a number of SIDM models with a set of free parameters, such as the total cross-section, the angular and velocity dependence and the nature of the scattering (elastic or inelastic). Most studies have assumed models that are isotropic, elastic and velocity-independent. Burkert (2000) performed the first simulations with a Monte-Carlo scheme where the numerical particles were treated analogously to physical DM particles. Since then many variants of SIDM have been studied, such as inelastic scattering (e.g. Essig et al., 2019; Huo et al., 2020; Shen et al., 2021) including multistate scattering Schutz & Slatyer (2015); Vogelsberger et al. (2019); Chua et al. (2020) or even multi-component DM (Todoroki & Medvedev, 2018; Vogelsberger et al., 2019). Also anisotropic cross-sections have been investigated (Robertson et al., 2017b; Banerjee et al., 2020; Nadler et al., 2020).

However, if the self-interaction cross-section is strongly anisotropic, particles scatter by tiny angles. This implies a much lower momentum and energy transfer per scattering event compared to an isotropic cross-section. Hence, small-angle scattering must be more frequent to have a similar effect on the DM distribution. Models having different angular dependencies might be compared by using the momentum-transfer cross-section. By frequent self-interactions (fSIDM), we refer to a limit where the scattering angles become infinitesimal small while the momentum transfer cross-section stays constant. In contrast, we refer to rare self-interactions (rSIDM) for less anisotropic differential cross-sections.

Frequent self-interactions have gained popularity in the context of galaxy cluster mergers because they can explain larger DM–galaxy offsets than rSIDM (Kahlhoefer et al., 2014; Fischer et al., 2021a,b). However, numerical schemes that treat numerical particles like physical ones are not capable of simulating fSIDM. Only recently, a general solution to this problem has been found. Fischer et al. (2021a) developed a new scheme that allows to model frequent scattering within N-body simulations.

However, previous fSIDM studies (Kahlhoefer et al., 2014, 2015; Kummer et al., 2018, 2019; Fischer et al., 2021a,b) only considered idealised cases that never took the full cosmological context into account. In contrast, for rSIDM there are a number of recently published simulations of cosmological boxes (Rocha et al., 2013; Peter et al., 2013; Vogelsberger et al., 2016; Robertson et al., 2019; Banerjee et al., 2020; Robertson et al., 2020; Stafford et al., 2020; Harvey et al., 2021; Stafford et al., 2021; Ebisu et al., 2022) or using zoom-in simulations (Vogelsberger et al., 2012; Zavala et al., 2013; Vogelsberger et al., 2014; Fry et al., 2015; Vogelsberger et al., 2016; Robertson et al., 2018; Despali et al., 2019; Robles et al., 2019; Vogelsberger et al., 2019; Zavala et al., 2019; Nadler et al., 2020; Vega-Ferrero et al., 2020; Bondarenko et al., 2021; Sameie et al., 2021; Shen et al., 2021; Bhattacharyya et al., 2022; Shen et al., 2022; Silverman et al., 2022; Sirks et al., 2022). These simulations have been used to study the phenomenology of SIDM models on various mass scales, such as dwarf galaxies, MW-like galaxies and galaxy clusters. Several properties of the DM haloes such as their density profile and their shape have been measured and predictions for observations, such as gravitational lensing, have been made. This enabled constraints to be put on the total cross-section of rSIDM models, while fSIDM models have remained poorly constrained. In this study, we investigate fSIDM, for the first time using a cosmological simulation.

This paper aims to study the effects of SIDM on large scales to understand the differences between fSIDM and isotropic rSIDM. In this first effort, we assume the self-interactions to be velocity-independent and elastic. We conduct DM-only cosmological N-body simulations using a full box as well as zoom-in simulations and study various properties of the DM distribution.

In Section 5.2 we briefly describe our numerical methods and present the setup for our cosmological simulations. The results are presented in Section 5.3. For example, we show the matter power spectrum, the halo mass function as well as density and shape profiles of DM haloes. A discussion of our results, their limitations, implications and further perspectives follows in Section 5.4. Finally, we summarise and conclude in Section 5.5. Additional details and plots are provided in the appendices.

5.2 Numerical Setup

In this section, we describe the numerical setup for this study. We give details of the code and algorithms that we have used as well as our simulations and their initial conditions.

In this paper, we used the cosmological N-body code GADGET-3, the predecessor GADGET-2 is described in Springel (2005). The implementation of rare and frequent self-interactions has previously been described in Fischer et al. (2021a,b). Additionally, we implemented the comoving integration for the SIDM module to perform cosmological simulations. A test problem that demonstrates that the comoving integration is working as expected can be found in Appendix 5.A. To match rare and frequent self-interactions we use the momentum

transfer cross-section,[4]

$$\sigma_{\tilde{\mathrm{T}}} = 4\pi \int_0^1 \frac{\mathrm{d}\sigma}{\mathrm{d}\Omega_{\mathrm{cms}}} (1 - \cos\theta_{\mathrm{cms}}) \mathrm{d}\cos\theta_{\mathrm{cms}} \,. \tag{5.1}$$

We simulated a full cosmological box and and also performed zoom-in simulations. All simulations are DM only and the self-interactions are always velocity-independent and elastic. In the case of rSIDM the differential cross-section is isotropic while fSIDM corresponds to a very anisotropic cross-section.

The size of the self-interaction kernel for each particle is set by the distance to the 64th nearest neighbour. Finally, we employ the following cosmological parameters: $\Omega_{\mathrm{M}} = 0.272$, $\Omega_\Lambda = 0.728$, $h = 0.704$, $n_s = 0.963$ and $\sigma_8 = 0.809$ (WMAP7, Komatsu et al., 2011).

To generate the initial conditions for the full box we use N-GenIC (Springel, 2015). The initial conditions are similar to box4 of the Magenticum simulations[5] with a comoving side length of $48\,\mathrm{Mpc}\,h^{-1}$. We run simulations with different resolutions and refer to those using the naming convention of Magenticum (hr and uhr). Our highest resolution run (uhr) contains $\sim 1.9 \times 10^8$ simulation particles. More details on the full cosmological box are given in Tab. 5.2.1. Moreover, we performed cosmological zoom-in simulations with different resolutions of the same region. The region is selected from a large box with a comoving side length of $1\,\mathrm{Gpc}\,h^{-1}$. Several publications (e.g. Planelles et al., 2013; Rasia et al., 2015) have used this box for zoom-in initial conditions and it was first described in Bonafede et al. (2011). In our zoom-in region, the most massive halo has a virial mass of $\sim 8.8 \times 10^{11}\,\mathrm{M}_\odot\,h^{-1}$. Further details can be found in Tab. 5.2.2. In addition, we provide in Appendix 5.B a convergence test of the density profile of the most massive halo.

For the analysis, we identify DM haloes using the friends-of-friends algorithm[6] implemented along with GADGET-3. The built-in module SUBFIND also identifies substructure within the haloes (Springel et al., 2001; Dolag et al., 2009). We use halo and subhalo positions, masses and radii as provided by SUBFIND. The virial radius, r_{vir}, and the virial mass, M_{vir}, are measured with the spherical-overdensity approach based on the over-density predicted by the generalised spherical top-hat collapse model (e.g. Eke et al., 1996). Here, r_{vir} is defined as the radius at which the mean density becomes larger than the one of the top-hat collapse model and M_{vir} is the mass inside r_{vir}. Every halo contains at least one subhalo, which is the primary subhalo located at the same position as the halo (determined by the location of most gravitationally bound particle). The primary subhalo typically contains most of the particles that belong to the halo.

[4] We implicitly assume identical particles, in this case, the definition is equivalent to the one recommended by Robertson et al. (2017b) and Kahlhoefer et al. (2017).

[5] Magneticum: `http://www.magneticum.org`

[6] A description of the friends-of-friends algorithm can, for example, be found in More et al. (2011).

name	l_{box} $[\mathrm{cMpc}\,h^{-1}]$	N_{DM}	m_{DM} $[\mathrm{M}_\odot\,h^{-1}]$	$\sigma_{\tilde{\mathrm{T}}}/m_\chi$ $[\mathrm{cm}^2\,\mathrm{g}^{-1}]$
hr	48	216^3	8.28×10^8	0.0, 0.1, 1.0
uhr	48	576^3	4.37×10^7	0.0, 0.1, 1.0

Table 5.2.1: Properties of the full cosmological box simulations. In detail we provide the name, the side length of the comoving box (l_{box}), the number of numerical DM particles (N_{DM}) and the mass of the numerical DM particles (m_{DM}) as well as the momentum transfer cross-section per physical DM particle mass ($\sigma_{\tilde{\mathrm{T}}}/m_\chi$). The non-zero cross-sections have been simulated using fSIDM and isotropic rSIDM. All simulations share the same initial conditions but with a different resolution.

name	$N_{\mathrm{high\,res}}$	m_{DM} $[\mathrm{M}_\odot\,h^{-1}]$	$\sigma_{\tilde{\mathrm{T}}}/m_\chi$ $[\mathrm{cm}^2\,\mathrm{g}^{-1}]$
1x	$\sim 4.51 \times 10^4$	8.3×10^8	0.0, 1.0
10x	$\sim 4.52 \times 10^5$	8.3×10^7	0.0, 1.0
25x	$\sim 1.13 \times 10^6$	3.3×10^7	0.0, 1.0
250x	$\sim 1.13 \times 10^7$	3.3×10^6	0.0, 1.0
2500x	$\sim 1.13 \times 10^8$	3.3×10^5	0.0, 1.0

Table 5.2.2: Properties of the zoom-in simulations. We provide the name of the simulation, the number of particles in the highly resolved region ($N_{\mathrm{high\,res}}$), the mass of the high resolution particles (m_{DM}) and the cross-sections we simulated ($\sigma_{\tilde{\mathrm{T}}}/m_\chi$). The non-zero cross-section has been simulated using fSIDM and isotropic rSIDM. All simulations share the same initial conditions but with a different resolution.

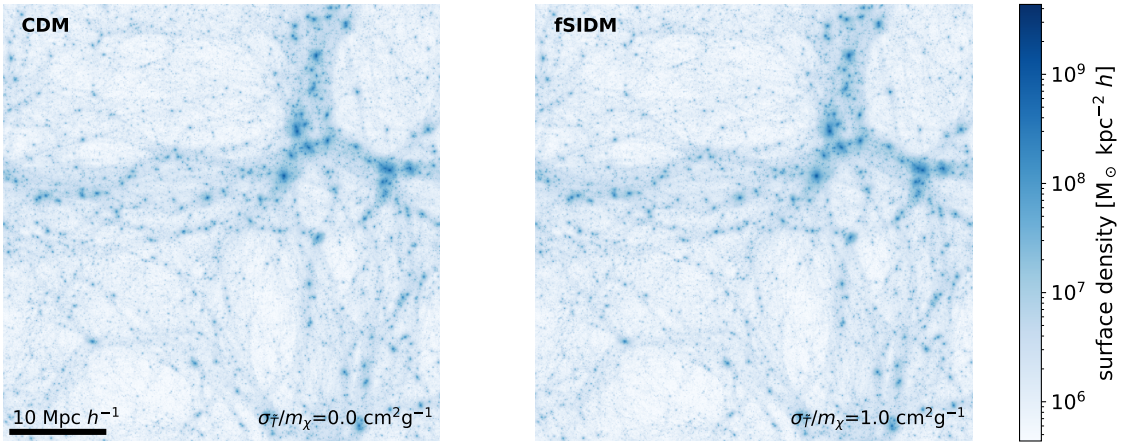

Figure 5.3.1: Surface density of the full cosmological box (uhr) at a redshift of $z = 0$. The panel on the left-hand side shows results from the CDM simulation and the one on the right-hand side displays the fSIDM simulation with $\sigma_{\tilde{T}}/m_\chi = 1.0\,\mathrm{cm}^2\,\mathrm{g}^{-1}$.

5.3 Results

In this section, we present the results of our simulations and compare the effects of DM models. To this end we study several statistical properties such as the matter power spectrum, the probability density function (PDF) of the DM densities, the two-point correlation function and the halo and subhalo mass function. We then study the impact of self-interactions on the density and circular velocity profile of DM haloes. Furthermore, we investigate how the shapes of haloes change when self-interactions are present. Besides, we study qualitative differences between rSIDM and fSIDM and discuss transferring constraints on the cross-section of rare scatterings to frequent self-interactions.

5.3.1 Surface density

In Fig. 5.3.1 we show the surface density of the full cosmological box for our CDM and fSIDM ($\sigma_{\tilde{T}}/m_\chi = 1.0\,\mathrm{cm}^2\,\mathrm{g}^{-1}$) simulations. At a cosmological redshift of $z = 0$, basically, no differences between the simulations are visible. Hence, fSIDM seems to agree well with the collisionless DM on large scales. Previous studies that examined the large-scale structure in rSIDM found that it looks like CDM, but differences arise on small scales (e.g. Rocha et al., 2013; Stafford et al., 2020). Hence SIDM keeps the success of CDM in explaining the large-scale structure but could be capable of resolving small-scale issues. In the next sections, we investigate quantitatively the effects of fSIDM and rSIDM.

5.3.2 Matter power spectrum

Cosmological structure is characterised by the matter power spectrum. Stafford et al. (2021) computed it for several cosmologies including isotropic SIDM. They found a suppression of small-scale structure with increasing cross-section, while on large scales SIDM behaves like

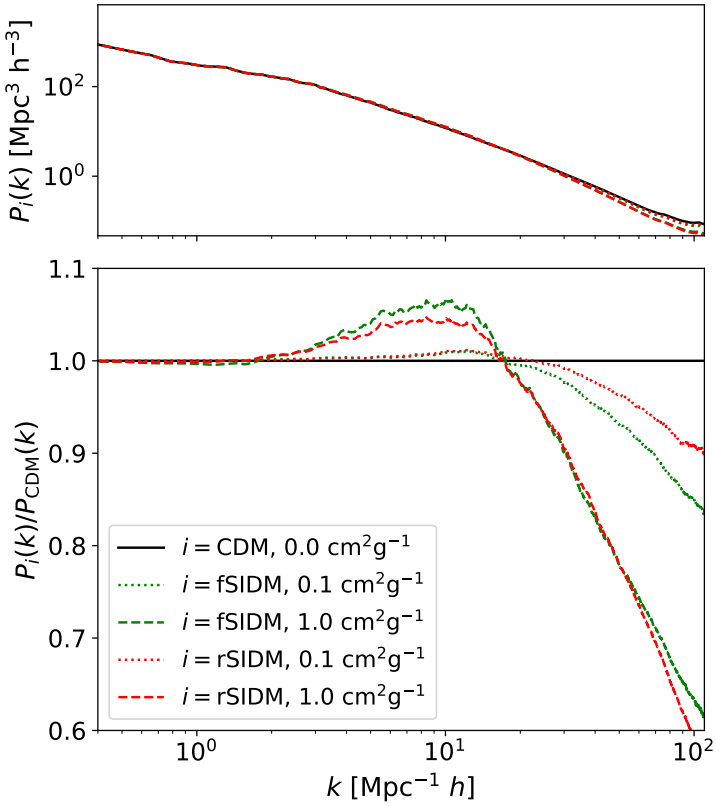

Figure 5.3.2: In the upper panel we show the matter power spectrum for the highest resolution box (uhr) and in the lower panel we display the ratio to CDM. The results are for a redshift of $z = 0$.

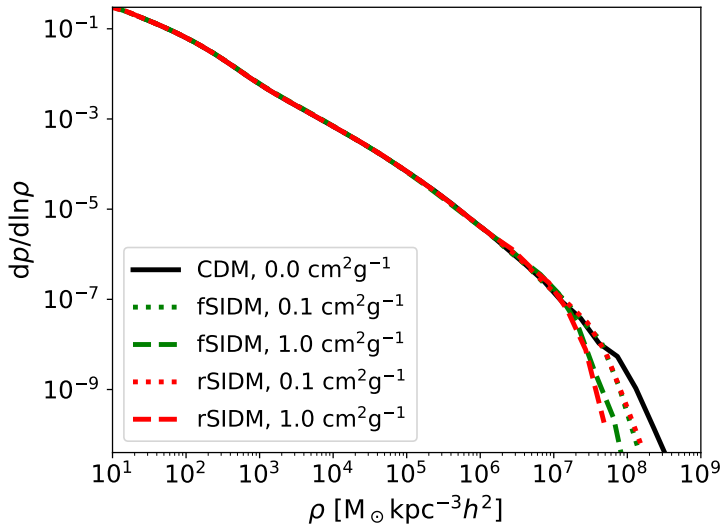

Figure 5.3.3: The probability to find a given density per logarithmic density bin is shown as a function of density for various simulations. The colours indicate the type of self-interaction and the line style gives the strength of self-interaction as indicated in the legend. The plot is for a redshift of $z = 0$ and produced from the high resolution full cosmological box simulations (uhr).

CDM.

In Fig. 5.3.2 we show the matter power spectrum of our cosmological full-box simulations and compare the various DM models. To compute the power spectrum we use the same code as in Grossi et al. (2008). In line with Stafford et al. (2021), we find that the self-interactions affect the small scales (high k-values) only and can lead here to substantial suppression of structures. The stronger the self-interactions, the stronger the suppression of structure formation on small scales. However, we only find small differences between the rSIDM and fSIDM simulations. In particular, for the larger cross-section of $\sigma_{\tilde{\mathrm{T}}}/m_\chi = 1.0\,\mathrm{cm}^2\,\mathrm{g}^{-1}$ the effects are very similar.

5.3.3 Distribution of dark matter densities

Here, we compute the volume-weighted probability to find a given density, i.e. the PDF for a random position within the cosmological volume. First, we use an oct-tree to find neighbours of the simulation particles. For each particle, we find the radius that contains 160 neighbouring particles (for the highest resolution run, uhr). Using that radius we estimate a physical density and divide it by the particle mass to obtain a volume that is associated with the particle. From all particles, we sum their associated volumes per logarithmic density bin and divide by the simulation volume and logarithmic density bin size. The result is shown in Fig. 5.3.3.

We find that the various DM models differ in the high-density regime only. Here, self-interactions suppress the highest densities compared to CDM. The suppression takes place for densities $\gtrsim 10^7\,\mathrm{M}_\odot\,\mathrm{kpc}^{-3}h^2$. In consequence, this leads to an increase for somewhat

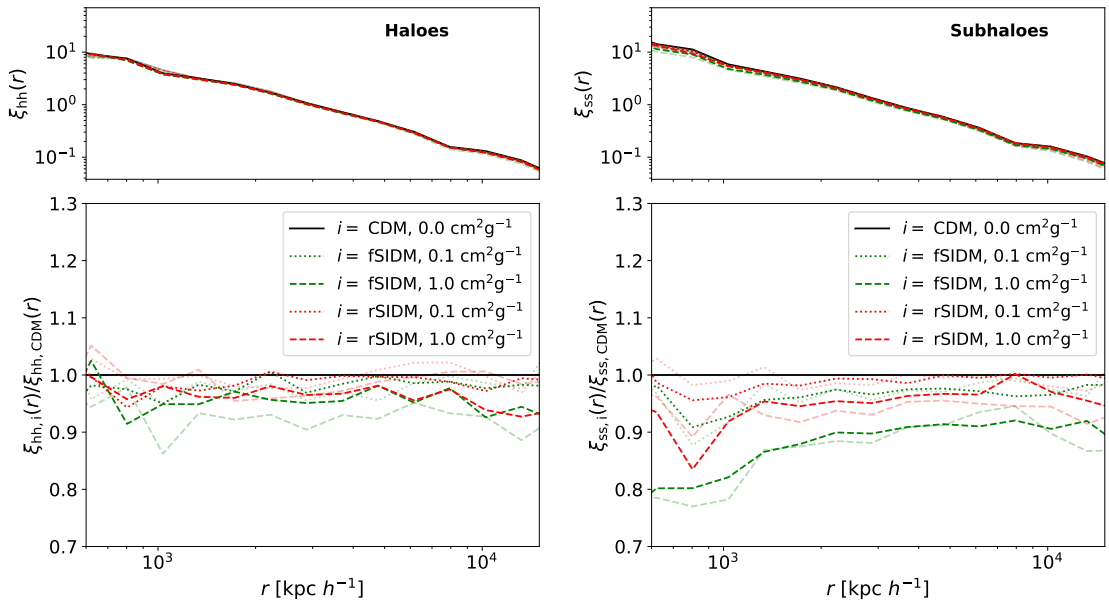

Figure 5.3.4: The two-point correlation function is shown for the higher resolution boxes (uhr, darker lines) and the lower resolution boxes (hr, fainter lines). For the left panel, we used the halo positions and computed the halo-halo correlation, $\xi_{\rm hh}(r)$. Likewise, we used the subhalo positions and computed the subhalo-subhalo correlation, $\xi_{\rm ss}(r)$, as displayed in the right panel. Note that we only considered haloes and subhaloes that have at least a mass of $\sim 9.6{\times}10^{10}\,{\rm M}_\odot\,h^{-1}$. Results for various DM models, as indicated in the legend, are shown for a redshift of $z = 0$.

lower densities $\sim 10^6$–$10^7\,{\rm M}_\odot{\rm kpc}^{-3}h^2$. However, the low-density regions ($\lesssim 10^6\,{\rm M}_\odot\,{\rm kpc}^{-3}h^2$) do not show any differences between the DM models.

The densest regions are most sensitive to DM self-interactions because the effect of self-interactions depends on the density and the velocity dispersion, which tends to be high in dense regions. However, we do not find large differences between rSIDM and fSIDM, especially for the smaller cross-section of $\sigma_{\tilde{\rm T}}/m_\chi = 0.1\,{\rm cm}^2\,{\rm g}^{-1}$ the models are very similar.

5.3.4 Two-point correlation function

In addition to the power spectrum, we can use the two-point correlation function to characterise the distribution of matter. Specifically, we compute the spatial two-point correlation function according to (Davis & Peebles, 1983),

$$\xi(r) = \frac{N_R}{N_D}\frac{DD(r)}{DR(r)} - 1\,. \tag{5.2}$$

We use the data points given by the simulation and draw random numbers to generate points from a uniform PDF. The number of data points is given by N_D, and N_R denotes the number of randomly distributed points. We compute the number of distances $DD(r)$ between data points within the interval $[r, r+\Delta r]$ as well as $DR(r)$, the number of distances

between data points and random points.

We compute the halo-halo correlation, $\xi_{\mathrm{hh}}(r)$, based on the halo positions and the subhalo-subhalo correlation, $\xi_{\mathrm{ss}}(r)$, based on the subhalo positions as identified by SUBFIND for the full cosmological box simulations. But we do not use all substructures, instead, we introduce a mass/resolution cut to avoid our results being affected by numerical artefacts. All systems with a mass of $M < 9.6 \times 10^{10}\,\mathrm{M}_{\odot}\,h^{-1}$ are excluded as they are poorly resolved. For the uhr runs this mass corresponds to 2200 particles and for the hr runs to 220 particles. As a consequence, we have much fewer positions (very roughly 3×10^3 for hr and uhr as well as haloes and subhaloes) for the computation of the two-point correlation function. In Fig. 5.3.4 we show the results for the halo positions (left panel) and the subhaloes (right panel). For the haloes, we do not find much of a difference among the DM models. In contrast, the comparison of the subhalo positions reveals a difference on small scales as well as larger scales. As expected, the stronger the cross-section the more structures on small scales are suppressed. For $\sigma_{\tilde{\Gamma}}/m_{\chi} = 1.0\,\mathrm{cm}^2\,\mathrm{g}^{-1}$ fSIDM simulations deviate more from CDM than the rSIDM simulations do, with the subhalo correlation function being roughly 20% lower on small scales for fSIDM than CDM. Note that these results depend on the chosen mass/resolution cut for subhaloes. The lower the cut the larger the deviations between the CDM and SIDM runs are.

The suppression of the subhaloes compared to haloes may arise from the fact that some of them are satellites and not exclusively primary subhaloes (see Sec. 5.2). The SIDM satellites could dissolve faster because they have lower central densities due to DM self-interactions. Hence they are not as strongly bound as their CDM counterparts, which makes them more prone to tidal effects. This could be enhanced by scattering between host and satellite particles. In the next section, we turn to the halo and subhalo mass function.

5.3.5 Halo and subhalo mass function

Here, we study the halo and subhalo mass function as well as the abundance of satellites.

In Fig. 5.3.5 we show the halo mass function (left panel) and the subhalo mass function (right panel). For the computation, we used the total mass of the haloes and subhaloes calculated by SUBFIND. At the high-mass end, we do not find a significant difference between CDM and the SIDM models. But at lower masses, self-interactions suppress the number of haloes and even more the number of subhaloes. However, the smallest objects we display here are not well resolved. Note, the mass cut previously used for Fig. 5.3.4 selects systems with a mass $\gtrsim 9.6 \times 10^{10}\,\mathrm{M}_{\odot}\,h^{-1}$. At least the largest fSIDM cross-section studied here gives us a significant reduction of the number of subhaloes above this cut. But for the haloes none of the cross-sections results in a significant reduction for masses $\gtrsim 9.6 \times 10^{10}\,\mathrm{M}_{\odot}\,h^{-1}$. The difference between the halo and subhalo mass function can only arise from satellites dissolving faster, as all non-satellites are haloes. Hence satellites, in particular low mass satellites, appear to be an interesting test bed for SIDM models. Several SIDM studies have focused on them (e.g. Kahlhoefer et al., 2019; Kaplinghat et al.,

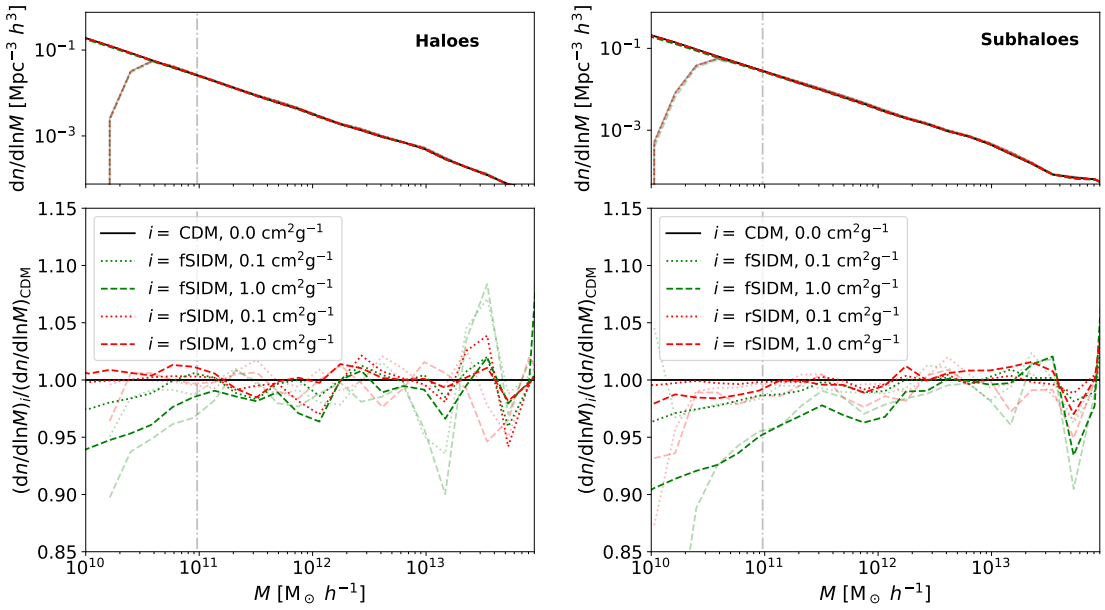

Figure 5.3.5: The halo mass (left panel) and the subhalo mass (right panel) function are shown for various simulations. We plot the number density of haloes/subhaloes per logarithmic mass bin as a function of the total halo/subhalo mass as identified by SUBFIND. The colours indicate the type of the self-interaction and the line style gives the strength of self-interaction as indicated in the legend. We display results of the higher resolution boxes (uhr, darker lines) and the lower resolution boxes (hr, fainter lines). The dash-dotted grey line indicates the mass limit of $\sim 9.6 \times 10^{10}\,\mathrm{M}_\odot\,h^{-1}$ that we applied previously for the two-point correlation function. The plots are for a redshift of $z = 0$.

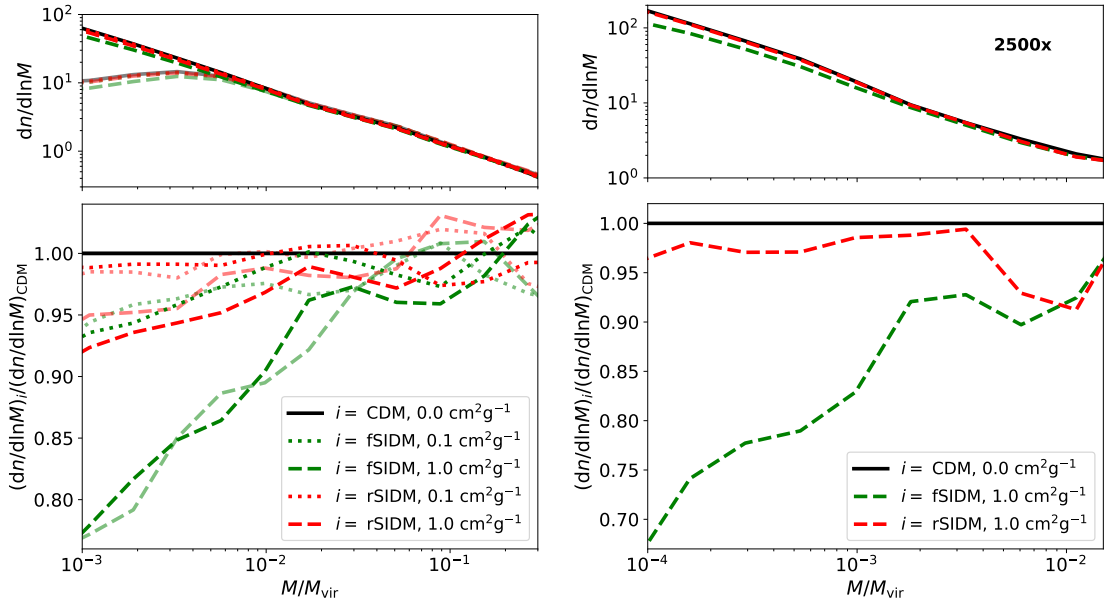

Figure 5.3.6: The number of satellites per logarithmic mass as a function of their total mass relative to the virial mass of their host. The left panel gives the result of the 100 most massive groups in our full cosmological box with the highest resolution and the lower resolution run (transparent). The right panel gives the same but for the three most massive objects in the best resolved zoom-in simulation. All subhaloes, except for the primary one, that are within a radius of $5\,r_{\rm vir}$ were considered satellites. The results are for a redshift of $z = 0$. Note, the least resolved satellites of the uhr and x2500 simulations used here contain about 100 particles.

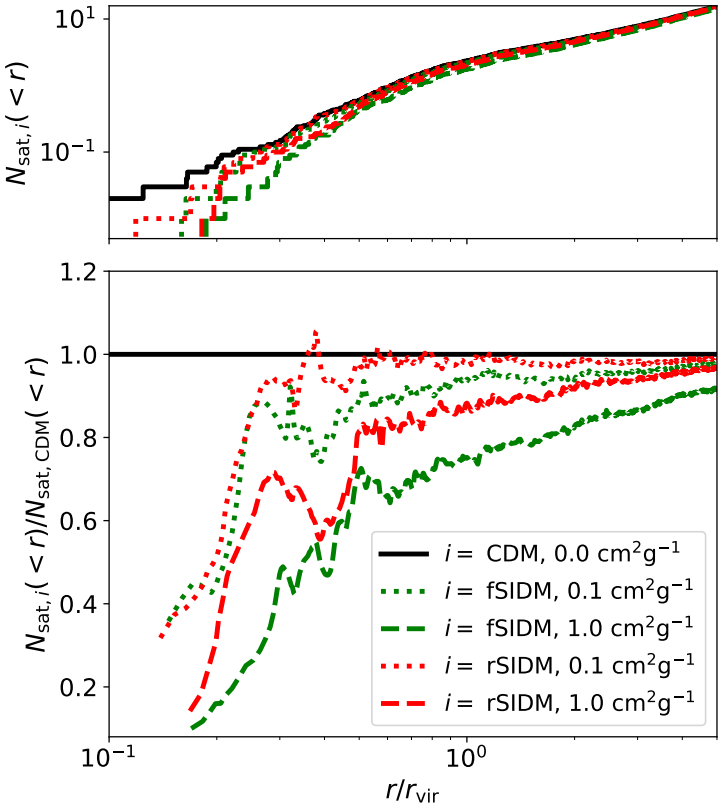

Figure 5.3.7: The average cumulative number of satellites per halo as a function of radius is shown for the uhr simulations at $z = 0$ (upper panel) as well as the ratio of the DM models to CDM (lower panel). The latter one has been smoothed a little. We use the subhaloes of the 100 most massive haloes and consider them satellites if they are more massive than $M > 9.6 \times 10^{10}\,\mathrm{M}_\odot\,h^{-1}$ and less massive than the primary subhalo.

2019; Banerjee et al., 2020; Nadler et al., 2020; Nishikawa et al., 2020; Sameie et al., 2020; Yang et al., 2020; Correa, 2021; Nadler et al., 2021; Sameie et al., 2021; Zeng et al., 2021).

In Fig. 5.3.6 we study the abundance of satellites for the DM models. For each group, we compute the number of satellites per logarithmic mass as a function of the satellite mass divided by the virial mass of the group. We select all subhaloes, except the primary one, within $5\,r_{\rm vir}$. The results for a selection criterion of $1\,r_{\rm vir}$ are shown in Appendix 5.C. For the full box simulations, we do this for the 100 most massive groups and take the mean (left panel). In contrast, for the zoom-in simulations, we only take the mean of the three most massive systems (right panel). The comparison between SIDM and CDM in the lower panel shows that self-interactions can suppress the abundance of satellites. The stronger the self-interactions the fewer satellites are present and low mass satellites are more affected than more massive ones. However, we have to note that the lowest mass satellites used in Fig. 5.3.6 are not well resolved. Although the halo mass function is not converged for the hr run at low masses (left panel), the differences to CDM, in particular for fSIDM with $\sigma_{\tilde{\rm T}}/m_\chi = 1.0\,{\rm cm}^2\,{\rm g}^{-1}$, seem to be converged. This makes it plausible that the effect for the lower masses is real. In a similar manner, Stafford et al. (2020) found the difference between cosmologies to be converged for density profiles below the convergence radius proposed by Ludlow et al. (2019). We find differences for better-resolved haloes at larger masses too, but not for the most massive satellites. For the larger cross-section of $\sigma_{\tilde{\rm T}}/m_\chi = 1.0\,{\rm cm}^2\,{\rm g}^{-1}$ frequent self-interaction seem to be much more efficient in reducing the number of satellites than rare scatterings. This is in line with the suppression of the spatial two-point correlation function of subhaloes at small scales (right panel, Fig. 5.3.4). It is also worth mentioning, that we found earlier, in a study of head-on collisions of unequal mass mergers (Fischer et al., 2021b), that fSIDM subhaloes dissolve faster than rSIDM subhaloes when they are matched in terms of $\sigma_{\tilde{\rm T}}/m_\chi$.

In addition, we study the radial dependence of the suppression of the satellite abundance in Fig. 5.3.7. Here we find that the effect of SIDM on the number of satellites becomes stronger at smaller distances to the host. As in Fig. 5.3.5 and 5.3.6 we find that fSIDM reduces the abundance of satellites stronger than rSIDM given the same value for $\sigma_{\tilde{T}}/m_\chi$. However, we have to note that for small radii the number of satellites we study here is low and thus the error on the ratios shown in Fig. 5.3.7 is sizeable. Thus we can only make a qualitative statement for the smallest radii, but not quantify the difference between the DM models.

That satellites can dissolve faster in the presence of SIDM has been found earlier. The evolution of a satellite and its lifetime depends on several aspects and physical mechanisms that are at play. In CDM, satellites are torn apart by tidal forces, which act against their gravitational self-binding. The more massive and the more concentrated a satellite is, the more resistant it is against the tidal forces and can survive longer. In the context of SIDM, a DM core can form, which flattens the gravitational potential and makes the satellite more prone to tidal disruption (Yang et al., 2020). However, if the satellite is

in a further evolution phase and undergoes core-collapse (e.g. Balberg et al., 2002; Koda & Shapiro, 2011; Essig et al., 2019) it is more protected against tidal disruption as it is even more concentrated than its CDM counterparts. Nishikawa et al. (2020) found that tidal stripping enhances the core-collapse in SIDM haloes, i.e. reduces the collapse time. A recent study, Zeng et al. (2021) found that it is nearly impossible for satellites to undergo core-collapse if self-interactions are velocity-independent. The evolution of a satellite is not only determined by tidal stripping and DM self-interactions between satellite particles, it is also affected by tidal heating and DM self-interactions between satellite and host particles. Whether tidal effects (stripping and heating) enhance or prevent core-collapse depends on the mass concentration of the satellite. The satellite-host interactions transfer energy into the satellite and thus contributes to the core formation. For a cross-section, which is decreasing with velocity (e.g. Loeb & Weiner, 2011; Tullin et al., 2012), this effect would become much less as the typical relative velocity between satellite and host particles is larger than between satellite particles. In consequence, the survival time of satellites is expected to depend crucially on the velocity dependence of the self-interactions. Banerjee et al. (2020) studied various SIDM models and found that the suppression of the satellite abundance is weaker if the cross-section is velocity-dependent. However, they also studied an anisotropic cross-section and did not find any significant deviation to an isotropic cross-section, this also includes satellite counts. It is worth pointing out that our fSIDM cross-section is more anisotropic. In practice, it might be infeasible to study it with an rSIDM scheme, as used by Banerjee et al. (2020), because the high scattering rate would require very small time steps. In addition, we should mention the work by Vogelsberger et al. (2019). They studied a MW-like halo with multi-state inelastic DM self-interactions and found that this type of interaction suppresses the abundance of small structures even for small cross-sections considerably.

Overall, satellites are not only interesting objects that constrain the strength of SIDM, but may also provide bounds on the angular and velocity-dependence of the differential cross-section. In Sec. 5.3.9 we discuss further potential strategies to constrain this angular dependence.

5.3.6 Density profiles

As we have seen in Fig. 5.3.3, in scenarios with SIDM the high-density regions are suppressed. In particular, density cores have been studied in the literature and used to constrain self-interactions (e.g. Correa, 2021; Sagunski et al., 2021; Ray et al., 2022). Recent strong lensing observations provide further evidence for DM cores in galaxy clusters (Limousin et al., 2022).

In cosmological simulations of rSIDM density and circular velocity profiles of haloes have been studied previously by Rocha et al. (2013); Robertson et al. (2019); Banerjee et al. (2020); Stafford et al. (2020).

In Fig. 5.3.8 we show median density profiles of the haloes for three different mass bins.

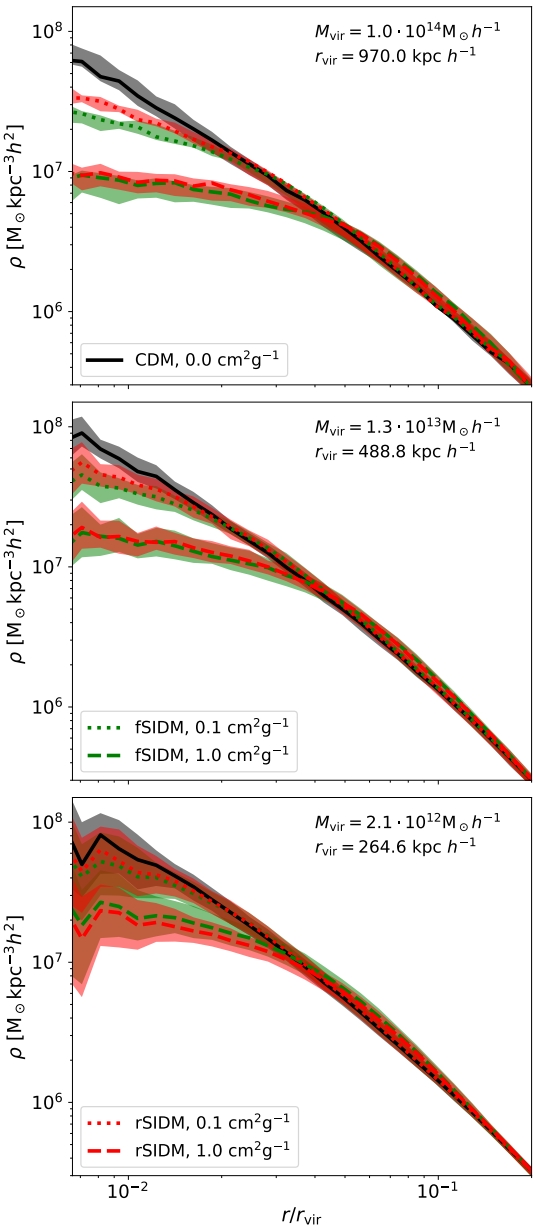

Figure 5.3.8: Median density profiles are shown for various halo mass bins and cross-sections. The density is plotted as a function of the radius in units of the virial radius. The shaded regions indicate the scatter among the haloes, the range between the 25th and 75th percentiles is displayed. The virial mass and the virial radius given in the panels indicate the median of the corresponding mass bin. All plots show the profiles for a redshift of $z = 0$ and are produced from the full cosmological box with the highest resolution. Note, we have used all particles, not only those that belong to the halo as identified by SUBFIND.

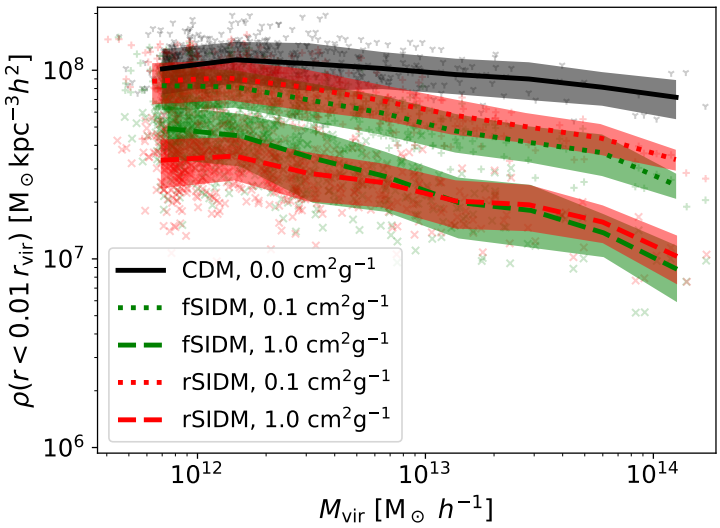

Figure 5.3.9: We display the central density of haloes as a function of their virial mass. The results of various simulations at a redshift of $z = 0$ are shown. The central density is measured as the mean density within a sphere of $0.01\,r_{\rm vir}$. Systems evolved with the smaller cross-section are marked by "+" and for the larger cross-section we use "×", the CDM case is indicated by "ϒ". In addition to the individual systems, we computed the mean of the distribution as a function of virial mass, indicated by the lines. The shaded region gives the standard deviation.

In the outer regions, the density profiles are very similar among the various DM models. But in the central region, we observe a density core for SIDM while CDM predicts cuspy haloes. The central density is lower for a larger cross-section and frequent self-interactions lead mostly to slightly larger cores than rare self-interactions, if a $\sigma_{\tilde{\Gamma}}$-matching (same momentum transfer cross-section for rSIDM and fSIDM) is employed. This is in agreement with previous findings of isolated haloes (Fischer et al., 2021a).

The central density of the individual haloes is shown in Fig. 5.3.9. Specifically, we computed the mean density within $0.01\,r_{\rm vir}$. As we have already seen above a larger self-interactions cross-section leads to haloes with lower central densities. For CDM we observe a slight decline of the central density with virial mass. But for the SIDM models, the decline is steeper. This implies an increasing difference between CDM and SIDM models with virial mass. Note that with increasing virial mass the velocity dispersion in the inner regions of the DM haloes increases and thus the self-interactions are more efficient.

5.3.7 Circular velocity

In addition to computing the density profile, we can also study the circular velocity,

$$v_{\rm circ}(r) = \sqrt{\frac{GM(<r)}{r}}\,, \tag{5.3}$$

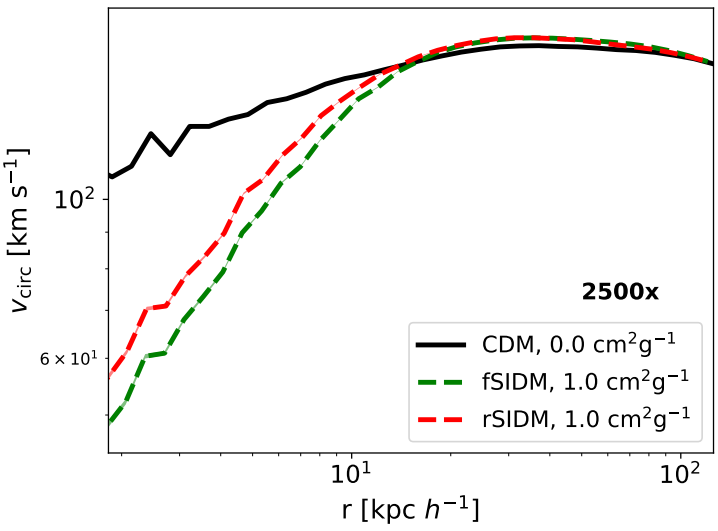

Figure 5.3.10: The circular velocity as a function of radius is shown for the most massive subhalo of our highest resolved zoom-in simulation at a redshift of $z = 0$.

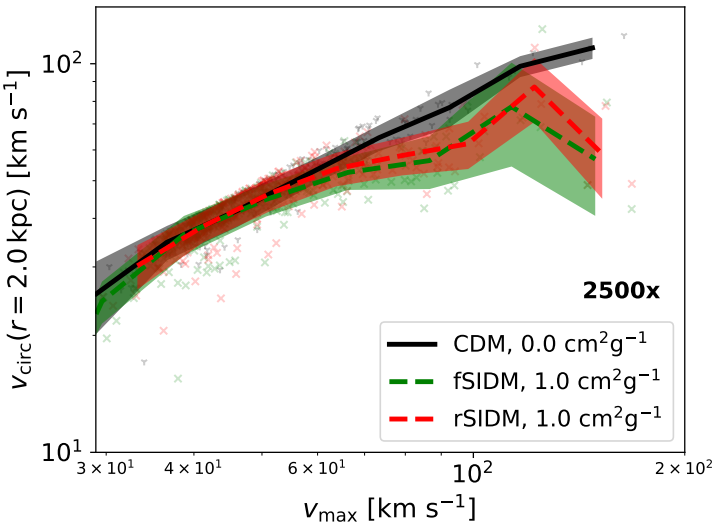

Figure 5.3.11: The circular velocity at 2 kpc vs. the maximum circular velocity measured from the circular velocity profile as shown in Fig. 5.3.10 is displayed. Each dot corresponds to one of the 300 most massive subhaloes of the highest resolved zoom-in simulation. The lines correspond to the mean and the shaded regions indicate the standard deviation.

as a function of the radius. In Fig. 5.3.10 we show the circular velocity profile for the most massive subhalo of the best-resolved zoom-in simulation. It is visible that in the inner regions the velocity that is needed for a circular orbit is less for SIDM compared to CDM. This is a direct consequence of the density core, i.e. the enclosed mass, $M(<r)$, in Eq. (5.3) is less. At larger radii, the circular velocity is the same across the DM models.

In order to trace the core formation in terms of $v_{\rm circ}$, we can measure it at a small radius and compare it to its maximum value. We do so in Fig. 5.3.11 and plot $v_{\rm circ}(2\,{\rm kpc})$ vs. $v_{\rm circ,max}$ for the 300 most massive subhaloes of the best resolved zoom-in simulation. For the most massive subhaloes, i.e. the ones with a larger value for $v_{\rm max}$, we find a difference between the DM models. The SIDM models tend to have lower circular velocities at 2 kpc than CDM. For fSIDM, $v_{\rm circ}$ is slightly lower than for rSIDM, which is in line with the lower densities found for fSIDM. At lower masses we do not find a significant difference, here a measure at 2 kpc may not be sensitive to the density core. Instead, a measure at smaller radii would be preferable to trace the density core.

Self-interactions have turned out to be interesting to explain the diversity of observed rotation curves (e.g. Oman et al., 2015). In particular, the response of SIDM to the gravitational potential of the baryons can increase the diversity of rotation curves (e.g. Creasey et al., 2017; Kamada et al., 2017; Kaplinghat et al., 2019). However, Zentner et al. (2022) claim that it is not clear whether observed galactic rotation curves are better explained by SIDM or CDM including baryons. For late-type dwarfs Roper et al. (2022) points out that the measured rotation curves could differ significantly from their circular velocity curves. Other studies had also previously indicated that the kinematic modelling of these objects might be problematic (e.g. Pineda et al., 2016; Read et al., 2016; Genina et al., 2018; Oman et al., 2019). In any case, this question can only be addressed once baryonic physics is taken into account in the N-body code, implying that our results cannot be directly compared to these findings. We leave a more in-depth discussion of these issues for future work.

5.3.8 Shapes

The shape of DM haloes can provide bounds on the strength of self-interactions. We use the tensor, $\mathbf{S}$, to compute the shape. For N point masses it is,

$$\mathbf{S} \equiv \frac{\sum_{n=1}^{N} m_n \, \boldsymbol{r}_n \otimes \boldsymbol{r}_n}{\sum_{n=1}^{N} m_n} \,, \tag{5.4}$$

with the particle mass m_n at position $\boldsymbol{r}_n$. In order to compute the shapes, we use the eigenvalues ($\lambda_1 \geq \lambda_2 \geq \lambda_3$). They are related to the semi-axes ($a \geq b \geq c$). In particular, we measure the axis ratios $s = c/a = \sqrt{\lambda_3/\lambda_1}$ and $q = b/a = \sqrt{\lambda_2/\lambda_1}$. Based on these two ratios we compute the triaxiality (Franx et al., 1991),

$$T \equiv \frac{a^2 - b^2}{a^2 - c^2} = \frac{1 - q^2}{1 - s^2} \,. \tag{5.5}$$

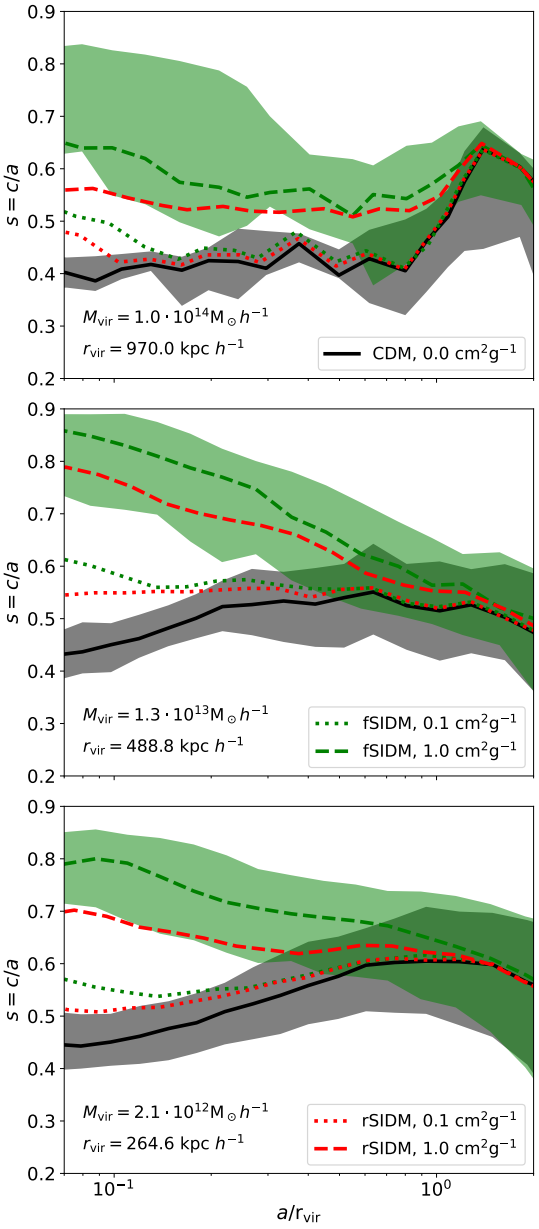

Figure 5.3.12: The median halo shapes for different mass bins are shown as a function of the median semi-major axis in units of the virial radius. We compute the median shape as well as the median semi-major axis from ellipsoids having the same volume. The shaded regions indicated the scatter among the haloes, the range between the 25th and 75th percentiles is displayed. For the sake of clarity, we show this only for the CDM simulation and the fSIDM run with the larger cross-section. The virial mass given in the panels indicates the median virial mass of the haloes of the corresponding mass bin. The same applies to the shown virial radius. Note, we are using the same mass bins as in Fig. 5.3.8. The shapes are computed from the highest resolved full cosmological box and for a redshift of $z = 0$.

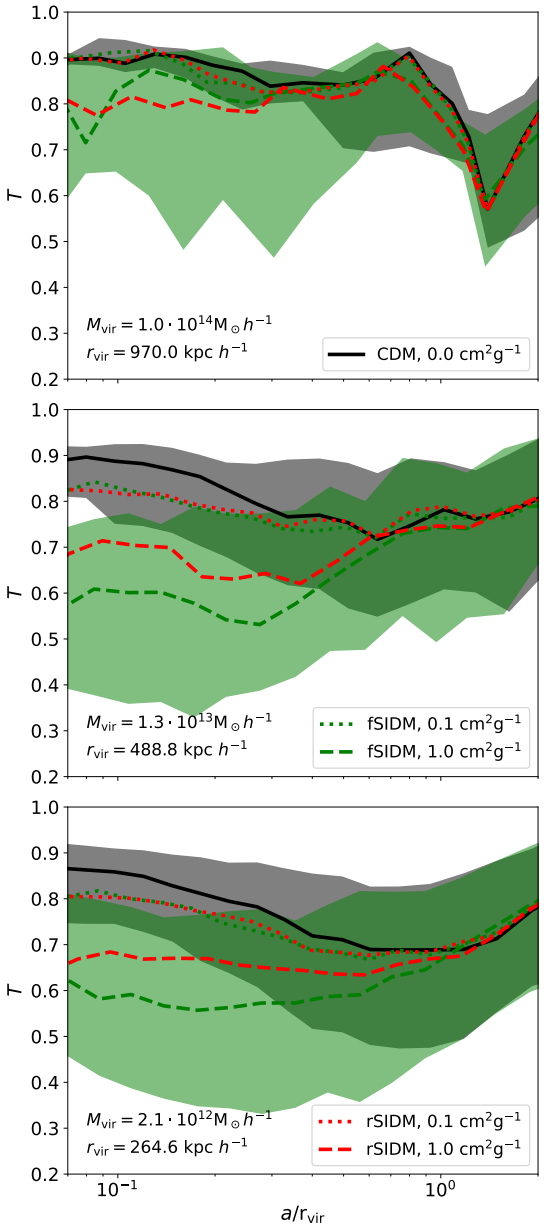

Figure 5.3.13: The same as in Fig. 5.3.12 but we show the triaxiality T instead of $s = c/a$. The triaxiality is computed according to Eq. (5.5).

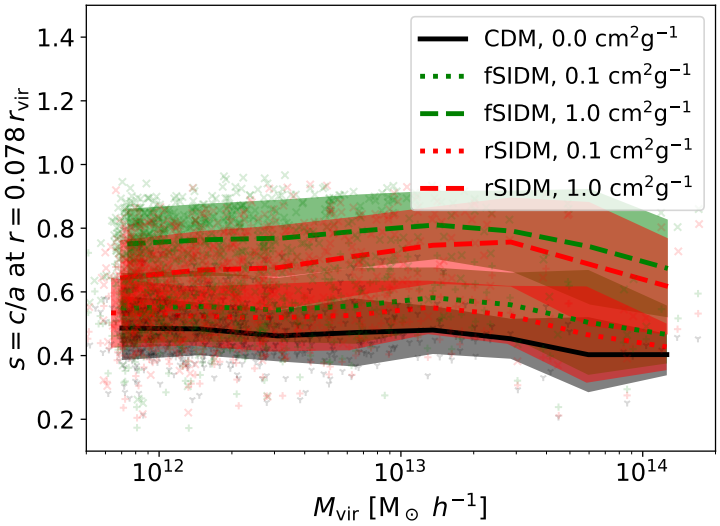

Figure 5.3.14: The shape of individual haloes as a function of their virial mass at a redshift of $z = 0$ is shown. The shapes are measured as $s = c/a$ within an ellipsoid that has the volume of a sphere of $0.078\,r_{\rm vir}$. Systems evolved with the smaller cross-section are marked by "+" and for the larger one we use "×", the CDM case is indicated by "ϒ". In addition to individual systems, we computed the mean of the distribution as a function of virial mass, indicated by the lines. The shaded region gives the standard deviation.

Our method to measure halo shapes is iterative, where during each iteration the computation of the tensor, $\mathbf{S}$, uses all particles within an ellipsoid. The orientation and axis ratios of this ellipsoid are based on $\mathbf{S}$ from the previous iteration, and the volume of the ellipsoid is kept constant throughout the iterations. We iterate until the two axis ratios (s and q) are converged. Note, in the literature various methods to measure the shape of haloes have been used (e.g. Zemp et al., 2011; Peter et al., 2013; Robertson et al., 2019; Banerjee et al., 2020; Chua et al., 2020; Sameie et al., 2018; Harvey et al., 2021; Vargya et al., 2021; Shen et al., 2022).

In Fig. 5.3.12 we show the median shapes for three halo mass bins. Note, for the computation we have used all particles, not only those that belong to the halo as identified by SUBFIND. The first mass bin contains only a few objects leading to more noise in the upper panel. At small distances from the centre, the self-interactions lead to rounder haloes, mainly depending on the strength of the self-interactions. This has been discovered earlier, e.g. Peter et al. (2013). The difference between fSIDM and rSIDM is small, with fSIDM leading to haloes that are a little more spherical than the rSIDM haloes, given a $\sigma_{\tilde{\Gamma}}$-matching. At larger radii, when more particles are included, the shapes become very similar between the different DM models. These additional particles are located at lower densities and are hence hardly affected by self-interactions. However, the SIDM shapes differ from CDM at radii beyond the density core more than the density profiles do. We have evaluated this in larger detail in Appendix 5.D. Furthermore, we find that

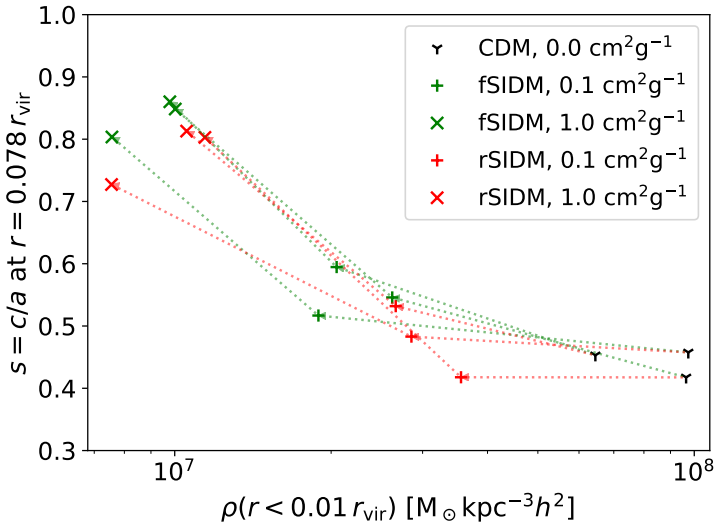

Figure 5.3.15: The shape within an ellipsoid with the volume of a sphere with a radius of $r = 0.078\,r_{\rm vir}$ is shown as a function of the central density within a sphere of $r = 0.01\,r_{\rm vir}$ for individual systems. The colours indicate the type of self-interactions and the symbols give their strength. We show the three most massive haloes (~ 1.2–$1.7 \times 10^{14}\,{\rm M}_\odot\,h^{-1}$) of the highest resolved full box simulation at a redshift of $z = 0$. How they evolve when increasing the cross-section is indicated by the arrows.

the radius where they start to differ from each other depends strongly on the strength of the self-interactions. This has been previously pointed out by Vargya et al. (2021) and suggested as a measure of the total cross-section.

In Fig. 5.3.13 we also show a complementary shape variable, the triaxiality T, as given in Eq. (5.5) for the same mass bins as in Fig. 5.3.12. We observe that T is decreasing with increasing cross-section, implying that the haloes become less prolate. For large radii, where the matter density becomes smaller, differences between the DM models vanish as expected.

We finally show the shape ($s = c/a$) measured in ellipsoids with a volume equal to a sphere with $0.078\,r_{\rm vir}$ of individual systems as a function of the virial mass in Fig. 5.3.14. As already expected from the shape profiles, we observe that the haloes become more spherically symmetric with increasing cross-section. Again, fSIDM leads to rounder haloes than rSIDM. There is no significant qualitative difference between the trend of rare and frequent scattering with virial mass. At the high-mass end, we have only very few objects such that the apparent decrease of s may not be significant.

5.3.9 fSIDM versus rSIDM

The main aim of this paper is to understand if and how the phenomenology of rare and frequent self-interactions can help to distinguish between them. In the following, we first investigate a potential degeneracy between rare and frequent self-interactions in terms of

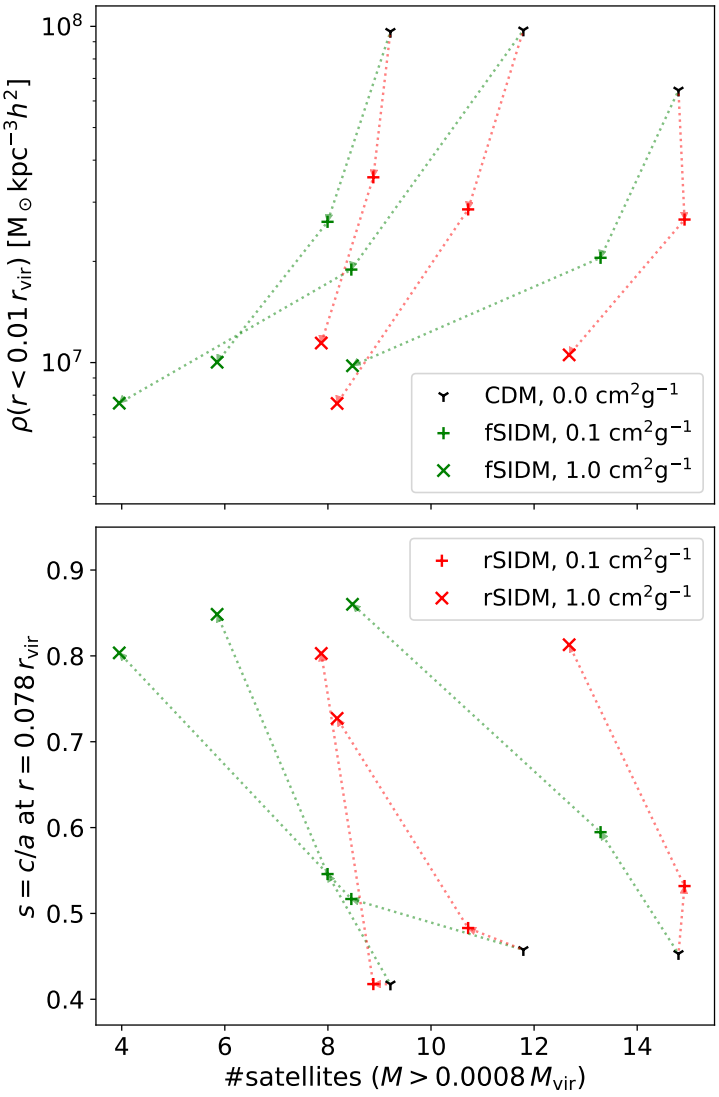

Figure 5.3.16: We show the 3 most massive haloes of our full box simulation at $z = 0$, the same as in Fig. 5.3.15. The upper panel gives the central density within a radius of $0.01\,r_{\rm vir}$ as a function of the number of satellites and the lower panel gives the shape of an ellipsoid that has the same volume as a sphere with an radius of $0.078\,r_{\rm vir}$ as a function of the number of satellites. For the satellite count, only satellites within $r_{\rm vir}$ and with a mass larger than $0.0008\,M_{\rm vir}$ were considered. This implies that every satellite is at least resolved by $\gtrsim 2200$ particles. The arrows connect the same systems across the simulations with various cross-sections.

halo shape and central densities. In Fig. 5.3.15 we plot the shape as a function of central density for individual systems. The arrows indicate how they change when increasing the cross-section. Here, we use the three most massive systems of the full box simulation (uhr). Although the values for the same object and cross-section differ from each other, this is not necessarily a qualitative difference. Rather it can be interpreted as an issue of matching rare and frequent self-interactions. As the two types of self-interaction roughly move in the same direction (in the shape–central density plane) when increasing the cross-section.

Secondly, we consider the number of satellites to find a qualitative distinction. In Sec. 5.3.5 we found that it can make a difference for the abundance of satellites whether DM self-interactions are frequent or rare. Compared to the differences we found for the central densities (Sec. 5.3.6) or the shapes (Sec. 5.3.8) the number of satellites seem to be more sensitive to the underlying form of the cross-section. In Fig. 5.3.16 we plot the central density (upper panel) and the shape (lower panel) as a function of the number of satellites for the same systems as in Fig. 5.3.15. We only count satellites that are within the virial radius and more massive than $0.0008\,M_{\rm vir}$, which corresponds to a resolution of $\gtrsim 2200$ particles. If fSIDM and rSIDM behave qualitatively the same, the systems should move along the same path in the plot when increasing the cross-section, regardless of whether the scattering is rare or frequent. We use arrows to indicate how the systems change with increasing cross-section. It becomes clear, that fSIDM and rSIDM are not scaled versions of each other but are qualitatively different. For a given number of satellites, we find the main halo to be less dense and more spherically symmetric for rSIDM compared to fSIDM. If this qualitative difference is still present in full physics simulations and strong enough to be observable, it could provide an avenue to distinguish between rSIDM and fSIDM.

5.3.10 Constraints on fSIDM

In this paper, we do not aim to compare our simulations to observations but previous studies of rSIDM may allow placing constraints on the velocity-independent fSIDM cross-section.

So far we have found that fSIDM and rSIDM behave similarly in many aspects. In particular, if we consider the density (Fig. 5.3.8) or shape (Fig. 5.3.12) profiles we find that the momentum transfer cross-section can roughly match fSIDM and rSIDM. This can allow transferring constraints of the cross-section for rSIDM to fSIDM. In many situations, we found that fSIDM has a slightly larger effect than rSIDM, when the same momentum transfer cross-section is considered. This implies that upper limits on the momentum transfer cross-section may be even more stringent for the case of fSIDM. Given this, the established upper limits on rSIDM could be viewed as conservative limits for the case of fSIDM. In particular, this applies to our shape measurements for the whole mass range we have studied and to the density profiles for the two most massive mass bins ($\gtrsim 10^{13}\,\mathrm{M}_\odot$, see also Fig. 5.3.9).

In this context the work of Sagunski et al. (2021) is relevant. They studied the core sizes of galaxy groups and clusters to derive limits on the self-interaction cross-section. Their

upper limits at a confidence level of 95% on the total cross-section are $\sigma/m_\chi = 1.1\,\mathrm{cm^2 g^{-1}}$ for groups and $\sigma/m_\chi = 0.35\,\mathrm{cm^2 g^{-1}}$ for clusters. In terms of the momentum transfer cross-section this corresponds to $\sigma_{\tilde{T}}/m_\chi = 0.55\,\mathrm{cm^2 g^{-1}}$ for groups and $\sigma_{\tilde{T}}/m_\chi = 0.175\,\mathrm{cm^2 g^{-1}}$ for clusters. As discussed above these limits should hold for fSIDM too.

Another relevant study is Peter et al. (2013). They examined the shapes of galaxy clusters and consider a velocity independent cross-section of $\sigma/m_\chi = 1.0\,\mathrm{cm^2 g^{-1}}$ (total cross-section) to be unlikely large. This corresponds to $\sigma_{\tilde{T}}/m_\chi = 0.5\,\mathrm{cm^2 g^{-1}}$ and should apply to fSIDM too. However, we have to note that Peter et al. (2013) used DM-only simulations. Robertson et al. (2019) showed that the shape of the ICM is hardly affected by the DM physics, but that the DM component becomes considerably rounder due to self-interactions, even if baryons are present. Furthermore, the presence of baryons makes the DM shapes become more round too, which rules in favour of excluding a cross-section of $\sigma_{\tilde{T}}/m_\chi \geq 0.5\,\mathrm{cm^2 g^{-1}}$ for rSIDM and fSIDM.

5.4 Discussion

In this section, we discuss the limitations and implications of our results. Our findings depend partially on SUBFIND, as we use the halo and subhalo positions as well as their mass and spatial extension. Only a few of our results are independent of SUBFIND, these are the matter power spectrum and the density PDF. We want to point out that there are a number of codes for identifying substructure (e.g. Knollmann & Knebe, 2009; Maciejewski et al., 2009; Tweed, D. et al., 2009; Behroozi et al., 2012; Han et al., 2017; Elahi et al., 2019). They employ different algorithms which may give somewhat different results Knebe et al. (2013).

We found that the abundance of satellites is sensitive to differences between rare and frequent DM scatterings. In particular, for low-mass satellites, the difference between the DM models becomes larger. As such it would be interesting to study those low-mass satellites with a higher resolution. In this context, a hybrid approach as presented in Zeng et al. (2021) is an efficient technique that could help to improve our results.

In general, we would expect to find the largest differences between rSIDM and fSIDM in systems that are far from equilibrium. However, there are systems that may be similar or even more sensitive to the shape of the differential cross-section. Mergers have received attention in the context of SIDM (Randall et al., 2008; Harvey et al., 2015; Kahlhoefer et al., 2014; Robertson et al., 2017a,b; Kim et al., 2017; Fischer et al., 2021a,b). It has been shown that the DM-galaxy offsets can produce discernible differences between DM models. In addition to offsets, the distribution of a collisionless component (such as galaxies or stars) can give a handle to constrain DM properties.

The main simplification of our simulations is the neglect of baryonic matter and the associated physics. While DM-only simulations may provide reasonably accurate results on large scales, they fail on scales where galaxies form. In particular, the inner regions of

haloes can be strongly affected by baryons. It is well known that feedback mechanisms from supernovae can create DM density cores too (Read & Gilmore, 2005; Governato et al., 2012; Pontzen & Governato, 2012; Di Cintio et al., 2013; Cintio et al., 2014; Brooks & Zolotov, 2014; Pontzen & Governato, 2014; Oñorbe et al., 2015; Tollet et al., 2016; Benítez-Llambay et al., 2019), but also black holes (e.g. Martizzi et al., 2013; Silk, 2017; Peirani et al., 2017). Recently, Burger et al. (2022) studied degeneracies between cores produced by supernova feedback and SIDM cores. They found that the velocity dispersion profile produced by self-interactions is closer to isothermal profiles than in cores that are generated by supernovae feedback in systems with bursty star formation. Nevertheless, there are properties that are less affected by baryons. We found that at large radii the halo shapes are more affected by self-interactions than the density profiles (see Appendix 5.D). At these radii, baryons play a less important role than in the core region. Vargya et al. (2021) studied a MW-like galaxy and proposed to compare the shape of the stellar and gas component to the shape of the total matter distribution at a radial range of 2–20 kpc. Thus the shapes at large radii (but still small enough to be affected by self-interactions) are more sensitive to DM physics than the central density or cores size because they are less influenced by baryonic physics. The same could be true for the abundance of satellites, at least as far as DM rich satellites are concerned.

Given a specific DM model, a single property can help constrain the momentum transfer cross-section, but is quite limited in providing bounds on the angular dependence of the differential cross-section. An observation, e.g. of the abundance of satellites, could be explained by rSIDM as well as by fSIDM with a different momentum-transfer cross-section. In combination with another property, such as the shape, it can become possible to derive bounds on the typical scattering angle as demonstrated in Section 5.3.9. For a given DM model, multiple measurements could lead to bounds on $\sigma_{\tilde{\mathrm{T}}}/m_\chi$, which are not compatible with each other and thus exclude the considered model.

In this context, we want to stress that matching cross-sections of various DM models is difficult because they typically behave qualitatively different. Strictly speaking, it is impossible for rare and frequent self-interactions and probably for further model variations too.

Several studies (Kaplinghat et al., 2016; Correa, 2021; Gilman et al., 2021; Sagunski et al., 2021) have suggested that the self-interaction cross-section should be velocity-dependent, i.e. decrease for higher velocities. We have not studied this, but a velocity dependence should lead to qualitatively different results and is a reasonable step to extend our study. Moreover, velocity-dependent scattering is well-motivated from a particle physics perspective. This is, in particular, the case for light mediator models, which interact frequently (e.g. Buckley & Fox, 2010; Loeb & Weiner, 2011; Bringmann et al., 2017).

Another important step forward would be to include baryonic matter and its feedback processes. At small radii, the mass distribution of haloes is typically dominated by the baryonic component. As explained above, feedback mechanisms such as outflows from

supernovae can alter the DM distribution and also produce cored profiles. By this, they can mitigate the core-cusp problem (e.g. Brooks et al., 2013; Brooks & Zolotov, 2014; Chan et al., 2015; Oñorbe et al., 2015; El-Badry et al., 2016) and the diversity problem (e.g. El-Badry et al., 2017). Thus it is important to take baryonic effects into account when constraining the properties of DM models using these small-scale problems.

5.5 Conclusions

In this paper, we have presented the first cosmological simulations of DM with frequent self-interactions. We have compared DM-only simulations of CDM, rSIDM and fSIDM in terms of various measures, such as the density PDF, the matter power spectrum, the two-point correlation function of haloes and subhaloes, and the halo and subhalo mass functions. In addition, we have investigated the density and circular velocity profiles of the DM haloes as well as their shapes. Finally, we have examined qualitative differences between fSIDM and rSIDM. Our main results from these simulations are as follows:

- On large scales, rSIDM and fSIDM are very similar to CDM, but deviate on small scales.

- Regarding the suppression of small-scale structures, rSIDM and fSIDM behave very similarly. This includes the power spectrum, the density PDF and the two-point correlation function as well as the density core formation and shapes of haloes.

- We found an interestingly large suppression of the abundance of satellites in fSIDM compared to rSIDM.

- It may be possible to distinguish observationally between rSIDM and fSIDM using a combination of measurements. One promising avenue is the combination of shape or density profile measurements with the abundance of satellites. Further investigations, such as full-physics simulations are needed to find out whether observations can discriminate between these DM models.

- Rare and frequent self-interactions behave similarly in many aspects. This often allows transferring upper limits on the cross-sections of rSIDM to fSIDM.

We have conducted cosmological DM-only simulations to understand phenomenological differences between large and small-angle DM scattering. Our results may prove helpful for more sophisticated studies that compare simulations to observations with the aim to discriminate between rSIDM and fSIDM. Such studies will include baryonic matter and baryonic physics, such as gas cooling, star formation, AGN, and associated feedback mechanisms. This is the subject of forthcoming work.

Acknowledgements

MSF thanks Lucas Valenzuela for the discussion on measuring halo shapes. This work is funded by the Deutsche Forschungsgemeinschaft (DFG, German Research Foundation) under Germany's Excellence Strategy – EXC 2121 "Quantum Universe" – 390833306, Germany's Excellence Strategy – EXC-2094 "Origins" – 390783311 and the Emmy Noether Grant No. KA 4662/1-1. Antonio Ragagnin acknowledges support from the grant PRIN-MIUR 2017 WSCC32. Klaus Dolag acknowledges support by the COMPLEX project from the European Research Council (ERC) under the European Union's Horizon 2020 research and innovation program grant agreement ERC-2019-AdG 882679. The simulations have been carried out on the computing facilities of the Computational Center for Particle and Astrophysics (C2PAP). Preprint numbers: TTP22-026, DESY-22-072.

Software: NumPy (Harris et al., 2020), Matplotlib (Hunter, 2007), SciPy (Virtanen et al., 2020)

Appendices

5.A Comoving Integration Test

Here we introduce a test problem for the comoving integration of frequent self-interactions and demonstrate that our implementation works.

Similar to the deceleration problem in Newtonian space presented in Fischer et al. (2021a), we construct a deceleration problem in an expanding space. Therefore, we have a background density modelled by many particles which are at rest (vanishing canonical momentum). A test particle of the same mass as the background particles has initially a non-zero velocity and is travelling through the background density. Due to the self-interactions, the test particle is scattering many times, which leads to a deceleration. For the test simulation, we only use the first step, the deceleration as described in section 2.1 of Fischer et al. (2021a), but not the second step, which re-adds the energy lost in the first one (described in section 2.2). This test problem is conducted without any other physics, i.e. gravity is not present.

In Fig. 5.A.1 we show the cosmic deceleration problem by plotting the canonical momentum of the test particle as a function of the scale factor. Note, in the absence of self-interactions the canonical momentum would stay constant over the cosmic expansion. We can see that the simulation result matches the analytical prediction. Hence we assume that the comoving integration is properly implemented.

5.B Convergence of density profiles

In Fig. 5.B.1 we study the convergence of the density profile of the most massive subhalo in the zoom-in simulation. We show the density for various resolutions and DM models as

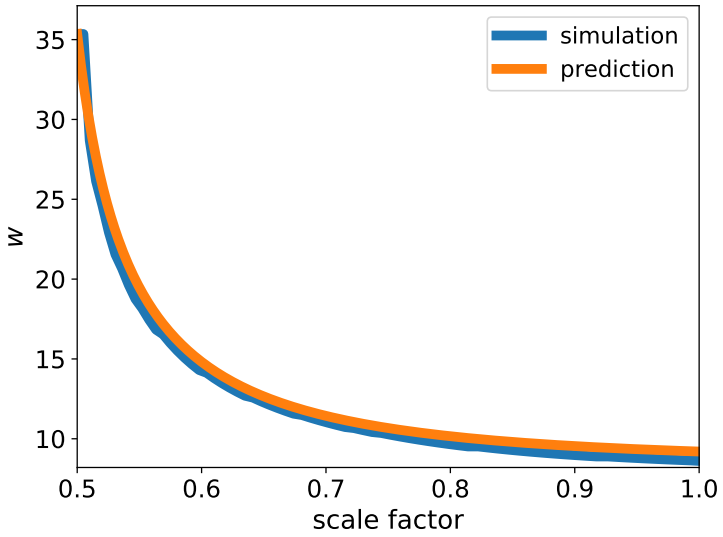

Figure 5.A.1: The cosmic deceleration problem in terms of the canonical momentum is shown. It is simulated from $a = 0.5$ to $a = 1.0$ with 122500 particles in a cubic box with a comoving side length of $1400\,\mathrm{kpc}\,h^{-1}$. The total mass is $22.8465 \times 10^{10}\,\mathrm{M}_\odot\,h^{-1}$, corresponding to a comoving density of $83.26\,\mathrm{M}_\odot\,\mathrm{kpc}^{-3}\,h^2$. The initial snapshot velocity of the test particle is $100\,\mathrm{kpc}\,\mathrm{Gyr}^{-1}$, which corresponds to an initial canonical momentum of $35.35534\,\mathrm{kpc}\,\mathrm{Gyr}^{-1}$. The particles are evolved with a cross-section of $\sigma_{\tilde{\mathrm{T}}}/m_\chi = 5 \times 10^5\,\mathrm{cm}^2\,\mathrm{g}^{-1}$ and the SIDM kernel sizes are computed using $N_{\mathrm{ngb}} = 64$.

given in Tab. 5.2.2. For all three DM models, we find that the density profiles converge. However, it seems that they converge at a different speed. Comparing the two best-resolved runs, CDM seems to converge the fastest, followed by fSIDM and rSIDM is slowest. The difference in the convergence speeds might be caused by the use of random numbers to model SIDM. For fSIDM they have a smaller influence on the particle trajectories than in rSIDM, which eventually could explain the deviation.

5.C Subhalo mass function

In Section 5.3.5 we studied the abundance of satellites as a function of mass. Here, we computed Fig. 5.3.6 with a smaller selection radius for the satellites. In Fig. 5.C.1 we only consider satellites within $1\,r_{\rm vir}$ as we have done previously in Sec. 5.3.9.

5.D Density and shape at larger radii

In this appendix, we quantitatively evaluate how much the density and shape profiles differ at larger radii between the DM models. We compute the shape of particles within elliptical shells using the tensor as given in Eq. (5.4). As in Sec. 5.3.8 we keep the volume of the shells during the iteration constant. Furthermore, we use the shells to compute the density profile too. This is in contrast to the profiles shown in Fig. 5.3.8 which were computed from spherical shells. For the computation, all particles are considered, not only those that belong to the halo as identified by SUBFIND. This implies that we also take the satellites into account, but it has almost no influence on the results shown here. We use the scatter between the individual objects (16th and 84th percentile) to estimate how significant the deviation between the DM models is. In Fig. 5.D.1 we show the results for the lowest mass bin of our uhr simulations. We find that the difference between the models for radii beyond the density core is somewhat larger for the shapes than the density profiles (see bottom row). That seems to be true for $r \lesssim 0.25\,r_{\rm vir}$ in the case of the smaller cross-section or $r \lesssim 0.4\,r_{\rm vir}$ for the larger cross-section. For most of the radial range we covered here, the SIDM shapes are rounder than the CDM shapes. In contrast, the picture for the density profiles is less clear. The density ratios are smaller (middle row) and the differences are noisier (bottom row). For studying DM physics, this may make the measurement of shapes at larger radii preferable compared to densities.

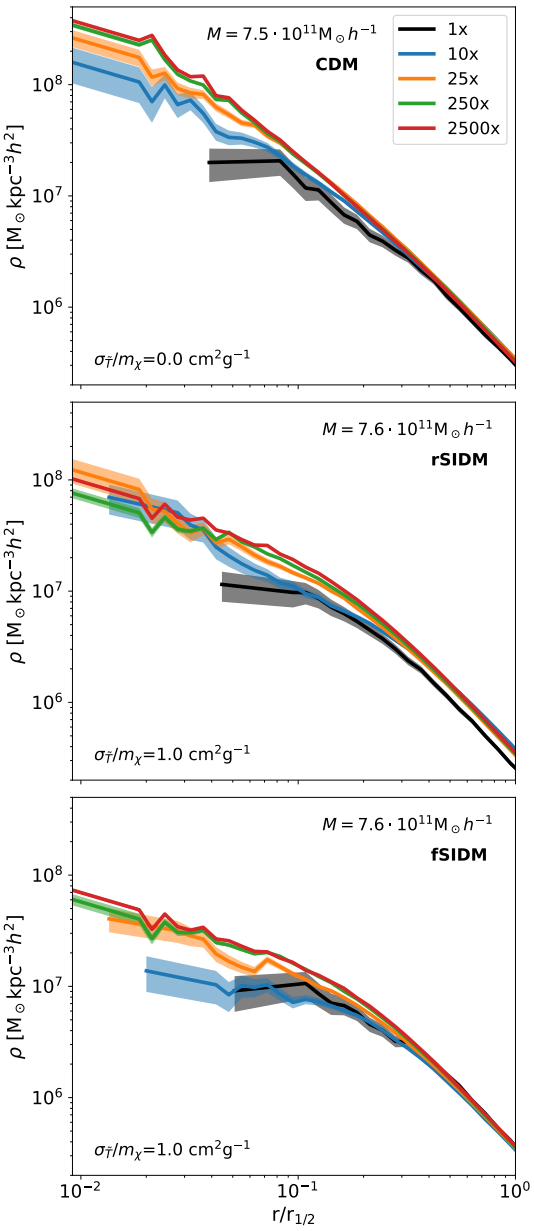

Figure 5.B.1: The density profile of the most massive subhalo in our zoom-in simulation is shown. In the top panel, we display the results for CDM, in the middle panel for rSIDM and the bottom panel for fSIDM. The colours indicate runs with different resolutions, further details can be found in Tab. 5.2.2. In the highest resolution run the halo is resolved by $\sim 2.3 \times 10^6$ particles.

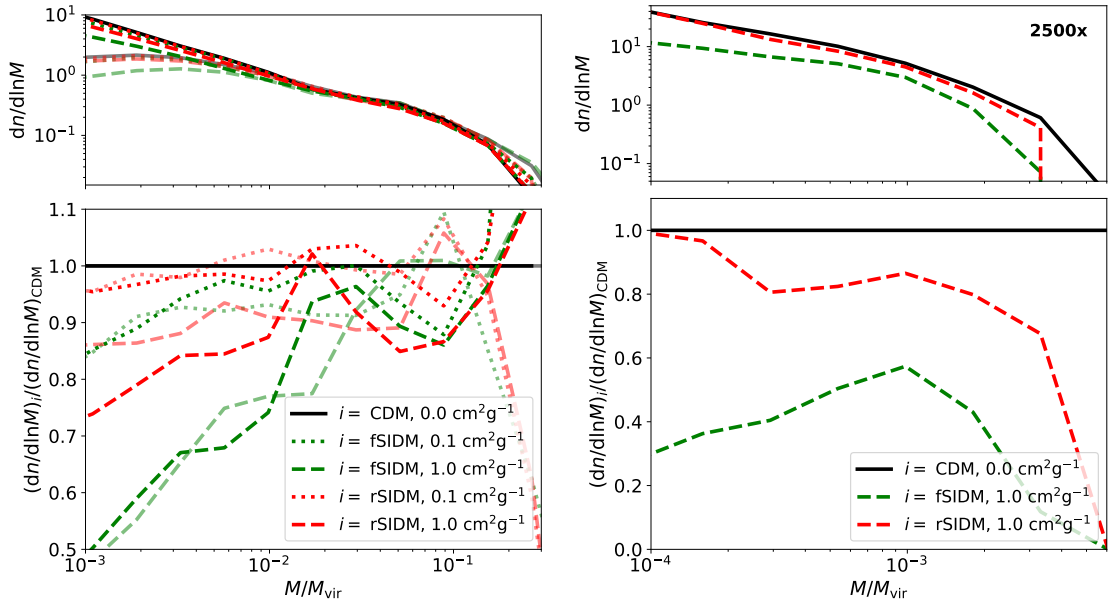

Figure 5.C.1: We display the number of satellites per logarithmic mass as a function of their total mass relative to the virial mass of their host. This is the same as in Fig. 5.3.6, but with a selection radius of $1\,r_{\rm vir}$.

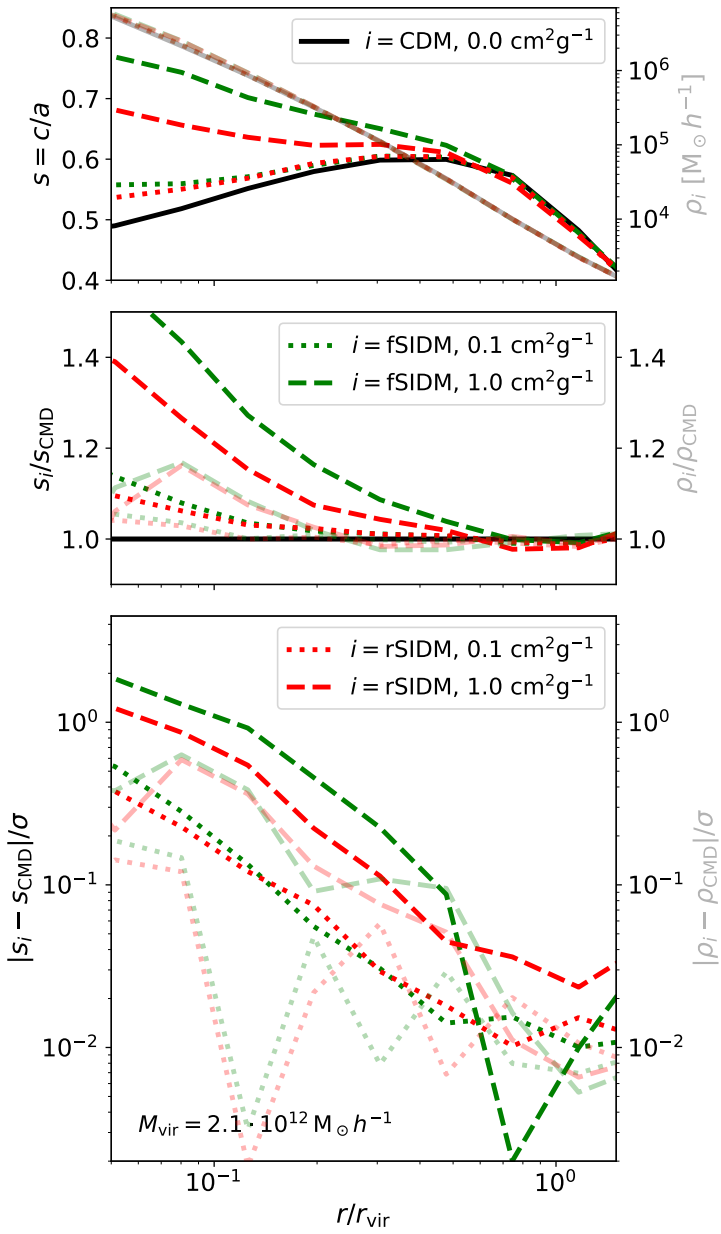

Figure 5.D.1: In the upper row, we display the median density (transparent) and shape profiles for the lowest halo mass bin (as in the bottom panels of Fig. 5.3.8, 5.3.12 and 5.3.13) of our uhr simulations at $z = 0$. The median mass of the haloes is $2.1 \times 10^{12}\,{\rm M}_\odot\, h^{-1}$. In the middle row, we show the ratio between the SIDM models and CDM. We further compute the difference of the SIDM models and CDM and divide it by the scatter among the individual systems. The result is displayed in the bottom row. The x-axis is in terms of the radius that a spherical shell with the same volume has. Here we use the mean of the two shell boundaries.

6 Conclusion and Outlook

In this final chapter, we first summarise and provide a conclusion from the work we have presented here and second give an outlook on further research perspectives of SIDM related to future surveys.

6.1 Conclusion

Many efforts are being undertaken to gain insights into the nature of DM. These include a variety of experiments, as well as astronomical surveys. Until now, it has not been possible to find evidence for DM particles in experiments, and it remains to be seen whether this will ever be possible. Thus, the only way to access the physics of DM for us today is through its influence on cosmological structures. In order to draw conclusions about the nature of DM from observations, we must understand the phenomenology of the various DM candidates. Since the formation of cosmic structures is a non-linear problem and several physical processes interacting with each other play an important role, especially at the level of galaxies, it is challenging to study DM analytically. Instead, simulations play a key role as a tool for studying the behaviour of DM models, making predictions and comparing them to observations.

In this thesis, we have developed a new numerical scheme that allows us to study a specific class of DM models. Before, it has not been possible to study fSIDM within the cosmological context. These DM models typically scatter about a tiny angle and thus need to interact frequently to leave a significant imprint in the DM distribution. Through a number of test problems, we have demonstrated the capability of our novel scheme for fSIDM to model the DM physics accurately. These are the very first simulations that faithfully model fSIDM from first principles. With the help of this new method, we have studied mergers of galaxies and galaxy clusters, as well as cosmological structure formation. We have focused on the angular dependence of the self-interactions to improve our understanding of qualitative differences between rSIDM and fSIDM. For our galaxy and galaxy cluster mergers studies, we investigated the offset between the DM component and galaxies for various MMRs. But we also investigated additional properties, such as halo shape and morphology. In our cosmological studies, we found a vanishing effect of self-interactions on large scales and investigated on small scales the density and shape profiles of haloes. Moreover, we discussed degeneracies between rare and frequent scattering as well as limits on the fSIDM cross-section for the first time. Overall, our studies included many aspects of the DM distribution and its dependence on DM model parameters. In the

following, we give the most important finding of our investigation:

- fSIDM could explain larger DM–galaxy offsets in mergers of galaxy clusters compared to rSIDM.
- Offset may not be the only quantity of interest for studies of mergers but also the morphological differences between fSIDM and rSIDM.
- Differences between frequent and rare scattering tend to be magnified for more unequal mass mergers.
- In the cosmological context rSIDM and fSIDM behave similarly in many aspects, which allows transferring rSIDM constraints to fSIDM.
- But we find that the abundance of satellites is substantially suppressed for frequent self-interactions compared to rare scattering.

Hence, there could be a chance to distinguish between rare and frequent self-interactions observationally with the help of systems that are far from equilibrium. Therefore multiple independent measures of different quantities like the shape or the number of satellites are needed. However, this requires further studies as we describe in Section. 6.2.

On a high abstraction level, we can conclude from this thesis that

- it is possible to model frequent scattering within N-body simulations
- and that it is relevant to do so because rare and frequent self-interactions result in a qualitatively different phenomenology.

In the best case, this work is a valuable contribution to the manifold DM research and brings us a little closer to solving the DM puzzle. In the next section, we provide an outlook on how the seemingly endless quest for DM may continue, focusing on SIDM.

6.2 Outlook

A plethora of DM models has been investigated through a huge variety of studies pursuing very different approaches. Nevertheless, we still know very little about the nature of DM. To improve on this situation and limit the available parameter space for DM models is the task of future studies.

Theory

To gain insight into the nature of DM, it is likely to be unavoidable to run computationally costly simulations and compare their results with observations to constrain DM models. For this purpose, it is important to model all relevant physical processes accurately. In this regard, there is still a lot of work to do. We have run DM-only simulations but baryons can play a crucial role on small scales. Thus future studies of fSIDM should incorporate

baryons, i.e. running hydrodynamical simulations including the relevant subgrid physics, such as star formation, supernovae, black holes and more. Other authors have already done so for simulations of rSIDM (e.g. Vogelsberger et al., 2014; Robertson et al., 2019; Sameie et al., 2021; Shen et al., 2021, 2022; Despali et al., 2022). The baryonic processes potentially contribute to a solution of small-scale issues but modelling them via subgrid prescriptions is unfortunately subject to considerable uncertainties. For example, the feedback of supernovae can create density cores in DM haloes too, but the strength of this effect in real galaxies is still under investigation. The effects of DM physics and baryonic processes can be qualitatively different such that degeneracies may help to learn about both, the role of baryons and DM physics (Burger et al., 2022). Consequently, improvements in modelling star formation, supernovae and AGNs will also help constrain DM physics. Numerous efforts are ongoing and will allow for more accurate simulations.

From the particle physics side, there exist a variety of interesting models. The time that mainly isotropic and velocity-independent scattering is studied has been passed. Nowadays, many studies assume more complicated models with cross-sections that are typically anisotropic and depend on the relative velocity of the scattering particles. Even further model variations with inelastic scattering or multi-component DM have been studied. As we have discussed in Section 2.3, some of the DM candidates may require to adjust the initial conditions of the simulations. In the future, we are likely to see studies of further model variations that will help us understand the phenomenological consequences of microphysical DM properties.

Our plan for future fSIDM studies is to include baryons in the simulations with their related processes such as star formation and supernovae. Furthermore, we want to study cross-sections that depend on the relative particle velocity as one would expect it for light mediator models. Ideally, we would be able to compare the simulation results to observations and derive new bounds on the DM self-interactions. If possible, this would not only include constraints on the momentum transfer cross-section but also the angular dependence of the differential cross-section.

Observations

Besides the theoretical and numerical efforts of modelling SIDM, we expect that there will be a lot of progress on the observational side with new instruments and their surveys. Recent and upcoming telescopes such as 4MOST (de Jong, 2019; Driver et al., 2019; Liske & Mainieri, 2019, e.g.), Euclid (Euclid Collaboration et al., 2020), James Webb Space Telescope (JWST, e.g. Windhorst et al., 2009), Rubin Observatory (Zhan & Tyson, 2018), Roman (Spergel et al., 2015) and the Square Kilometer Array (SKA, e.g. Carilli & Rawlings, 2004; Braun et al., 2015) will allow to tighten the constraints on DM models. In the following we highlight some aspects, for a more detailed review we refer to Buckley & Peter (2018) or the one by Drlica-Wagner et al. (2019) dedicated to the Rubin Observatory.

Offsets between galaxies and the DM component in mergers of galaxy clusters could

provide evidence for DM self-interactions. No significant offsets have been found to date, but with upcoming surveys, this could change. Wide-field radio surveys thanks to SKA and weak lensing studies with telescopes like Roman, will observe more objects and allow for measurements with higher accuracy. However, current upper limits from cluster core sizes might imply a fairly small offset for mergers, especially for rSIDM, whether those could be observable needs further investigation. Nevertheless, DM–galaxy offsets are of interest as an independent measure that in combination with other measures could allow constraining the angular dependence of the self-interactions. Even if no significant offsets will be found this allows to put upper limits on the self-interaction cross-section. A null observation would imply tighter constraints on fSIDM than rSIDM. Eventually, also BCG oscillations in merger remnants could give insight into the nature of DM. However, to be able to judge this, further work from the simulation side is needed.

Stafford et al. (2021) investigated the constraining power of weak lensing surveys with upcoming telescopes such as Euclid, Rubin Observatory and Roman. They found that cosmic shear measurements should be able to rule out SIDM models with $\sigma/m_\chi > 10\,\mathrm{cm}^2\,\mathrm{g}^{-1}$. In comparison to other methods (see Section 2.3.4) this seems to be weak. But at least it is an independent measure.

The JWST will be able to observe galaxies from the era of reionization. New observations of this epoch of the Universe are of interest for DM physics and may allow for new constraints on models such as WDM and SIDM. Observations of the star formation of ultra-faint dwarf galaxies and the matter power spectrum at early cosmic times could lead to further bounds on DM models (e.g. Governato et al., 2015; Chau et al., 2017; Boylan-Kolchin et al., 2015, 2016; Weisz & Boylan-Kolchin, 2017).

The SKA will observe the gas dynamics ($\mathrm{H_I}$ data) in numerous galaxies including dwarfs with an unprecedented spatial resolution and sensitivity at redshift $z \simeq 0$ (Duffy et al., 2012; de Blok et al., 2015; Adams & Oosterloo, 2018; Koribalski et al., 2020). These observations are complementary to upcoming optical and near-infrared surveys probing the stellar content of dwarfs, such as Euclid and the Rubin Observatory. Additionally, weak lensing studies with these telescopes may allow us to infer the density profile of dwarf galaxies. In consequence, we will have a wealth of data on dwarfs which will provide a valuable testbed for DM physics. The abundance of satellites is also of particular interest to constrain DM models. In Section 5.3.9 we have shown that it may allow us to distinguish between rSIDM and fSIDM if combined with an independent measure. Future surveys will provide a wealth of data, not only about MW satellites, but also about the satellites from other galaxies. In this context, Gaia has already provided valuable information about the MW that allows us to study DM physics. Forthcoming data releases of Gaia (DR4, DR5) will improve the situation even further. In addition, we will also gain more knowledge about Galactic and extragalactic stellar streams, which could allow drawing new conclusions about DM (e.g. Pearson et al., 2022).

Overall, the planned missions and surveys suggest that the coming years will be exciting

for the research on DM. We can be curious about the new insights we will gain into the nature of DM.

List of Figures

List of Tables

Bibliography

Aartsen M., et al., 2016, JCAP, 2016, 022

Abbott B. P., et al., 2017, Phys. Rev. Lett., 119, 161101

Ackerman L., Buckley M. R., Carroll S. M., Kamionkowski M., 2009, Phys. Rev. D, 79, 023519

Ackermann M., et al., 2015, Phys. Rev. Lett., 115

Adams E. A. K., Oosterloo T. A., 2018, A&A, 612, A26

Adrián-Martínez S., et al., 2016, Physics Letters B, 759, 69

Agnese R., et al., 2018, Phys. Rev. Lett., 120

Agnese R., et al., 2019, Phys. Rev. D, 99

Agrawal P., Cyr-Racine F.-Y., Randall L., Scholtz J., 2017, JCAP, 2017, 022–022

Ahn K., Shapiro P. R., 2005, MNRAS, 363, 1092

Allgood B., Flores R. A., Primack J. R., Kravtsov A. V., Wechsler R. H., Faltenbacher A., Bullock J. S., 2006, MNRAS, 367, 1781

Amodeo, S. Ettori, S. Capasso, R. Sereno, M. 2016, A&A, 590, A126

Andrade K. E., Fuson J., Gad-Nasr S., Kong D., Minor Q., Roberts M. G., Kaplinghat M., 2021, MNRAS, 510, 54

Angulo R. E., Hahn O., 2022, Living Reviews in Computational Astrophysics, 8

Angus G. W., Diaferio A., 2009, MNRAS, 396, 887

Aprile E., et al., 2019a, Phys. Rev. Lett., 123

Aprile E., et al., 2019b, Phys. Rev. Lett., 123

Arbey A., Mahmoudi F., 2021, Progress in Particle and Nuclear Physics, p. 103865

Arnaud Q., et al., 2018, Phys. Rev. D, 97

Arun K., Gudennavar S., Sivaram C., 2017, Advances in Space Research, 60, 166

Atwood W. B., et al., 2009, ApJ, 697, 1071

Bahé Y. M., 2021, MNRAS, 505, 1458

Bai Y., Hamada Y., 2018, Physics Letters B, 781, 187

Baker T., et al., 2021, Rev. Mod. Phys., 93, 015003

Balberg S., Shapiro S. L., 2002, Phys. Rev. Lett., 88, 101301

Balberg S., Shapiro S. L., Inagaki S., 2002, ApJ, 568, 475

Banerjee A., Adhikari S., Dalal N., More S., Kravtsov A., 2020, JCAP, 2020, 024

Bar N., Blas D., Blum K., Kim H., 2021, Phys. Rev. D, 104, 043021

Bartelmann M., 2010, Classical and Quantum Gravity, 27, 233001

Battye R., Garbrecht B., McDonald J., Pace F., Srinivasan S., 2020, Phys. Rev. D, 102

Behroozi P. S., Wechsler R. H., Wu H.-Y., 2012, ApJ, 762, 109

Bennett C. L., et al., 1996, ApJ, 464, L1

Bennett C. L., et al., 2003, ApJS, 148, 1

Bennett C. L., et al., 2013, ApJS, 208, 20

Bento M. C., Bertolami O., Rosenfeld R., Teodoro L., 2000, Phys. Rev. D, 62, 041302

Benítez-Llambay A., Frenk C. S., Ludlow A. D., Navarro J. F., 2019, MNRAS, 488, 2387

Berezhiani Z., Dolgov A., Mohapatra R., 1996, Physics Letters B, 375, 26

Bett P., 2012, MNRAS, 420, 3303

Bhattacharyya S., Adhikari S., Banerjee A., More S., Kumar A., Nadler E. O., Chatterjee S., 2022, ApJ, 932, 30

Blinnikov S. I., Khlopov M. Y., 1983, Soviet Ast., 27, 371

Boddy K. K., Feng J. L., Kaplinghat M., Shadmi Y., Tait T. M. P., 2014, Phys. Rev. D, 90, 095016

Boddy K. K., Kaplinghat M., Kwa A., Peter A. H. G., 2016, Phys. Rev. D, 94, 123017

Boddy K. K., et al., 2022, Astrophysical and Cosmological Probes of Dark Matter (arXiv:2203.06380)

Boldrini P., 2022, Galaxies, 10

Boldrini P., Mohayaee R., Silk J., 2020, MNRAS, 492, 3169

Bonafede A., Dolag K., Stasyszyn F., Murante G., Borgani S., 2011, MNRAS, 418, 2234

Bondarenko K., Sokolenko A., Boyarsky A., Robertson A., Harvey D., Revaz Y., 2021, JCAP, 2021, 043

Boylan-Kolchin M., Springel V., White S. D. M., Jenkins A., Lemson G., 2009, MNRAS, 398, 1150

Boylan-Kolchin M., Weisz D. R., Johnson B. D., Bullock J. S., Conroy C., Fitts A., 2015, MNRAS, 453, 1503

Boylan-Kolchin M., Weisz D. R., Bullock J. S., Cooper M. C., 2016, MNRAS, 462, L51

Bradač M., Allen S. W., Treu T., Ebeling H., Massey R., Morris R. G., von der Linden A., Applegate D., 2008, ApJ, 687, 959

Braun R., Bourke T. L., Green J. A., Keane E., Wagg J., 2015, PoS, AASKA14, 174

Bringmann T., Kahlhoefer F., Schmidt-Hoberg K., Walia P., 2017, Phys. Rev. Lett., 118, 141802

Brooks A. M., Zolotov A., 2014, ApJ, 786, 87

Brooks A. M., Kuhlen M., Zolotov A., Hooper D., 2013, ApJ, 765, 22

Buckley M. R., Fox P. J., 2010, Phys. Rev. D, 81, 083522

Buckley M. R., Peter A. H., 2018, Physics Reports, 761, 1

Buckley M. R., Zavala J., Cyr-Racine F.-Y., Sigurdson K., Vogelsberger M., 2014, Phys. Rev. D, 90

Buen-Abad M. A., Essig R., McKeen D., Zhong Y.-M., 2022, Physics Reports, 961, 1

Bullock J. S., Boylan-Kolchin M., 2017, ARA&A, 55, 343

Burger J. D., Zavala J., Sales L. V., Vogelsberger M., Marinacci F., Torrey P., 2022, MNRAS

Burgess C., Pospelov M., ter Veldhuis T., 2001, Nuclear Physics B, 619, 709

Burkert A., 2000, ApJ, 534, L143

Buschmann M., Co R. T., Dessert C., Safdi B. R., 2021, Phys. Rev. Lett., 126, 021102

Cappellari M., et al., 2006, MNRAS, 366, 1126

Carilli C., Rawlings S., 2004, New Astron. Rev., 48, 979

Carlson E. D., Machacek M. E., Hall L. J., 1992, ApJ, 398, 43

Carr B., Kühnel F., 2022, SciPost Physics Lecture Notes

Chan T. K., Kereš D., Oñorbe J., Hopkins P. F., Muratov A. L., Faucher-Giguère C.-A., Quataert E., 2015, MNRAS, 454, 2981

Chandrasekhar S., 1943, ApJ, 97, 255

Chau A., Mayer L., Governato F., 2017, ApJ, 845, 17

Chu X., Garcia-Cely C., Murayama H., 2019, Phys. Rev. Lett., 122, 071103

Chu X., Garcia-Cely C., Murayama H., 2020, JCAP, 2020, 043

Chua K. T. E., Dibert K., Vogelsberger M., Zavala J., 2020, MNRAS, 500, 1531

Churazov E., et al., 2010, MNRAS, 404, 1165

Cintio A. D., Brook C. B., Dutton A. A., Macciò A. V., Stinson G. S., Knebe A., 2014, MNRAS, 441, 2986

Cline J. M., Liu Z., Xue W., 2012, Phys. Rev. D, 85, 101302

Cline J. M., Liu Z., Moore G. D., Xue W., 2014, Phys. Rev. D, 89, 043514

Clowe D., Bradač M., Gonzalez A. H., Markevitch M., Randall S. W., Jones C., Zaritsky D., 2006, ApJ, 648, L109

Cole D. R., Dehnen W., Read J. I., Wilkinson M. I., 2012, MNRAS, 426, 601

Colin P., Avila-Reese V., Valenzuela O., 2000, ApJ, 542, 622

Colin P., Avila-Reese V., Valenzuela O., Firmani C., 2002, ApJ, 581, 777–793

Correa C. A., 2021, MNRAS, 503, 920

Craig M. W., Davis M., 2001, New Astron., 6, 425

Creasey P., Sameie O., Sales L. V., Yu H.-B., Vogelsberger M., Zavala J., 2017, MNRAS, 468, 2283

Cui X., et al., 2017, Phys. Rev. Lett., 119

Cyr-Racine F.-Y., Sigurdson K., 2013, Phys. Rev. D, 87, 103515

Cyr-Racine F.-Y., de Putter R., Raccanelli A., Sigurdson K., 2014, Phys. Rev. D, 89

Cyr-Racine F.-Y., Sigurdson K., Zavala J., Bringmann T., Vogelsberger M., Pfrommer C., 2016, Phys. Rev. D, 93, 123527

Davé R., Spergel D. N., Steinhardt P. J., Wandelt B. D., 2001, ApJ, 547, 574

Davis M., Peebles P. J. E., 1983, ApJ, 267, 465

Dawson W. A., 2013, PhD thesis, University of California, Davis

Dawson W. A., et al., 2012, ApJ, 747, L42

Day F., Krippendorf S., 2018, Galaxies, 6, 45

Deriaz E., Peirani S., 2018, Multiscale Modeling & Simulation, 16, 583

Despali G., Sparre M., Vegetti S., Vogelsberger M., Zavala J., Marinacci F., 2019, MNRAS, 484, 4563–4573

Despali G., Walls L. G., Vegetti S., Sparre M., Vogelsberger M., Zavala J., 2022, Constraining SIDM with halo shapes: revisited predictions from realistic simulations of early-type galaxies (arXiv:2204.12502)

Di Cintio A., Brook C. B., Macciò A. V., Stinson G. S., Knebe A., Dutton A. A., Wadsley J., 2013, MNRAS, 437, 415

Dodelson S., Widrow L. M., 1994, Phys. Rev. Lett., 72, 17

Dolag K., Borgani S., Murante G., Springel V., 2009, MNRAS, 399, 497

Donnert J. M. F., 2014, MNRAS, 438, 1971

Donnert J. M. F., Beck A. M., Dolag K., Röttgering H. J. A., 2017, MNRAS, 471, 4587

Dooley G. A., Peter A. H. G., Vogelsberger M., Zavala J., Frebel A., 2016, MNRAS, 461, 710

Doubrawa L., Machado R. E. G., Laganá T. F., Lima Neto G. B., Monteiro-Oliveira R., Cypriano E. S., 2020, MNRAS, 495, 2022

Driver S. P., et al., 2019, Published in The Messenger vol. 175, pp. 46-49, March 2019.

Drlica-Wagner A., et al., 2019, Probing the Fundamental Nature of Dark Matter with the Large Synoptic Survey Telescope (arXiv:1902.01055)

Duffy A. R., Meyer M. J., Staveley-Smith L., Bernyk M., Croton D. J., Koribalski B. S., Gerstmann D., Westerlund S., 2012, MNRAS, 426, 3385

Dutton A. A., Macciò A. V., 2014, MNRAS, 441, 3359

Dyer C. C., Ip P. S. S., 1993, ApJ, 409, 60

Ebisu T., Ishiyama T., Hayashi K., 2022, Phys. Rev. D, 105

Eckert D., Ettori S., Robertson A., Massey R., Pointecouteau E., Harvey D., McCarthy I. G., 2022, Constraints on dark matter self-interaction from the internal density profiles of X-COP galaxy clusters (arXiv:2205.01123)

Efstathiou G., Schaye J., Theuns T., 2000, Philosophical Transactions of the Royal Society of London. Series A: Mathematical, Physical and Engineering Sciences, 358, 2049

Eke V. R., Cole S., Frenk C. S., 1996, MNRAS, 282, 263

El-Badry K., Wetzel A., Geha M., Hopkins P. F., Kereš D., Chan T. K., Faucher-Giguère C.-A., 2016, ApJ, 820, 131

El-Badry K., et al., 2017, MNRAS, 473, 1930

Elahi P. J., Cañas R., Poulton R. J. J., Tobar R. J., Willis J. S., Lagos C. d. P., Power C., Robotham A. S. G., 2019, Publications of the Astronomical Society of Australia, 36

Elbert O. D., Bullock J. S., Garrison-Kimmel S., Rocha M., Oñorbe J., Peter A. H. G., 2015, MNRAS, 453, 29

Elbert O. D., Bullock J. S., Kaplinghat M., Garrison-Kimmel S., Graus A. S., Rocha M., 2018, ApJ, 853, 109

Essig R., McDermott S. D., Yu H.-B., Zhong Y.-M., 2019, Phys. Rev. Lett., 123, 121102

Euclid Collaboration et al., 2020, A&A, 642, A191

Fairbairn M., 2022, Symmetry, 14

Fan J., Katz A., Randall L., Reece M., 2013, Physics of the Dark Universe, 2, 139

Feng J. L., Kaplinghat M., Tu H., Yu H.-B., 2009, JCAP, 2009, 004

Ferreira E. G. M., 2021, A&A Rev., 29, 7

Fischer M. S., Brüggen M., Schmidt-Hoberg K., Dolag K., Kahlhoefer F., Ragagnin A., Robertson A., 2021a, MNRAS, 505, 851

Fischer M. S., Brüggen M., Schmidt-Hoberg K., Dolag K., Ragagnin A., Robertson A., 2021b, MNRAS, 510, 4080

Fischer M. S., Brüggen M., Schmidt-Hoberg K., Dolag K., Kahlhoefer F., Ragagnin A., Robertson A., 2022, Cosmological simulations with rare and frequent dark matter self-interactions (arXiv:2205.02243)

Foot R., 2004, Int. J. Mod. Phys. D, 13, 2161

Foot R., Vagnozzi S., 2015, Phys. Rev. D, 91, 023512

Foreman-Mackey D., Hogg D. W., Lang D., Goodman J., 2013, PASP, 125, 306

Frandsen M. T., Sarkar S., Schmidt-Hoberg K., 2011, Phys. Rev. D, 84, 051703

Franx M., Illingworth G., de Zeeuw T., 1991, ApJ, 383, 112

Fry A. B., et al., 2015, MNRAS, 452, 1468–1479

Gaia Collaboration et al., 2016, A&A, 595, A1

Galilei G., 1610, Sidereus nuncius. Thomas Baglioni, doi:10.3931/e-rara-695

Gardner S., McDermott S. D., Yanny B., 2021, Progress in Particle and Nuclear Physics, 121, 103904

Garzilli A., Magalich A., Ruchayskiy O., Boyarsky A., 2021, MNRAS, 502, 2356

Genina A., et al., 2018, MNRAS, 474, 1398

Genina A., Read J. I., Fattahi A., Frenk C. S., 2021, MNRAS, 510, 2186

Gilman D., Bovy J., Treu T., Nierenberg A., Birrer S., Benson A., Sameie O., 2021, MNRAS, 507, 2432

Gnedin O. Y., Ostriker J. P., 2001, ApJ, 561, 61

Governato F., et al., 2012, MNRAS, 422, 1231

Governato F., et al., 2015, MNRAS, 448, 792

Griest K., 1988, Phys. Rev. D, 38, 2357

Grossi M., Branchini E., Dolag K., Matarrese S., Moscardini L., 2008, MNRAS, 390, 438

Han J., Cole S., Frenk C. S., Benitez-Llambay A., Helly J., 2017, MNRAS, 474, 604–617

Harris C. R., et al., 2020, Nature, 585, 357–362

Harvey D., et al., 2014, MNRAS, 441, 404

Harvey D., Massey R., Kitching T., Taylor A., Tittley E., 2015, Science, 347, 1462

Harvey D., Robertson A., Massey R., Kneib J.-P., 2017, MNRAS, 464, 3991

Harvey D., Chisari N. E., Robertson A., McCarthy I. G., 2021, MNRAS, 506, 441–451

Hernquist L., 1990, ApJ, 356, 359

Hooper D., Serpico P. D., 2007, Phys. Rev. Lett., 99

Hopkins P. F., et al., 2018, MNRAS, 480, 800

Hu W., Barkana R., Gruzinov A., 2000, Phys. Rev. Lett., 85, 1158

Hubble E. P., 1929, ApJ, 69, 103

Hunter J. D., 2007, Computing in Science Engineering, 9, 90

Huo R., Kaplinghat M., Pan Z., Yu H.-B., 2018, Physics Letters B, 783, 76

Huo R., Yu H.-B., Zhong Y.-M., 2020, JCAP, 2020, 051

Jee M. J., Hughes J. P., Menanteau F., Sifón C., Mandelbaum R., Barrientos L. F., Infante L., Ng K. Y., 2014, ApJ, 785, 20

Jee M. J., et al., 2015, ApJ, 802, 46

Kahlhoefer F., 2017, International Journal of Modern Physics A, 32, 1730006

Kahlhoefer F., Schmidt-Hoberg K., Frandsen M. T., Sarkar S., 2014, MNRAS, 437, 2865

Kahlhoefer F., Schmidt-Hoberg K., Kummer J., Sarkar S., 2015, MNRAS, 452, L54

Kahlhoefer F., Schmidt-Hoberg K., Wild S., 2017, JCAP, 2017, 003

Kahlhoefer F., Kaplinghat M., Slatyer T. R., Wu C.-L., 2019, JCAP, 2019, 010

Kamada A., Kaplinghat M., Pace A. B., Yu H.-B., 2017, Phys. Rev. Lett., 119, 111102

Kant I., 1755, Allgemeine Naturgeschichte und Theorie des Himmels. Johann Friederich Petersen

Kant I., 1787, Kritik der reinen Vernunft. Johann Friederich Hartknoch

Kaplan D. E., Krnjaic G. Z., Rehermann K. R., Wells C. M., 2010, JCAP, 2010, 021

Kaplinghat M., Keeley R. E., Linden T., Yu H.-B., 2014, Phys. Rev. Lett., 113, 021302

Kaplinghat M., Tulin S., Yu H.-B., 2016, Phys. Rev. Lett., 116, 041302

Kaplinghat M., Valli M., Yu H.-B., 2019, MNRAS, 490, 231

Kim S. Y., Peter A. H. G., Wittman D., 2017, MNRAS, 469, 1414

Kim S. Y., Peter A. H. G., Hargis J. R., 2018, Phys. Rev. Lett., 121, 211302

Klypin A. A., Trujillo-Gomez S., Primack J., 2011, ApJ, 740, 102

Knebe A., et al., 2013, MNRAS, 435, 1618

Knollmann S. R., Knebe A., 2009, ApJS, 182, 608–624

Kochanek C. S., White M., 2000, ApJ, 543, 514

Koda J., Shapiro P. R., 2011, MNRAS, 415, 1125

Kolb E. W., Seckel D., Turner M. S., 1985, Nature, 314, 415

Komatsu E., et al., 2011, ApJS, 192, 18

Kong D., Kaplinghat M., Yu H.-B., Fraternali F., Piña P. E. M., 2022, The Odd Dark Matter Halos of Isolated Gas-Rich Ultra-Diffuse Galaxies (arXiv:2204.05981)

Koribalski B. S., et al., 2020, Astrophysics and Space Science, 365

Kormann K., Reuter K., Rampp M., 2019, The International Journal of High Performance Computing Applications, 33, 924

Kummer J., 2019, PhD thesis, University of Hamburg, Germany

Kummer J., Kahlhoefer F., Schmidt-Hoberg K., 2018, MNRAS, 474, 388

Kummer J., Brüggen M., Dolag K., Kahlhoefer F., Schmidt-Hoberg K., 2019, MNRAS, 487, 354

Kusenko A., Steinhardt P. J., 2001, Phys. Rev. Lett., 87, 141301

Lacey C., Cole S., 1993, MNRAS, 262, 627

Lage C., Farrar G., 2014, ApJ, 787, 144

Lelli F., 2022, Nature Astronomy, 6, 35

Limousin M., Beauchesne B., Jullo E., 2022, Dark Matter in Galaxy Clusters: a Parametric Strong Lensing Approach (arXiv:2202.02992)

Liske J., Mainieri V., 2019, The Messenger, 177, 61

Loeb A., 2022, ApJ, 929, L24

Loeb A., Weiner N., 2011, Phys. Rev. Lett., 106

Ludlow A. D., Schaye J., Bower R., 2019, MNRAS, 488, 3663

Lynden-Bell D., Eggleton P. P., 1980, MNRAS, 191, 483

Machado R. E. G., Lima Neto G. B., 2015, MNRAS, 447, 2915–2924

Machado R. E. G., Monteiro-Oliveira R., Lima Neto G. B., Cypriano E. S., 2015, MNRAS, 451, 3309

Maciejewski M., Colombi S., Springel V., Alard C., Bouchet F. R., 2009, MNRAS, 396, 1329–1348

Markevitch M., 2005, Chandra observation of the most interesting cluster in the Universe (arXiv:astro-ph/0511345)

Markevitch M., Gonzalez A. H., Clowe D., Vikhlinin A., Forman W., Jones C., Murray S., Tucker W., 2004, ApJ, 606, 819

Martizzi D., Teyssier R., Moore B., 2013, MNRAS, 432, 1947

Massey R., Kitching T., Richard J., 2010, Reports on Progress in Physics, 73, 086901

Mastropietro C., Burkert A., 2008, MNRAS, 389, 967

Meadows N., Navarro J. F., Santos-Santos I., Benítez-Llambay A., Frenk C., 2019, MNRAS, 491, 3336

Meneghetti M., Yoshida N., Bartelmann M., Moscardini L., Springel V., Tormen G., White S. D. M., 2001, MNRAS, 325, 435

Meneghetti M., et al., 2020, Science, 369, 1347

Milgrom M., 1983, ApJ, 270, 365

Miralda-Escude J., 2002, ApJ, 564, 60

Mohapatra R. N., Teplitz V. L., 2000, Phys. Rev. D, 62, 063506

Mohapatra R. N., Nussinov S., Teplitz V. L., 2002, Phys. Rev. D, 66, 063002

Moliere G., 1948, Zeitschrift für Naturforschung A, 3, 78

Molnar S. M., Broadhurst T., 2015, ApJ, 800, 37

Molnar S. M., Broadhurst T., 2017, ApJ, 841, 46

Molnar S. M., Broadhurst T., 2018, ApJ, 862, 112

Monaghan J. J., Lattanzio J. C., 1985, A&A, 149, 135

Mondino C., Taki A.-M., Van Tilburg K., Weiner N., 2020, Phys. Rev. Lett., 125, 111101

Monteiro-Oliveira R., Cypriano E. S., Machado R. E. G., Lima Neto G. B., Ribeiro A. L. B., Sodré L. J., Dupke R., 2016, MNRAS, 466, 2614

Moore B., Gelato S., Jenkins A., Pearce F. R., Quilis V., 2000, ApJ, 535, L21

More S., Kravtsov A. V., Dalal N., Gottlöber S., 2011, ApJS, 195, 4

Moura M. T., Machado R. E. G., Monteiro-Oliveira R., 2020, MNRAS, 500, 1858

Nadler E. O., Banerjee A., Adhikari S., Mao Y.-Y., Wechsler R. H., 2020, ApJ, 896, 112

Nadler E. O., Banerjee A., Adhikari S., Mao Y.-Y., Wechsler R. H., 2021, ApJ, 920, L11

Navarro J. F., Frenk C. S., White S. D. M., 1996, ApJ, 462, 563

Ng K. Y., Pillepich A., Wittman D., Dawson W. A., Hernquist L., Nelson D. R., 2017, Offsets between member galaxies and dark matter in clusters: a test with the Illustris simulation (`arXiv:1703.00010`)

Nishikawa H., Boddy K. K., Kaplinghat M., 2020, Phys. Rev. D, 101, 063009

Oh K. S., Lin D. N. C., Richer H. B., 2000, ApJ, 531, 727

Oman K. A., et al., 2015, MNRAS, 452, 3650

Oman K. A., Marasco A., Navarro J. F., Frenk C. S., Schaye J., Benítez-Llambay A. r., 2019, MNRAS, 482, 821

Outmezguine N. J., Boddy K. K., Gad-Nasr S., Kaplinghat M., Sagunski L., 2022, Universal gravothermal evolution of isolated self-interacting dark matter halos for velocity-dependent cross sections (arXiv:2204.06568)

Oñorbe J., Boylan-Kolchin M., Bullock J. S., Hopkins P. F., Kereš D., Faucher-Giguère C.-A., Quataert E., Murray N., 2015, MNRAS, 454, 2092

Palanque-Delabrouille N., Yèche C., Schöneberg N., Lesgourgues J., Walther M., Chabanier S., Armengaud E., 2020, JCAP, 2020, 038

Palmroth M., et al., 2018, Living Reviews in Computational Astrophysics, 4, 1

Particle Data Group et al., 2020, Progress of Theoretical and Experimental Physics, 2020

Pearson S., Price-Whelan A. M., Hogg D. W., Seth A. C., Sand D. J., Hunt J. A. S., Crnojevic D., 2022, Mapping Dark Matter with Extragalactic Stellar Streams: the Case of Centaurus A (arXiv:2205.12277)

Peccei R. D., Quinn H. R., 1977, Phys. Rev. Lett., 38, 1440

Pedregosa F., et al., 2011, Journal of Machine Learning Research, 12, 2825

Peel A., Lanusse F., Starck J.-L., 2017, ApJ, 847, 23

Peirani S., et al., 2017, MNRAS, 472, 2153

Perivolaropoulos L., Skara F., 2021, Challenges for ΛCDM: An update (arXiv:2105.05208)

Peter A. H. G., Rocha M., Bullock J. S., Kaplinghat M., 2013, MNRAS, 430, 105

Pillepich A., et al., 2017, MNRAS, 473, 4077

Pineda J. C. B., Hayward C. C., Springel V., Mendes de Oliveira C., 2016, MNRAS, 466, 63

Planck Collaboration et al., 2014, A&A, 571, A1

Planck Collaboration et al., 2016, A&A, 594, A1

Planck Collaboration et al., 2020, A&A, 641, A1

Planelles S., Borgani S., Fabjan D., Killedar M., Murante G., Granato G. L., Ragone-Figueroa C., Dolag K., 2013, MNRAS, 438, 195

Pollack J., Spergel D. N., Steinhardt P. J., 2015, ApJ, 804, 131

Pontzen A., Governato F., 2012, MNRAS, 421, 3464

Pontzen A., Governato F., 2014, Nature, 506, 171

Poole G. B., Fardal M. A., Babul A., McCarthy I. G., Quinn T., Wadsley J., 2006, MNRAS, 373, 881

Power C., Navarro J. F., Jenkins A., Frenk C. S., White S. D. M., Springel V., Stadel J., Quinn T., 2003, MNRAS, 338, 14

Rampf C., 2021, Reviews of Modern Plasma Physics, 5, 10

Randall S. W., Markevitch M., Clowe D., Gonzalez A. H., Bradač M., 2008, ApJ, 679, 1173

Rasia E., et al., 2015, ApJ, 813, L17

Ray T. S., Sarkar S., Shaw A. K., 2022, Constraints on dark matter self-interaction from galactic core size (arXiv:2202.12247)

Read J. I., Gilmore G., 2005, MNRAS, 356, 107

Read J. I., Goerdt T., Moore B., Pontzen A. P., Stadel J., Lake G., 2006, MNRAS, 373, 1451

Read J. I., Iorio G., Agertz O., Fraternali F., 2016, MNRAS, 462, 3628

Robertson A., 2021, MNRAS, 504, L7

Robertson A., Massey R., Eke V., 2017a, MNRAS, 465, 569

Robertson A., Massey R., Eke V., 2017b, MNRAS, 467, 4719

Robertson A., et al., 2018, MNRAS, 476, L20–L24

Robertson A., Harvey D., Massey R., Eke V., McCarthy I. G., Jauzac M., Li B., Schaye J., 2019, MNRAS, 488, 3646–3662

Robertson A., Massey R., Eke V., Schaye J., Theuns T., 2020, MNRAS, 501, 4610–4634

Robles V. H., Kelley T., Bullock J. S., Kaplinghat M., 2019, MNRAS, 490, 2117

Rocha M., Peter A. H. G., Bullock J. S., Kaplinghat M., Garrison-Kimmel S., Oñorbe J., Moustakas L. A., 2013, MNRAS, 430, 81–104

Rodríguez-Torres S. A., et al., 2016, MNRAS, 460, 1173

Rogers K. K., Peiris H. V., 2021, Phys. Rev. Lett., 126, 071302

Roper F. A., Oman K. A., Frenk C. S., Benítez-Llambay A., Navarro J. F., Santos-Santos I. M. E., 2022, The diversity of rotation curves of simulated galaxies with cusps and cores (arXiv:2203.16652)

Rubin V. C., Ford W. Kent J., 1970, ApJ, 159, 379

Sagunski L., Gad-Nasr S., Colquhoun B., Robertson A., Tulin S., 2021, JCAP, 2021, 024

Salucci P., 2019, A&A Rev., 27, 2

Sameie O., Creasey P., Yu H.-B., Sales L. V., Vogelsberger M., Zavala J., 2018, MNRAS, 479, 359

Sameie O., Chakrabarti S., Yu H.-B., Boylan-Kolchin M., Vogelsberger M., Zavala J., Hernquist L., 2020, Simulating the "hidden giant" in cold and self-interacting dark matter models (arXiv:2006.06681)

Sameie O., et al., 2021, MNRAS, 507, 720

Sarkar A., Sethi S. K., Das S., 2017, JCAP, 2017, 012

Schrabback, Tim et al., 2021, A&A, 646, A73

Schutz K., Slatyer T. R., 2015, JCAP, 2015, 021

Semertzidis Y. K., Youn S., 2022, Science Advances, 8, eabm9928

Shao S., Cautun M., Frenk C. S., Reina-Campos M., Deason A. J., Crain R. A., Kruijssen J. M. D., Pfeffer J., 2021, MNRAS, 507, 2339

Shapiro S. L., 2018, Phys. Rev. D, 98, 023021

Shen X., Hopkins P. F., Necib L., Jiang F., Boylan-Kolchin M., Wetzel A., 2021, MNRAS, 506, 4421

Shen X., Brinckmann T., Rapetti D., Vogelsberger M., Mantz A., Zavala J., Allen S. W., 2022, X-ray morphology of cluster-mass haloes in self-interacting dark matter (arXiv:2202.00038)

Shi Y., Zhang Z.-Y., Wang J., Chen J., Gu Q., Yu X., Li S., 2021, ApJ, 909, 20

Silk J., 2017, ApJ, 839, L13

Silverman M., Bullock J. S., Kaplinghat M., Robles V. H., Valli M., 2022, Motivations for a Large Self-Interacting Dark Matter Cross Section from Milky Way Satellites (arXiv:2203.10104)

Sirks E. L., Oman K. A., Robertson A., Massey R., Frenk C., 2022, MNRAS, 511, 5927

Smoot G. F., et al., 1992, ApJ, 396, L1

Sokolenko A., Bondarenko K., Brinckmann T., Zavala J., Vogelsberger M., Bringmann T., Boyarsky A., 2018, JCAP, 2018, 038

Spergel D. N., Steinhardt P. J., 2000, Phys. Rev. Lett., 84, 3760–3763

Spergel D., et al., 2015, Wide-Field InfrarRed Survey Telescope-Astrophysics Focused Telescope Assets WFIRST-AFTA 2015 Report (arXiv:1503.03757)

Springel V., 2005, MNRAS, 364, 1105

Springel V., 2015, N-GenIC: Cosmological structure initial conditions (ascl:1502.003)

Springel V., Farrar G. R., 2007, MNRAS, 380, 911

Springel V., White S. D. M., Tormen G., Kauffmann G., 2001, MNRAS, 328, 726

Springel V., et al., 2005, Nature, 435, 629–636

Springel V., Frenk C. S., White S. D. M., 2006, Nature, 440, 1137–1144

Springel V., Pakmor R., Zier O., Reinecke M., 2021, MNRAS, 506, 2871

Stafford S. G., Brown S. T., McCarthy I. G., Font A. S., Robertson A., Poole-McKenzie R., 2020, MNRAS, 497, 3809

Stafford S. G., McCarthy I. G., Kwan J., Brown S. T., Font A. S., Robertson A., 2021, MNRAS, 508, 2537–2555

Steigman G., Turner M. S., 1985, Nuclear Physics B, 253, 375

Tanaka S., Yoshikawa K., Minoshima T., Yoshida N., 2017, ApJ, 849, 76

Taylor P., Massey R., Jauzac M., Courbin F., Harvey D., Joseph R., Robertson A., 2017, MNRAS, 468, 5004

Todoroki K., Medvedev M. V., 2018, MNRAS, 483, 3983

Tollet E., et al., 2016, MNRAS, 456, 3542

Trevisani N., 2018, Universe, 4

Tsai Y.-D., McGehee R., Murayama H., 2022, Phys. Rev. Lett., 128, 172001

Tulin S., Yu H.-B., 2018, Phys. Rep., 730, 1

Tulin S., Yu H.-B., Zurek K. M., 2013a, Phys. Rev. D, 87

Tulin S., Yu H.-B., Zurek K. M., 2013b, Phys. Rev. Lett., 110

Tullin S., et al., 2012, PLoS ONE, 7, e44270

Turner H. C., Lovell M. R., Zavala J., Vogelsberger M., 2021, MNRAS, 505, 5327

Tweed, D. Devriendt, J. Blaizot, J. Colombi, S. Slyz, A. 2009, A&A, 506, 647

Udalski A., Szymanski M., Kaluzny J., Kubiak M., Mateo M., 1992, Acta Astron., 42, 253

Vannerom D., 2019, PoS, DIS2019, 111

Vargya D., Sanderson R., Sameie O., Boylan-Kolchin M., Hopkins P. F., Wetzel A., Graus A., 2021, Shapes of Milky-Way-Mass Galaxies with Self-Interacting Dark Matter (arXiv:2104.14069)

Vega-Ferrero J., Dana J. M., Diego J. M., Yepes G., Cui W., Meneghetti M., 2020, MNRAS, 500, 247

Viel M., Becker G. D., Bolton J. S., Haehnelt M. G., 2013, Phys. Rev. D, 88, 043502

Villanueva-Domingo P., Mena O., Palomares-Ruiz S., 2021, Frontiers in Astronomy and Space Sciences, 8

Virtanen P., et al., 2020, Nature Methods, 17, 261

Vogelsberger M., Zavala J., 2013, MNRAS, 430, 1722

Vogelsberger M., Zavala J., Loeb A., 2012, MNRAS, 423, 3740

Vogelsberger M., Zavala J., Simpson C., Jenkins A., 2014, MNRAS, 444, 3684

Vogelsberger M., Zavala J., Cyr-Racine F.-Y., Pfrommer C., Bringmann T., Sigurdson K., 2016, Mon. Not. Roy. Astron. Soc., 460, 1399

Vogelsberger M., Zavala J., Schutz K., Slatyer T. R., 2019, MNRAS, 484, 5437

Vogelsberger M., Marinacci F., Torrey P., Puchwein E., 2020, Nature Reviews Physics, 2, 42

Voskresenskaya O., Tarasov A., 2012, Moliere's multiple scattering theory revisited (arXiv:1204.3675)

Wang J.-W., Bi X.-J., Yin P.-F., 2021, Phys. Rev. D, 104

Weinberg S., 1978, Phys. Rev. D, 40, 223

Weisz D. R., Boylan-Kolchin M., 2017, MNRAS, 469, L83

Wilczek F., 1978, Phys. Rev. Lett., 40, 279

Windhorst R. A., et al., 2009, in astro2010: The Astronomy and Astrophysics Decadal Survey. p. 317

Wittman D., Golovich N., Dawson W. A., 2018, ApJ, 869, 104

Wright T., 1750, An original theory or new hypothesis of the universe. H. Chapelle, doi:10.3931/e-rara-28672

Yang D., Yu H.-B., 2021, Phys. Rev. D, 104

Yang D., Yu H.-B., An H., 2020, Phys. Rev. Lett., 125

Yang S., Du X., Zeng Z. C., Benson A., Jiang F., Nadler E. O., Peter A. H. G., 2022, Gravothermal solutions of SIDM halos: mapping from constant to velocity-dependent cross section (arXiv:2205.02957)

Yoshida N., Springel V., White S. D. M., Tormen G., 2000a, ApJ, 535, L103–L106

Yoshida N., Springel V., White S. D. M., Tormen G., 2000b, ApJ, 544, L87–L90

Yoshikawa K., Yoshida N., Umemura M., 2012, ApJ, 762, 116

Zavala J., Vogelsberger M., Walker M. G., 2013, MNRAS, 431, L20

Zavala J., Lovell M. R., Vogelsberger M., Burger J. D., 2019, Phys. Rev. D, 100, 063007

Zemp M., Gnedin O. Y., Gnedin N. Y., Kravtsov A. V., 2011, ApJS, 197, 30

Zeng Z. C., Peter A. H. G., Du X., Benson A., Kim S., Jiang F., Cyr-Racine F.-Y., Vogelsberger M., 2021, Core-collapse, evaporation and tidal effects: the life story of a self-interacting dark matter subhalo (arXiv:2110.00259)

Zentner A., Dandavate S., Slone O., Lisanti M., 2022, A Critical Assessment of Solutions to the Galaxy Diversity Problem (arXiv:2202.00012)

Zhan H., Tyson J. A., 2018, Reports on Progress in Physics, 81, 066901

Zhang C., Yu Q., Lu Y., 2015, ApJ, 813, 129

Zhang C., Yu Q., Lu Y., 2016, ApJ, 820, 85

ZuHone J. A., 2011, ApJ, 728, 54

Zwicky F., 1933, Helvetica Physica Acta, 6, 110

Zwicky F., 1937, ApJ, 86, 217

de Blok W., Fraternali F., Heald G., Adams B., Bosma A., Koribalski B., 2015, PoS, AASKA14, 129

de Jong R. S., 2019, Nature Astronomy, 3, 574

de Laix A. A., Scherrer R. J., Schaefer R. K., 1995, ApJ, 452, 495

de Martino I., Chakrabarty S. S., Cesare V., Gallo A., Ostorero L., Diaferio A., 2020, Universe, 6, 107

van den Aarssen L. G., Bringmann T., Pfrommer C., 2012, Phys. Rev. Lett., 109, 231301

Eidesstattliche Versicherung

Hiermit versichere ich an Eides statt, die vorliegende Dissertationsschrift selbst verfasst und keine anderen als die angegebenen Hilfsmittel und Quellen benutzt zu haben.

Hamburg, den 20ten Juni, 2022

Moritz S. Fischer